ABSTRACT

Title of Dissertation: INVESTIGATING A POSSIBLE LUNAR COLD SPOT FORMATION MECHANISM: MODELING GRANULAR WAVES IN SURFACE REGOLITH USING SOFT SPHERE DISCRETE ELEMENT METHOD

Eric Frizzell
Doctor of Philosophy, 2024

Dissertation Directed by: Dr. Christine Hartzell
Department of Aerospace Engineering

Lunar Cold Spots (LCS) are recently classified ephemeral features appearing as halos around fresh impact craters on the Moon. LCS can only be observed by examining nighttime surface regolith temperatures; there is no other indicator of their presence. They appear cold as compared to the background, a suspected consequence of reduced thermal inertia regolith (to about 40 cm depth) in the halo. The reduction in thermal inertia implies that there is some event associated with the impact that dilates ('fluffs up') surface material over a large radial extent. The LCS halo extends a much greater distance than could be explained by ejecta alone (the average extent is 100 crater radii), with the halo being occasionally punctured by low thermal inertia rays that extend even further. Cold Spots are ubiquitous, occurring across all terrains of the Moon and representing an approximated 1% of total surface area. However, the LCS formation mechanism is unknown. In this work, we use the Soft Sphere Discrete Element Method (SSDEM) to model granular wave propagation in conditions analogous to the lunar surface and near-surface. Our

investigated hypothesis is that LCS form as the result of a granular wave propagating radially outward from an impact site.

First, we characterize the behavior of near surface grains experiencing a laterally propagating granular wavefront when they are exposed to vacuum and low-gravity. We simulate piston impacts into long channels filled randomly with Hertzian particles and observe the emergence of a solitary wave (SW, packetized energy propagation) which lofts particles in its wake. We term this mechanism SW Induced Dilation (SID) and see that the amount of fluffing that occurs is enhanced with larger piston impact speeds and as the initial compaction (packing fraction) of the bed increases. We initially observed this effect in an idealized scenario and so we undertake a scaling analysis to predict how SID would manifest in lunar conditions. We show that particle forces experienced in a 3D granular wavefront follow the same scaling relationships as in a 1D chain. We then balance 3D wavefront forces with gravitational overburden to determine an equation that predicts lofting depth (depth to which bulk dilation could be expected to occur) as a function of material properties and the magnitude of particle-particle collisional velocities along the channel floor. Our loft depth equation agrees well with simulated results and predicts a depth within the same order of magnitude as the 40 cm LCS halo depth. However, the existence of a surface SW (and thus, dilation) requires external energy input to be driven along the floor of the channel.

Second, we consider a possible driver for the surface dilating wave by characterizing the decay of an initial pulse through chains of buried boulders. On the Moon, the surface regolith (a uniform layer of fine, $<$100 micron sized particles) covers an underlying layer of larger scale ejecta (boulders). In granular assemblies, the decay of a wave is typically governed by a fixed number of particles since energy is lost through collisions. We suspect that meter scale boulders

may be able to support energy propagation over the km scale distances of the LCS halo. Through measuring wave decay in scaled up versions of the channels from our initial work, we see that the decay rate in 3D systems is governed by the same concepts as in a 1D chain: particle number governs decay distance, power law decay in time. We use the lofting equation to estimate the requisite collisional velocity (4 m/s) of particles within the buried layer's wavefront needed to initiate SID in the surface layer. We see this velocity threshold exceed over hundreds of meters, within an order of magnitude of LCS halo scale distances.

The results of this thesis point to the following formation mechanism: cold spot regolith is fluffed up by a surface solitary wave driven from below by the decay of impact energy through boulders at the regolith-megaregolith boundary. However, this hypothesis requires experimental validation. Understanding cold spot formation has implications for both science and engineering efforts on the Moon. Cold spot regolith fluffing represents yet another surface modification processes altering the already complex history of the Moon (and solar system) entrained in the regolith. If our proposed mechanism is proven to be true, cold spots can also reveal details about local subsurface topography such as the size distribution of buried boulders. The location of buried features may be an important consideration for future large scale construction efforts. Finally, our proposed mechanism suggests that high speed impacts on any low-gravity, low-pressure planetary surface covered with regolith and possessing an underlying layer of larger boulders would display cold spots around young craters.

INVESTIGATING A POSSIBLE LUNAR COLD SPOT FORMATION MECHANISM: MODELING GRANULAR WAVES IN SURFACE REGOLITH USING SOFT SPHERE DISCRETE ELEMENT METHOD

by

Eric Scott Frizzell

Dissertation submitted to the Faculty of the Graduate School of the
University of Maryland, College Park in partial fulfillment
of the requirements for the degree of
Doctor of Philosophy
2024

Advisory Committee:
- Dr. Christine Hartzell, Chair/Advisor
- Dr. Raymond Sedwick
- Dr. James Baeder
- Dr. Derek Richardson
- Dr. Nicholas Schmerr, Dean's Representative

© Copyright by
Eric Frizzell
2024

Preface

The surface is fine and powdery. I can - I can pick it up loosely with my toe. It does adhere in fine layers like powdered charcoal to the sole and sides of my boots. I only go in a small fraction of an inch. Maybe an eighth of an inch, but I can see the footprints of my boots and the treads in the fine sandy particles.

- Neil A. Armstrong, Tranquility Base (Apollo 11), July 20, 1969

Dedication

To my Mom, who is my sunshine.

Acknowledgments

This work would not have happened without Christine. Thank you, Christine, for giving me direction when I couldn't find it on my own, for being patient while I spent so much time going down rabbit holes, for introducing me to planetary science and for reminding me to be proud of what I've accomplished. Thank you for knowing what a cold spot is, having an idea of how they form and letting me work on your idea.

This work also would not have occurred without the LRO Diviner team, to whom I am grateful. Thank you for classifying and cataloging lunar cold spots. Thank you especially to Tyler Powell and Jean-Pierre Williams for taking my questions and providing helpful career advice.

Thank you to my committee, who's guidance has been instrumental in my education and development as an independent researcher. Thanks to Jim for helping me understand something I should have picked up on long ago: the difference between implicit and explicit time marching (your CFD class was wonderful). Thanks to Derek for some very helpful discussions about DEM and some very interesting talks about birds. Nick, thank you for helping me see the Moon for the Moon; as more than just the pretend spheres in my pretend box. Ray, thank you for introducing me to research, for teaching me how to effectively troubleshoot (I think of you every time I use 'keyboard' to enter the MATLAB debugging window) and for sharing some very helpful and personal advice when I was truly struggling. Finally, Christine, thanks again for all the kale and sorry about all the questions concerning your manure pile.

Thanks to my family (Mom, Dad, Stef, Peter, Robin, PJ) for supporting me in whatever I do. Brother Peter, sister Stef, thanks for always being proud of me. Mom and Dad, thank you for providing for me and helping me build the kind of life that allowed me to take a mulligan and go back to school. Dad, thanks for teaching me to always be aware of my surroundings. Mom, you are the best; I don't have enough words to describe your importance to me and impact on my life and path.

One of the reasons I am most thankful for my time at UMD is that I was so lucky and incredibly fortunate to meet Wanyi. To my partner, Wanyi, thank you for being by my side for this entire adventure, for helping me grow and learn, for reminding me to take deep breaths and keep my shoulders down, and for all the massage when I knotted my neck and shoulders up with stress and worry anyway. Thank you for forgiving my hanger, for putting up with my super sensitivity, and for being patient with me while I put my life on hold to finish this thesis. Thank you for being such a genius and helping me do maths I forgot how to do and for proofing all my most important presentations, posters, and emails. Thanks to all the Ng's for being so supportive and treating me as one of their own.

Thank you, Zack, for marrying me (you know I can't help making this joke). But even more, who is my brother, my hiking partner the best gift giver and planner, the smartest human and an incredible Euchre partner. Thank you for being in my life. Thanks to all the Beauvais for supporting me just the same as my own family and letting me be 'cousin Eric'.

Thank you, Travis, who I will always think of any time I cut an onion or boil noodles. You are a very good friend, sherpa and brother. Your pig passing abilities are unrivaled. Thanks for always being there to take my call and for getting me to talk when I need to, but am pretending that I don't: 'no solitude for Eric'.

I had a very good time living in College Park Woods and am now very good friends with my housemates and neighbors. Thanks to Emily and Katie for letting me spend countless hours in their living room, hosting all the parties, and convincing me to make plans and hangout when I would have been a hermit in my room all weekend instead. You are such good friends and you have the best dogs (thanks Poppy, thanks Atlas for all the pets). Antonio, Barry, Daniel thank you for a great year at Dewberry. I miss getting to see you all daily. Daniel, thank you for being my champion. Antonio, thank you for the walks, the talks, and all the pokémon. Barry, thanks for all the haircuts. Brian, Luke, Travis, thank you for several great years at Drake PL. Thank you Luke for letting me play the drums for you and for introducing me to John Prine. Brian, thank you for teaching me how to say no. Travis, thank you for everything. Laura, thanks for all the cake.

Spencer and Wanyi, thank you for being excellent homework buddies.

Emily and Alvin, thanks for all the grocery store trips and for being our glue when needed.

Thanks to all my friends in the Planetary Surfaces in Spacecraft Lab: Melissa, Charles, Ian, Anmol, Grace, Cecily, Yun, Jackson, Tom. Thanks to Melissa for going to Fart Club meetings with me and for participating in the secret war (it's never over). Thank you, Charles, for being so positive and supportive and that one time with the carrot cake. Thank you, Ian, for solving all our problems in your sleep. Thank you, Tom, for getting me going on LIGGGHTS.

Thanks to all my friends in the Space Power and Propulsion lab who let me 'build my character' with them: Elaine, Pratik, John, Arber, Matt, Adam (my twin), Drew, AJ, Melissa and Pooh Bear and Jarred. Elaine, thank you for being my running partner and perhaps the single greatest inspiration in my decision to try grad school. Pratik thank you for all the support, the internship, and encouraging me to do strength exercises and not just run. Thank you, John, for all the disc golf and poké drives around campus. Thank you, Matt, for all the trivia. Arber <3.

Through the JPL Planetary Science Summer School, I learned a ton about mission design, but probably more importantly made some excellent friends. Thank you to Ali, Amanda, Christina and Mallory. Ali, thanks for reminding me how hard modeling is. Amanda, your sheer positivity is infectious and it is such a joy to be in your presence. Christina, you may be the most organized person I know and thanks for all the hugs. Mallory, you are an amazing leader and mom, I don't know how you juggle all these things so well. Thank you for being my advocate and confidant and encouraging me to network when I say I'd rather hide.

During my time at UMD I received a ton of support from the Aerospace Department and I am thankful to all of you who are still here and who have passed through while I've been around. Thanks especially to Aileen who has been a behind the scenes guiding hand to my success. Thank you also to my undergrad and SGT Honor Society mentor Chris as well as Matt, Renee, and Briana. I must also thank the A James Clark Foundation for making me a Clark Scholar and looking out for my best interest. I am also grateful to the National Science Foundation for granting me a Graduate Research Fellowship (Grant No. DGE 1840340). I was also funded by (and am deeply grateful to) the Chuck Edwards Memorial Scholarship, H. Russell Knust Memorial Scholarship, Space and Satellite Professionals International (SSPI) Scholarship, Academy of Distinguished Alumni Scholarship in Aerospace Engineering (Dr. Chris Jones). These funding sources were instrumental in my ability to focus on my studies and participate in student groups. Thanks to all the presidents and board members of UMD Women in Aero and Astronautics (WIAA) who I served under and with, especially Rosemary and Sky. Through WIAA I had an outlet for helping and learned how to be a better ally.

There are many, many people I'd like to thank for being a part of my greater education and life journey and I'm also going to wind down now. I'll mention those who were most instrumental

in my return to school. Kevin, thank you for talking my ear off about your passion for using engineering to solve medical problems (the feedback controller spoon for Parkinson's patients is a particularly poignant memory). Your wedding flower-robot lives forever in my mind. Thank you, Hyden, for opening my eyes and for all the good times at the Portage District Library. Steven and Misael, thank you for getting me through high school. Jack thank you for being my lifelong friend. Thank you to my cousin, Alex, for keeping me calm. Thank you to my cousin, Andy, and my uncle, David, for inspiring me. Thank you, Michael, for always sending happy cat and for all the nature walks. I'm not sure if I'd ever be able to achieve flow without some nice music to listen to so I'd like thank the following artists: Blue Harvest, Shingo Nakamura, Bloodgroove and Kikis, Tiesto.

Finally, this work could not have happened without Past Eric. Thank you for putting in all the work to make this happen. Thank you for always looking out for us.

Nature and natural are words with particular weights that are perhaps not relevant now. We are part of a biosphere that sustains us. Half the DNA in your body is not human DNA, you are a biome like a swamp, with a particular balance or ecology that is hard to keep going – and indeed it will only go for a while after which it falls apart and you die. The world is your body, you breathe it, drink it, eat it, it lives inside you, and you only live and think because this community is doing well. So: nature? You are nature, nature is you. Natural is what happens. The word is useless as a divide, there is no Human apart from Nature, you have no thoughts or feelings without your body, and the Earth is your body, so please dispense with that dichotomy of human/nature, and attend to your own health, which is to say your biosphere's health.

- Kim Stanley Robinson

Table of Contents

Preface ii

Dedication iii

Acknowledgements iv

Table of Contents ix

List of Tables xii

List of Figures xvi

List of Abbreviations xxix

Chapter 1: Introduction and Motivation 1
- 1.1 Background . . . 8
  - 1.1.1 The Lunar Surface . . . 9
  - 1.1.2 Granular Dynamics . . . 14
  - 1.1.3 Summary . . . 18

Chapter 2: Code Selection and Validation 19
- 2.1 Modeling choices . . . 19
  - 2.1.1 Contact Model: Hooke vs Hertz . . . 19
  - 2.1.2 Continuum vs particle based . . . 20
  - 2.1.3 Soft Sphere Discrete Element Method . . . 21
  - 2.1.4 LIGGGHTS . . . 21
- 2.2 Two-body validation . . . 22
  - 2.2.1 Normal Force . . . 23
  - 2.2.2 Cohesion . . . 24
  - 2.2.3 Normal Impact . . . 24
  - 2.2.4 Oblique Impact . . . 26
  - 2.2.5 Sliding . . . 26
  - 2.2.6 Rolling . . . 27
  - 2.2.7 Twisting . . . 28
- 2.3 1D wave validation . . . 29
- 2.4 Summary . . . 33

Chapter 3: Simulation of Lateral Impulse Induced Inertial Dilation at the Surface of a Vacuum-Exposed Granular Assembly 34
3.1 Introduction . . . 34
3.1.1 Waves in granular media . . . 38
3.2 Methodology . . . 41
3.2.1 Soft Sphere Discrete Element Method and contact model . . . 41
3.2.2 Model validation . . . 44
3.2.3 Simulating 3D wave propagation . . . 47
3.2.4 Granular bed preparation . . . 48
3.2.5 Bed tapping . . . 53
3.2.6 Wave generation . . . 55
3.2.7 Computation details . . . 57
3.2.8 Data analysis . . . 57
3.2.9 Shock validation . . . 65
3.2.10 Test plan . . . 68
3.3 Results and discussion . . . 69
3.3.1 Impulse-induced granular dilation . . . 69
3.3.2 Surface dilation quantification . . . 74
3.3.3 Effect of wave initiation region . . . 88
3.3.4 Discussion of solitary waves . . . 90
3.3.5 Dilation and scaling discussion . . . 94
3.3.6 Relevance to LCS . . . 97
3.4 Summary and conclusions . . . 100

Chapter 4: Material parameter influence on the expression of Solitary-Wave-Induced Surface Dilation 102
4.1 Introduction . . . 102
4.1.1 Granular SWs . . . 104
4.1.2 SW-Induced Surface Dilation . . . 105
4.1.3 Lunar Cold Spots . . . 107
4.2 Methodology . . . 108
4.2.1 Simulation setup . . . 109
4.2.2 Contact model . . . 117
4.2.3 SW wavefront particle force . . . 120
4.2.4 Data analysis . . . 123
4.2.5 Data generation and availability . . . 126
4.2.6 Investigated parameters . . . 127
4.3 Results and Discussion . . . 130
4.3.1 3D SW wavefront forces . . . 130
4.3.2 Scaling . . . 140
4.3.3 Dilation . . . 143
4.3.4 Blast loading . . . 155
4.3.5 Outbursts . . . 156
4.3.6 Discussion . . . 158
4.4 Conclusions . . . 163

Chapter 5: Runout distance in buried boulder scale granular channels 165
5.1 Introduction . . . 165
5.1.1 LCS and a possible progenitor . . . 166
5.1.2 Surface regolith vs megaregolith . . . 168
5.1.3 Energy decay in granular chains . . . 169
5.1.4 Formation hypothesis . . . 171
5.2 Methodology . . . 171
5.2.1 Simulation overview . . . 172
5.2.2 Overburden pressure . . . 175
5.2.3 Data analysis . . . 177
5.2.4 Investigated parameters . . . 180
5.3 Results and Discussion . . . 181
5.3.1 Runout results . . . 181
5.3.2 Discussion . . . 192
5.4 Conclusions . . . 197

Chapter 6: Conclusion and Future Work 199

Appendix A: Contact model 204

Appendix B: Wave Visualization 211

List of Tables

2.1 SSDEM Parameters for particle-particle validation 23
2.2 1D Particle Properties. Steel values are those used in [79] and soft particles values are selected from Table 2.1. 30
2.3 1D Validation Model Comparison. The *LIGGGHTS* Hertz contact model is compared to the implementation of TN from AE. 32

3.1 1D Particle Properties. Steel values are those used in [79]. The soft particles are the same size as the steel particles, but with the material properties used in our 3D simulations (see section 3.2.4). 45
3.2 SSDEM Parameters for 3D validation. 50
3.3 Insertion parameters to achieve various ϕ_0 for varied channel geometries. 51
3.4 Tapping Duration. New ϕ_0 are reported for various tapping duration of the loose, medium, and compact beds at the same amplitude and frequency. The ϕ_0 designations correspond to those from Table 3.3 for Loose (54.7%), Medium (58.7%), and Compact (62.0%). 54
3.5 Computation details. Processing time and storage requirements for shocking the different beds. Simulated time for all tests below is 1.5 s. Each test used all 128 cores of a single node. 58
3.6 Sound speed and bulk modulus in beds of various ϕ_0. ρ_{bulk} is computed using the particle density from Table 3.2 with mean ϕ_0 from Table 3.3 corresponding to the Loose, Medium, and Compact channels in the 2 m long, 20 cm deep configuration. 66
3.7 Bed height change for different seed groups. Mean (μ) and deviation (σ) are taken from the height change in the measurement region for each seed group in Fig. 3.14. 76
3.8 Wave characteristics for the velocity sweeps in the compact (C), medium (M) and loose (L) packed beds. The average initial overlap correspond to δ_0 = 4.82, 4.81 and 4.23 μm (L,M,C respectively), see sec. 3.2.4 for details. The columns correspond to packing fraction, piston velocity, initial (shock) wave front speed, propagating (solitary) wave front speed, particle velocity within the solitary wave front, maximum overlap experienced by particles following the passage of the solitary wave front, the ratio of particle to wave front speeds, and the at rest height change (from the initial 20 cm bed height) following the wave's passage. . 78
3.9 Δz in beds of various length. c_p is the solitary wave speed and $\Delta\rho$ is computed as a percent difference from a bed initially filled 20 cm deep with particles. . . . 82
3.10 c_p and v_p in beds of various height. We show the input v_p used to generate solitary waves of different c_p. 85

4.1 Channel properties for testing sensitivity to elastic modulus. We give the average initial conditions, velocity limits, and assess the appropriateness of our time step choice in channels of varying E. δ_0 decreases as E increases since the spring repulsion between particles increases and they push apart, resulting in a slightly looser channel (smaller ϕ_0). The largest δ_0 (experienced by the particles with E = 5 MPa) is about 0.3% of R which is sufficiently small. Δt is well below 1% of τ_c for most cases, though this limit is exceeded slightly in few of the cases (up to 1.46% of τ_c). We determined that these tests were still run at a sufficiently small time step given the agreement of the behavior of the SW in theses channels with expectation (sec. 4.3.1). Other particle parameters are constant (R = 1.25 mm, ρ = 2.5 g/cc). We performed two series of tests in these channels, one with v_0 constant at 10 m/s and one where v_0 was a constant portion of c_m (∼20% c_m). A dashed line indicates 'same as above'. 112

4.2 Channel properties for testing sensitivity to density. We give the average initial conditions, velocity limits, and assess the appropriateness of our time step choice in channels of varying ρ. The largest δ_0 (experienced by the particles with ρ = 25 g/cc) is about 1% of R which is approximately the limit used in [67]. We judged this large overlap to be acceptable since most cases we evaluated use smaller ρ. δ_0 increases as ρ increases since, as a result of increased mass, the particles have a reduced spring repulsion force. The particles are able to interpenetrate further as ρ increases, leading to more 'compact' (larger ϕ_0) channels. Δt is well below 1% of τ_c for all cases. Other particle parameters and impact velocity are constant (R = 1.25 mm, E = 5 MPa, v_0 = 10 m/s). 113

4.3 Channel properties for testing sensitivity to particle size. Particle properties are set with to base case values (E = 5 MPa, ρ = 2.5 g/cm^3, v_0 = 10 m/s). We pour the particles to a medium packing fraction (around 58%) which was chosen as a balance between reducing channel preparation time while achieving a level of ϕ_0 that would still result in SID. We take the elastic limit to be L_e = 9.43 mm/s for all cases since c_m does not depend on R. 114

4.4 Investigated parameters. We give the range of parameter values for the physical quantities evaluated in our SID sensitivity analysis. We give the range of values used as input values in our simulations along with the relevant characteristic condition (with lunar particles referenced for material properties and similar low gravity DEM simulations referenced for simulated parameters). If there is a relevant reference we provide this here as well. Grain properties are given for lunar surface particles (regolith at depths of 0 to 40 cm). 128

4.5 Goodness of fit. Scaling parameter and r^2 for the cases inspected. Particles are set using the base parameters and then one or more of the components are varied corresponding to the values in fig. 4.5. For the case with varied v_0 and varied E, E values are found in Table 4.1. Packing fraction corresponds to compact (C), medium (M), and loose (L) ϕ_0. 134

4.6 Validity details. We assess the physical realness of our results be comparing wave speed, particle speed within the wavefront (v_m) and the maximum overlap particles in the wavefront experience. In all cases the base material parameters are used and the varied parameter of interest is changed to the value given in the table for each test. Impact velocity is set to v_0 = 10 m/s in all cases, except for the velocity sweep which used based material parameters and the velocity listed. ϕ_0 for each of the cases can be found in across Tables 4.1, 4.2 and 4.3, with most being filled to compact fillings except the particle size sweep and lunar-like particles which are filled to a medium ϕ_0. The measured (simulated) values are taken as an average of a given quantity over the entire channel depth - we disregard the deviations in this table and consider the mean values to get a sense of the scaling. For each test we calculate sound speed c_0 (as the average over a depth of $160R$ using eq. 4.4) and compare it to the generated PSW wave speed (c_w) and the DSW speed (c_p) which are found using the same procedure as in [177]. We note that c_w and c_p can fall below the v_0 impact speed since they average over the entire depth of the channel and v_0 is only maintained by impacts along the floor. We do not give a c_p for the E = 5 GPa case as the measurement contained too much noise, caused by outbursts (sec. 4.3.5). We also collect v_m and compare it to the elastic limit (L_e, also found in Tables 4.1, 4.2 and 4.3). Finally, we collect the maximum overlap experienced over the course of each test and compare it to particle radius. The case of E = 50 GPa was included as a reference and was not simulated, hence the 'n/a' for simulated quantities. 139

4.7 Loft depth (z_{LD}) and critical radius (R_c) for various material parameters and gravity environments. We solved eq. 4.10 for R in the case where z_{loft} = 0 (the critical radius, R_c, which is the size of the largest particles that could be lofted by SID) and for R = 1.25 mm (the size of the particles we used in our simulations for the cases in the table) to find lofting depth, z_{LD}, the depth to which we expect particles to obtain a vertical velocity (and therefore show bulk density changes). The parameters (besides the listed varied parameter) are set to the base properties, with v_0 = 10 m/s and ϕ_0 = 62%. 144

4.8 Prediction vs comparison table. We find z_{SD} for cases that exhibit gentle SID. We manually identified the depth at which $\%\Delta\rho$ exceeds 1% by examining the different frames of Fig. 4.10, multiplying the depth identified as z_{SD} by the particle R for the corresponding case to recover dimensional units. A value of 0 indicates no dilation or compaction and a value of n/a means that there was no identifiable z_{SD} (e.g., the lofting depth greater than the channel depth). We then compare z_{SD}, z_{LD}, and bed height change. 153

4.9 Blast loading table. We give the mean ($\overline{BL}$) and deviation (σBL) length of the BL zone for various cases. Each entry represents several tests conducted with the base particle properties and with the indicated test parameter varied over the range from sec. 4.2.6. Units are given in non dimensional channel length (L/R). The velocity sweep case for v_0 comes from a channel with R = 0.5 mm particles. The table is sorted by smallest deviation to largest. 156

5.1 Channel geometries. We show channel length (L) and height (H) for varied particle size (sorted by increasing radius, R). The scale number compares the chosen particle to the base case (R = 1.25 mm) from [177]. Channels contain around 560,000 particles depending on the exact packing fraction achieved. 173
5.2 Initial conditions and timestep considerations. We provide the achieved packing fraction and corresponding δ_0 for channels filled with the various particle sizes we consider when particles (ρ = 3 g/cm^3) are soft (E = 5 MPa) vs hard (E = 50 GPa). We also show the corresponding material sound speed c_m which informs the maximum v_0 that can be used following the approximate $0.2c_m$ limit used in [177] and ch. 4. We then use the maximum v_0 considered here (10 m/s for E = 5 MPa, 1 km/s for E = 50 GPA) to find the smallest collision time (τ_c, see [177]) our particles will undergo. Here we confirm that our SSDEM time step (Δt) is appropriate (it is less than 1% of collision time, [67]). 175
5.3 Overburden pressure. We examine pressurization effects using the hard boulders from Table 5.2 (E = 50 GPa, R = 1.25 m). For these sized particles, h_{op} = 100 m. Note that maximum overburden pressure is just more than half of Earth sea level atmospheric pressure. 177
5.4 Runout results. We show the runout distances from our simulations for absolute, transition, and dilation runout for the various parameters we considered. The parenthetical term following each parameter indicates material properties where S and H denote soft and hard particles, respectively, and B represents boulders (particles with material properties R = 1.25 m, E = 50 GPa and ρ = 3 g/cc). For all three cases we collect runout distance (D_A, D_T, D_D) in terms of number of particle radii traveled along the channel before the respective criteria is met (sec. 5.2.3). For transition and dilation runout we also log the time (t_{D_T}, t_{D_D}) and non-dimensional overlap (δ_{D_T}, δ_{D_D}) at the respective runout distance. Note that ρ, ν and e are omitted from the table as they had virtually no influence on runout. The table is broken into sections with the top, middle, and bottom corresponding to material property, impactor momentum and packing effects, respectively. v_p is fixed at 20% of c_m except in the varied velocity tests and all channels are of height $160R$, except for the h_c cases. 183
5.5 Dilated runout fit coefficients and multiplier estimation. We first list the coefficients that result from fitting the various parameters that influence D_D to a generalized power law of the form $D_D = Cx^{p_1} + p_2$, where x should be replaced by the parameter of interest. The right half of the table estimates the amount by which to scale D_D (D_D multiplier) when the designated parameter changes from the base to the target value (with units defined where necessary). We find the multiplier by plugging the fit parameters on the left hand side of the table into the generalized power law, assessing D_D for the base and target quantities, then taking the ratio of the target to the base value. As an example, if the velocity of impact into our channel increased from 1 km/s to 25 km/s, we'd expect D_D (which is $391R$ in the boulder case from Table 5.4) to increase to $1{,}877R$. 189

List of Figures

1.1 **Lunar Cold Spot.** An infrared image of the Lunar Cold Spot at 151.7°E, 4.1°S first shown in [1], Fig. 3 (this image is taken from an updated version in [10], Fig. 11). This source crater (small red dot at the center of the image) is 1.55 km in diameter and has a Cold Spot (blue region) area greater than 19,000 km^2. Some of the salient features are labeled, with the dashed line representing the average 100 crater radii size of the LCS halo (not to scale). The color bar from the original image represents night-time surface temperature differences, with the green background regolith as the baseline at 0 K. The blue reduced thermal inertia halo represents cooler temperatures (than background) of more than 2 K. Low thermal inertia rays are seen to extend much further than the average LCS halo. 3

1.2 **Lunar Surface Structure.** Figure of the upper lunar crust from [9], their Fig. 4.22, showing our regions of interest. The red box at the surface (not to scale) shows approximately the suspected depth extent (0 to 40 cm) of the LCS reduced thermal inertia regolith. 11

1.3 **(a) Lunar Surface.** The high cohesion of the lunar surface can be seen in the steep walls of the Surveyor 3 landing pad footprint. NASA photograph AS12-48-7110, Apollo 12 Principal Investigator Richard J. Allenby Jr., National Space Science Data Center. **(b) Regolith agglutinates.** Agglutinates are fused assemblies of smaller regolith particles and represent larger members of particles (mm scale) from the lunar surface regolith size distribution. Image from [14]. 12

1.4 **(a) Idealized 2D Compacted Grains.** The combined area of the particles and the void within them is represented by S. The area of S will change as the dimensions of the central trapezoid change due to grain movement. The inter-particle distance, w, is defined as the distance between the centers of particles a and b. **(b) Trapezoidal Area.** Normalized trapezoidal area is plotted against normalized inter-particle distance. See [37] sec. 3.1.3, for the relevant equations. From left to right, grains a and b begin in contact and the distance between them grows. The trapezoidal area (representative of the void) grows and then decreases. 15

2.1 **(a) Force vs δ.** Particles with an overlap will remain stuck together when gravity is turned on as long as, for a specified gravity, the normal force does not exceed 0. We show the force evolution as particles are pushed together or separated for levels of gravity above, below, and approximately equal to the threshold g **(b) δ vs time.** The validation test is run for the three gravity cases. The particles remain in contact when expected and show a new steady δ at at the $F = 0$ crossing from Figure 2.1a. 25

2.2 **Input e vs post impact e.** User input e is recovered exactly for all values. 25
2.3 **(a) e_t' vs θ_i.** Tangential coefficient of restitution vs impact angle shows that the expected behavior is reproduced after the threshold impact angle. **(b) ω' vs θ_i.** Post collision angular velocity vs impact angle shows that the expected behavior is reproduced after the threshold impact angle. 27
2.4 **Distance vs time.** Particle position vs time shows that after being given an initial velocity v_0 the particle comes to rest at the expected distance. 28
2.5 **Torque and Distance vs time** We show the time dependence, for both our implementation and that of [74], of torque (left axis) and position (right axis) of the particle in this test. 29
2.6 **(a) ω vs t.** Angular velocity vs time shows that a particle with no rolling viscous damping ($\gamma_r = 0$) stops spinning, but experiences continual oscillations after stopping **(b) ω vs t.** The same plot as Fig. 2.6a, but with $\gamma_r = 2$ shows that the particle stops spinning and and comes to rest with a small amount of overshoot with sufficient damping. 30
2.7 **(a) Granular Assembly.** Reproduction of a 5 by 5 square packing of particles from [79]. The incident particle (26) is given a velocity in the negative y direction (v_{im}), initiating a normal impact with the target particle (23). Force is transmitted solely along the force chain of numbered particles and their evolution is plotted in Figure 2.7b. **(b) Peak Force tracking.** We plot force in the y direction vs time for each of the particles within the impacted chain from Figure 2.7a using steel properties from Table 3.1 and v_{im} = 1 m/s. As in [79] we find c_w by identifying the peak forces in particles 8, 13, 18, and 23 (red circles). The slope of the line which is fit to the the particle positions and corresponding time of maximum force is c_w, the processes is shown in the upper right corner. 31
2.8 **Normalized wave speed vs impact velocity.** c_w reported for varied v_{im} are normalized by $c_w(v_{im} = 1$ m/s). We normalize c_w at $v_{im} = 1$ m/s instead of at vanishing v_{im} ([84]) in order to include the data points from AE. Our tests as well as the results from AE recover the expected power law dependence. 33

3.1 **Normalized wave speed vs impact velocity.** c_w reported for varied v_{im} are normalized by $c_w(v_{im}$ = 1 m/s). We normalize c_w at v_{im} = 1 m/s instead of at vanishing v_{im} (as in [84]) in order to include the data points from [79]. Our tests are in agreement with theirs and recover the expected power law dependence. 47

3.2 **Channel Schematic.** A channel 2 m in length is filled 20 cm deep with particles (total of $\sim 5 \times 10^5$ particles) and a shock was initiated at the left wall ($v_p = 10$ m/s) in the +y direction at t = 0 s. Here we show the channel's response several time steps after shock initiation (t = 0.1 s). The bold black line represents the simulation domain with the channel of particles occupying the bottom ∼half. Particles are colored with their order of magnitude force relative to 10^{-8} N which reveals a clearly evident solitary wave around y = 1 m. There are two boxed regions highlighted which are shown in expanded views (not to scale). **Box A** shows a zoomed in a view of the wave front near the surface, overlaid with a sensor grid (sec. 5.2.3) in dashed black lines. The shock front is (qualitatively) ∼15 particle diameters in size. A single sensor (one grid element in A) would find its properties by averaging the properties of all particles in the sensor at each time step. We provide top view (A1) and side view (A2) graphics of the sensor grid in box A to demonstrate how they are used in data analysis. Sensor particles are collected from the particles that rest on top of the 1D y-grids (A1). Side view elements are gridded in two dimensions (A2). To find average properties at a given radial position we take the average over sensor elements in the same column ("column average"). The "depth average" is taken over all grid elements at a specified depth. **Box B** is zoomed in on the floor-wave interface. The sheet of particles frozen to the floor is visible along the bottom. The highest force in the solitary wave is the dark spot slightly behind the front. Data visualization as seen here and in subsequent figures is performed using open source visualization software Ovito ([154]). 49

3.3 **Depth vs δ_0.** Depth dependence of δ_0 for the loose, medium, and compact 2 m long 20 cm deep channels from Table 3.3. Simulated results are represented by circles and the dashed lines show the result of eq. 3.6 with the ϕ_0 from the first three entries of Table 3.3. These three packings correspond to average δ_0 of 4.82, 4.81 and 4.23 μm (loose, medium, compact respectively). The compact δ_0 is smaller than the loose since δ_0 is the average overlap here, not the total (as discussed in the text). 53

3.4 **Average Particle Force (Y) vs time.** Force evolution vs time for P waves created at varied v_p from a sensor at 7.5 cm depth and radial position 1 m in a 2 m channel filled 20 cm deep with particles. The color legend represents different v_p with units in m/s. Lines have been added for clarity. Identified peaks are plotted as a black circle and this is taken to be the time at which the wave front passed through the sensor. 59

3.5 **Height vs Time.** Average sensor particle height over time for a sensor at y = 1 m in a 2 m channel filled 20 cm deep with particles (compact filling). Height increase is initiated by arrival of the wave, falling back down from a peak to a position greater than the initial height when the wave is supersonic. Color legend corresponds to different v_p (m/s). The dashed lines in the zoomed in portion (boxed in red) show the variance in bed height change for the v_p = 10 m/s case taken from a 15 second simulation (not pictured). The oscillations we see between 1.3 and 1.5 s (our averaging window) occur about the at rest bed height from the longer duration simulation. 61

3.6 **Sensor location vs logged peak force time.** For varied v_p we show the measurements used to find c_w at a depth of 4 cm. A fit of the measurements in the first 15 cm gives c_w (fit lines not shown). The initial linear fit is used to remove outliers more than 2σ from the mean before finding the final linear fit. Color corresponds to wave v_p (m/s). The slope of the linear fits for each trend correspond to reported c_w in Figure 3.7. The propagating solitary wave speed c_p is a linear fit to the data after 30 cm. 62
3.7 **Depth vs c_w for varied v_p.** Using the slope found from Figure 3.6 we show c_w and its depth dependence for varied v_p in a 2 m channel filled 20 cm deep with particles (compact packing). Acoustics waves are grouped together and produce roughly the same c_w, while shocks show an increase in c_w with v_p. The red dashed trend line shows that the predicted sound speed, $(\sqrt{3}/2)c_0$ (eq. 4.4) agrees with our numerical sound speed (bluest data points, corresponding to low v_p) 63
3.8 **Average δ vs time.** δ evolution vs time for P waves created at varied v_p from a sensor at 7.5 cm depth and radial position 1 m in a 2 m channel filled 20 cm deep with particles (compact filling). Lines have been added for clarity. The legend colors correspond to v_p (m/s). The overlap the particles experience as a result of the shock, δ_m, corresponds to the maximum. The red line (v_p $\sim$7.5 m/s) is discontinuous between 0.2-0.25 s while the particles in the cell are completely detached. δ_m is the maximum overlap experienced in the sensor as the result of the wave which is not necessarily the maximum overlap in the wave front. 64
3.9 **Depth averaged c_w vs v_p for varied geometries**. We show wave speed vs incident speed for the 1D case as well as three different ϕ_0 for the 3D bed corresponding to the loose, medium, and compact levels of packing from Table 3.3. . . 67
3.10 **Mach number vs v_p for varied geometries**. Wave speeds for different v_p resulting in shocks in the 1D (plus marker) and 3D shocks (circles) are normalized against c_0. The solitary wave speed c_p is corresponds to the star markers. 68
3.11 **P wave visualization.** Various parameter visualizations of a 2 m long channel filled 20 cm deep with particles (compact filling) at t = 0.133 s after P shock initiation (v_p = 10 m/s). In order of top to bottom, the panels color the particles by their force magnitude, z-velocity, velocity magnitude, normal stress (yy), and shear stress (yz). We show the legend scale and units inlaid on the right of the channel in each panel. Dashed lines are guides corresponding to labels which are described in the text. The initial shock decays to steady solitary wave and is maintained across the entirety of the channel. 70
3.12 **S wave visualization.** Various parameter visualizations of a 2 m long channel filled 20 cm deep with particles (compact filling) at t = 0.133 s after S shock initiation (A = 3.1831x10^{-5} m). In order of top to bottom, the panels color the particles by their force magnitude, z-velocity, velocity magnitude, normal stress (yy), and shear stress (yz). We show the legend scale and units inlaid on the right of the channel in each panel. Dashed lines are guides corresponding to labels which are described in the text. 71

3.13 **Dilation visualization.** Particles are colored by their displacement in height as compared to their initial position for the compact 2 m channel filled 20 cm deep with particles. The top channel experienced a P shock wave while the bottom channel experienced an S shock wave. 73
3.14 Δz **vs Radial position.** Color legend corresponds to seed number configuration and red dashed lines indicate the measurement region. We generated shocks (v_p = 10 m/s) in loose beds 2 m in length filled 20 cm deep with particles. The randomness of the packing has little effect on post shock dilation. 75
3.15 Δz **vs radial position for varied** v_p**.** The color legend shows v_p in m/s for waves initiated in a compact bed 2 m in length filled 20 cm deep with particles. Acoustic waves ($v_p \leq 0.1$ m/s) show no bed height changes. Waves in the transition region ($0.1 < v_p \leq 1$ m/s) begin to show some dilation, but it does not persist across the channel. The remainder of the v_p investigated induce shocks, which see uniform dilation across the channel. 79
3.16 **Average** δ_m/δ_0 **vs radial position for varied** v_p**.** Normalized maximum particle overlap over the length of a 2 m channel filled 20 cm deep with particles (compact filling) is shown for the same waves created in Figure 3.15. While all induced waves experience a region of initial rapid decay in δ_m, only the shocks decay to solitary waves which propagate with constant δ_m (until they terminate). The strongest waves are maintained across the entire channel. The colors correspond to the same v_p legend as in Fig. 3.15, but is omitted here so as not to obscure the trends. 80
3.17 $\Delta\rho$ **vs** $M = c_p/c_0$**.** Dilation vs Mach speed for the compact, medium, and loosely packed beds. The black dashed line at 0 is the compact-dilation threshold and the red dashed line corresponds to the RSE. 81
3.18 Δz **vs radial position for varied channel lengths.** Change in bed height is tracked in different beds filled 20 cm deep with the loose configuration of particles. A uniform, though small, amount of dilation occurs across all channels. Color legend corresponds to channel length. 82
3.19 **Average** δ_m **vs R.** We show normalized δ_m across the 4 m channel for three different v_p cases. The solitary waves generated with the two largest v_p sustain a roughly constant δ_m over the entire length. 83
3.20 Δz **vs radial position for varied fill height.** There is a slight increase in the post impulse height change with decreasing bed height (2 m long beds filled at the loose packing configuration). 84
3.21 **Depth vs** c_p**.** While the initially induced c_w were the same, c_p is greatest for the smallest channel fill height. Constant v_p cases are marked with circles and constant c_p with a plus sign (the case for the 30 cm channel marked with an x marker is both constant v_p and c_p). 84
3.22 Δz **vs channel height.** Shows cases for constant v_p and for roughly constant propagating c_w . Δz is given instead of $\Delta\rho$ since the different initial bed heights influences the percent difference calculation. The single data point at 30 cm can be considered as both constant v_p and constant c_p. 85

3.23 Δz **vs radial position for different** ϕ_0**.** We examine the dilation sensitivity to ϕ_0 by initiating shocks in beds (2 m in length filled 20 cm deep) corresponding to the loose, medium, and compact ϕ_0 from Table 3.3. In each case, the height change is uniform across the bed, besides the initiation region and the end wall region. The heap near the end wall is the result of particles ejected as the wave reflects off the end wall. Red dashed lines indicate the measurement region. . . . 87
3.24 **Bulk density change vs** ϕ_0**.** Percentage change in volume fraction is computed as an average of height changes the measurement region from Figure 3.23 assuming the entire vertical extent of the bed has undergone dilation. Since the dilation band is a fraction of the total bed height, these values are lower bounds. Results are included for both poured and tapped beds. 88
3.25 **Particle height change.** Each particle is color coded to show it's change in height. We show results for loose (top), medium (middle), and compact (bottom) packing of 2 m beds filled 20 cm deep with particles after a shock was initiated at v_p = 10 m/s. The extent of dilation increases with ϕ_0 and, in the case of the compact bed, a consistent portion of the near surface (to about 5 cm in depth) experienced more than 0.2 cm increase in height. 89
3.26 $\sigma\Delta z$ **vs radial position.** Deviation is computed for the radial positions in common across the parameters investigated. The legend shows the test from which the deviation is computed. 90
3.27 **Depth vs** σc_w**.** Deviation is computed for the depths in common across the parameters investigated. The legend shows the test from which the deviation is computed. 91
3.28 **Shock profile and particle height change for various test cases.** Each frame shows the profile of the initiated shock region and the resulting bed height change. The left images show the particle force (same legend as in Fig. 3.2) and the right image colors particles by their z displacement with the embedded color legend in units of m/s. The channels correspond to the thin strip (top), top half (middle), bottom half (bottom) test cases. 92
3.29 **Interacting waves.** Solitary waves with equal strength (v_p = 10 m/s) are generated in opposite directions from each end of a 2 m long channel filled 20 cm deep with particles (ϕ_0 = compact). From top to bottom the frames correspond to t = 0.093, 0.099, 0.104 and 0.195 s. Particles are colored corresponding to the order of magnitude of force experienced (same scale as in Fig. 3.2). The strength of each wave is maintained during and after the collision. The shape of the wavefront is largely maintained, though there is less curvature to the wavefront near the floor of the channel as the waves approach their terminal points (bottom frame). 93
3.30 **Mach # vs** v_m**.** Equation 3.9 is divided by c_0 corresponding to the loose (L), medium (M) and compact (C) packed assemblies to produce the predicted soliton speed (dashed lines) for a range of v_m. For the corresponding simulated results (various markers) we find $M = c_p/c_0$ and plot against v_m from table 3.8. Simulated results are only plotted for tests at $v_p \geq 1$. 94

3.31 z **vs force balance.** The lofting depth z_{loft} occurs when $F_{gravitational}$ and $F_{wavefront}$ are equal (denoted by the solid black line). The simulated and Lunar trends are produced using the material parameters described in the text along with eq. 3.12. When the fraction is greater than 1, wave front forces in the vertical direction exceed gravitational forces and particles will loft above the depth $z_{loft} = z(F_{wf}/F_g = 1)$. 97

3.32 z_{loft} **vs shock strength.** We solve equation 3.12 for z_{loft} at varying shock strengths (δ_m/δ_0). The expected lofting depths are approximately achieved for the strongest solitary waves ($\delta_m/\delta_0 = 5$) for both the Moon (cyan) and our simulated (black) conditions. There is a consistent nearly order of magnitude scaling of z_{loft} between our simulated case and the Lunar environment. 99

4.1 **Cold Spot density vs depth.** The lower X axis represents bulk density (black) and the upper X axis represents the percent change in bulk density density (blue), where negative percent change represents dilation. The y axis shows depth in cm and is the shared by both trends. The lunar surface regolith (black solid line) and LCS (black dashed line) are predicted using the method and fit parameters from [1]. Bulk density change (dotted blue line) takes ρ_{LCS} to be a percent difference from $\rho_{background}$. This percent difference can be thought of as 'dilation expected as the result of LCS formation' and we will use it as a reference later when viewing Figs. 4.4 and 4.10. 108

4.2 **Particle size distributions.** We plot cumulative percent of particles greater than a given size vs particle radius (mm). We use the lunar surface particle distribution from Fig 7.9 of [14] (data harvested with [186]) corresponding to the 63% Agglutinate soils (solid black line). The black dashed line is this same trend from [14], but increased by just over one order of magnitude (20x). The dashed line is the distribution from which we determine our bi-disperse (red Xs) and tri-disperse (blue circles) mixtures. The dashed orange line shows the particle size for the base case monodisperse distribution used in this paper (and in [177]) while the solid orange line shows the size distribution for the monodisperse 'lunar-like' particles used in this paper. 115

4.3 **Wavefronts.** We take a cut from various channels to qualitatively demonstrate the piston shock wavefront (top frame) compared to DSW wavefronts with varied curvature as a result of generation in channels of varied material parameters. Particles are colored by the order of magnitude of the force they experience relative to a heuristically chosen reference force (F_{ref}, usually 10^{-6} or 10^{-9} N). The cut for the shock frame (top image) is from the beginning of the channel (adjacent to the left wall), while the SW cuts (all subsequent images) are taken so that we can align their leading edge. In all cases the channel height is $160R$. The particle properties are set to the base parameters and each frame is from a channel with varied parameters. The second and third frames are beds of increased E, but with v_0 a constant portion of c_m (their wavefront shape is roughly the same). The fourth frame is from a channel of reduced particle size (R = 0.125 mm) and with v_0 = 10 m/s a smaller portion of c_m. There is less curvature to the wavefront. In the fifth frame we show a channel of R = 12.5 mm (v_0 = 10 m/s) which shows the least curvature out of all the cases. The dashed red lines are guides to compare the wavefronts across the different channels. 117

4.4 **Bulk volume change vs depth.** Percent change in volume ($\%\Delta\rho$) on the x axis vs normalized (by particle radius) depth for varied levels of ϕ_0. **Left)** Channels of 2 meters in length filled 20 cm deep with particles were filled to the loose (L), medium (M), and compact (C) ϕ_0 as described in sec. 4.2.1 were subjected to piston impacts at v_p = 10 m/s. The color scale represents ϕ_0. As ϕ_0 increases, dilation (negative values of $\%\Delta\rho$) increases in both the depth at which it begins (greater than z/R = 100 for ϕ_0 = C) and the peak dilated magnitude (around 14% at $z/R\sim$10) affected. **Right)** The piston impact speed is varied in a single channel of particles (R = 0.5 mm, ϕ_0 = M), with the color legend corresponding to v_p. Dilation increases with increasing v_p. In both plots, the solid line represents the expected LCS percent volume change from Fig. 4.1, normalized by an average lunar surface particle radius of R = 250 μm ([14]). 125

4.5 F_m **vs** ρ**,** v_0**,** E**, and** R **for varied cases.** Each plot shows average force in our 3D simulated waves vs the parameter of interest (v_0 in the upper right (UR), ρ in the upper left (UL), E in the lower left (LL) and R in the lower right (LR). The average simulated force for the given test is represented by a single data point and dashed lines are the corresponding fit. Solid lines show expected power law trends and are described in the legend of each individual plot. **UR)** Legend entries for the v_0 case are turned off due to over crowding. Star markers represent base case material properties, with cyan, red, and black colors corresponding to compact, medium, and loose ϕ_0, respectively. Solid markers are increased density (ρ = 25 g/cc) and open circles are reduced density (ρ = 0.8 g/cc) which (respectively) increase and decrease the force experienced by particles as a result of the wavefront. The pink trends correspond to varied particle sizes, where the lowest forces are experienced by the smallest particles (R = 125 μm, pink circles) and the highest forces experienced by the largest particles (R = 125 μm, pink plus sign). The green trends represent increasing modulus of elasticity, where E ranges from 5 (green filled circle) to 500 MPa (open green circle). The data and trend in blue represent a campaign of varied v_0 and E, with v_0 scaled to remain a constant portion of c_m. **LL)** We show the base case (with varied R) in red, with blue and cyan corresponding to slightly greater and smaller densities (respectively). **LR)** We included a comparison case of varied E and ρ in addition to R as the blue points which show how the force changes between the base particles and the lunar-like particles (ϕ_0 $\sim$58% and v_0 = 10 m/s. The upper solid blue line shows the expected scaling based on changing E, ρ and R while the lower solid black line shows the expected R^2 scaling. We did not calculate a fit for the comparison case given the paucity of points, but it is clear that the simulated results match the expected scaling. 131

4.6 **Normalized depth** (z/R) **vs average** F_m**.** We show average simulated force at each depth for 3D assemblies of varied size, where the color legend corresponds to particle diameter. Channels are filled to the medium ϕ_0 level of packing and are listed in Table 4.3. Simulated forces are circles and the plus sign markers show the computed force via eq. 4.9 for the given particle radius, base material parameters, and in input velocity of v_0 = 10 m/s. 133

4.7 **Normalized depth vs** δ **for varied** ρ**,** v_0**,** E**, and** R**.** Depth z on the y axis is normalized by particle radius (R) with overlap (δ) on the x axis. We show the trends for varied v_0 in the upper right (UR), ρ in the upper left (UL), E in the lower left (LL) and R in the lower right (LR). Each color legend gives the value to the respective varied parameter with circles, pluses, and dashes corresponding to δ_0, δ_m, and the prediction from eq. 4.2 (respectively). δ_m and δ_0 'pinch' together as depth increases and SID only occurs when there is a substantial difference between the two. 137

4.8 **Loft depth vs maximum lofted particle size.** We show the lofting depth on the y axis which is the depth to which particles of a given size (radius, R, on the x axis) can attain an upwards velocity as the result of the SW wavefront. 142

4.9 **Lofted height vs varied material parameters.** We show normalized percent change in bed height vs a sweep of various material and simulation parameters. The plots correspond to varied **A)** elastic modulus, **B)** radius, **C)** gravity, **D)** density, **E)** sliding friction , **F)** cohesion, **G)** restitution, **H)** Poisson's ratio, **I)** rolling friction **J)** rolling viscous damping **K)** momentum ratio and **L)** dispersity. In each case, the solid black line corresponds to percent bed height change of the reference case (generally a channel filled to 20 cm with particles of R = 1.25 mm, E = 5 MPa, and ρ = 2.5 g/cc. **A)** Shows the case for constant v_0 = 10 m/s in blue and the case where v_0 is a constant portion of c_m in cyan. The single red point corresponds to the lunar-like particles (ρ = 3 g/cc, R = 125 μm) with v_0 = 10 m/s. **D)** Shows bed height change vs particle density for various levels of ϕ_0, with the compact, medium, and loose channels corresponding to blue, red, and cyan markers (respectively). **F)** The data point for k_c = 0 was left off given the log nature of the x-axis, but showed the same bed height change as in cases with cohesion ($\Delta z \sim 2\%$). 146

4.10 **Dilation vs depth.** We show normalized depth (z/R) on the y axis vs percent bulk volume change on the x axis for cases of varying material parameters. Each plot has its own color legend corresponding to the varied parameter of interest. In all but the first case, only a single parameter is varied, with other parameters set to the base case from sec. 4.2.1 and v_0 = 10 m/s. The first plot shows the case of varied E and varied v_0, with v_0 held to the same portion ($\sim$20%) of c_m. The plots correspond to varied **A)** elastic modulus and impact velocity, **B)** elastic modulus, **C)** R, **D)** gravity, **E)** sliding friction, **F)** rolling friction, **G)** rolling viscous damping, **H)** density, **I)** velocity (with lunar-like particles), **J)** cohesion energy density, **K)** dispersity and **L)** impactor momentum ratio. Note that the case for restitution was left off as it is essentially identical to the plot for ν. In all cases the solid black line is the depth-normalized LCS expected bulk dilation from Fig. 4.1. 147

4.11 **Dilated channels.** Particles are colored by the percent height change with respect to their initial (pre-SW) state. We use *OVITO* to create the image and normalize particle vertical displacement by R, then find the percent difference compared to the initial 160R channel height. We show the color scale (C.S) for each frame in a box immediately to the left of the post-SW channel, where darkest blue is represented by the lower value and dark red by the higher value. Each box also includes details on the particle E and R as will as the percent height change corresponding to Fig. 4.9. Frames 1-3 show channels with the base parameters and increasing E while frame 4 shows the case corresponding to the lunar-like particles. All channels experienced a piston impact at v_0 = 10 m/s. Dilation is 'gentler' for the softer particle channels which corresponds to uniform (and smaller in magnitude) dilation that is present in shallow surface depths. As the particles become harder the SID is 'stronger' and most of the particles in the channel are thrown up and set back down in looser heaps. 149

4.12 **Blast loading via δ_m.** We show the normalized maximum overlap in the SW wavefront (δ_m/δ_0) vs channel length normalized by particle size (L/R) for varied properties. The color legends refer to varied **A)** density, **B)** impact speed, **C)** momentum ratio, **D)** gravity, **E)** radius and **F)** E (for the case with constant v_0 = 10 m/s). When applicable, we indicate the end of the BL zone (end of the PSW, the dissipative region near the left wall) as the black crossed circle. We find the end of the BL zone using the procedure outlined in sec. 4.2.4 (when δ_m/δ_0 becomes close to the average steady value in the DSW). The material parameters have very little effect to the end of the BL zone, which is generally between 200 and 300 R. Changes to momentum have more of an effect on the lateral extent of the BL zone, with increased velocity (frame B) increasing the length of the region somewhat, while changes to momentum by tuning the density of the impactor particles (frame C) could either extend the region quite a bit (out to 800R) or result in no identifiable BL zone for low impactor density. Because we track δ_m as the maximum δ experienced by a particle (as opposed to just the δ experienced by the initial wavefront), plot 6 for varied E is capturing effects from outbursts when E is large. 157

4.13 **Outburst vs DSW.** Particles are colored by their force magnitude experienced relative to a reference force of 10^{-6} N. The color legend is the same for all frames with the darkest blue at -2 (meaning the force a dark blue particle experiences is 2 orders of magnitude below the reference force) and the darkest red at 7. The images show the same channel (base parameters, but with E set to 500 MPa). From Table 4.6, the sound speed for this channel is c_0 = 40.2 m/s. Each frame represents a different value of the initial piston velocity used, with the frames corresponding to (from top to bottom) a v_0 of **1)** 10 m/s, **2)** 31.6 m/s, **3)** 56.3 m/s, **4)** 74.9 m/s and **5)** 100 m/s (which is approximately 20% of c_m). Frames are taken at different (arbitrary) times and and are selected so that the leading wavefronts (approximate PSW in frames 1 and 2 vs DSW in the others) are aligned. In frames 3-5, the energy delivered through any impact with the driven floor (including glancing oblique impacts) are large enough that a single well defined SW wavefront is created and maintained across the lateral extent of the channel. In frames 1 and 2 the conditions (geometrical arrangement of particles) that provide sufficiently large impact energies lead to occasional outbursts which, while they do not generate a coherent wavefront, are still able to dilate surface particles. . . . 159

5.1 **Hypothesis diagram.** Diagram of our hypothesis laid over the near surface structure figure from [9]. Boxed in red is the approximate cold spot region. The megaregolith wave (red) propagating to the right (impact occurred off the page to the left) drives the surface dilating wave (blue). 172

5.2 **Determining $D_{A,T}$.** Normalized particle overlap vs normalized distance (D/R) for varied particle sizes. The dashed box zooms in on where D_A and D_T are measured, we manually select the 1.05 crossing (the dashed black line in the zoomed portion). Note that we can observe the absolute runout when we define it as we have (δ_m/δ_0 = 1.05), but the actual absolute runout (δ_m/δ_0 = 1) extends beyond the bounds of our $1600R$ channels. The transition region between two regimes of power law decay is also manually selected as the bend in each of the curves (D_T, corresponding to the red plused-circle points). While the actual trends are a bit obscured, they can be better viewed in Fig. 5.3,D. Open red circles represent the maximum overlap at D_D and we identify their channel location using Fig. 5.5. 179

5.3 **Normalized overlap vs normalized lateral distance.** We plot the maximum overlap normalized by the initial overlap at each radial position along the channel after a wave has been initiated and until it has reached the end of the channel, with channel position normalized by particle radius. Red circles indicate D_D as in Fig. 5.2. The color legends in the different plots correspond to varied **A)** size (soft), **B)** channel height, **C)** overburden pressure, **D)**, size (hard), **E)** friction, **F)** piston density ratio, **G)** piston velocity, **H)** packing fraction, **I)** coefficient of restitution. Note that D_D is not marked in cases A and H since soft particles cannot support v_m that exceed v_D (see Fig. 5.5). 184

5.4 **Normalized overlap vs time.** We plot the maximum overlap normalized by the initial overlap at each radial position along the channel, with channel position normalized by particle radius. Red circles indicate D_D. The black dashed line is the same in all the plots, showing the universal power law decay with time seen in 1D granular chains. The color legends in the different plots correspond to varied **A)** R (soft), **B)** h_c, **C)** P_{op} **D)**, R (hard), **E)** μ, **F)** ρ_p/ρ, **G)** v_p, **H)** ρ, **I)** e. Note that D_D is not marked in cases A and H since soft particles cannot support v_m that exceed v_D (see Fig. 5.5). 185

5.5 **Maximum particle velocity vs time.** We plot the maximum particle velocity experienced in the decaying wavefront at each radial position along the channel, with channel position normalized by particle radius. The solid black lines represents the v_D velocity threshold, below which we do not anticipate a surface dilating wave to be supported. The color legends in the different plots correspond to varied **A)** R (soft), **B)** h_c, **C)** P_{op} **D)**, R (hard), **E)** μ, **F)** ρ_p/ρ, **G)** v_p, **H)** ρ, **I)** e. 186

5.6 **Dilated runout trends.** We plot dilated runout vs varied parameter for the values from Table 5.4 and the fits from Table 5.5. The plots form left to right show D_D vs velocity, channel height, friction parameter and piston vs background particle density ratio (respectively). The power law fit (dashed line) coefficients correspond to those in Table 5.5. 190

5.7 **Decay fits. Left)** Absolute runout distance vs particle radius for varied tests using the 160R tall channel and $v_p = 0.2c_m$. We consider D_A for hard particles (E = 50 GPa, red x) and soft particles (E = 5 MPa, black circle). The blue dashed line is a single combined fit to the measurements of soft and hard particles following a power law of R. **Right)** Dilation runout distance vs particle radius. Here we only consider the hard particles and show D_D for those cases conducted in the h_c = $160R$ (pink plus) and $h_c = 10R$ (red circle) cases. The single black star represents D_D from the $10R$ channel, scaled up with velocity, friction, and density ratio, as described in the text. The dashed lines are a power law fit with R for the h_c = $160R$ case and an assumed power law trend for the other two cases. 193

B.1 **Wave Visualization.** Wave propagation seen through force visualization. We performed the shocking procedure on a 2 m channel filled 20 cm deep with grains (compact packing). Each particle is colored based on a scale that represents the order of magnitude force experienced, relative to 10^{-8} N. Frame (a) is the settled particle bed. In Frame (b), the shock has been initiated and the wavefront is uniform. In Frame (c) the wave is propagating as a solitary wave and the front has acquired curvature due to slower surface speeds than those at depth. Frame (d) shows the beginning of the reflected floor wave and mobilization of surface particles in the first 1m of the channel is already evident. In Frame (e) the shock has just reached the end wall and Frame (f) shows that the reflected wave terminates before it can travel back down the channel. The reflected floor wave reaches the surface grains, though note the thin strip of particles that do not experience a force from this reflection. These are the fully detached particles. Frame (g) show that the surface modification remains while the bed begins to settle. The small high force region at the surface in the middle of the channel is the result of an ejected particle returning to the surface, which does not further modify bed height. 212

List of Abbreviations

BL	Blast Loading
DEM	Discrete Element Method
DSW	Driven Solitary Wave
EMT	Effective Medium Theory
EPSD	Elastic-Plastic-Spring-Dashpot
LAMMPS	Large-scale Atomic/Molecular Massively Parallel Simulator
LCS	Lunar Cold Spots
LIGGGHTS	LAMMPS Improved for General Granular and Granular Heat Transfer Simulations
LRO	Lunar Reconnaissance Orbiter
PSW	Piston-initiated Solitary Wave
P-Wave	Primary or Pressure Wave
RSE	Random Seed Error
SID	Solitary Wave Induced Dilation
SSDEM	Soft Sphere Discrete Element Method
SW	Solitary Wave
S-Wave	Secondary or Shear Wave

Chapter 1: Introduction and Motivation

Lunar Cold Spots (LCS, [1]) are recently classified global, but ephemeral, features of unknown origin appearing around fresh impact craters on the Moon. LCS can only be observed by examining nighttime surface regolith temperatures; there is no other indicator of their appearance. These Cold Spots were first noticed (with an Apollo era radiometer, [2]) as isolated regions of reduced thermal inertia (typically, the surface has highly uniform thermal inertia [3]). It wasn't until [4] used Diviner, a thermal infrared radiometer aboard the Lunar Reconnaissance Orbiter (LRO, [5]) to systematically map lunar surface temperatures that LCS could be characterized. [1] used the night-time temperature map to catalog LCS, identifying them as regions of surface temperature more than 2 K colder than background regolith. Since then, [6] extended the catalog by about 200 cold spots, bringing the total known population to nearly 2,500 craters. As a 'fingerprint' of the impact, LCS have already been used to discern details about the original impactor population ([6]) as well as a guide to finding the most recently exposed surface material ([7]). Other similar analysis may become even more common place thanks to recently updated nighttime thermal maps ([8]) that reveal LCS halos to have a greater extent and more detailed structure than previously known. LCS are enigmatic, however, and their origin is mysterious despite our recently growing knowledge of their nature. [1] linked the colder surface temperatures to reduced thermal inertia resulting from a 'fluffing' of the upper 10s of cm of surface regolith. Determining

such a fluffing mechanism remains elusive, a task complicated by the unique features of the LCS halo.

The LCS halo is much larger than the source crater, extending an average distance on the order of 100 crater radii. We emphasize that this represents an area much larger than could be perturbed by impact ejecta (on the order of 2000 km^2 for a 1 km diameter crater in [1]). These Cold Spots occur across the entire surface, indiscriminate of morphology (they occur in both the highlands and the mare). LCS, therefore, represent a non-insignificant portion of the lunar surface (around 1%, [1]). The largest cataloged LCS surrounds the 2.3 km diameter crater reported in [6], implying that all LCS appear around 'simple' craters, those less than $\sim$20 km in diameter [9]). Some aspects of the LCS halo mimic proximal impact ejecta, presenting as a coherent halo nearer to the source and fading with radial distance. However, there are several features of the halo (highlighted in Fig. 1.1) that are unexplainable given our understanding of cratering processes (sec. 1.1.1).

First, beyond the coherent halo there is a patchy of region of reduced thermal inertia mixed with background regolith, making the assessment of LCS extent difficult. Furthermore, some regions of the halo exhibit low thermal inertia rays that extend well beyond the average halo distance. Finally, while many LCS exhibit halos that are radially uniform, the LCS in this image exhibits a region (more than 90° of arc) of abrupt termination on its right hand side. This channelized nature must be a result of some detail of the impact, the surface, or both. Beyond just their appearance (and as mentioned previously) LCS are unique in that they are only seen around young craters. The newest LCS have bright thermal signatures, but older LCS begin to fade and craters older than roughly 1 Myr ([11] identified a 2 Myr old crater using an Apollo boot-print) do not exhibit reduced thermal inertia halos. The method of LCS erasure is not entirely known,

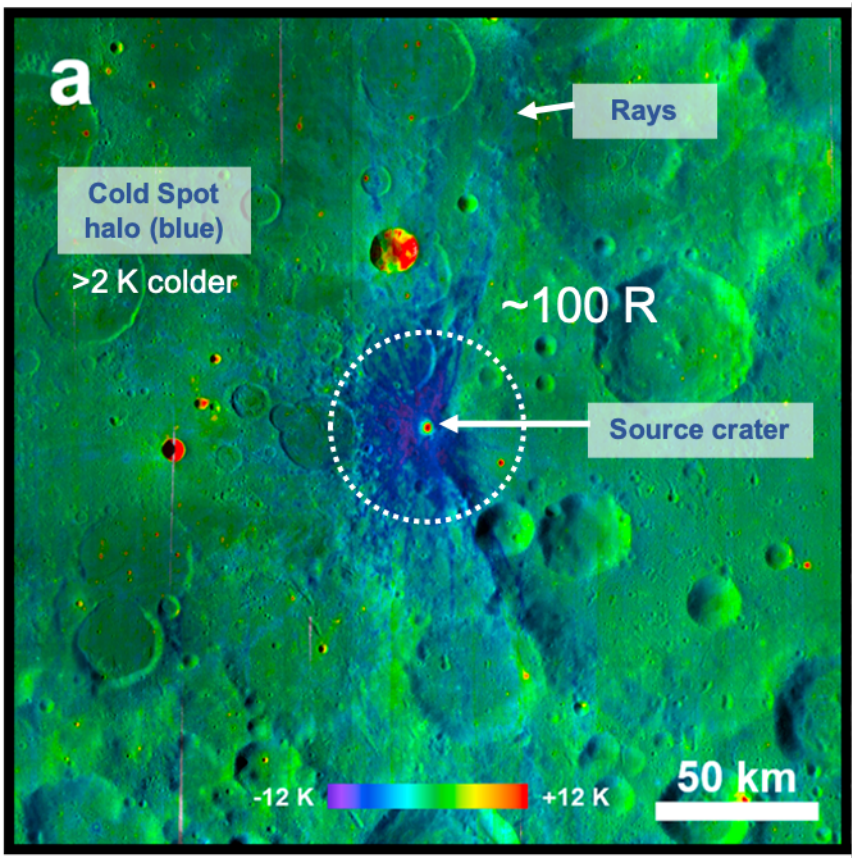


Figure 1.1: **Lunar Cold Spot.** An infrared image of the Lunar Cold Spot at 151.7°E, 4.1°S first shown in [1], Fig. 3 (this image is taken from an updated version in [10], Fig. 11). This source crater (small red dot at the center of the image) is 1.55 km in diameter and has a Cold Spot (blue region) area greater than 19,000 km^2. Some of the salient features are labeled, with the dashed line representing the average 100 crater radii size of the LCS halo (not to scale). The color bar from the original image represents night-time surface temperature differences, with the green background regolith as the baseline at 0 K. The blue reduced thermal inertia halo represents cooler temperatures (than background) of more than 2 K. Low thermal inertia rays are seen to extend much further than the average LCS halo.

though space weathering or seismic shaking are the suggested culprits. It is suspected that vibrations from secondary impacts ([6], [12]) are the likely cause, driving the loosened regolith back to a more compacted state. Tying all these features together is some unknown fluffing mechanism.

Understanding how LCS form has implications for solar system evolution as well as in-situ activities anticipated as part of and following the Artemis missions ([13]). The regolith

(from which all our current in-situ measurements come: [14], [15], [16]) contains a history of both the Moon's formation (details about the impacts which generated regolith, sec. 1.1.1) as well as a record of solar evolution transmitted to the surface-most grains via the solar wind. As such, whatever mechanism leads to reduced bulk density in the LCS halo modifies the history recorded in the regolith and must be better understood. Looking forward, large scale construction efforts (lunar base or mining) could unintentionally modify the surface far from the construction site, depending on what the actual fluffing mechanism is. For example, there may need to be requirements placed on the magnitude of blast loading at a certain depth so as not to further modify the surface or to not interfere with other local human activities.

There are three processes identified in [1] that could drive LCS formation: 1) a cascading series of secondary impacts, 2) lateral gas flow derived from either the impactor or target and 3) some link to seismic events (ruled out by [1]). Shock induced micro-fracturing ([17]) could be a possible 4th LCS formation mechanism, or perhaps several of these processes work together to generate reduced bulk density surface regolith. Micro-fracturing (method 4) almost certainly does contribute to near crater reduction in thermal inertia, but the micro-fracture halo is thought to be only half the size of the LCS halo for similar sized source craters ([18]). Furthermore, the long rays extending outside the coherent LCS halo seem to be problematic for both high stress near-impact fracturing as well as method 2 (gas flow). Ruling out method 3 (seismic events) was justified based on a comparison to terrestrial seismic events ([19]), but regolith has been shown to exhibit distinct and peculiar behaviors in low gravity environments ([20]) compared to terrestrial settings. It may be possible that subsurface pressure waves released by an impact on the Moon induce previously unknown effects. While there are potential solutions and problems within each of these methods, [1] highlighted that, regardless of the specific driver of the formation process,

LCS seem to be the result of a granular flow initiated by particle-particle collisions. In this work we model these particle-particle collisions using a simulated regolith analog (a long channel filled with small particles) in which we characterize the waves generated via an impulse. Our focus is therefore most closely related to method 1, though we highlight that we are not modeling ejecta emplacement, but the transmission of an impulse as a granular wave.

This thesis considers an answer to the question succinctly stated in [3]: "By what process does the regolith become fluffier?" We posit that LCS are formed as the result of laterally propagating impulse energy (in the form of a granular wave) which is able to re-arrange grains thanks to the low gravity and vacuum environment of the Moon. We employ a numerical modeling approach to characterize the dynamic behavior of vacuum exposed surface regolith experiencing the impulse of impact as a laterally propagating granular wave. We study both the near surface dynamics and a possible subsurface driver. The main contributions of this work are:

- An open source methodology for studying low gravity granular wave behavior
- The first demonstration of near surface particle lofting and bulk dilation as the result of a laterally propagating wavefront
- A theory for predicting the depth extent of induced dilation as a function of impact velocity along the floor of a granular channel
- Confirmation that the wave decay in 3D randomly packed granular assembly is the same as in 1D chains (particle number controls decay distances, decay follows a power law in time)
- A proposed mechanism for the generation and long range propagation of a surface dilating wave (impact energy decay in buried boulders)

Thesis Statement

The grain-scale analysis undertaken in this work will elucidate the Lunar Cold Spot formation mechanism. We will either validate one formation mechanism (grain-grain impacts) as a likely contender or we will rule it out, suggesting support for other possible progenitors. We will explore several concepts unique to low gravity granular dynamics settings and demonstrate a previously unobserved granular process. Ultimately, this work will provide strong evidence for our hypothesis, that cold spot regolith is fluffed up by a surface solitary wave driven from below by the decay of impact energy through boulders at the regolith-megaregolith boundary. The implications of the formation mechanism may be relevant to many natural environments across the solar system and future human construction efforts on the Moon.

Thesis Outline

First we provide additional background through the literature review in sec. 1.1, covering the lunar near-surface structure and wave transmission in granular assemblies. Ch. 2 discusses the selection of our contact model, simulation software and an initial validation against basic granular physics. Ch. 3 provides a validation of our 3D wave generation methodology in an idealized case and details on our investigations of grain motion near the surface of a vacuum exposed granular channel (grain lofting does occur in this scenario!). Ch. 4 considers the scaling of the lofting mechanism of ch. 3, showing that the near surface particle lofting a granular wave can induce scales appropriately to the lunar environment (when the grains we simulate have the same material properties as lunar surface regolith). Ch. 5 considers the driving mechanism

of the surface lofting in ch. 3 and 4, in the form of a buried granular wave propagating in meter scale boulders. Ch. 3 through 5 have been written with the intent that they will be stand alone publications and appear here with minimal modifications (we note the state of the work (published/submitted/prepared) at the beginning of each chapter). Finally, in ch. 6 we provide concluding thoughts and point to avenues of future work.

Publications

Journal Articles

- Frizzell, E.S., Hartzell, C.M. Runout distance in buried boulder scale granular channels. Journal TBD (in prep, 2024).
- Frizzell, E.S., Hartzell, C.M. Material parameter influence on the expression of Solitary-Wave-Induced Surface Dilation. Granular Matter (in prep, 2024).
- Frizzell, E.S., Hartzell, C.M. Simulation of lateral impulse induced inertial dilation at the surface of a vacuum-exposed granular assembly. Granular Matter 25, 75 (2023). `https://doi.org/10.1007/s10035-023-01363-6`

Conferences

- Frizzell, E.S. and Hartzell, C.M. (2024). Effect of Subsurface Topography and Bulk Density Variations on Solitary Wave Induced Surface Dilation as a Lunar Cold Spot Formation Mechanism. Lunar and Planetary Science Conference, 55, Abstract #2012. Poster.
- Frizzell, E.S. and Hartzell, C.M. (2023). Material Property and Particle Distribution Effects

on Unconfined Inertial Dilation. Lunar and Planetary Science Conference, 54, Abstract #2737. Talk.

- Frizzell, E.S. and Hartzell, C.M. (2022). Simulations of a Laterally Propagating Rarefaction Shockwave at the Interface Between a Randomly Packed 3D Cohesive Granular Assembly and Vacuum in Microgravity. AGU Fall Meeting, 2022, Abstract #EP32D-1335. Poster.

- Frizzell, E.S. and Hartzell, C.M. (2021). Post-Impact Granular Dilation on Airless Bodies. Combined NASA Exploration Science Forum and European Lunar Symposium, 2021. Abstract #09, Thursday, July 22, 8:39am. Electronic Poster.

- Frizzell, E.S. and Hartzell, C.M. (2020). Simulations of Post-Impact Granular Dilation on Airless Bodies. AGU Fall Meeting, 2020. Abstract #EP041-09. Electronic Poster.

Invited Talks

- Frizzell, E.S. and Hartzell, C.M. (2023) Investigating a possible Lunar Cold Spot Formation Mechanism, George Washington University FRIday Engineering and Science Seminar Series, 11/03/2023.

1.1 Background

Lunar Cold Spots exist in the vacuum exposed surface material of the Moon; the regolith. In this section we review the details of lunar surface regolith and the sub-layer buried below it (the upper megaregolith). The motion of regolith is well described by granular dynamics and we

provide an introduction to the physics of grains. Finally, we are interested in the propagation of an impulse through this granular media and so we review existing works that consider wave propagation in regolith.

1.1.1 The Lunar Surface

The Moon's surface is binary in the sense that we see either bright, anorthositic highlands or dark, basaltic mare. The highlands represent the majority of the surface, and there is consensus that their uniform composition (primarily of anorthite plagioclase, a silicate) results from crystalization of this less dense (compared to magma) mineral from within a global Lunar Magma Ocean (more than 4 BYa [21], [22]). The formation, floating, and cooling was rapid (on a planet forming time scale), leaving behind a floating 25 km to 30 km thick crust. The mare experienced sustained heating due to volcanism long after the cooling of the highlands crust, resulting in their smoother appearance, darker color (higher iron content), and younger age. Since the crustal crystallization, it is readily apparent that both the mare and the highlands have been pummeled by impactors. Here we briefly consider the impact process and the resultant generation of surface regolith and megaregolith.

Impact cratering

The Moon's heavily cratered surface reveals that impacts of planetary bodies by meteors are commonplace. Craters are formed as the result of hyper velocity impacts in the range of 15 - 25 km/s (slightly slower than earlier in the solar systems history). The contact generates a cavity in which there is impact melt, brecciation, and vaporization of surface material and 'a

roughly hemispherical shock front propagates outward from this cavity and into the target' [9]. In this thesis we are primarily concerned with the behavior of this outward propagating wave front and not near crater effects like melting and fracturing (LCS halos exist far from the source crater). However, understanding impact processes gives important context for understanding the substrate in which LCS appear; the regolith. The impactor population follows a power law distribution with size [23] (orders of magnitudes more small than large impactors) meaning that large, basin forming impacts are rare while micrometeoroids impact the surface nearly continuously in comparison. These largest, but rare, impacts fracture an initially uniform (see 1.1.1) crust and generate large scale ejecta, some of which go on to generate secondary impact craters. Secondary cratering and smaller impactors may not fracture the crust, but they continue to modify earlier large scale ejecta and this process is repeated down to the micrometeroid scale, where the smallest impactors nearly continually rework the surface most material. This impact process has lead to the current surface to crust structure, a representation of which we show in Fig. 1.2. In this image we are most interested in the upper regions corresponding to large scale ejecta (megaregolith) between 10 m and 2 km depth and the surface regolith from the surface to an average depth of 10 m. The surface represents the most highly reworked material on the Moon and the LCS halo exists in only the very near surface of the regolith.

Regolith

The surface regolith is a fine grained granular material (average size < 100 μm, [14]) that covers nearly the entire lunar surface, shielding the underlying bedrock from most external influences. We show an an image of the surface in Fig. 1.3a. The size distribution of regolith

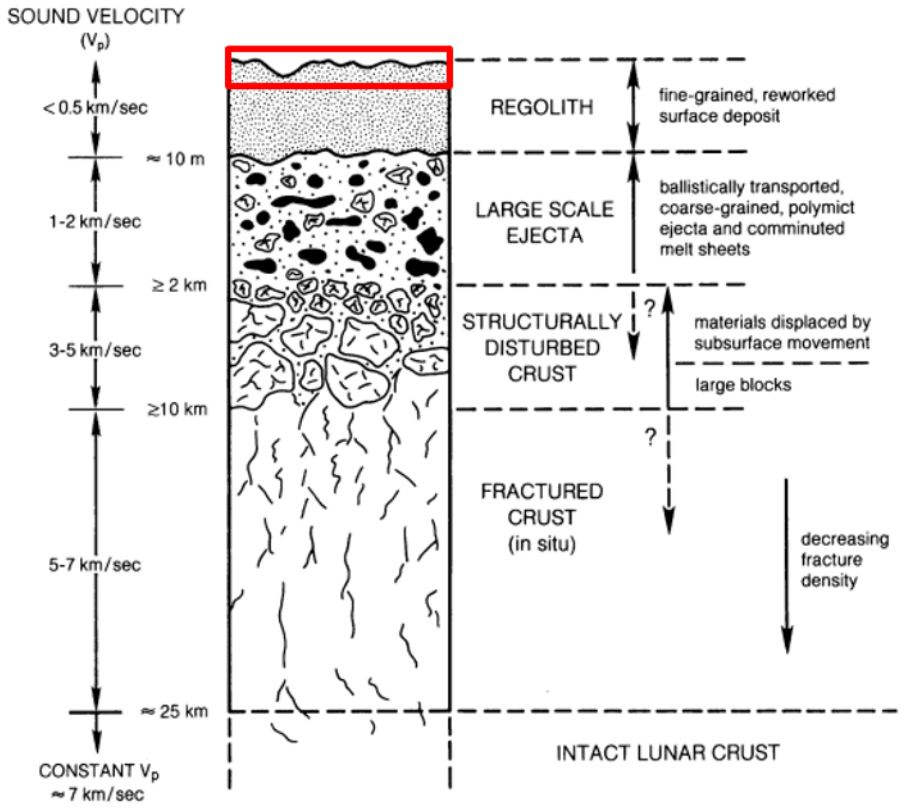
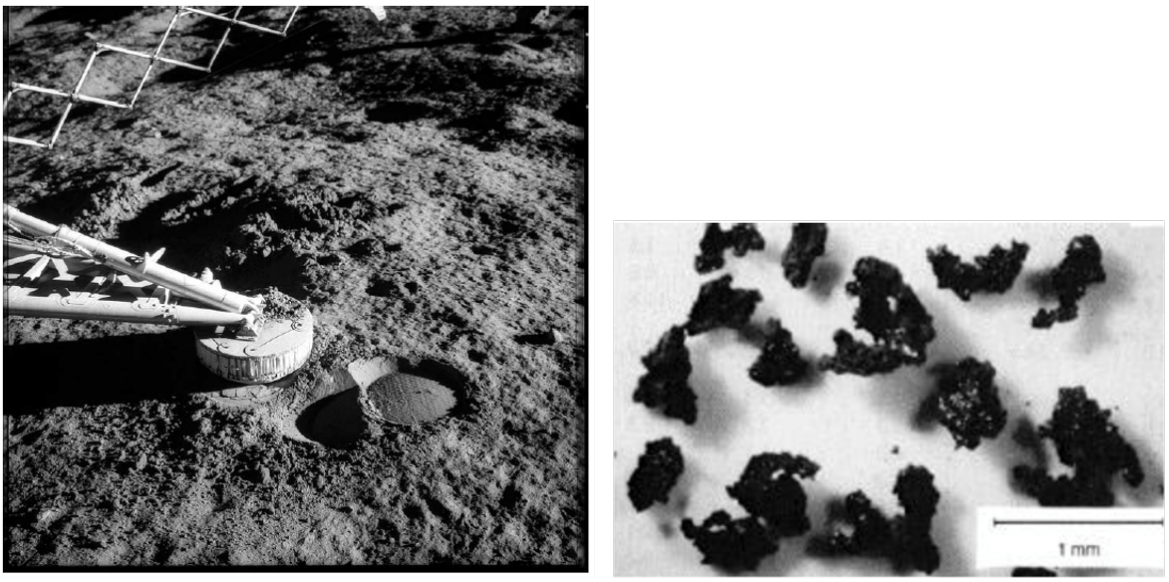


Figure 1.2: **Lunar Surface Structure.** Figure of the upper lunar crust from [9], their Fig. 4.22, showing our regions of interest. The red box at the surface (not to scale) shows approximately the suspected depth extent (0 to 40 cm) of the LCS reduced thermal inertia regolith.

grains is highly uniform and it is the dominant presence at the surface. Even though cm scale rocks and larger boulders are present, the surface regolith is often referred to as the 'rock-free regolith' [1]. Compositionally, highlands regolith is anorthositic while the maria are basaltic. As a result of their formation mechanism (impact-induced disintegration of rocks), regolith grains (ranging from the smallest single micron sized grains, to the largest glass bonded rock aggregates mm in size, 'agglutinates') are highly angular. We show an image of surface agglutinates in Fig. 1.3b. Since the regolith is exposed to vacuum, these angular grains do not undergo terrestrial erosion processes ([24]) which enables higher cohesion than is seen in Earth-bound soils. These factors (high cohesion, angular grains in a size distribution spanning three orders of magnitude)

combined with lower lunar gravity lead to a relatively loose range of packing fraction (a measure of compactedness) for bulk regolith at the surface. The surface regolith tends toward a more compacted state within its range (42% to 50%, [15]) as the result of secondary impacts and seismic shaking ([25]). Using a regolith grain density of 3 g/cc ([25]) along with these levels of compaction results in surface bulk density less than 2 g/cc. Bulk density quickly increases with depth as a result of gravitational compaction from overlying regolith (see Fig. 4.1). The regolith layer is thought to terminate abruptly, undergoing a sharp transition to the layer below (the megaregolith) around a depth of 5 m in the mare the and 15 or 20 m in the highlands ([7], [26]).



(a) (b)

Figure 1.3: **(a) Lunar Surface.** The high cohesion of the lunar surface can be seen in the steep walls of the Surveyor 3 landing pad footprint. NASA photograph AS12-48-7110, Apollo 12 Principal Investigator Richard J. Allenby Jr., National Space Science Data Center. **(b) Regolith agglutinates.** Agglutinates are fused assemblies of smaller regolith particles and represent larger members of particles (mm scale) from the lunar surface regolith size distribution. Image from [14].

Megaregolith

Historically, the term megaregolith has been used to describe any of the layers of material below the regolith down to intact lunar crust. [27] has a good review of the term's history and clarifies the distinction between the upper megaregolith which exists over ∼1-3 km in depth and the deeper lower megaregolith which extends beyond the upper region to around 20 km in depth. While the lower megaregolith consists of bedrock that has been fractured in place, the upper megaregolith is a result of brecciated and ballistically transported ejecta (corresponding to the 'large scale ejecta' region in Fig. 1.2). It is the upper megaregolith that will prove to be most relevant in this thesis as it is the layer directly in contact with the regolith. The abrupt nature of the transition between the regolith and the upper megaregolith is supported by both radar observations and seismic studies. There is a sharp jump in sound speed between the layers and ground penetrating radar shows the appearance of meter-scale boulders around 20 m in depth. Lunar seismic studies ([28], [29], [30]) confirm an abrupt jump in the sound speed, from around 100 m/s ([31]) at the surface to more than 300 m/s in the upper megaregolith. Orbital radar observations ([32], [33]) suggest meter scale boulders sit just below the regolith, and this seems to be confirmed by the ground penetrating rover on the Yutu-2 over ([26]). The results in [26] show further stratification even in just the first meters of the upper megaregolith (see their Fig. 2). Just below the surface regolith (12 to 24 m depth) are a layer of 1 to 3 m boulders, followed by another layer (24 to 40 m) of mostly finer regolith interspersed with some boulders. We suspect Lunar Cold Spot formation to be a consequence of the interface between these two layers (micron sized surface regolith and boulder sized megaregolith). Assuming this grain-grain interface is important to study, we need a method that can characterize the dynamics of grain motion and

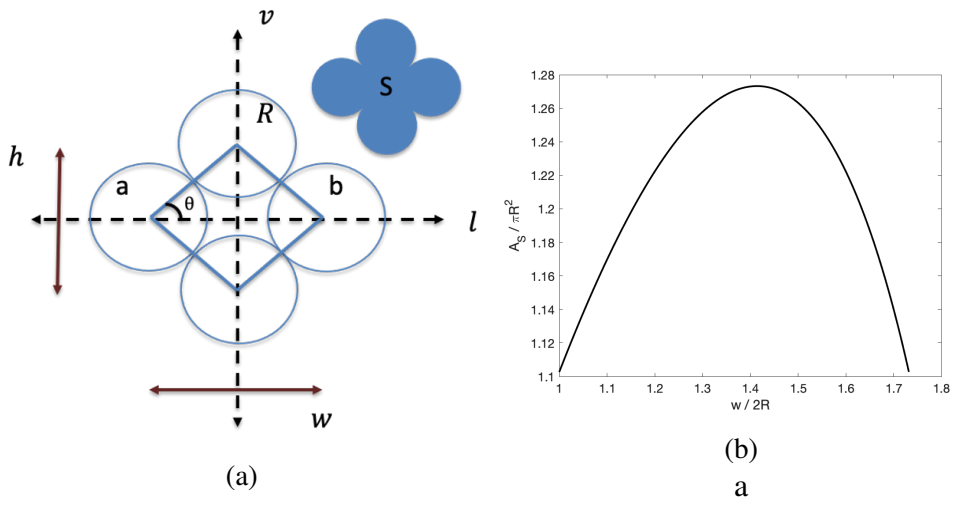
interaction.

1.1.2 Granular Dynamics

Granular materials are assemblies of macroscopic particles (grains). Everyday examples include baking flour, beach sand, river bed gravel or a jar of mixed nuts. Understanding the behavior of granular materials has implications for a huge range of topics including agricultural, industrial, geological as well as planetary formation. Describing the physics of these grains (granular dynamics) encompasses an enormous size range, ranging from micron sized powders to boulder size rocks that take part in planetesimal generation. This means that descriptions of behavior are sometimes only relevant within a certain regime. As energy per grain in the system increases, the assembly exhibits properties of first solid, then liquid, and even kinematic gas states ([34]). When grains are in a solid state ('quasi-static'), forces are transmitted through distinct chains, introducing the possibility for some grains to be shielded, feeling no effect from an outside disturbance. In fact, there are many unique behaviors that arise in granular assemblies, one often cited case being the 'brazil nut effect' (size segregation from shaking, [35]). Other unique behaviors have come to light as we visit low gravity environments (like asteroids or the Moon), there is a good review in [20]. Here we focus on two main topics in the realm of granular mechanics: dilation and wave propagation.

Granular dilation

Granular dilation is the de-compaction (or rarefaction) of a confined granular assembly due to an external energy source. One type of granular dilation is the result of imposed shearing, also



(a) (b)

a

Figure 1.4: **(a) Idealized 2D Compacted Grains.** The combined area of the particles and the void within them is represented by S. The area of S will change as the dimensions of the central trapezoid change due to grain movement. The inter-particle distance, w, is defined as the distance between the centers of particles a and b. **(b) Trapezoidal Area.** Normalized trapezoidal area is plotted against normalized inter-particle distance. See [37] sec. 3.1.3, for the relevant equations. From left to right, grains a and b begin in contact and the distance between them grows. The trapezoidal area (representative of the void) grows and then decreases.

known as Reynolds's dilation. Reynolds first described this behavior as bulk volume increase that results from grain deformation when applied to a 'strongly compacted' granular material ([36]). The definition of strongly compacted is situation dependent and ultimately the behavior of granular assemblies is heavily influenced by the configuration ('packing') of the grains. We visualize granular dilation using the 2D example from [37], pictured as the assembly of four spherical grains from within a compacted granular medium (Fig. 1.4a). As the inter-particle distance between particle a and b changes, the area of the central trapezoid increases or decreases (shown in Figure 1.4b). Extending the example to 3D, the effect of the dilation is to change the bulk volume. Thus, the initial state of the particles effects how the void spaces of the granular packing change with applied force.

Adding vibrational energy to a granular assembly is another way to achieve dilation. Con-

sider a clear, cylindrical container filled to some fill height, h_0, with grains. The container sits upon a device that allows for its base to be repeatedly tapped at an adjustable rate. If the grains within the container were initially very loose, you would expect any frequency of tapping to cause the grains to compact. The new height of grains in the channel, h_n, would be reduced as a result of the compaction ($h_n < h_0$). However, if the grains in the cylinder were initially *strongly compacted*, then some frequencies would cause the grains in the channel to dilate, and the container fill height would increase ($h_n > h_f$). This procedure describes the tapping experiments of [38], [39] and [40]. Tapping can be a slow or fast procedure depending on the frequency of the input, but requires sustained external energy infusion. The generation of an LCS halo being coincident with impact seems to imply a rapid change to surface regolith bulk density as the result of a single infusion of energy.

The method of granular dilation we are interested in this work is inertial dilation, which is a more energetic re-arrangement of the grains in the assembly. Grains undergo an inertial flow regime and experience grain-grain collisions as though they were a kinetic gas, so shear and normal stresses are dependent on the rate of momentum exchange between the particles ([41]). One type of granular dilation wave observed on Earth is the culprit beyond 'silo quaking' ([42], [43], [44], [45]), an engineering challenge for granular materials in storage silos. Silos become jammed when a plug develops (i.e., flow is halted). If the jam is rapidly removed, rarefaction shock waves are generated which travel to the top of silo, inducing audible popping noises and potentially damaging the silo. The tapping mentioned in the prior paragraph is one way to resolve the jam without generating rarefaction shocks. We suspect that a laterally propagating wave in the regolith, initiated by the impact, may induce such an inertial dilation given the low gravity and exposure to vacuum of the regolith.

Waves in regolith

Wave propagation can only occur in a granular medium as the result of force transmission along the points of contact between grains. In the simplest case (a 1D chain), the first particle in a long row of identical particles is given a velocity in the direction of the chain, resulting in a succession of impacts that propagate the initial impact energy. In a real 3D granular medium (like the regolith), the force of an impact spreads out randomly along multiple paths, giving way to a complex force chain network. However, large enough impulses generate pulses that travel as uniform wave fronts, maintaining a coherent shape despite the randomness of the packing ([46], [47]). These pulses are known as solitary waves, which were first studied by [48] as an application of Hertz elastic theory to a 1D chain subject to impacts. Understanding solitary waves in both 1D and 3D granular media is still an active field of study as their behavior is highly dependent on the initial state of the media through which they travel. We review these topics concerning solitary waves in sec. 3.1.1 and 4.1.1. Here we've just briefly introduced these topics so we can consider them in the context of waves propagating in regolith.

Understanding wave propagation in regolith is an active field of study, though most recent works are primarily motivated by understanding waves in asteroid regolith (a much weaker gravity environment than the Moon). One driver for this is the interest generated by visits to small bodies Bennu ([49]) and Itokawa ([50]). Newly revealed features of theses small bodies have generated questions regarding the distribution of boulders and regolith on their surfaces. For example, [51] and [52] studied size sorting effects of impacts and seismic pulses in the context of small bodies. Another driver of the focus on asteroid surfaces is the recent Double Asteroid Redirect Test, DART ([53]), in which the DART spacecraft was used as a hypervelocity impactor

into the secondary of a binary system. Among the goals of DART were to understand changes to the orbit and any modifications induced on the secondary. [54] investigated if distal post impact seismic shaking caused by an impact like DART could loft grains (only a single grain layer at the surface). [55] studied vertically propagating seismic waves that dissipated rapidly and supported that perturbation would be confined to an external layer. The studies carried out in [56] and [57] considered how the energy of an impact would decay in an asteroid, questioning if the signal would be similar to what occurs in terrestrial settings ('jolt') or would exhibit decay akin to what is seen on the Moon ('reverberation'). On Earth a seismic pulse is easily identifiable as a brief, but large, spike in wave amplitude. On the other hand, signals on the Moon have long codas ([58]). Though there has been a good deal of study of Lunar seismicity, the works mentioned in this section were focused on understanding the interior structure of the Moon as opposed to the (relatively) small motion of grains at the surface.

1.1.3 Summary

This thesis considers vertical particle lofting as the result of a laterally propagating wave front. We believe we are the first to study and characterize this suspected method for a vacuum exposed granular channel experiencing low gravity to undergo surface dilation. Based on the quality of the regolith (a granular material) and the behavior of waves within such a material (predicted by Hertz theory), we now have guidelines by which to select our simulation method.

Chapter 2: Code Selection and Validation

This chapter covers details concerning our rationale for contact model selection and software selection. Mostly, we cover additional two body validation tests of our chosen simulation tool. Largely, details concerning the determination of our methodology are woven throughout the introduction and background of ch. 3, since that goal of that chapter is to validate our model choices. Here we will briefly expound on some of these decisions and point the reader to relevant sections where appropriate.

2.1 Modeling choices

In this work we will use a particle-based simulation tool, *LIGGGHTS*, that models contacts between particles that can experience small overlaps (Soft Sphere Discrete Element Method) using Hertz elastic theory.

2.1.1 Contact Model: Hooke vs Hertz

Our Hertzian contact model (see Appendix A) employs a nonlinear spring force, where the force experienced by contacting grains depends on particle-particle overlap following a power law ($\delta^{3/2}$). Modeling contact forces using a Hooke model (linear force dependence on overlap) is another common choice. Both are valid choices ([59], [60]). However, since solitary waves in

granular media were originally described using Hertz law ([48]), a choice which has since been validated by many ([61], [62]), we will use Hertz law here too. We discuss the selection of Hertz model further in sections 3.1.1 and 3.2.1 since we consider impacts at speeds near the elastic limit (or just past).

2.1.2 Continuum vs particle based

Impacts, especially crater producing ones, are typically modeled with continuum methods. For example, both [63] and [18] used a modified versions of *iSALE*, a Finite Element Method shock physics code, to model lunar crater formation. However, as detailed by [64] (see sec. 3.2.1), continuum methods are not able to account for grain rearrangement leading to dilation. [63] also pointed out that dilation taking place during the crater formation process is often unaccounted for in continuum modeling and so they modified *iSALE* to include dilatancy. Their implementation relies on calculating a dilation coefficient (calculated from the shear forces experienced by their finite element nodes), which accurately reproduces simple and complex crater geometry. [63] even saw a thin sheet of increased porosity (i.e, dilation) at the surface beyond their newly formed (simulated) crater, though their focus was porosity enhancement beneath a newly formed crater. This near surface porosity was explained as a modification induced by the shock-free surface interaction, but a shock wave traveling over LCS scale distances through the regolith layer seems highly unlikely given the rapid dissipation that would occur therein. Furthermore, the simple crater in [63] was around 4 km in diameter and they extended their simulated domain a few km beyond this, but a LCS halo for this sized crater should extend around 200 km. To understand how impact induced distal porosity could be generated, we require a modeling method that can

resolve the dynamics of individual grains. For this the Discrete Element Method (DEM) is a natural choice.

2.1.3 Soft Sphere Discrete Element Method

The first use of DEM modeling is typically attributed to [65], where it was used to describe the mechanical interactions of discs and spheres. DEM was later used for modeling asteroid accretion ([66]). This application of DEM is 'event driven', where collisions are (relatively) sparse. Collisions happen at distinct intervals based on orbital dynamics and the time step can be set by propagating from event to event. On the other hand, when the arrangement of grains is not sparse, computation time for an event driven method becomes intractable. The Soft Sphere Discrete Element Method (SSDEM) handles this problem by employing a very small time step (a portion of the collision time, see [67]. There are many studies considering the distinct behaviors of grains in low-gravity environments using DEM, see sec. 3.2.1 for an overview. Here we are specifically interested in understanding wave propagatin in regolith and we will attempt to do so using SSDEM solver *LIGGGHTS*.

2.1.4 LIGGGHTS

Ultimately, we selected *LIGGGHTS* ([68]) as our SSDEM simulation method of choice. Using pre-assemble software had several benefits which we list below. *LIGGGHTS* stands for *LAMMPS* Improved for General Granular and Granular Heat Transfer Simulations. *LAMMPS* stands for Large-scale Atomic/Molecular Massively Parallel Simulator. As you may suspect, we did not choose *LIGGGHTS* based on its name. Instead the following factors drove our decision:

- Open source
- Parallelized for High Performance Computing (HPC)
- Use in the literature (see sec. 3.2.1)
- A wide variety of force models, including ready to use implementations of those we are specifically interested in (several flavors of Hertz and Hooke contact models, varied friction, rolling friction and cohesion models)
- Pre-built functions that exist for particle creation (pouring via *ins/stream*) and particle motion (tapping via *fix/move/wiggle*)
- Planetary Surfaces and Spacecraft Lab heritage ([69], [70])
- Ability to add/modify force models
- Ability to model aspherical particles

Though we did not ultimately pursue the last two items in this thesis, they would be interesting avenues by which to extend this work. There are always difficulties encountered any time one works with a code that is not their own, and this work was no exception to that rule. To ensure that the behaviors of grains in our simulations are physical we performed several basic physics validation tests.

2.2 Two-body validation

While the ability of *LIGGGHTS* to reproduce experiments has been extensively demonstrated, issues with the force model can be masked by choice of parameters or bulk behavior.

Table 2.1: SSDEM Parameters for particle-particle validation

Property	Symbol	Test 1	Test 2	Test 3	Test 4	Test 5	Test 6	Test 7
Time Step [μs]	Δt	50	50	50	50	50	50	50
Particle Diameter [m]	D	1	1	1	1	1	1	1
Particle Density [kg/m^3]	ρ	1	1	1	1	1	1	1
Young's Modulus [MPa]	E	5	5	5	5	5	40	5
Poison's Ratio	ν	0.3	0.3	0.3	0.3	0.3	0.49	0.3
Coefficient of Static Friction	μ_s	0.3	0.3	0.3	0.3	0.5	0.8	0.3
Rolling Friction	μ_r	0	0	0	0	0	0.2	0.8
Rolling Viscous Damping	γ	0	0	0	0	0	0.0	0.3
Cohesion energy density [J/m^3]	k_c	0	1000	0	0	0	0	0
Gravity level [m/s^2]	g	9.81	0.25 - 0.38	0	0	9.81	9.81	9.81
Coefficient of Restitution	e	0.3	0.06	0.06-1	1	0.06	0.06	0.06

We validate the two-body force interactions (sphere-sphere, sphere-wall) of our model using the same validation tests as [71] which were used to validate another SSDEM code. Seven tests are performed and described in the following subsections which validate each component of the force model described in section 3.2.1. Table 2.1 shows the parameters for each test which are similar to those in [71] except where noted in the description of each test. For any particle-wall interactions, the wall is an infinite plane with the same material properties as the particle. We discovered and resolved an issue with the implementation of the Hertz tangential force model which affected the sliding test. After correcting the model implementation, all tests pass successfully and we validate all components of our model function as expected at the particle scale.

2.2.1 Normal Force

Five spheres are dropped exactly on top of each other and come to rest on a plane. There is no translational motion and the particles do not acquire any angular velocity, indicating that all

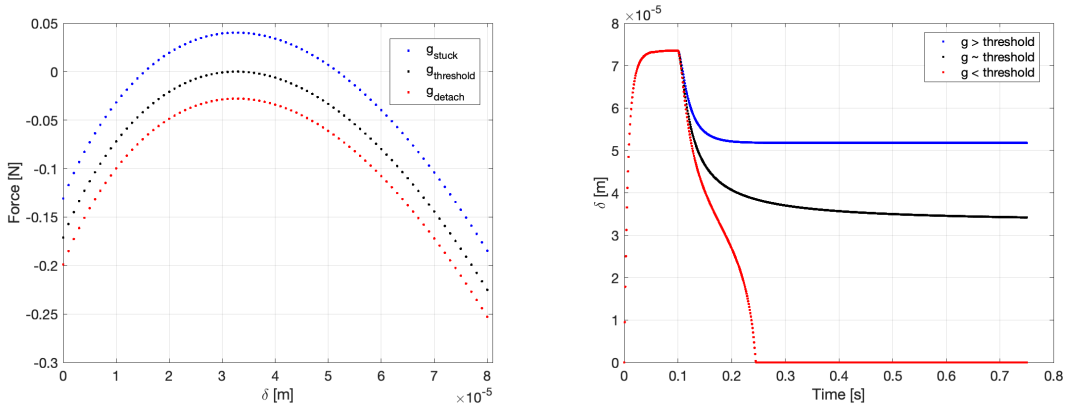
force remains in the normal direction as is expected and confirming the base normal model (eq. A.1, A.4).

2.2.2 Cohesion

One sphere is fixed in place and a second sphere is moved toward the first from below until the particles are in contact ($\delta_n > 0$). After creating the contact, the particles settle until the forces they experience are steady at which point gravity is turned on. The particles will remain in contact as long as the condition $0 \geq -k_n\delta_n^{3/2} + k_cA_c + mg$ can be satisfied. For the Test 2 particle properties in Table 2.1, this threshold is $g \approx 0.3268\ m/s^2$. Our acceleration parameters are different than those in [71] since they tested a constant force cohesive model while we test a model based on contact area (A_c, eq. A.7) which changes with δ_n. Figure 2.1 shows the agreement of the this test with expectation, confirming our model produces valid results with the addition of SJKR cohesion (eq. A.8).

2.2.3 Normal Impact

Two particles are inserted into a domain without gravity and given equal and opposite velocities so that they collide. The post impact coefficient of restitution (e', eq. 2.1 for particles i and j is measured to confirm that the velocity after the collision agrees with the user input coefficient of restitution (e). The test is repeated for all values of coefficient of restitution for Test 3 in Table 2.1. The 1-1 relationship in Figure 2.2 confirms that the normal damping (eq. A.4) works as expected for all values of e. Note that the DEM software used in [71] allows values of e as low as 0 while *LIGGGHTS* places a lower bound of $e = 0.06$. We use the *LIGGGHTS* lower



(a) (b)

Figure 2.1: **(a) Force vs δ.** Particles with an overlap will remain stuck together when gravity is turned on as long as, for a specified gravity, the normal force does not exceed 0. We show the force evolution as particles are pushed together or separated for levels of gravity above, below, and approximately equal to the threshold g **(b) δ vs time.** The validation test is run for the three gravity cases. The particles remain in contact when expected and show a new steady δ at at the $F = 0$ crossing from Figure 2.1a.

bound in all of our tests when the corresponding test in [71] is set to 0, which does not have any influence on our results.

$$e' = \frac{v'_j - v'_i}{v_j - v_i} \tag{2.1}$$

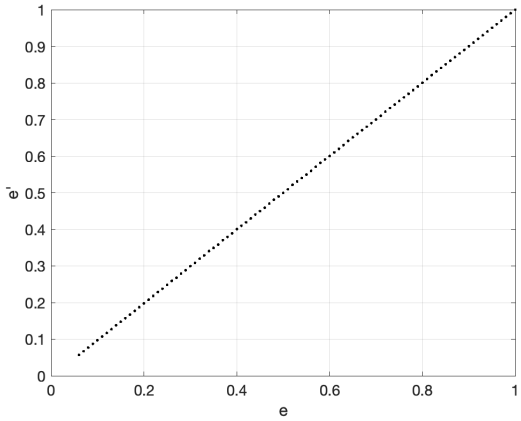


Figure 2.2: **Input e vs post impact e.** User input e is recovered exactly for all values.

2.2.4 Oblique Impact

A single particle is launched with impact angle, θ_i, at the floor. Above a threshold θ_{th} (eq. 2.2) the particle is in the sliding regime throughout the collision ([72]). Post collision angular velocity (ω') and tangential coefficient of restitution (e_t') should follow equations 2.3 and 2.4 ([73]) in this regime. This behaviour is recreated when combining the normal and tangential forces of our model (eq. A.8, A.12), see Figure 2.3a. Particle parameters are those for Test 4 in Table 2.1.

$$\theta_{th} = arctan\left(\frac{7}{2}\mu_s(1+e)\right) \tag{2.2}$$

$$\omega' = -\frac{5}{2}\frac{\mu_s(1+e)v_{0,n}}{D/2} \tag{2.3}$$

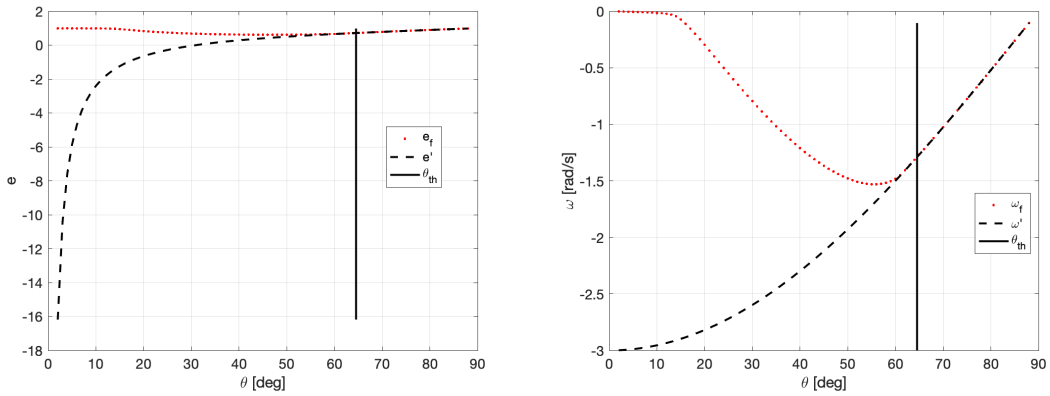
$$e_t' = 1 - \frac{\mu_s(1+e)}{tan(\theta)} \tag{2.4}$$

2.2.5 Sliding

A single particle is allowed to settle on a flat surface before being given a tangential velocity $v_{t,0} = 5\ m/s$ .The particle should come to rest within $10^{-3}\ m$ of the predicted distance. For the particle parameters for Test 5 in Table 2.1 this is $d = 2.5484\ m$ (eq. 2.5).

$$d = \frac{v_0^2}{2\mu_s g} \tag{2.5}$$

Here we initially experienced a discrepancy between expectation and performance when



(a) (b)

Figure 2.3: **(a)** e_t' **vs** θ_i**.** Tangential coefficient of restitution vs impact angle shows that the expected behavior is reproduced after the threshold impact angle. **(b)** ω' **vs** θ_i**.** Post collision angular velocity vs impact angle shows that the expected behavior is reproduced after the threshold impact angle.

we found that the particle stopped about 20 cm short of d. We found that the *LIGGGHTS* Hertz tangential model (as of release 3.8.0) uses a scaling for the sliding friction that is $|k_t\delta_t| \leq \mu_s|F_n|$ as opposed to the full tangential force as prescribed in the Hertz model (see section 3.2.1). After we updated the threshold and scaling to be based on F_t the particle came to rest after 2.54841 m, an error of 10^{-5} m. We have shown that our implementation produces expected results with respect to the sliding threshold and tangential overlap history (eq. A.12) components of our model.

2.2.6 Rolling

A single particle is allowed to settle on a flat surface before being given a velocity of 1 m/s. The particle should slide and then roll, experiencing constant torque before coming to a stop. The parameters in Table 2.1 for Test 6 are those from [74] instead of [71] so that we could compare position and torque profiles. Figure 2.5 shows that our model accurately captures expected rolling

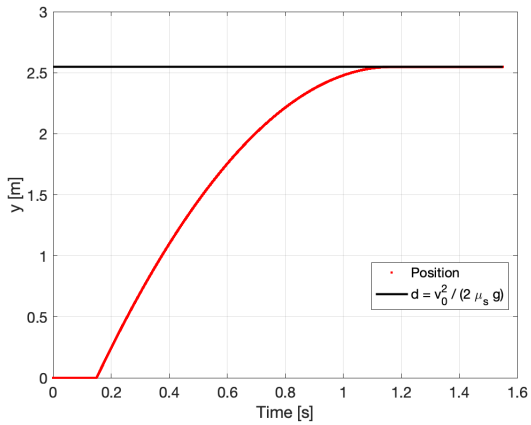


Figure 2.4: **Distance vs time.** Particle position vs time shows that after being given an initial velocity v_0 the particle comes to rest at the expected distance.

torque behavior (eq. A.13). The small difference in final position is attributable to a slightly stiffer rolling spring constant in *LIGGGHTS* than in [74] (they use their equation 7c while *LIGGGHTS* uses equation 7b). The difference in torque profile after the particle has stopped is attributable to the difference in tangential force model implementation. In the *LIGGGHTS* implementation of the tangential force the damping parameter (eq. A.4) depends on a user input coefficient of restitution. The implementation from [74] uses a code called PFC2D/3D which does not use a fixed coefficient of restitution to compute the damping coefficient ([75]), but instead that of [76] in which the coefficient of restitution varies based on impact speed. Appropriateness of each model is debated in the literature and outside the scope of our work.

2.2.7 Twisting

Given an initial angular velocity, a particle resting on a plane should eventually come to rest. *LIGGGHTS*'s [74] implementation of rolling friction (eq. A.13) captures twisting (torsional) friction due to the use of incremental relative rotation angle ([77]). With the particle properties

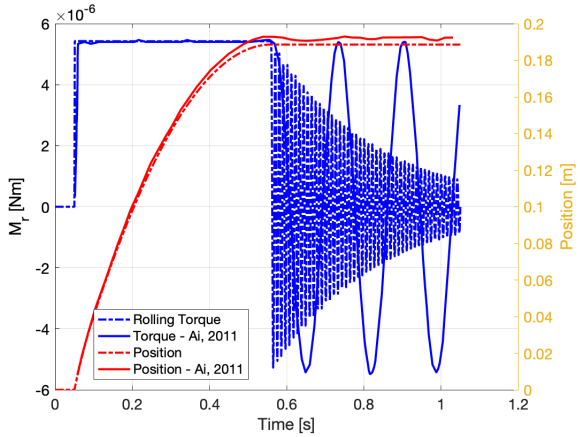
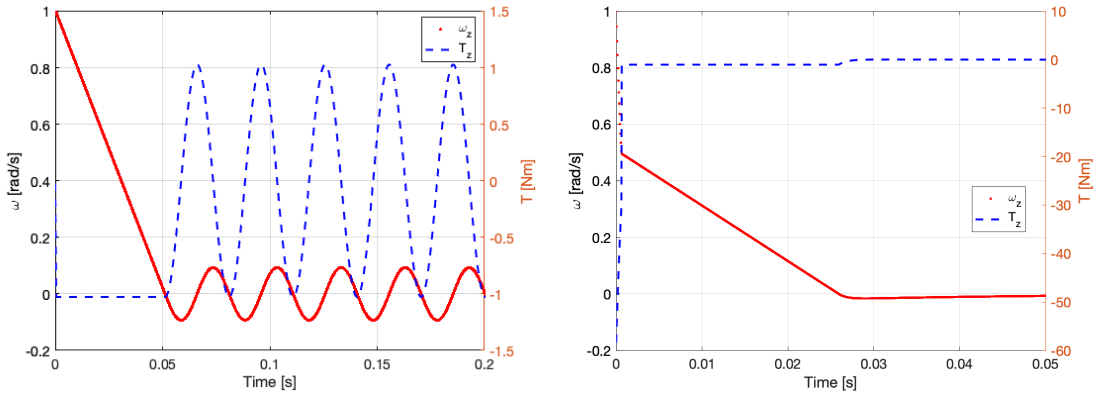


Figure 2.5: **Torque and Distance vs time** We show the time dependence, for both our implementation and that of [74], of torque (left axis) and position (right axis) of the particle in this test.

corresponding to Test 7 in Table 2.1, the particle experiences constant torque and reaches oscillation about a stopped equilibrium state (Figure 2.6a). To mitigate this oscillation, we apply a rolling damping coefficient (eq. A.15) of $\gamma_n = 2.0$. This is on the same order as used for terrestrial particles in [78] and we can see that the particle comes to rest after the rotational energy has been depleted, with very little overshoot.

2.3 1D wave validation

Before moving to a 3D assembly, we validate our ability to recreate expected wave speeds in a 1D particle chain subject to normal impact at speed v_{im}. We can use these results later to compare 1D chain behavior to a 3D assembly. We first check our ability to find c_w in a quasi 1D chain of particles seen in Figure 2.7a as in [79] which was validated experimentally ([80]). Note that we will refer to [79] as AE in this chapter. We use the peak force tracking method (shown and described in Figure 2.7b) to replicate their results for steel particles. Steel particle simulation



(a) (b)

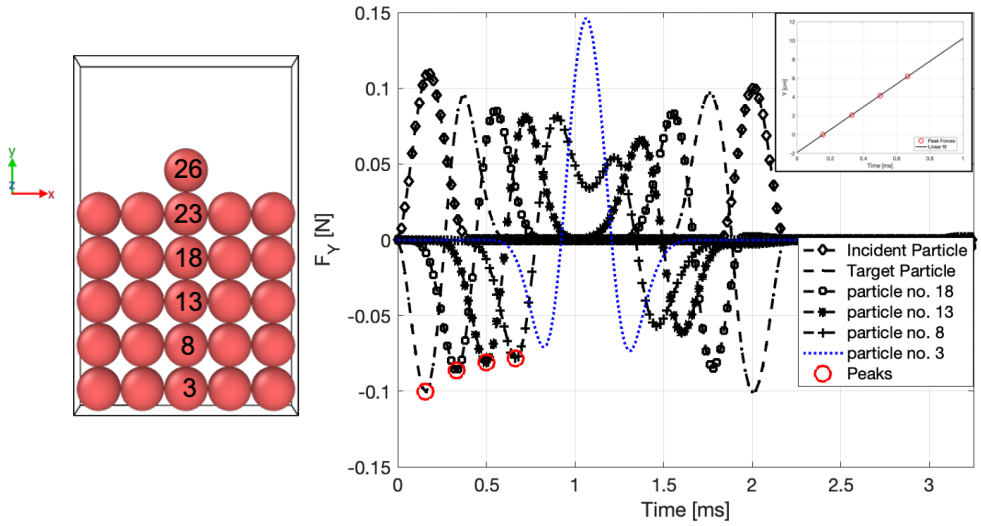
Figure 2.6: **(a)** ω **vs t.** Angular velocity vs time shows that a particle with no rolling viscous damping ($\gamma_r = 0$) stops spinning, but experiences continual oscillations after stopping **(b)** ω **vs t.** The same plot as Fig. 2.6a, but with $\gamma_r = 2$ shows that the particle stops spinning and and comes to rest with a small amount of overshoot with sufficient damping.

Table 2.2: 1D Particle Properties. Steel values are those used in [79] and soft particles values are selected from Table 2.1.

Particle Type	Steel	LRE
E [Pa]	2.1×10^{11}	5×10^{6}
ν	0.28	0.2
μ_s	0.5	0.7
R [mm]	10.32	10.32
ρ [kg/m^3]	7870	2500
c_m [m/s]	5.84×10^{3}	47.14
Δt [s]	10^{-10}	10^{-6}

parameters are provided in Table 2.1.

In Table 2.3 we show our computed c_w and find the percent difference from the AE reported c_w, which are in good agreement. The lower speeds ($v_{im} \leq 1.0$ m/s) are within 3% of the values given by AE which can be attributed to the differences in integration scheme (AE uses Euler implicit integration ([81]), *LIGGGHTS* uses higher order velocity Verlet integration ([82]). The difference of 11% between our results is attributable to differences in choice of cohesion model. Both implementations are described in [83] and AE implements a cohesive pressure distribution



(a) (b)

Figure 2.7: **(a) Granular Assembly.** Reproduction of a 5 by 5 square packing of particles from [79]. The incident particle (26) is given a velocity in the negative y direction (v_{im}), initiating a normal impact with the target particle (23). Force is transmitted solely along the force chain of numbered particles and their evolution is plotted in Figure 2.7b. **(b) Peak Force tracking.** We plot force in the y direction vs time for each of the particles within the impacted chain from Figure 2.7a using steel properties from Table 3.1 and v_{im} = 1 m/s. As in [79] we find c_w by identifying the peak forces in particles 8, 13, 18, and 23 (red circles). The slope of the line which is fit to the the particle positions and corresponding time of maximum force is c_w, the processes is shown in the upper right corner.

Table 2.3: 1D Validation Model Comparison. The *LIGGGHTS* Hertz contact model is compared to the implementation of TN from AE.

v_{im} [m/s]	0.25	0.5	0.7	1.0	3.0
c_w [m/s] [79]	498.39	558.09	614	657	774
c_w [m/s] LIGGGHTS	500.68	573.32	621.13	669.44	860
% difference	0.45	2.73	1.16	1.89	11.11

for elastic-perfectly plastic spheres (section 2) while *LIGGGHTS* uses the pressure distribution as described for adhesive elastic spheres (section 4). The different pressure distributions are valid during plastic loading, hence the larger difference at higher v_{im}.

We now extend this test for a greater range of v_{im} and check that softer particles exhibit the same trend. The soft particle parameters are given in Table 2.2 and were selected from Table 2.1 while leaving the particle size the same as in [79] and scaling the time step for the lower strength particles. We should find that weak impacts produce constant speed acoustic waves within the assembly and strong impacts produce shocks that follow a nonlinear power law dependence on the impact velocity. The expected power law dependence for shocks is $c_w \propto v_{im}^{1/5}$ ([84]), where c_w is the wave speed in particle chain as a result of normal impact. Figure 2.8 shows the results of these tests, reporting the normalized sound speed against v_{im}. We clearly see the expected weak impact acoustic waves and strong impact shocks. The normalized c_w for the soft particle acoustic waves is larger than that of steel since the normalization at v_{im} = 1 m/s is closer to the acoustic wave region for the soft particles than for steel. We reproduce the expected power law dependence for shocks, regardless of material properties. Given the agreement with expectations we can be confident that our choice of model and its implementation in *LIGGGHTS* accurately reproduces this 1D physical phenomenon.

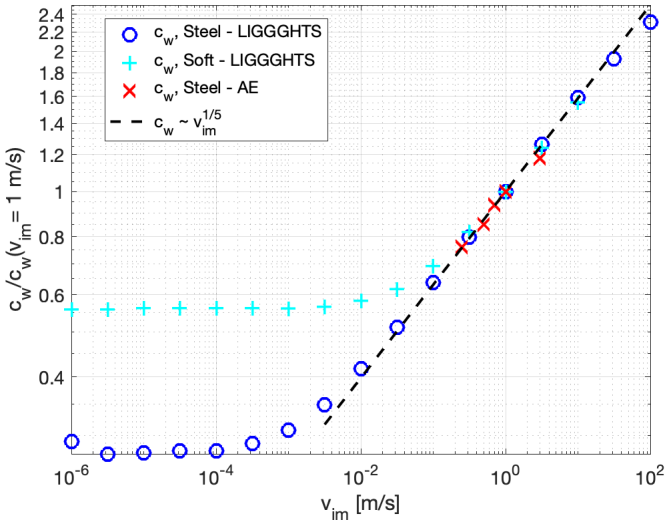


Figure 2.8: **Normalized wave speed vs impact velocity.** c_w reported for varied v_{im} are normalized by $c_w(v_{im} = 1 \text{ m/s})$. We normalize c_w at $v_{im} = 1$ m/s instead of at vanishing v_{im} ([84]) in order to include the data points from AE. Our tests as well as the results from AE recover the expected power law dependence.

2.4 Summary

In this chapter we chose to use a particle-based simulation methodology as opposed to a continuum based method; individual grain motion is likely an important piece of the LCS formation puzzle ([1]). We will use a Hertz based contact model due to our need to model initial high speed impacts that generate granular shocks as well as the solitary waves that subsequently form. Given these criteria we selected *LIGGGHTS*, an open source SSDEM particle solver. Having settled the foundations of the methods utilized in this work we can now move on to applying them.

Chapter 3: Simulation of Lateral Impulse Induced Inertial Dilation at the Surface of a Vacuum-Exposed Granular Assembly

This section appeared in its original form in: Frizzell, E.S., Hartzell, C.M. Simulation of lateral impulse induced inertial dilation at the surface of a vacuum-exposed granular assembly. *Granular Matter* 25, 75 (2023). See the online version for supplementary information (videos). Reproduced with permission from Springer Nature.

3.1 Introduction

Granular dilation is the property of a compacted granular material (packing fraction $\phi > 0.58$, [85]) to undergo bulk volume increase as a result of shear-induced grain deformation, first documented by [36]. This dilation is commonly studied in applications ranging from natural (tectonic-induced dilation, [86]) to industrial (dilation waves in grain silos, [87]). Bulk density increase via granular dilation can occur gradually as a result of inter-grain contacts (through vibration ([40]) or at a shear surface interface ([88])) or as the result of a more kinematic rearrangement of particles due to large strain rates ([89], [41]). The latter ('inertial dilation') occurs during rapid granular flow, where grain movement can be modeled by the kinetic theory of gasses ([90]) and particle motion is dominated by collisions. However, the movement of grains in this regime is not well characterized and few studies exist that examine this behavior in microgravity

([20]). Recently we have seen that, often, granular materials in microgravity and low confinement pressure do not behave as expected. Some examples include the unexpected properties of Bennu's surface as revealed by OSIRIS-REx ([91]) and parabolic-flight experiments that reveal microgravity suppression of secondary granular flow ([92]). Examples specific to high speed impacts include the ability of a single pulse from a granular wave to produce previously unknown effects. [51] showed that, while long thought to only occur as the result of shaking, the Brazil Nut Effect can occur as the result of a single granular pulse. [52] also saw that boulder stranding will occur far from the impact source as the result of only a single impulsively generated wave. Given these examples, inertial dilation under microgravity and unconfined upper boundary deserves further exploration.

In this paper we are particularly interested in the behavior of surface grains far away from the source of impact-triggered ground shocks ([93]) on the Moon ([94]). Do surface grains on the Moon exhibit a different response to the regimes of wave strength experienced as an impulse travels and evolves than they do on the Earth? We have found no prior work that quantifies vertical bulk volume changes induced by laterally propagating granular waves at the surface of a mechanically free interface under reduced gravity. The literature largely focuses on waves traveling vertically toward the free surface ([95], [87], [96], [55], [54]) or shock studies that quantify the lateral extent of dilation behind the shock front ([97]) at atmospheric or greater confinement pressures ([98], [99]). Furthermore, experiments examining lateral shock propagation can be limited given difficulty in preparing long samples and uncertainty of results caused by invasive measurement techniques ([98]). Given the challenges of experiments studying long range wave propagation and recreating the Lunar environment, we employ particle based modeling to study laterally propagating surface waves. Numerical simulations of terrestrial impact cratering re-

sponse by [63] showed that a narrow dilation band exists in the near surface as a result of an impact, but their modeling method is unable to account for individual grain motion. Dilation is restricted to near surface depths since the confining pressure of the overburden (grains supported by a particle at depth) quickly turns shear forces towards compaction ([17], [100]). Experiments indicate that both the magnitude ([88]) and vertical extent ([63]) of the dilation band will increase in the Moon's microgravity environment. Experiments by [85] confirmed that exposure to vacuum maximizes post impact dilation. We investigate how the surface grains in this dilation band region respond to laterally propagating waves. Our motivation for exploring this topic is rooted in the common appearance of the mysterious Lunar Cold Spots (LCS), distal regions of reduced bulk density surrounding craters on the Moon ([1]).

While LCS are a common feature of young craters ([6]) and occur across all terrains of the Moon, their formation mechanism remains unknown. The LCS is apparent as a relatively cold halo (as compared to background regolith) and is the result of reduced surface bulk density (ρ_{bulk}) in the near surface (to 40 cm depth). The cold spot begins about 10 crater radii away from the source crater and can extend radially to more than 100 crater radii, abruptly terminating in some regions while gradually fading in others. The regions nearer to the crater ($<$ 10 crater radii) show signs of lateral transport while there is no observable surface modification in the distal reduced thermal inertia region. The expected dilation varies between 1% and 10% over the first 40 cm of depth. Taking the percent difference of the average LCS and background bulk densities at the surface results in just over 4% dilation which is about the same as that caused by silo rarefaction waves on Earth (up to 5%, [87]). Hemispherical shock waves propagating outward from an impact [94] are essentially lateral waves at the surface and represent a potentially significant mechanical disturbance in the same region where LCS form (i.e., very low confinement pressure).

Nearest to the impact site, regolith will undergo fragmentation, melting, or even vaporization depending on the strength of the initiated shock, but the waves decay as they propagate outward. The distal regions surrounding a LCS would be subjected to waves of varying strengths following an impact. Given that the LCS region of expression is limited to a narrow surface band of regolith exposed to vacuum we hypothesize that inertial dilation induced by lateral surface waves is at least involved in the LCS formation process. However, a surface wave would need to travel over large distances ($\sim$100 km) to be relevant in LCS formation. In this paper, we study the dynamics of surface grains under microgravity following the passage of a single, impulsively generated granular wave. Our objective is to simulate laterally propagating waves and determine if they can reduce surface bulk density when waves are active at the grain-vacuum interface.

We present a simulation of a laterally propagating granular wave in a long, open-to-vacuum channel generated by piston impact. We consider an idealized assembly of randomly packed monodisperse spheres as an initial proof of concept. Since we are interested in the ability of surface grains far from the source crater to undergo dilation, we generate a single wave via an impulse and allow it to evolve laterally across the length of the channel. The channel is filled with deformable particles and we measure the assembly's dilation response to both acoustic and shock waves by measuring the at rest bed height following the passage of a wave. We provide a brief overview of waves in granular media (sec. 3.1.1) in the literature before describing our simulation methodology (sec. 3.2). We then provide results from simulations that explore the influence of wave speed, wave type, boundary effects, and initial conditions on volumetric changes in the bed and characterize the observed dilation (sec. 3.3).

3.1.1 Waves in granular media

Waves propagating in a granular medium as the result of an impact fall into two distinct regimes: weak and strong. Weak impacts produce a pressure wave with propagation speed dependent on confinement pressure, whereas strong impacts produce a pressure wave with a non-linear power law dependence on impact force due to geometrical effects of the particle contacts ([101]). Furthermore, depending on both the duration of an initial impulse as well as the pre-compression in the grains, the generated waves can exhibit stationary, oscillatory, dispersive, and even non-decaying responses. While a comprehensive overview of the different responses is provided in [62], we briefly introduce three important categories here. Acoustic waves are generated via weak impacts and result in waves traveling at the sound speed, c_0, but with high dispersion. Strong impacts produce waves with pressure-independent speed and when there is high dissipation, these waves are shocks. Between these two extremes are solitary waves, which travel while maintaining strength and shape (the result of a balance between dispersion and nonlinear effects). These waves can be generated on impact or as the decay product of a shock. Solitary waves are the most compelling for our purposes here given the large extent of LCS. [48] first characterized propagating solitary waves in a 1D granular chain subject to an impulse and confirmed the results experimentally. When the pre-compression in the grains is zero (or very low), the assembly is considered to be weakly compressed. In other words, when the compression induced by an impulse is much greater than the initial pre-compression, the assembly is weakly compressed. This leads to a scenario where waves propagating in the chain are dominantly influenced by nonlinear effects, a regime of propagation dubbed the 'sonic vacuum' by [48]. Following their introduction, solitary waves in 1D chains have been investigated by many, both experimentally ([102]) and

numerically ([103], [104], [105], [106]). Solitary waves have been similarly confirmed and explored in 2D ([107], [108], [109], [110], [111], [112], [113], [114]). The study of solitary waves is still ongoing. One branch of focus lies in the tunability of a solitary wave's existence based on the randomness of the packing ([115], [116]) or the stiffness ratios between particles ([111]). Another focus is on granular wave response in the very low confinement pressure regime which is not fully understood ([117], [118]). [84] found wave speed relationships for sound waves and shocks in a randomly packed 2D bed of particles near the jamming transition (very low pressure). [55] continued in this vein, characterizing seismic wave speeds at confinement pressures as low as 0.1 Pa in a 3D randomly packed bed, but they studied vertically propagating waves and were not concerned with the grain-vacuum interface. In the context of the vacuum and microgravity of the Lunar surface, the first layer of surface grains is close to the zero pre-compression regime as the initial overlap (δ_0) approaches zero at small depths (eq. 3.6). However, on the depth scale of the LCS (40 cm), grains will experience gravitational loading (Fig. 3.3) and are also confined laterally by neighboring particles. The wave propagation regime may therefore vary based on the strength of an applied disturbance.

Even in 3D granular assemblies on Earth, solitary waves can be sustained and propagate in a weakly dispersive regime. [119] first used a large area impulse to generate a solitary wave which could be used to detect buried objects. [120] mentioned [119] as an example when commenting on the robustness of solitary waves in 3D, though this is usually in the context of understanding how granular materials can be used to selectively disperse the waves [121], [122]. [123] may have created solitary waves in their 3D granular bed but had a channel of insufficient length to make a distinction between a solitary and semi-permanent wave. While experiments by [57] found that a single granular pulse is generated by low speed normal impacts, the resultant lateral signal

attenuated as the pulse expanded. However, the tests of [57] were conducted at atmospheric confinement pressures which leads to increased pre-compression on particles at the surface as compared to the Lunar (vacuum exposed) case. The most recent work on this topic ([124]) studied the effects of increasing pre-compression on the behavior of solitary waves. A solitary wave that was highly stable at some small initial loading transitioned to acoustic-like propagation as the pre-compression was increased. While the investigation in our paper builds on these prior works, we are most interested in observing grain-scale dynamics and the resultant dilatory response in the bulk due to lateral waves propagating in different regimes (acoustic, solitary, shock).

The sound speed of compressive waves at (45 m/s, Surveyor landing data - [125]) and near (100 m/s, 4 m depth, Apollo seismic experiments - [31]) the Lunar surface are known, but these in-situ experiments did not examine the response of the near surface grains distal to impacts. To investigate grain motion far from the impact, we must understand how a randomly packed 3D granular medium influences the expression of granular wave fronts. For waves traveling laterally, there is an increase in the wave speed with depth ([123]), increased friction ([126]), increased cohesion ([127]), denser initial packing ([128]), and increased gravity ([129]). [126] also found that the assembly's preparation history has considerable effect on wave propagation in the medium. Both sound speed ([130], [131]) and dispersion ([123], [122]) increase in a 3D assembly as compared to the one and two dimensional cases. However, dispersion also decreases with decreasing confinement pressure ([132], [133]) and the Lunar surface represents an environment with a unique balancing of these competing factors.

Our focus differs from other recent works exploring waves in granular media: we characterize bulk volume change induced by laterally propagating surface waves far away from the impact site. To the best of our knowledge, no work has yet investigated the behavior of randomly packed,

cohesive grains at and near the surface of a low gravity and mechanically free surface after experiencing a lateral impulse. We use these recent studies to guide our wave generation process and to serve as a validation case for our simulations before measuring bulk volume changes in the assembly as the result of a passing wave.

3.2 Methodology

Here we describe our modeling approach (a simulation domain representative of an idealized granular assembly exposed to vacuum) and our particle seeding and settling routine used to generate the assembly. We also describe our wave generation procedure and our data analysis methods. We demonstrate that the grain rearrangement we observe as well as the waves created within our assembly are physical.

3.2.1 Soft Sphere Discrete Element Method and contact model

To investigate surface dilation as a result of passing granular waves, we model a granular channel using *LIGGGHTS* [1] ([68]), an extensively validated open-source Soft Sphere Discrete Element Method (SSDEM) solver. While wave propagation in a granular medium can be modeled using Effective Medium Theory (EMT) ([134]), EMT cannot account for grain rearrangement leading to dilation ([135], [64]), variation in packing parameters ([127]) or relaxation mechanisms ([136]). Discrete Element Method (DEM) ([65]) integrates the equations of motion for every particle in the system to resolve contact forces. [137] showed that 3D DEM simulations produce realistic stress-strain dilation behavior. DEM shows good agreement with experiments when studying wave propagation through a granular material ([95], [138], [126], [111], [139]).

[1] https://www.cfdem.com/media/DEM/docu/Manual.html

SSDEM integrates equations of motion at a very small time steps to allow for deformation by way of particle overlap. The time step must be much less than the Hertzian collision time (τ_c) to accurately resolve elastic forces ([67]). SSDEM has been used by many to study grain dynamics in low gravity environments ([140], [67], [141], [77], [142], [143], [55]). We select *LIGGGHTS* due to its open source nature, ease of contact force addition and modification, ease of scalability for parallel processing, and ability to simulate non-spherical particles. *LIGGGHTS*' predecessor *LAMMPS* has been used to study waves in a granular media ([111], [144], [132]). *LIGGGHTS* has been used to study regolith and regolith simulant behavior ([145], [146]) and to model inertial dilation during shear flow ([147]).

Our granular assembly is a collection of spheres subject to Hertz contact law ([148]) which accurately captures wave propagation in granular media ([61]). We also include static and rolling friction ([74]) and cohesion ([149]). Our model is quite similar to [77] with the addition of cohesion. We summarize our force model with the equations below, a full description is provided in appendix A. This example considers a single contacting pair of monodisperse particles (radius R), for multiple contacts the force will be summed for all neighbor particles (any particle within cutoff radius $R/2$). When two particles come into contact they begin to experience a nonlinear restorative elastic force. The force experienced by the particle depends on its stiffness, k, and the amount of overlap δ. The overlap is the sum of the particle radii less the distance between their centers, $\delta = R_1 + R_2 - \|\mathbf{x}_1 - \mathbf{x}_2\|$, with $\mathbf{x}_i$ the particle state. Subscripts n and t refer to the normal (eq. 3.1) and tangential (eq. 3.2) components in the collision frame, respectively. There is also a damping contribution which depends on damping coefficient, γ, and relative velocity, v. The normal direction includes a cohesive force dependent on the cohesion energy density, k_c, and contact area, A_c. The tangential component is limited to a portion of the normal force as

determined by the friction coefficient μ_s.

$$\mathbf{F}_n = -k_n \delta_n^{3/2} - \gamma_n v_n + k_c A_c \tag{3.1}$$

$$\begin{aligned} \mathbf{F}_t &= -k_t \delta_t^{3/2} - \gamma_t v_t \\ \mid F_t \mid &\leq \mu_s \mid F_n \mid \end{aligned} \tag{3.2}$$

Our rolling friction model (provides packing support and mimics aspherical particles) is an elastic-plastic-spring-dashpot (EPSD) model which includes a spring torque ($\mathbf{M}_{r,k}$) and a viscous damping torque ($\mathbf{M}_{r,d}$). We show the full rolling torque in eq. 3.3, though the viscous damping component is neglected in this work.

$$\mathbf{M}_r = \mathbf{M}_{r,k} + \mathbf{M}_{r,d} \tag{3.3}$$

In equation 3.4 we give the governing equations which are integrated at each step. Torque, normal and tangential contact forces, and gravity are included. Gravitational force is $\mathbf{F}_g = m\boldsymbol{g}$, with g the gravitational acceleration vector. $\mathbf{r}_{c,i}$ is the vector connecting the centers of the colliding particles, I_i the equivalent moment of inertia of the contact, and $\boldsymbol{\omega}_i$ the angular velocity:

$$\begin{aligned} m_i \ddot{\mathbf{x}}_i &= \mathbf{F}_{n,i} + \mathbf{F}_{t,i} + \mathbf{F}_{g,i} \\ I_i \frac{d\boldsymbol{\omega}_i}{dt} &= \mathbf{r}_{c,i} \times \mathbf{F}_{t,i} + \mathbf{M}_{r,i} \end{aligned} \tag{3.4}$$

Hertz theory is valid when the contact deformation is elastic. As an example, impact velocity for steel grains is limited to 1 m/s (see estimates in [62], page 80). Above this speed, there are effects from possible plastic deformation at the contact site. The study by [150] used Hertz theory with deformable particles to simulate granular shocks at low pressures. [150] point out that the shock speed in the bulk is limited by the material sound speed of the particles themselves (∼6000 m/s for steel). We give the equation for solid sound speed (c_m, [151]) in eq. 4.5, which depends on the density (ρ), Young's modulus (E), and Poisson ratio (ν).

$$c_m = \sqrt{\frac{(1-\nu)E}{(1+\nu)(1-2\nu)\rho}} \tag{3.5}$$

3.2.2 Model validation

We inspected a few simple test cases to ensure that our model accurately captures the underlying physics. First, we repeated the unit test cases of [71] which confirm single particle behavior (sphere-sphere, sphere-wall). While the ability of *LIGGGHTS* to reproduce experiments has been extensively demonstrated, issues with the force model can be masked by bulk behavior. All tests were ultimately successful, though we did uncover and resolve one such issue. Initially a test evaluating the stopping distance of a particle sliding on a wall saw the particle stopping sooner than expected. As of the most recent version of *LIGGGHTS* (release 3.8.0) the Hertz tangential force model implements the threshold and rescaling for Coulomb friction based on only the tangential spring force (eq. A.9) as opposed to the full tangential force (eq. A.12) which includes damping (eq. A.10). We provide the corrected model in section 3.2.7.

We then validated our ability to produce expected shock wave speeds in a 1D particle chain

subject to normal impact at speed v_{im}. We used the same simulation setup as [79] (validated experimentally in [80]), creating a 5x5 square packed grid of particles into which a normal incident particle impacts a single particle in the packing. This creates a pressure wave within the chain which we track by finding the peak force within each particle and then fit the resultant particle position vs time data to find the wave speed in the chain. We performed this test for the same steel particle properties used in [79] as well as for softer particles which have properties closer to those used in our 3D simulation. The parameters are summarized in Table 3.1.

Table 3.1: 1D Particle Properties. Steel values are those used in [79]. The soft particles are the same size as the steel particles, but with the material properties used in our 3D simulations (see section 3.2.4).

Particle Type	Steel	Soft
E [Pa]	2.1×10^{11}	5×10^{6}
Δt [s]	10^{-10}	10^{-6}
ν	0.28	0.2
μ_s	0.5	0.7
R [mm]	10.32	10.32
ρ [kg/m^3]	7870	2500
c_m [m/s]	5.84×10^{3}	47.14
c_0 [m/s]	361.87 ± 9.09	8.57 ± 0.03

We conduct the normal impact tests for the same speeds as evaluated in [79] and extend the range to induce both sound waves and shocks. We should find that weak impacts produce constant speed acoustic waves within the assembly and strong impacts produce shocks that follow a nonlinear power law dependence on the impact velocity. The expected power law dependence for shocks is $c_w \propto v_{im}^{1/5}$ ([84]), where c_w is the initial wave speed as a result of normal impact. Figure 3.1 shows the results of these tests, reporting the normalized sound speed against v_{im}. We have good agreement with [79] and we clearly see the expected weak impact-induced acoustic

waves (constant c_w) and strong impact-induced shocks ($c_w \propto v_{im}^{1/5}$). Taking the average c_w for $v_{im} \leq 10^{-4}$ m/s in Figure 3.1, we find the sound speed, c_0 (reported in Table 3.1). The normalized c_w for the soft particle acoustic waves is larger than that of steel since the normalization at v_{im} = 1 m/s is closer to the acoustic wave region for the soft particles than for steel. We reproduce the expected power law dependence for shocks, regardless of material properties. Given the agreement with expectations, we can be confident that our choice of model and its implementation in *LIGGGHTS* accurately reproduces this 1D physical phenomenon.

It is important to note that while the shocks resulting from the greatest v_{im} ($>$ 10 m/s) follow the expected power law, in reality the particles experiencing this impulse would be subject to plastic effects and possibly fragmentation too. The Hertz model elastic limit (1 m/s) for steel particles is about $\sim 0.02\%$ of c_m. Using that same criteria on the soft particles gives an elastic limit speed of $\sim v_{im}$ = 0.1 m/s which is where the soft particles have just turned toward the power law in Figure 3.1. The elastic limit for the soft particles is much closer to the sound speed than is the case with the steel particles. Since the experiments in [79] probe v_{im} that produce shocks traveling in the assembly at speeds $> 2c_0$ we want to explore a similar range. To do so, we use an upper limit to particle impact velocities to 20% of c_m, corresponding to v_{im} of about 10 m/s which produce shocks traveling at speeds $< 3c_0$. However, we must remember the limitations of the model (plasticity, fragmentation) when considering results for v_{im} that are orders of magnitude above the elastic limit, even if they do reproduce the expected shock power law. As we'll see later, in our 3D assembly we are more interested in the decay products of the strongest shocks than the shocks themselves. These decay products are waves that travel at lower speeds than the initial shock and experience particle-particle impact velocities that are mostly less than the elastic limit (sec. 3.8).

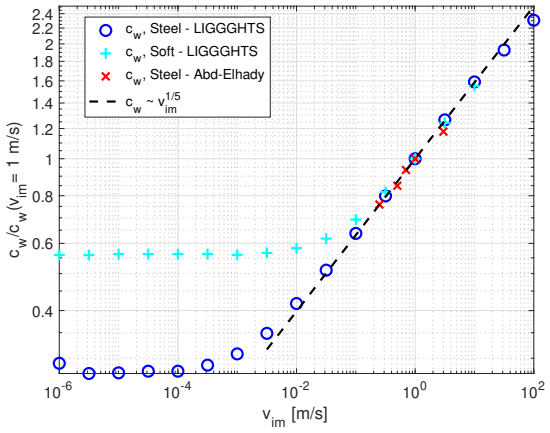


Figure 3.1: **Normalized wave speed vs impact velocity.** c_w reported for varied v_{im} are normalized by $c_w(v_{im}$ = 1 m/s). We normalize c_w at v_{im} = 1 m/s instead of at vanishing v_{im} (as in [84]) in order to include the data points from [79]. Our tests are in agreement with theirs and recover the expected power law dependence.

3.2.3 Simulating 3D wave propagation

The remainder of this paper focuses on our 3D simulation of waves in granular media and the resultant volume change. We model a radial strip in the path of a pressure wave extending outwards from the source using a randomly packed channel of particles. A schematic of the channel is shown in Figure 3.2. A fixed floor and end walls keep the particles within the channel which is longer in the direction of wave propagation (+y) than it is in width (x). The fill height of particles (z) and the length of the channel vary while the width of the channel is fixed at 2 cm which is larger than the ≈5 particle diameter wall sheath size ([152]). Periodic boundary conditions in x allow for the simulated strip to be representative of a length of grains that experience a radially expanding pressure wave ([153]). There is a shrink wrap boundary condition on the ceiling of the simulation to allow for the trajectory of any particles ejected vertically from the bed and we enforce a uniform gravitational field of g_L = 1.625 m/s^2 in the -z direction. We generate both

compressive (P) and shear (S) waves (sec. 4.2.1). After a single wave pulse is generated, the simulation continues until the wave has terminated and any volumetric changes have reached an at-rest state (sec. 3.2.8). We evaluate wave speed and volume change using sensor particles as well as a virtual sensor network (seen in Figure 3.2 and described sec. 5.2.3). First, we describe the preparation of our granular assembly.

3.2.4 Granular bed preparation

This work seeks only to demonstrate that granular impulse-induced dilation can occur at the free surface of a granular medium, it does not seek to recreate the exact conditions and behavior of the Lunar regolith. We use the properties of regolith as a rough guideline for material parameter selection. Our assembly is filled with monodisperse particles of 2.5 mm in size which is within the size range distribution for Lunar regolith. While the actual distribution has a mean particle size around 100 μm ([14]), we use one order of magnitude larger particles to keep computation time tractable. Similarly, we set particle elastic modulus (E) low so that our time step is not prohibitively small. Friction, cohesion, and particle density are within the range given in [15], Tables 9.4, 9.5, and 9.12. There have been a range of values estimated for ν of Lunar regolith, ours is closest to the estimate in [155]. Our coefficient of restitution is in the appropriate range determined in experiment ([156]) and similar to that used in other SSDEM simulations of regolith behavior ([157], [158]). The coefficient of rolling friction (μ_r) is the same as used in [77]. We set rolling viscous damping by determining a value that allowed a single spinning particle to come to rest with minimal overshoot and no lingering oscillation. We found this to be $\gamma_{d,r} = 2$ which is close to the value in [78] where they conducted SSDEM simulations of tumbler flow using the

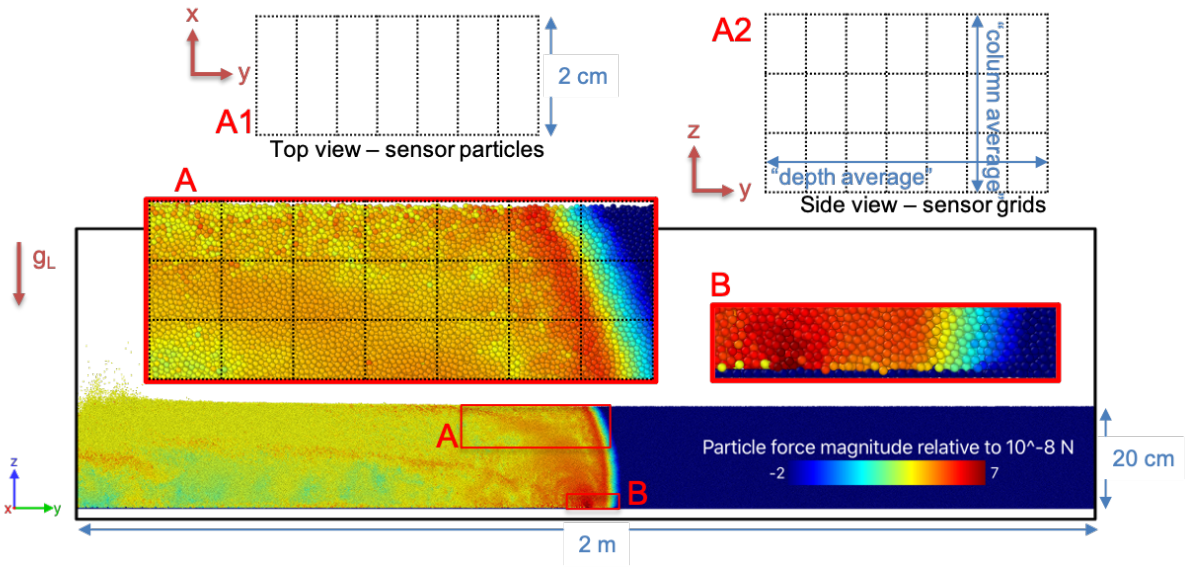


Figure 3.2: **Channel Schematic.** A channel 2 m in length is filled 20 cm deep with particles (total of $\sim 5 \times 10^5$ particles) and a shock was initiated at the left wall ($v_p = 10$ m/s) in the +y direction at t = 0 s. Here we show the channel's response several time steps after shock initiation (t = 0.1 s). The bold black line represents the simulation domain with the channel of particles occupying the bottom ∼half. Particles are colored with their order of magnitude force relative to 10^{-8} N which reveals a clearly evident solitary wave around y = 1 m. There are two boxed regions highlighted which are shown in expanded views (not to scale). **Box A** shows a zoomed in a view of the wave front near the surface, overlaid with a sensor grid (sec. 5.2.3) in dashed black lines. The shock front is (qualitatively) ∼15 particle diameters in size. A single sensor (one grid element in A) would find its properties by averaging the properties of all particles in the sensor at each time step. We provide top view (A1) and side view (A2) graphics of the sensor grid in box A to demonstrate how they are used in data analysis. Sensor particles are collected from the particles that rest on top of the 1D y-grids (A1). Side view elements are gridded in two dimensions (A2). To find average properties at a given radial position we take the average over sensor elements in the same column ("column average"). The "depth average" is taken over all grid elements at a specified depth. **Box B** is zoomed in on the floor-wave interface. The sheet of particles frozen to the floor is visible along the bottom. The highest force in the solitary wave is the dark spot slightly behind the front. Data visualization as seen here and in subsequent figures is performed using open source visualization software Ovito ([154]).

same rolling friction model. Mechanical properties are uniform across particles and are set as in Table 3.2 during both the pouring phase and shocking phase, with exceptions for the coefficient of restitution and rolling viscous damping which are described in the following paragraph. After we set the material parameters and bed geometry, particles are poured into the channel and then

settle under Lunar gravity. We chose to pour particles as our primary preparation method over other methods ([159]) as it allowed for greater control and uniformity of the achieved packing fraction, ϕ. ϕ should have a large influence on granular bed reaction to perturbations ([160]). In this paper we use $\phi_0 = V_{particles}/V_{bulk}$, where ϕ_0 is the initial packing fraction and $V_{particles}$ is the volume of particles within the larger bulk volume, V_{bulk}. We'll report ϕ_0 as a percent in this paper.

Table 3.2: SSDEM Parameters for 3D validation.

Quantity	Symbol	Value
Friction Coefficient	μ_s	1.0
Rolling Friction	μ_r	0.8
Rolling Visc. Damping	$\gamma_{d,r}$	2
Coeff. of Restitution	e	0.5
Cohesion energy density	k_c	1000 [J/m^3]
Young's Modulus	E	$5x10^6$ [Pa]
Poisson Ratio	ν	0.2
Particle Density	ρ	2500 [kg/m^3]
Particle Radius	R	1.25 [mm]
Time Step	Δt	10^{-6} [s]

Particles are poured using the *LIGGGHTS ins/stream* function. We designate a total number of particles to be inserted, a rate of insertion, and an area over which to insert the particles. The area of insertion matches the channel area (width$\times$length) and is defined as a plane 10 cm above the desired fill height. Through a 20 cm extrusion of this plane, we create an insertion volume in which the particles are created. Since particles are not allowed to overlap, some are inserted and then allowed to exit the insertion region before more particles are created. To study initial packing and boundary effects, we need to fill a range of channel lengths to different fill heights and with varied ϕ_0. More compact beds are created when the insertion rate approaches one

particle per insertion and looser beds are created when the particle insertion rate approaches the total number of particles to be inserted. The insertion routine creates one tenth of the requested particles every 0.1 s, so an insertion rate of 100,000 particles/s would see 10,000 particles created in ten 0.1 s intervals over one second. The values we used to produce varied ϕ_0 are given in Table 3.3. We'll use three levels of packing (loose, medium, compact) to describe our assemblies which correspond to $\phi_0 \sim 55$, 59, and 62 (respectively). These ϕ_0 correspond to bulk densities in the range of 1375 - 1550 g/cm^3. Particle insertion takes one second for the loose packing configuration, three seconds for medium packing, and about 30 seconds of simulation time for the compact packing. To reduce preparation time, most of our simulations occur in loose assemblies. We note that the coefficient of restitution also influences ϕ_0, with low e producing looser beds and high e producing more compact beds ([161]). Since a lower coefficient of restitution reduces settling time ([55]), we set e = 0 while particles are poured. We found that a rolling viscous damping set as in Table 3.2 reduced the range of achievable ϕ_0 so we also set $\gamma_{d,r}$ = 0 during the pouring phase.

Table 3.3: Insertion parameters to achieve various ϕ_0 for varied channel geometries.

Channel Length (m)	Channel Height (cm)	Total Particles (#)	Insertion Rate (particles/s)	$\langle\phi_0\rangle \pm \sigma\phi_0$	Type
2	20	536,180	600,000	54.72 ± 1.67	Loose
2	20	575,410	200,000	58.65 ± 1.31	Medium
2	20	607,953	18,900	61.96 ± 1.03	Compact
2	10	270,641	600,000	54.20 ± 1.70	Loose
2	30	814,649	600,000	54.60 ± 1.70	Loose
1	20	267,545	300,000	54.66 ± 1.72	Loose
3	20	804,763	900,00	54.72 ± 1.67	Loose
4	20	1,072,258	1,200,000	54.72 ± 1.65	Loose

After particle insertion has ended, e and $\gamma_{d,r}$ are set to the values in Table 3.2. The top

layer of particles (particles with height greater than the specified fill height) are deleted to ensure a smooth surface. Finally, we allow the assembly to settle under Lunar gravity. At this point the bed is at rest and particles are not moving, though there is substantial energy from the filling procedure resonating within the bed due to the spring-like nature of our particles. As the bed settles energy is slowly dissipated and a lower energy state facilitates wave tracking. To speed this process, we remove kinetic energy from the bed by setting all particle velocities to zero every 25 ms. We found that allowing the particles to reach an average force of 10^{-11} N was sufficiently settled to be considered steady state, where we could readily identify both acoustic waves and shocks (Section 3.2.9). Once we reach a steady state, we save a copy of the particle states to bypass preparing the bed for each simulation run.

We compare the simulated and expected δ_0 (average particle overlap at t = 0 s) dependence on depth in Figure 3.3. As an approximation we use [102] to find δ_0 as the result of a static force applied to a 1D chain of beads (eq. 3.6). If a 1D chain of beads is vertically oriented, then the force on a single bead is equivalent to the weight of the particles above it in the chain. For our 3D bed we define the load as $F_0 = \rho_p \phi \times z\pi R^2 \times g$, the overburden force which can be thought of as the weight of the column of material supported by a single particle at depth z. Figure 3.3 shows that this approximation works well near the surface but is an overestimate as depth increases. This is because eq. 3.6 gives the total overlap on the particle in a 1D column, while our simulated δ_0 is an average over the number of contacts (around $\sim$6 neighbors). A single particle at a depth z in a 3D assembly is supported by several neighbors which distributes the load, resulting in a smaller δ_0 than in the 1D case. The loosest bed is closest to the estimate since there are less neighbors to average the total δ_0 over than in a more compact bed. The compact bed δ_0 is therefore smaller than the loose bed in Figure 3.3. We confirmed that the total overlap is greatest in the compact

bed and smallest in the loose bed as depth increases (not shown), but we found the average δ_0 to produce sound speeds closer to those measured (sec. 3.2.8).

$$\delta_0 = \frac{2\left(\frac{3(1-\nu^2)}{4E}F_0\right)^{2/3}}{R^{1/3}} \tag{3.6}$$

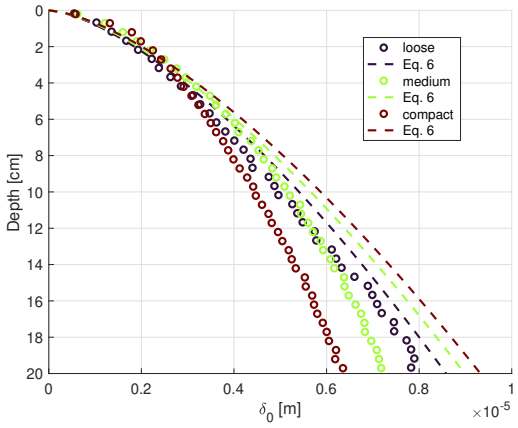


Figure 3.3: **Depth vs δ_0.** Depth dependence of δ_0 for the loose, medium, and compact 2 m long 20 cm deep channels from Table 3.3. Simulated results are represented by circles and the dashed lines show the result of eq. 3.6 with the ϕ_0 from the first three entries of Table 3.3. These three packings correspond to average δ_0 of 4.82, 4.81 and 4.23 μm (loose, medium, compact respectively). The compact δ_0 is smaller than the loose since δ_0 is the average overlap here, not the total (as discussed in the text).

3.2.5 Bed tapping

For some cases we tap the bed before settling occurs to achieve different packing fractions. We base our tapping procedure on that of [39] and [40], but we use the particles on the floor of the assembly as a virtual shaker instead of inserting a physical base plate into the simulation (inspired by the virtual piston in the following section). We use the same sheet of particles that will be used to make up the rough particle floor (described in the prior section) as our tapping mechanism. Tapping commences when we direct the sheet to oscillate, with each particle in the

sheet directed to follow a sine wave: $z_t = z_0 + Asin(2\pi ft)$. We use the same frequency tapping as in [40] (f = 30 Hz) but a larger tapping displacement amplitude (A = 0.5 mm) which allows for a shorter required tapping duration when altering ϕ_0. The bed is tapped for a specified time, after which the top most particles are again removed. We removed the same amount of particles from all tapped cases so that they were a consistent height which resulted in beds filled 15 cm deep with particles (starting from the 20 cm deep beds). Table 3.4 shows the tapping duration used to achieve various ϕ_0 starting from the loose, medium, and compact configurations. We tapped the loose bed to several different states and ran a single comparison case in the medium and compact beds. The last row in the table shows that beds with varied ϕ_0 converge to the same final state, confirming our model accurately captures bulk volume change due to shearing.

Table 3.4: Tapping Duration. New ϕ_0 are reported for various tapping duration of the loose, medium, and compact beds at the same amplitude and frequency. The ϕ_0 designations correspond to those from Table 3.3 for Loose (54.7%), Medium (58.7%), and Compact (62.0%).

Tapping duration (s)	ϕ_0 after tapping	ϕ_0 before tapping
0.25	56.14 ± 1.51	Loose
0.5	56.90 ± 1.43	Loose
1	58.21 ± 1.31	Loose
2.5	59.84 ± 1.22	Loose
5	61.04 ± 1.17	Loose
7.5	61.54 ± 1.14	Loose
10	61.83 ± 1.14	Loose
10	61.86 ± 1.16	Medium
10	62.17 ± 1.17	Compact

3.2.6 Wave generation

We generate horizontal P and S waves within the assembly to capture the bounding directions of shear stresses that may be present as the result of an impact. We use a virtual approach to generate a single wave as opposed to a physical piston ([84], [162], [55]) or bender element ([163]). A sheet of particles in the channel within one particle diameter of the left wall (y = [0,2R]) are designated as a virtual piston ([164], [165]) or virtual bender element ([166]). Looking at Figure 3.2, the sheet would be made up of all particles that reside to the left of an x plane located at y = 2R (all particles directly adjacent to the left wall). To generate a single P wave with the virtual piston, all particles within the sheet are assigned a designated velocity (v_p) in the +y direction at the beginning of the simulation. We'll consider the +y direction to be the radial direction pointing away from the crater. As opposed to compression with the piston, a bender element induces strain in an assembly through the small displacement (in the z direction here) of a thin plate. We generate a single period S wave ([166], [144]) with the virtual bender by directing the sheet of particles to follow oscillatory motion following the same formula from the tapping procedure, $z_t = z_0 + Asin(2\pi ft)$, for one period. The frequency is set high so that we do not have to determine the resonance frequency of the bed, the assembly will damp our signal out to the resonance frequency ([166]). Generating the shear wave with the entire sheet of particles reduces (but does not negate) P wave interference compared to physical bender elements ([139]). The velocity that the particles within the sheet obtain is $v_z = 2\pi Afcos(2\pi ft)$, with maximum velocity $v_{z,max} = 2\pi Af$. We will consider this max velocity to be equivalent to v_p for the P waves and can vary A to generate waves of difference speeds ($A = v_p/(2\pi f)$). With f = 50 kHz, this corresponds to a period of 2×10^{-5} s which occurs over 20 simulation time steps.

We then subject the bed to these varied v_p to generate acoustic waves and strong shocks (Section 3.2.9). The strong shocks rapidly decay to solitary waves that travel at reduced, though still supersonic, speeds and with very little dissipation. We can call these waves solitary since they propagate over distances (on the scale of meters) much longer than their spatial extent. The size of the shock front is around $\sim$15 particle diameters, (fig. 3.2), which is larger than the 5 particle diameter size in a 1D chain and less than the 100 particle diameter width in the 3D wave of [123]. Only a single pulse is generated down the channel which is characteristic of blast loading ([62]) - the duration of the imparted piston impulse is rapid. This makes sense given that our loading time is essentially the Hertz collision time. On the time step before shock initiation, we fix a sheet of particles ($0 \leq z < 2R$, Fig. 3.2B) to the floor so that the shock travels over a rough surface and bypasses the non-physical particle-wall interaction as has been done in both experiment and recreated in DEM ([167], [71]). The simulation then runs until the generated wave reaches the end wall, reflects, and terminates which then sees the assembly enter an at-rest state, where the only motion present is a result of the slow dissipation of the forces leftover from the passing of the shock within our spring-like grains and the particles can be considered at-rest. The total simulation time is set to allow the lowest induced wave speed to travel across the longest channel. We found a simulated time of 1.5 s to be sufficient for the cases we analyzed. We take measurements every 1 ms for the first 0.25 s and then every 10 ms thereafter. The higher resolution data covers the period when volume changes occur and allows for enough resolution to compute the induced c_w (Section 3.2.8). After the wavefront passes and any lofted particles have returned to the surface, a slow gravitational settling begins. The settling is accompanied by small volumetric changes, though we show in Fig. 3.5 that this oscillation is about a steady, at-rest value. Further details on the dilation measurement and behavior are discussed in section 3.2.8.

We reduce the resolution of output data in the settling region to aide with data storage logistics given that the output from a single simulation run can exceed 50 GB.

3.2.7 Computation details

Bed preparation occurs on our standalone 44-core workstation (dual Intel E5-2699V4 processors and 128 GB of 2400 MHz DDR4 RAM) and shock simulations are run using the University of Maryland High Performance computing cluster, Zaratan (128 cores, dual AMD 7763 64-core processors, and 512 GB of AMD EPYC 7763, 2.45 GHz base RAM per node). We verified that there was no difference in results after shocking the prepared bed between our server and the cluster. A summary of computation time is provided in Table 4.5. Details from shock runs are given for v_p = 10 m/s which is the upper bound for computation time. Run times for lower velocities are slightly reduced from those reported here as there is less energy input into the system, reducing overall particle movement. We provide the *LIGGGHTS* input files used for bed preparation, tapping, settling, and shocking at our public repository ([168]). The corrected tangential force model (sec. 3.2.2) is included there as well. The restart files that are the prepared beds are hosted at [169] along with the full output from a single shock simulation run. We can provide additional simulation data upon request, however with the input scripts and restart files we have provided any reader could download *LIGGGHTS* and reproduce our shock simulations.

3.2.8 Data analysis

We perform post processing of *LIGGGHTS* output files in *MATLAB*, using both sensor particles and a virtual sensor grid (see section 3.2.8 and Figure 3.2) to measure volume changes

Table 3.5: Computation details. Processing time and storage requirements for shocking the different beds. Simulated time for all tests below is 1.5 s. Each test used all 128 cores of a single node.

Length (m)	Height (cm)	Particles (#)	$\langle\phi_0\rangle$	Clock time (hr)	Storage (GB)
2	20	536,180	54.72	1.08	49.06
2	20	575,410	58.65	1.12	54.06
2	20	607,953	61.96	1.29	57.85
2	30	814,649	54.60	1.51	72.30
2	10	270,641	54.20	0.91	23.70
1	20	267,545	54.66	0.83	23.83
3	20	804,763	54.72	1.48	108.26
4	20	1,072,258	54.72	2.36	150.87

and track pressure waves. We lay a 0.5 cm $\times$ 0.5 cm grid over the yz dimension and find average grain properties (e.g., ϕ, δ, average pressure, etc.) over the grains in that sensor grid element. With the exception of ϕ_0, the average properties for the bin are the mean value for all particles that are wholly within the grid bounds. We give an example of the time evolution of average particle force in Figure 3.4, which represents a single grid element from Figure 3.2, box A/A2. We can then use the sensor grid to find average properties for the entire granular assembly. For example, the first peak force from Figure 3.4 would find the peak force for each sensor grid element and then average across the sensor grid elements at all radial positions at a given depth to find the average value at that depth. Similarly, averaging over the sensor grid elements at each depth for a given radial position gives an average value at that radial position.

Packing fraction

In this work we use a simple calculation to find the packing fractions we have reported so far. Since our particle data is already binned into the 2D sensor grid, we add the volume of all the particles within the cell and then divide by the volume of the cell to find ϕ_0. Any particles

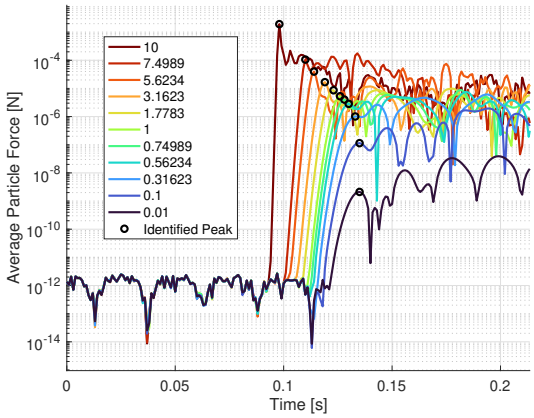


Figure 3.4: **Average Particle Force (Y) vs time.** Force evolution vs time for P waves created at varied v_p from a sensor at 7.5 cm depth and radial position 1 m in a 2 m channel filled 20 cm deep with particles. The color legend represents different v_p with units in m/s. Lines have been added for clarity. Identified peaks are plotted as a black circle and this is taken to be the time at which the wave front passed through the sensor.

residing within one particle radius of the grid element boundary have their volume split into the correct grid element. If the particle resides along the boundary between two grid elements, we find the volume of the hemispherical cap that resides in the adjacent grid element. For particles near the intersection of four grid elements we compute the volume of the slice residing in the corner grid element in addition to the hemispherical caps in the adjacent bins. Averaging over all of the sensor grid elements at a given depth leads to an average ϕ_0 at each depth. Then, averaging over all depths (except the very surface grid element) leads to the packing fractions as presented in Table 3.4. We neglect the particle overlaps in this volume calculation since the impact on our results will be small given the averaging we perform ([170]).

Dilation

We evaluate the height of the grains in the assembly at each radial position to measure the change in packing fraction as was done in [39]. Percent change in bed height is equivalent to

percent change in packing fraction when the change in bed height is much less than the height of the bed ($\Delta z \ll z$). Instead of the sensor grid used to measure wave speed, we now consider sensor columns. The topmost particles in each column are our sensor particles (Fig. 3.2, A1). Each column is 0.5 cm in width as before and measuring the height of particles in this column over time leads to Figure 3.5, which shows the height of the top most particles above the initial fill height. Particle height is averaged over the top N_h sensor particles in the column. $N_h \approx \frac{x*0.5}{2\pi R}$ which is the approximate number particles that could fit side by side determined by the area of the column in the xy plane divided by the particle area. We then take a percent difference as compared to the initial bed height to find the volume change that occurred as a result of the wave's passing. We average over the last 0.2 s of values to get the final bed height as there is some small oscillation that occurs. The oscillations are a result of the settling in the bed as the spring-system dissipates the energy of the shock which we discussed in section 4.2.1. We measured the deviation due to the oscillations in our final at rest bed height values to be less than the oscillation observed during sustained tapping tests which found a steady state value that ϕ_0 oscillated about ([39]). We report one sample case to confirm the bed is in an at rest height, despite observed oscillations. Using the 2 m long bed filled 20 cm deep with the compact filling the bed is shocked at the same v_p = 10 m/s and is allowed to run for ten times the duration of our normal tests (15 seconds). Over the last 0.2 seconds, the mean and deviation change in bed height ($\mu\Delta z, \sigma\Delta z$) in the 1.5 s test are (0.373 cm, 28.32 μm) compared to (0.369 cm, 0.121 μm) in the 15 s case. The mean $\pm$ variance from the 15 s case are plotted as dashed lines on the zoomed in portion of Figure 3.5. The bed height change between t = [1.3, 1.5] s is already oscillating about the at rest Δz from the 15 s test.

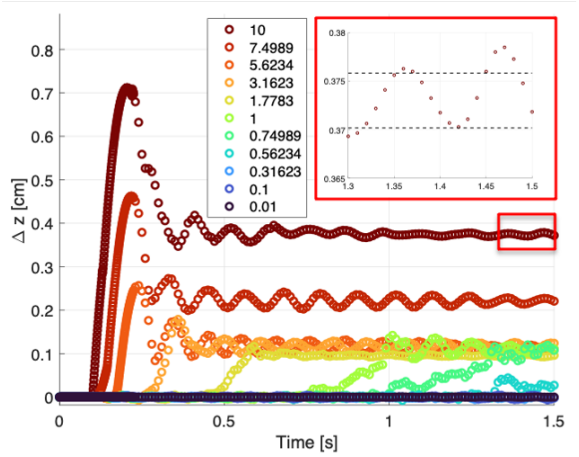


Figure 3.5: **Height vs Time.** Average sensor particle height over time for a sensor at y = 1 m in a 2 m channel filled 20 cm deep with particles (compact filling). Height increase is initiated by arrival of the wave, falling back down from a peak to a position greater than the initial height when the wave is supersonic. Color legend corresponds to different v_p (m/s). The dashed lines in the zoomed in portion (boxed in red) show the variance in bed height change for the v_p = 10 m/s case taken from a 15 second simulation (not pictured). The oscillations we see between 1.3 and 1.5 s (our averaging window) occur about the at rest bed height from the longer duration simulation.

Wave speed

The generated wave speed (c_w) is determined by tracking the first peak force within each bin. Figure 3.4 shows that shocks ($v_p > 1$ m/s) have an easily identifiable peak, while the acoustic waves ($v_p < 1$ m/s) see a smaller and later increase in average force. The first peak is determined as the first maximum found that is one order of magnitude greater than the initial average particle force. This threshold is required to identify sound wave peaks, which can have average particle forces on the same order of magnitude of the initial force. The first peak force gives us the time of the wave's passing through each sensor and, along with the sensor's position, can be used to find wave speeds Figure 3.6 shows these results for sensors from y = [0, 50 cm] at a single depth within the channel. The plot is semi-log in time (x-axis) to illustrate that there are two different

regimes of propagation. The shock wave regime is accompanied by substantial dissipation and this results in an initial brief region of deceleration for the c_w of the strongest impacts. We find c_w by constructing a linear fit to the points in the first 15 cm of the channel (y = [0, 15] cm). This will be an underestimate since the wave speed is decelerating. After decelerating ($t > 0.01$ s), the wave speed is still supersonic and appears to travel as a solitary wave with constant speed. We'll call the solitary wave speed the propagating wave speed, c_p, which is found with a linear fit to the data from y = [30, 50 cm].

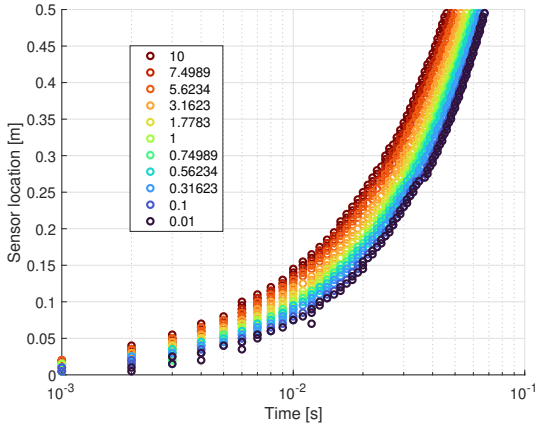


Figure 3.6: **Sensor location vs logged peak force time.** For varied v_p we show the measurements used to find c_w at a depth of 4 cm. A fit of the measurements in the first 15 cm gives c_w (fit lines not shown). The initial linear fit is used to remove outliers more than 2σ from the mean before finding the final linear fit. Color corresponds to wave v_p (m/s). The slope of the linear fits for each trend correspond to reported c_w in Figure 3.7. The propagating solitary wave speed c_p is a linear fit to the data after 30 cm.

This process is then repeated at every depth, the results of which we show (for shocks) in Figure 3.7. As expected, c_w increases with depth ([123]). We can also predict the sound speed using equation 4.4 ([62], eq. 1.7) along with the calculated δ_0 (Fig. 3.3). Equation 4.4 is derived for a 'strongly compressed' (which is the case for sound waves) 1D particle chain and does not include effects from some of the physical properties in our model (friction, cohesion) so it slightly

over predicted c_0. Applying a scaling factor of $\sqrt{3}/2$ yields the prediction of c_0 in Fig. 3.7 which agrees well with our numerical sound speeds.

$$c_0^2 = \frac{E(2R)^{1/2}}{3(1-\nu^2)m}\delta_0^{1/2}6R^2 \tag{3.7}$$

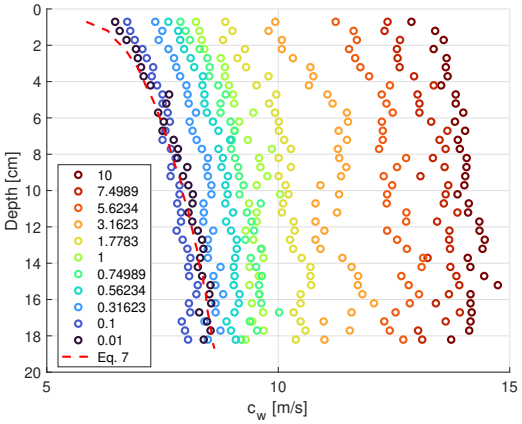


Figure 3.7: **Depth vs c_w for varied v_p.** Using the slope found from Figure 3.6 we show c_w and its depth dependence for varied v_p in a 2 m channel filled 20 cm deep with particles (compact packing). Acoustics waves are grouped together and produce roughly the same c_w, while shocks show an increase in c_w with v_p. The red dashed trend line shows that the predicted sound speed, $(\sqrt{3}/2)c_0$ (eq. 4.4) agrees with our numerical sound speed (bluest data points, corresponding to low v_p) .

Particles in the wavefront

To asses the strength and quality of the generated waves we will collect the maximum velocity (v_m) and maximum overlap (δ_m) experienced by the particles in the wave front. To do this, we find the maximum δ over time in each virtual sensor. Figure 3.8 shows the average overlap vs time in a single sensor for varying wave speeds. We use the average of the maximum sensor overlaps over all depths when reporting a single value for the overlap induced by the wave front (δ_m), see, for example, Fig. 3.16. Note that δ_m does not correspond with the peak force

(Fig. 3.4) except in the case of the largest v_p. δ continues to grow following the impulse as the a result of collisions behind the wave front, so δ_m should be considered the maximum overlap experienced by a force sensor following the wave's passage (as opposed to the maximum overlap in the wave front). Notice that particles experiencing wave fronts induced by the largest v_p ($\geq$ 5.6 m/s) undergo a period of unloading directly following δ_m. This occurs as surface particles are ejected following passage of the wave front. At times they are even completely detached from their neighbors as particles within the sensor experience lofting. The maximum velocity in the collision is collected using the same procedure, though a separate plot is not shown here since finding v_m is more straightforward (coincides with time of peak force).

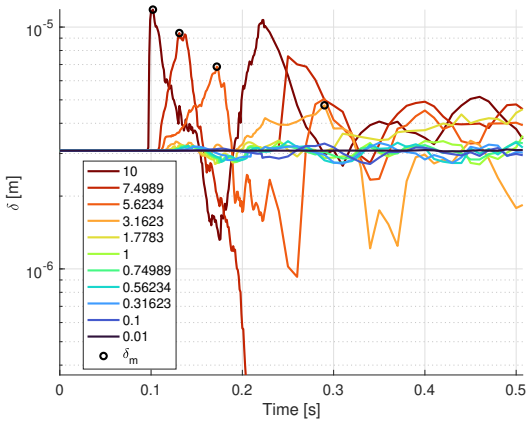


Figure 3.8: **Average δ vs time.** δ evolution vs time for P waves created at varied v_p from a sensor at 7.5 cm depth and radial position 1 m in a 2 m channel filled 20 cm deep with particles (compact filling). Lines have been added for clarity. The legend colors correspond to v_p (m/s). The overlap the particles experience as a result of the shock, δ_m, corresponds to the maximum. The red line (v_p $\sim$7.5 m/s) is discontinuous between 0.2-0.25 s while the particles in the cell are completely detached. δ_m is the maximum overlap experienced in the sensor as the result of the wave which is not necessarily the maximum overlap in the wave front.

Particle stress

To gain a general understanding of the mechanics behind any surface dilation we observe, visualizing particle pressures over time is a valuable tool. We use *LIGGGHTS*' computed stresses to visualize shock characteristics (sec. 3.3.1) which are computed as the virial stress. For our granular system, this reduces to a kinetic energy contribution and a pairwise energy contribution from neighboring particles, see eq. 3.8:

$$S_{ab} = -\left[mv_a v_b + \frac{1}{2}\sum_{n=1}^{N}(r1_a F1_b + r2_a F2_b) \right] \tag{3.8}$$

The stress (S) elements a and b take values x, y, and z to form all 6 elements of a symmetric tensor (xx, yy, zz, xy, xz, yz). The stress occurs when particles (located at relative position r1 and r2) moving at relative velocity (v) experience forces (F1 and F2) during a collision. Units are reported in pressure$\times$volume (N$\times$m) so that tracking instantaneous deformable particle volume is not necessary. Though [171] concluded that the virial stress is equivalent to the Cauchy stress, this has been debated in the literature. Commenting on this debate is outside the scope if our work. We use the *LIGGGHTS* provided calculation for simplicity and use the results only to guide a qualitative analysis of the surface dilation mechanism.

3.2.9 Shock validation

We used a 2 m channel filled 20 cm deep with particles to verify the expected weak/strong shock behavior. In a 3D randomly packed assembly, we should obtain the same power law relationship from Section 3.2.2 as has been seen in experiments ([47], [118]) and in SSDEM

([55]). Averaging across all depths we find the average induced c_w and c_p for a given v_p and this is plotted in Figure 3.9. We clearly see the expected weak/strong regions. The waves produced by low v_p produce acoustic waves of the same speed (about 7 m/s). c_0 is taken as the average of the c_w of the acoustic waves ($v_p \leq 0.1$ m/s) and the results for the different beds are summarized in Table 3.6. In the same table, we estimate the bulk modulus by rearranging $c_0 = \sqrt{E_{bulk}/\rho_{bulk}}$ ([90]) and neglecting cohesion. The largest v_p produce c_w that increase with increasing v_p and we obtain the same $v_p^{1/5}$ power law as in [84].

Table 3.6: Sound speed and bulk modulus in beds of various ϕ_0. ρ_{bulk} is computed using the particle density from Table 3.2 with mean ϕ_0 from Table 3.3 corresponding to the Loose, Medium, and Compact channels in the 2 m long, 20 cm deep configuration.

ϕ_0 (%)	ρ_{bulk} (g/cm)	c_0 (m/s)	E_{bulk} (kPa)
54.72	1.37	6.55	58.78
58.65	1.42	7.01	69.78
61.96	1.55	7.51	87.42

We report the P shock wave speed in Figure 3.9 so that we can compare results from the 1D assembly from Figure 3.1 in addition to varied ϕ_0 in the 3D beds. Both the 1D and 3D cases follow the expected 1/5 power law. The magnitude of speeds are comparable between 1D and 3D in our simulations which is due to the slower speeds in a 1D assembly as compared to 3D ([130]) but a larger particle size in the 1D experiment ($\sim$10 mm for 1D, 1.25 mm for 3D) and larger particles lead to larger sound speed (eq. 4.4) . The reduction in bulk modulus as compared to the 1D case reduces c_w for the same v_p, while the reduced bulk density shifts the transition from acoustic waves to shocks to larger v_p. Wave speed in the 3D bed increases with increasing ϕ_0 since a denser particle bed has more contacts and force can be transmitted more quickly. Given our agreement with expectations, we conclude that the acoustic and shock waves simulated in

our assembly are physical. We note here that the averaging obscures some evidence that the near surface waves increase in speed faster, closer to $v_p^{1/4}$. That c_w increases more quickly than expected at the surface is an expected result - anomalous behavior in granular assemblies at low confinement pressure remains an open topic ([172], [64], [136], [117], [118]). However, given the noise in our current c_w identification method (due to both fit method and data resolution) a detailed investigation of this result is not conducted.

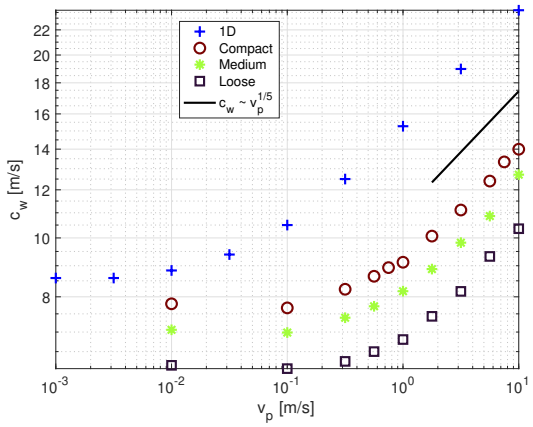


Figure 3.9: **Depth averaged c_w vs v_p for varied geometries**. We show wave speed vs incident speed for the 1D case as well as three different ϕ_0 for the 3D bed corresponding to the loose, medium, and compact levels of packing from Table 3.3.

At this point we can continue the model validity discussion of section 3.2.2. Figure 3.10 now includes the solitary wave speed c_p and normalizes all wave speeds against c_0 to retrieve the Mach number ($M = c/c_0$). While we see that the largest v_p produce shocks that follow the expected power law, these v_p are an appreciable fraction of c_m. In reality, the produced c_w would be affected by plasticity near the contact site or even fragmentation for the largest v_p. Despite our particles undergoing contacts with velocities beyond the elastic limit as the shock is initially created, the shocks produced in our assembly travel at speeds $< 2c_0$ which is in line with the assembly shock speeds explored in [79]. We are also more interested in the wave as it travels at

its solitary wave speed (c_p), since it is in this state when consistent dilation is initiated across the channel. Our c_p do not exceed $1.4c_0$ and so the effects of impact-site-plasticity and fragmentation would be less significant for particles in the channel that are not directly adjacent to the impact site. In table 3.8, we show that the particle velocities experienced within the solitary wave front don't exceed 200 mm/s (with the elastic limit around 100 mm/s).

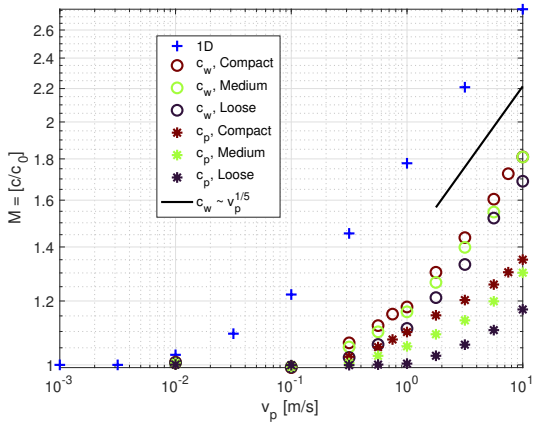


Figure 3.10: **Mach number vs v_p for varied geometries**. Wave speeds for different v_p resulting in shocks in the 1D (plus marker) and 3D shocks (circles) are normalized against c_0. The solitary wave speed c_p is corresponds to the star markers.

3.2.10 Test plan

Having confirmed the validity of our method, we can now examine various cases to determine if and when surface dilation will occur due to generated waves. We characterize this surface dilation with respect to wave speed, wave type, packing configuration, and boundary effects (particle fill height, length of channel). The channel length and fill height tests determine if the geometry of the container has an impact on our results. Finally, varied wave speeds will reveal if surface dilation can occur for sound waves or shocks. The wave type test will determine the dependence of dilation on P and S waves. Varied ϕ_0 will determine the dilation response

sensitivity to initial conditions. We also briefly consider the case of two colliding waves. The results of these tests are shared in the following section.

3.3 Results and discussion

We find that in all cases, a single wave is created which can persist across the entire length of the channel, depending on the input v_p. When v_p is large enough to generate a shock, the wave undergoes a rapid initial decay, but then propagates at reduced speed, although still supersonic, across the channel. The propagating wave appears to be a solitary wave as it travels with minimal dissipation and maintains its shape. Even for barely supersonic solitary waves, surface dilation occurs as long as the wave is maintained. However, sustained dilation only occurs as the result of a compressive (P) wave. We first provide a qualitative description of grain motion during the induced dilation before quantifying the resultant bulk volume change and discussing implications.

3.3.1 Impulse-induced granular dilation

Our laterally propagating P shock waves initially experience a rapid exponential decay in force before reaching a steady value that is maintained for a distance, in some cases across the entire channel. Despite the decrease in speed from the initial c_w, the solitary wave speed c_p is still supersonic. As the solitary wave propagates along the channel, particles in the near surface are mobilized after the wave front passes by, with the top most layers detaching and following a parabolic trajectory (seen in Fig. 3.5). The sensor elements in the top row of Figure 3.2, box A confirm this behavior. Looking closely at the surface grains and using the top box boundary as a guide, we see that the grid elements on the right (just before and after wave front passage)

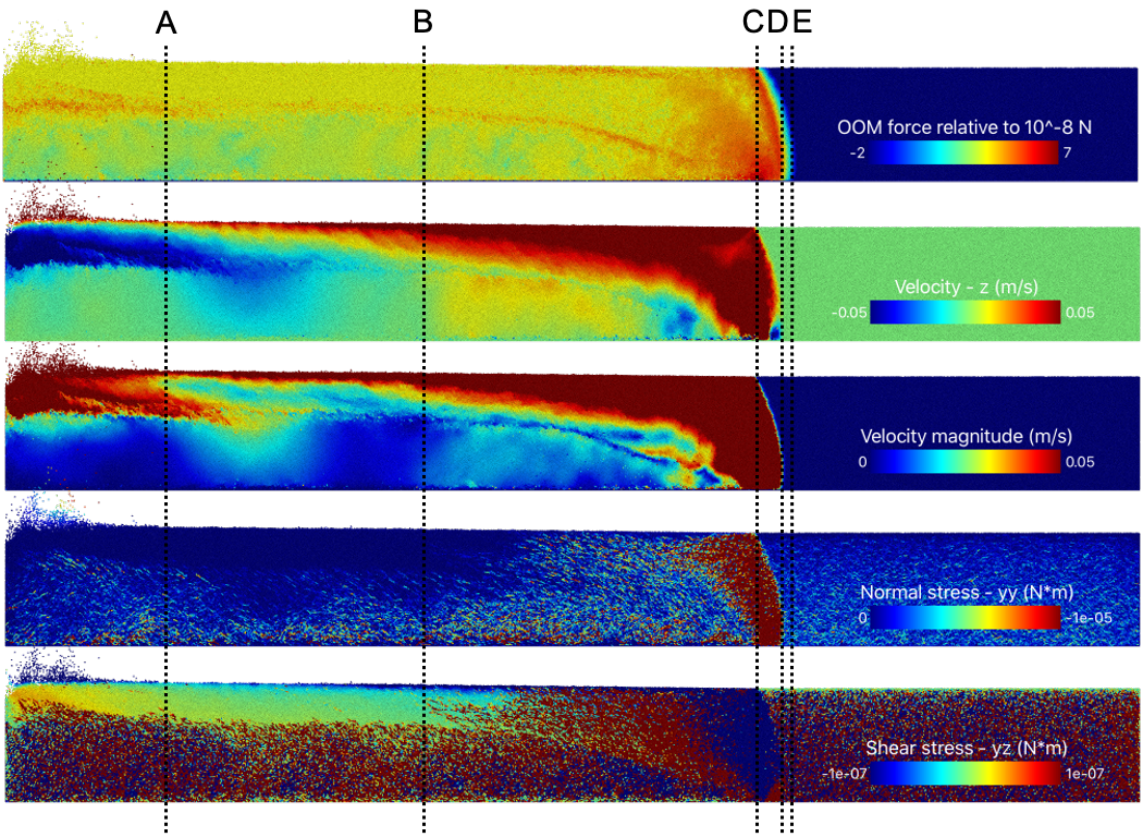


Figure 3.11: **P wave visualization.** Various parameter visualizations of a 2 m long channel filled 20 cm deep with particles (compact filling) at t = 0.133 s after P shock initiation (v_p = 10 m/s). In order of top to bottom, the panels color the particles by their force magnitude, z-velocity, velocity magnitude, normal stress (yy), and shear stress (yz). We show the legend scale and units inlaid on the right of the channel in each panel. Dashed lines are guides corresponding to labels which are described in the text. The initial shock decays to steady solitary wave and is maintained across the entirety of the channel.

still have a flat uniform surface that is in line with the initial height of the bed while those on the left do not, as the bulk of the assembly has dilated to fill the sensor element with particles. In the wake of the solitary wave front, a secondary wave is reflected off the floor and travels vertically upward. The reflected floor wave reaches the surface particles while they are in an inertial state. We refer the reader to frames c-f of Fig. B.1 and Fig. 3.29 to see the floor wave. Ultimately, the solitary wave reflects off the end wall but disperses rapidly and does not travel back down the channel. The reflected end-wall wave only affects surface modification at the very end of the

channel (y = [1.5, 2] m in Fig. 3.15, for example). The final settled height of the particles is increased across the bed, except very near the wave generation site and at the end wall (seen in section 3.3.2). In the appendix, we provide frames from various times during the simulation to show how the force profile of the wave evolves (Fig. B.1).

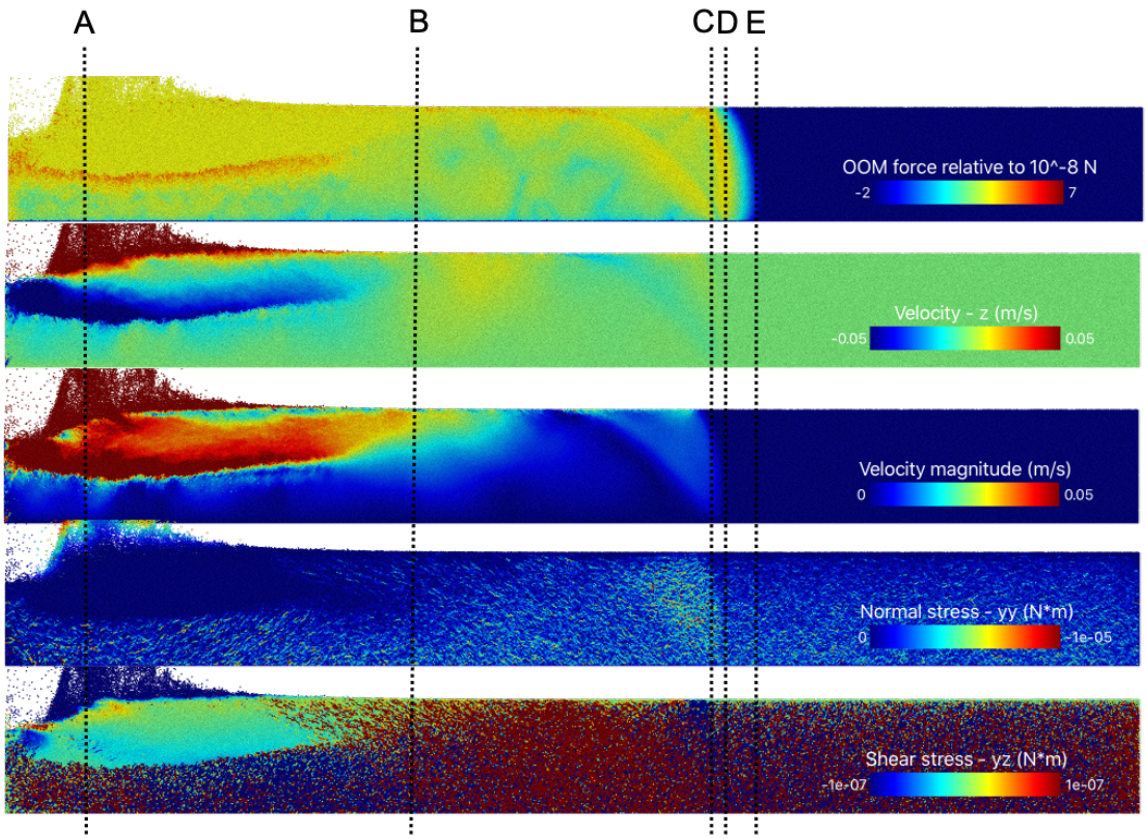


Figure 3.12: **S wave visualization.** Various parameter visualizations of a 2 m long channel filled 20 cm deep with particles (compact filling) at t = 0.133 s after S shock initiation (A = 3.1831x10^{-5} m). In order of top to bottom, the panels color the particles by their force magnitude, z-velocity, velocity magnitude, normal stress (yy), and shear stress (yz). We show the legend scale and units inlaid on the right of the channel in each panel. Dashed lines are guides corresponding to labels which are described in the text.

The details of the surface dilation mechanism are most easily seen by evaluating the response of the assembly across several physical parameters at the same time. Figure 3.11 and Figure 3.12 visualize force, velocity, normal stress (yy), and shear stress (yz) of the same assem-

bly at a single time step after being subjected to P and S shocks (respectively). Surface dilation occurs for a P wave but not for an S wave of comparable strength. Section 3.3.2 will quantify this result, but we characterize the differences between the two waves here using the alphabetical labels in Figures 3.11 and 3.12 as a guide. Consider a single radial position along the channel. As the P solitary wave arrives in Figure 3.11, the particles at this radial position first experience an increase in force (E - force panel). Rapidly thereafter they experience the peak force which is aligned with the arrival of the compressive wave front (D - force and normal stress panels). Particles attain a velocity at this point too, though it is initially only a lateral velocity and the particles are pushed in the radial direction into their neighbors (D, z-velocity and velocity magnitude panels). However, this y-velocity is quickly converted into an upwards z-velocity looking just to the left of D in the z-velocity panel. The compressive front triggers particle ejection through a frictional collision with neighboring particles. Following this, the shear front arrives, seen as a rapid transition from negative to positive yz-shear stress seen at C in the shear stress panel. At this point, the region between A and B is completely detached (zero normal and shear stress as seen in those respective panels) and particles experience a ballistic trajectory. Left of A, particles are falling back down and the initial stress profile starts to reestablish. Note the presence of a vortex immediately following the compressive front (D, z-velocity and normal stress panels) of the particle-floor boundary. The highest forces present as a result of the shock are at the shear wave front and floor interface (C, force and shear stress panels). The shear front following the compressive wave sustains the wave and drives dilation to occur across the entire channel.

Without the strong compressive front, the initial S shock (Fig. 3.12) does not generate a solitary wave and is unable to trigger distant dilation. The strength of the wave has decayed by the same time the P solitary wave has reached an equivalent radial distance (E, force panel). The

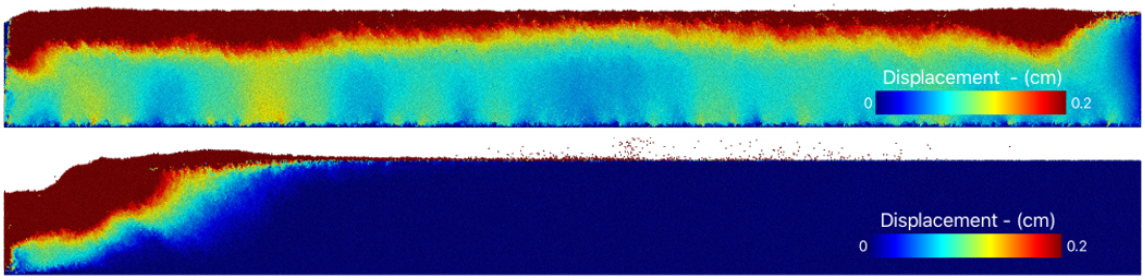


Figure 3.13: **Dilation visualization.** Particles are colored by their displacement in height as compared to their initial position for the compact 2 m channel filled 20 cm deep with particles. The top channel experienced a P shock wave while the bottom channel experienced an S shock wave.

bender element does not completely remove P wave effects (as expected) and there is a weaker compressive wave front visible (D, normal stress panel). The particles acquire a small velocity from the compression, but it is never converted into a z-velocity (B-D, z-velocity panel). There is no high force region at the particle-floor interface maintaining the solitary wave as with the P wave and this is due to the difference in shear stress profile. The scale of the shear stress direction flip (C, shear stress panel) is greatly reduced in the S wave case and cannot sustain the wave. There is a region of detachment which is confined to be close to the initiation site (0 stress between A and B in the normal and shear stress panels), whereas the P wave detachment region formed a band of lofted particles that persisted across the entire channel. We show in section 3.3.2 that dilation from the S wave is confined to the near initiation region while the P-wave-resultant dilation spans the channel in a near surface band that resembles the detachment band in Figure 3.11. Given that dilation only occurs over long distances for the compressive wave, the remainder of the results section focuses on our P wave simulations.

3.3.2 Surface dilation quantification

This section focuses on quantifying height change (and therefore dilation) away from the initiation site. We find the wave-induced height change for a given test by taking the average at-rest bed height from a measurement region in between red dashed lines in the following plots that provides some margin from the walls. We exclude the region nearest to the left wall where the initial shock is active since surface particles are ejected due to the larger impact speeds experienced within the shock front. As is the case in blast-loaded 1D particle granular systems (those that undergo a short impulse), the decay region of our shocks is a function of path length. As seen in Fig. 3.16, the v_p that produce shocks all decay to their stationary strength by approximately the same point in the channel. The decay region length depends on the number of particles in the path of the force chain. In our simulations, the decay region ends after roughly 30 cm which is longer than the 5 cm that would be the case in 1D chain ($\sim$10 particle diameters,[62]). To avoid the region perturbed by the shock (and similarly, the region in which the solitary wave decays after reflection off the end wall) with some extra margin, we ignore the height change of particles within 50 cm of the initiation (left) and end (right) walls in the final bed height change calculation.

Wave type effects

We first subjected the same compact bed to the strongest shocks, v_p = 10 m/s for the P wave and corresponding bender displacement amplitude A = 3.1831$\times 10^{-5}$ m for the S wave. Figure 3.13 shows particle height change as a result of the shock waves. We see that volume change is only affected beyond the initiation region by P waves and a solitary wave is not maintained

after S wave generation. The force profile in the P front is in the same direction of propagation while the S front is transverse to propagation ([173]). As discussed in the prior section, the lateral compressive force in the P wave triggers a frictional collision with neighboring particles, allowing particles in the wake of the shock to attain a positive z velocity. Since there is no surface dilation occurring as the result of even the strongest S wave shock, we consider only P waves going forward. Note that the region of most extreme dilation (the dark red band along the surface of the P wave height change in Figure 3.13) corresponds with the detachment region as seen in the normal and shear stress shock profile in Figure 3.11.

Random seeding effects

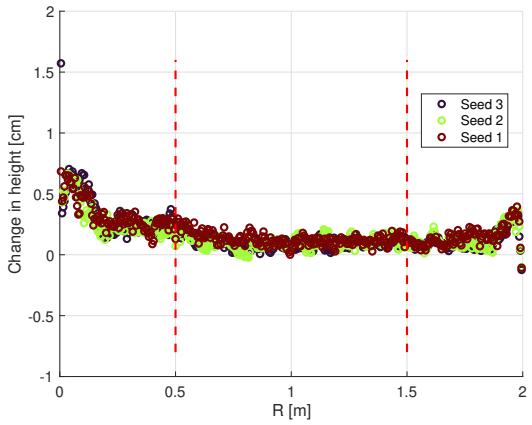


Figure 3.14: Δz **vs Radial position.** Color legend corresponds to seed number configuration and red dashed lines indicate the measurement region. We generated shocks (v_p = 10 m/s) in loose beds 2 m in length filled 20 cm deep with particles. The randomness of the packing has little effect on post shock dilation.

Next we determine dilation error bars by evaluating the deviation in post-impulse bed height change due to randomness of the initial packing. Changing the seed numbers passed to the particle creation and insertion algorithm changes the initial packing of the bed. We perform this

test by shocking (v_p = 10 m/s) the loosely poured bed configuration in a 2 m channel filled 20 cm deep. We prepare three identical beds and only vary the prime seeds passed for each case. The results from each test are quite similar as can be seen in Figure 3.14. There is very little effect of the randomness of packing on the dilation response. We quantify this variability by finding the deviation in post-impulse height change. We compute the mean ($\mu\Delta z$) and deviation ($\sigma\Delta z$) across all radial positions within the measurement range and the results are provided in Table 3.7. $\sigma\Delta z$ is a result of the randomness in the packing along the channel within a single test and all three seed groups are comparable. Since we want to know how comparing results between two assemblies is affected by the preparation history, we take the random seed error (RSE) to be the deviation of $\mu\Delta z$. This results in an RSE of 0.0172 cm or approximately 0.2 mm (or 0.1 % bulk volume change in beds filled 20 cm deep with particles).

Table 3.7: Bed height change for different seed groups. Mean (μ) and deviation (σ) are taken from the height change in the measurement region for each seed group in Fig. 3.14.

Group	$\mu\Delta z$ (cm)	$\sigma\Delta z$ (cm)
Seed 1	0.0964	0.0432
Seed 2	0.1017	0.0500
Seed 3	0.1284	0.0501

Wave speed effect

We perform a velocity sweep over three decades in v_p (0.01 to 10 m/s) for P waves an all three packing configurations (loose, medium, compact) to evaluate wave speed influence on impulse-induced dilation. In this section, all tests were run in 2 m channels filled 20 cm deep. The details for all the tests are given in Table 3.8 which reports on the properties of the generated

waves, the state of particles within the wave front, and the resultant dilation induced by the wave (as seen through height change). In all three cases, we see that that low v_p generate acoustic waves which travel at the sound speed and do not induce dilation. Waves in the transition region begin to induce some post-impulse bed height change, but only the solitary waves (which decay from the strongest shocks) trigger dilation across the entire channel (shown for the compact case in Fig. 3.15). Even for these strongest shocks, the speed of particles within the front are much less that the wave speed (small v_m/c_p) and v_m barely exceeds the Hertz elastic collision limit (0.1 m/s). While the compact and medium packed assemblies show dilation for all cases $v_p > 1$ m/s, the loose packed channel showed either slight dilation or slight compaction. We believe this variation indicates that the loose packed channel ($\phi_0 = 54.72\%$) is at or near the crossover threshold between initial conditions that lead to compaction instead of dilation. This is less than the crossover $\phi_0 = 58\%$ in [85], but that makes sense given our reduced gravity conditions and addition of cohesion. Although all v_p investigated for the loose ϕ_0 were performed in the same bed, the RSE (∼0.2 mm) is only fully exceeded for the case at $v_p = 10$ m/s. This may indicate that randomness of the packing allows for variable volume change around the compaction-dilation threshold. We should also point out that there is a discrepancy in the acoustic wave speed reported for the loose bed between the c_w and c_p reported speeds in Table 3.8 . The two speeds should be approximately the same for acoustic waves as is the case with the compact and medium packed channels. This discrepancy highlights that our wave tracking method (peak force 3.2.8) is better suited for tracking stronger waves with greater ϕ_0 because the increase in peak force is more abrupt in these cases and the peak force coincides with the end of an exponential force increase. As the peaks become less sharp, the determination of when the shock passes through the sensor becomes more challenging. Using a first arrival wave speed based on δ would likely resolve this

issue.

Table 3.8: Wave characteristics for the velocity sweeps in the compact (C), medium (M) and loose (L) packed beds. The average initial overlap correspond to δ_0 = 4.82, 4.81 and 4.23 μm (L,M,C respectively), see sec. 3.2.4 for details. The columns correspond to packing fraction, piston velocity, initial (shock) wave front speed, propagating (solitary) wave front speed, particle velocity within the solitary wave front, maximum overlap experienced by particles following the passage of the solitary wave front, the ratio of particle to wave front speeds, and the at rest height change (from the initial 20 cm bed height) following the wave's passage.

ϕ_0	$v_p = 10^n$ (m/s)	c_w (m/s) $\mu \pm \sigma$	c_p (m/s) $\mu \pm \sigma$	v_m (mm/s) $\mu \pm \sigma$	δ_m (μm) $\mu \pm \sigma$	$\sim \frac{v_m}{c_p}$ x10^{-3}	Δz (mm) $\mu \pm \sigma$
C	-2	7.79 ± 0.52	7.53 ± 0.17	0.64 ± 0.15	4.16 ± 0.09	0.09	0.00 ± 0.02
C	-1	7.67 ± 0.33	7.50 ± 0.18	5.65 ± 0.93	4.67 ± 0.14	0.75	0.00 ± 0.02
C	$-1/2$	8.23 ± 0.34	7.69 ± 0.16	7.47 ± 5.23	4.84 ± 0.57	0.97	0.00 ± 0.02
C	$-1/4$	8.65 ± 0.36	7.90 ± 0.16	22.33 ± 15.75	6.47 ± 1.86	2.83	0.04 ± 0.06
C	$-1/8$	8.94 ± 0.41	8.07 ± 0.17	28.71 ± 13.41	7.21 ± 1.50	3.56	0.35 ± 0.37
C	0	9.12 ± 0.37	8.25 ± 0.17	34.19 ± 5.43	7.86 ± 0.64	4.15	1.14 ± 0.22
C	$1/4$	10.07 ± 0.49	8.65 ± 0.20	32.77 ± 6.01	7.34 ± 0.49	3.79	1.12 ± 0.11
C	$1/2$	11.12 ± 0.52	9.04 ± 0.23	42.30 ± 10.37	7.41 ± 0.85	4.68	1.07 ± 0.11
C	$3/4$	12.40 ± 0.41	9.45 ± 0.22	78.96 ± 10.32	9.90 ± 0.79	8.36	1.16 ± 0.14
C	$7/8$	13.34 ± 0.43	9.78 ± 0.23	117.11 ± 7.87	12.77 ± 0.53	11.97	2.31 ± 0.22
C	1	14.00 ± 0.31	10.14 ± 0.20	181.17 ± 7.17	16.94 ± 0.55	17.87	3.84 ± 0.56
M	-2	7.06 ± 0.57	7.05 ± 0.15	0.13 ± 0.06	4.61 ± 0.19	0.02	0.00 ± 0.02
M	-1	6.99 ± 0.49	6.97 ± 0.17	2.69 ± 0.53	4.90 ± 0.20	0.39	0.00 ± 0.02
M	$-1/2$	7.39 ± 0.50	7.04 ± 0.17	3.90 ± 3.32	5.04 ± 0.43	0.55	0.02 ± 0.06
M	$-1/4$	7.72 ± 0.48	7.19 ± 0.18	10.69 ± 7.92	5.84 ± 0.95	1.49	0.20 ± 0.24
M	0	8.17 ± 0.53	7.39 ± 0.19	20.57 ± 3.91	6.90 ± 0.43	2.78	0.59 ± 0.12
M	$1/4$	8.89 ± 0.52	7.65 ± 0.21	20.21 ± 3.97	6.65 ± 0.45	2.64	0.62 ± 0.07
M	$1/2$	9.82 ± 0.62	7.96 ± 0.23	30.88 ± 6.42	7.01 ± 0.56	3.88	0.56 ± 0.08
M	$3/4$	10.86 ± 0.53	8.40 ± 0.25	65.38 ± 8.99	9.75 ± 0.71	7.78	0.81 ± 0.13
M	1	12.71 ± 0.50	9.12 ± 0.30	151.46 ± 9.23	15.75 ± 0.77	16.61	3.07 ± 0.65
L	-2	6.17 ± 0.93	7.10 ± 0.46	0.34 ± 0.12	4.49 ± 0.24	0.05	-0.07 ± 0.08
L	-1	6.09 ± 0.97	7.09 ± 0.42	1.65 ± 0.61	4.66 ± 0.26	0.23	-0.08 ± 0.08
L	$-1/2$	6.26 ± 0.91	7.09 ± 0.42	2.91 ± 2.87	4.83 ± 0.44	0.41	-0.07 ± 0.08
L	$-1/4$	6.50 ± 0.90	7.10 ± 0.44	9.12 ± 8.51	5.58 ± 1.06	1.28	0.00 ± 0.12
L	0	6.80 ± 0.95	7.12 ± 0.51	19.11 ± 4.37	6.67 ± 0.48	2.68	0.16 ± 0.11
L	$1/4$	7.43 ± 0.97	7.28 ± 0.48	19.51 ± 4.96	6.48 ± 0.49	2.68	0.19 ± 0.10
L	$1/2$	8.17 ± 0.91	7.51 ± 0.56	31.39 ± 6.85	7.03 ± 0.55	4.18	-0.09 ± 0.12
L	$3/4$	9.32 ± 0.85	7.83 ± 0.65	75.40 ± 9.36	10.10 ± 0.77	9.63	-0.30 ± 0.18
L	1	10.36 ± 0.54	8.31 ± 0.77	141.24 ± 5.69	15.27 ± 0.56	17.00	0.96 ± 0.43

In terms of the strength of the wave, the strongest solitary wave ($v_p = 10$, dark red) exhibits

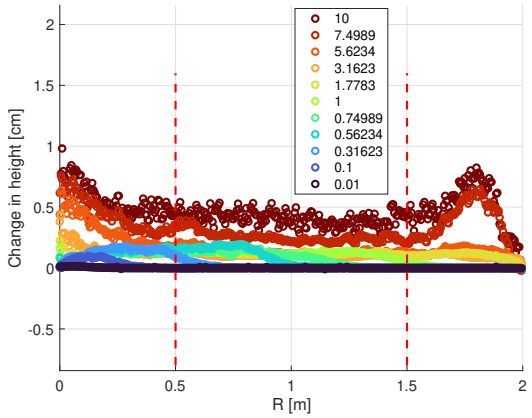


Figure 3.15: Δz **vs radial position for varied** v_p**.** The color legend shows v_p in m/s for waves initiated in a compact bed 2 m in length filled 20 cm deep with particles. Acoustic waves ($v_p \leq 0.1$ m/s) show no bed height changes. Waves in the transition region ($0.1 < v_p \leq 1$ m/s) begin to show some dilation, but it does not persist across the channel. The remainder of the v_p investigated induce shocks, which see uniform dilation across the channel.

a constant δ_m across the entire channel (see fig. 3.16), i.e., there is minimal dissipation after the shock initially decays. Solitary waves corresponding to shocks initiated at $1 < v_p \leq 10^{0.875}$ m/s (orange - red) maintain a constant δ_m for some distance across the channel and then begin to decay, but maintain $\delta_m > \delta_0$. For those waves initiated by shocks at $10^{-0.5} < v_p \leq 1$ m/s (light blue - green), δ_m decays back to δ_0 after the solitary wave terminates. The rest of the waves ($v_p \leq 10^{-0.5}$, black - dark blue) are purely acoustic and never attain a constant δ_m before returning to δ_0. Be aware that taking the average over the measurement region causes larger deviations and tends to under report δ_m for the intermediate v_p cases since we average over a region in which the solitary wave is no longer active. The remainder of our tests are conducted using the strongest solitary wave (from $v_p = 10$ m/s) since it induces the greatest dilation response.

To understand the strength of the waves inducing dilation we show Figure 3.17 which plots resultant dilation vs Mach number in channels of different ϕ_0. We find the Mach number $M = c_p/c_0$ using the solitary wave speeds from Table 3.8 and the sound speed from Table 3.6.

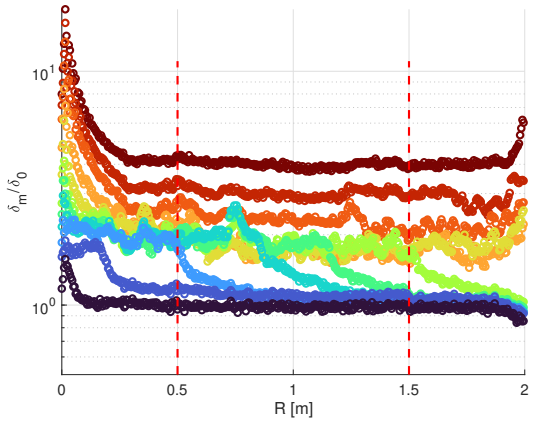


Figure 3.16: **Average δ_m/δ_0 vs radial position for varied v_p.** Normalized maximum particle overlap over the length of a 2 m channel filled 20 cm deep with particles (compact filling) is shown for the same waves created in Figure 3.15. While all induced waves experience a region of initial rapid decay in δ_m, only the shocks decay to solitary waves which propagate with constant δ_m (until they terminate). The strongest waves are maintained across the entire channel. The colors correspond to the same v_p legend as in Fig. 3.15, but is omitted here so as not to obscure the trends.

$\Delta\rho$ is the percent change in bulk density taken as the impulse-induced height change from Table 3.8 divided by the bed height (for example, $\Delta\rho = 100 \times \Delta z/20$ cm in a channel filled to 20 cm with particles). The acoustic waves from all tests ($M = 1$) are all clustered around $\Delta\rho = 0$, as expected. However, once the waves are no longer acoustic (i.e., barely supersonic), dilation begins to occur. Disregarding the loose case (since it barely exceeds the RSE), the intermediate strength solitary waves in the medium ($1.02 < M < 1.2$) and compact ($1.07 < M < 1.26$) exhibit roughly constant height change. The strongest solitary wave sees more than a doubling in $\Delta\rho$ over the constant height change region, however the v_m experienced by these particles do exceed the static limit (though, less than 2x) so they may be more influenced by plastic deformation in reality. Nevertheless, these results show that barely supersonic solitary waves can excite surface dilation.

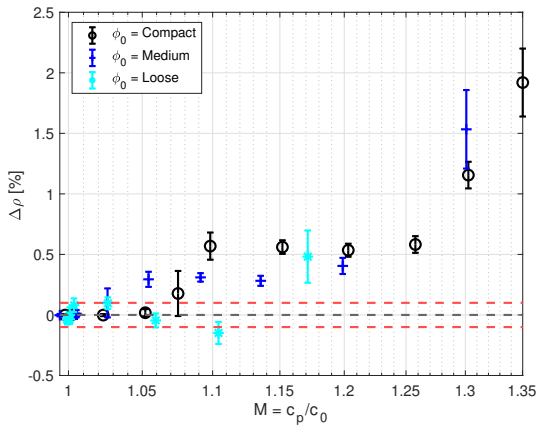


Figure 3.17: $\Delta\rho$ **vs** $M = c_p/c_0$**.** Dilation vs Mach speed for the compact, medium, and loosely packed beds. The black dashed line at 0 is the compact-dilation threshold and the red dashed line corresponds to the RSE.

Boundary effects: channel length

To test the effect of channel length, we prepared channels of varied lengths (1 to 4 m) at the same loose packing to reduce computation time. Each bed is subjected to a single shock at $v_p = 10$ m/s. The resultant solitary wave induces uniform dilation across the channel that is approximately the same regardless of the length of the assembly (Fig. 3.18). Note that the value for $\Delta\rho$ in the 4 m channel differs from the 2 and 3 m channels by more than the RSE (Table 3.9). We attribute this to the slightly larger c_p attained in the 4 m channel. Given that a wall can influence results for up to half a meter (at the start or end of the channel), the 1 m channel is not long enough to include an uncorrupted measurement region. There is therefore a minimum required channel length, but otherwise we find that the length of the assembly does not have an effect on our results, which agrees with [164].

To evaluate how the solitary waves evolve in the longer channel, we show the wave profile in Figure 3.19. Figure 3.19 shows the normalized overlap experienced along the length of the

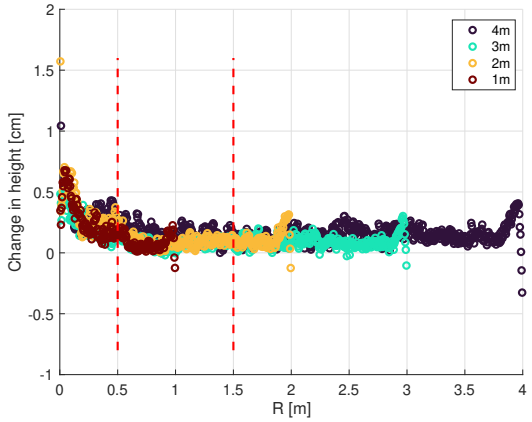


Figure 3.18: Δz **vs radial position for varied channel lengths.** Change in bed height is tracked in different beds filled 20 cm deep with the loose configuration of particles. A uniform, though small, amount of dilation occurs across all channels. Color legend corresponds to channel length.

channel. The strongest solitary wave which decayed from a shock initiated at v_p persisted across the entire channel. The solitary wave generated using $v_p = 1$ m/s terminated earlier (around 1 m) than the same v_p generated wave in the compact case (Fig. 3.16, around 1.5 m). This might suggest that a more densely packed assembly can maintain the same strength wave over a longer distance. We show the dilation resulting from these three tests in Table 3.9 and we see similar behavior (both dilation and compaction) as the loose bed in the prior section.

Table 3.9: Δz in beds of various length. c_p is the solitary wave speed and $\Delta\rho$ is computed as a percent difference from a bed initially filled 20 cm deep with particles.

Length (m)	v_p (m/s)	c_p (m/s) $\mu \pm \sigma$	$\Delta\rho$ (%)
2	10.0	8.29 ± 0.55	0.482
3	10.0	8.20 ± 0.36	0.379
4	10.0	8.36 ± 0.38	0.771
4	5.62	7.41 ± 0.52	-0.033
4	1.0	6.66 ± 0.73	0.001

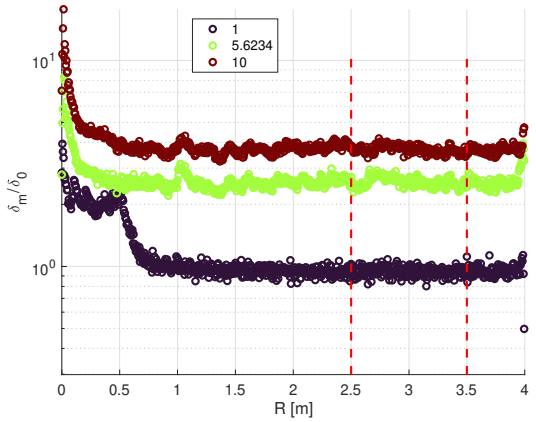


Figure 3.19: **Average δ_m vs R.** We show normalized δ_m across the 4 m channel for three different v_p cases. The solitary waves generated with the two largest v_p sustain a roughly constant δ_m over the entire length.

Boundary effects: channel depth

With a 2 m length channel we filled assemblies to depths of 10, 20, and 30 cm ('fill height') to investigate any height effects on the surface dilation. We again use the loose packing to reduce preparation time. There is a slight increase in height change with a decrease in bed height (Fig. 3.20).

The change in bed height dependence on channel depth is a result of an increased propagation speed in the bed as the fill height decreases, as was also observed in [174]. In our simulations we see that the maximum speed in the solitary wave is essentially the v_p used to initiate the wave. This is evident in Figure 3.21 where we show how c_p varies with depth. We first initiated shocks within each of the three channels at $v_p = 10$ m/s (constant v_p) and c_p is just over 10 m/s at the floor of the assembly in each of the constant v_p cases. As a result of the wave speed dependence on δ and the δ dependence on the overburden force, the speed of the generated wave must be greatest at the bottom floor of the channel. Surface particles in a taller assembly therefore will

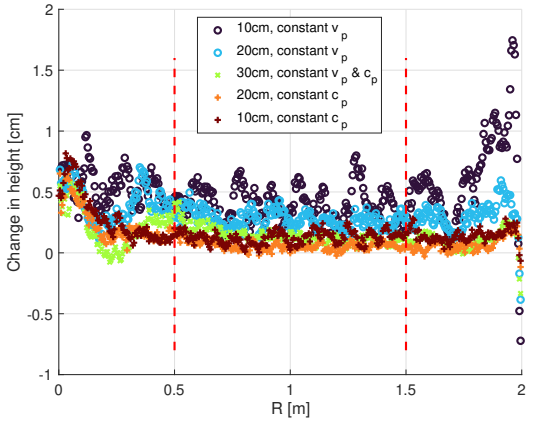


Figure 3.20: Δz **vs radial position for varied fill height.** There is a slight increase in the post impulse height change with decreasing bed height (2 m long beds filled at the loose packing configuration).

experience reduced speeds as compared to a shorter assembly since, for the same floor speed, they will undergo a greater reduction in speed due a larger gravity gradient.

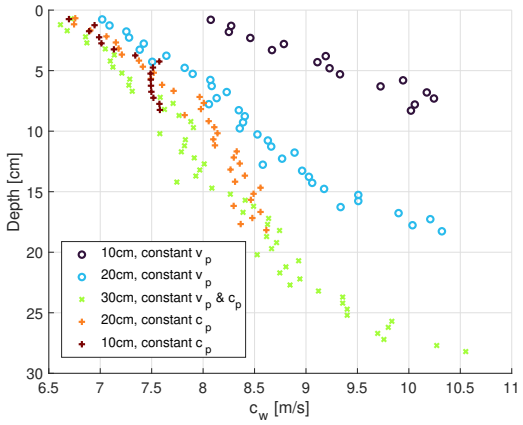


Figure 3.21: **Depth vs** c_p**.** While the initially induced c_w were the same, c_p is greatest for the smallest channel fill height. Constant v_p cases are marked with circles and constant c_p with a plus sign (the case for the 30 cm channel marked with an x marker is both constant v_p and c_p).

To verify that it is the wave speed change that leads to greater bed height change (as opposed to some geometrical effect of a shorter channel) we reduced the input v_p in the 10 and 20 cm deep channels. Reducing v_p generates solitary waves with speeds in the wavefront that are

roughly the same as those in 30 cm channel with $v_p = 10$ m/s. The input v_p and resultant c_p are given in table 3.10 and compared to the constant v_p height changes in Figure 3.22. The height change for the constant v_p cases appears to be linearly decreasing as bed height increases while the height change for the constant c_w is much closer to constant.

Table 3.10: c_p and v_p in beds of various height. We show the input v_p used to generate solitary waves of different c_p.

Height (cm)	v_p (m/s)	c_p (m/s) $\mu \pm \sigma$
10	10.0	9.54 ± 0.55
20	10.0	7.72 ± 0.36
30	10.0	7.01 ± 0.30
20	8.8	7.32 ± 0.36
10	7.5	7.09 ± 0.28

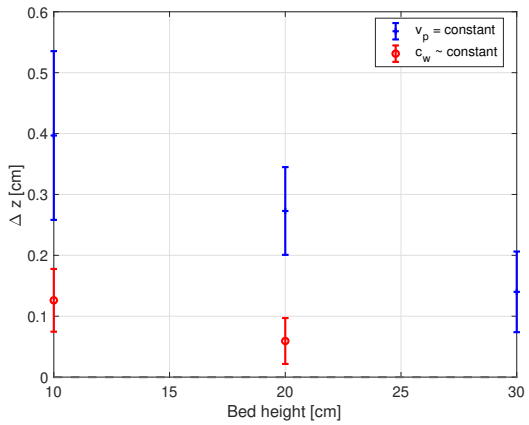


Figure 3.22: Δz **vs channel height.** Shows cases for constant v_p and for roughly constant propagating c_w . Δz is given instead of $\Delta\rho$ since the different initial bed heights influences the percent difference calculation. The single data point at 30 cm can be considered as both constant v_p and constant c_p.

Initial packing effects

We excite shocks at $v_p = 10$ m/s in the loose, medium, and compact beds to evaluate the influence of ϕ_0 on impulse-induced bed height change. Similar to the work from [85], we expect that granular dilation will be the most pronounced for the initially compacted bed and decreases as the packing becomes looser. Figure 3.23 confirms this trend. Quantifying the percent change in height, Figure 3.24 shows that dilation occurs even for the loosest bed and considering the random seeding error. The crossover initial state between a compaction and dilation result is $\phi_0 < 0.55$, lower than the 0.58 crossover seen in [85]. The reduced threshold is attributable to the reduction in gravity and increase in cohesion of our assembly. We also tested whether preparation history had an effect on resultant dilation by tapping the loosest bed to the ϕ_0 reported in Table 3.4 and then initiating shocks each bed (see sec. 3.2.5). Figure 3.24 includes the results of the poured and tapped beds. Similar results are produced regardless of the bed preparation method, as we see the same linear trend in the tapped beds as the poured beds. The slight increase in the percent dilation for the tapped bed over the poured beds is the result of the reduced bed height (15 cm deep tapped beds, see sec. 3.2.5) as determined in section 3.3.2. The method of bed preparation does not influence the dilation response beyond the randomness of the packing.

Figure 3.25 shows a visualization of the resultant impulse induced dilation for the three poured ϕ_0. This visualization confirms that our data analysis method accurately captures surface dilation and it shows the depth dependence of particle mobility. The band in which particles expand upwards increases in lateral extent as ϕ_0 increases. For the compact case, the particles are most mobile in depths down to about one third of the total channel height (~ 8 cm), although the majority of the channel has experienced upward particle motion (dilation) as the result of a

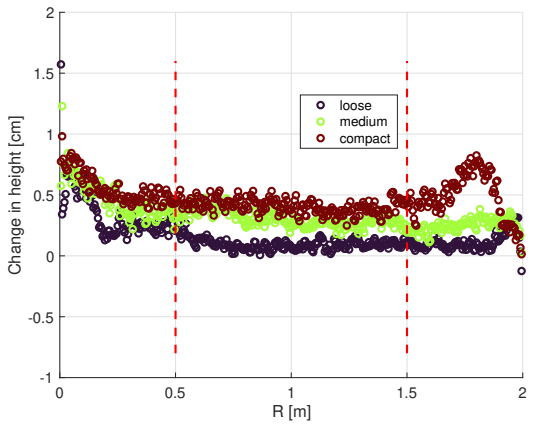


Figure 3.23: Δz **vs radial position for different** ϕ_0**.** We examine the dilation sensitivity to ϕ_0 by initiating shocks in beds (2 m in length filled 20 cm deep) corresponding to the loose, medium, and compact ϕ_0 from Table 3.3. In each case, the height change is uniform across the bed, besides the initiation region and the end wall region. The heap near the end wall is the result of particles ejected as the wave reflects off the end wall. Red dashed lines indicate the measurement region.

solitary wave.

Error analysis

To compare results across the different parameter spaces, we find the deviation in wave speed and dilation response for each case evaluated. Since deviation of the height change (Fig. 3.26) is taken from the measurement region (0.5 m away from the end walls) the 1 m channel is neglected in computing the deviation for the channel length cases. The deviation in the wave speed (Fig. 3.27) is taken from depths in common across the cases and the range is [0,20] cm for all cases except the height analysis, which only has depths up to 10 cm in common across the three heights investigated.

In both the case of dilation and wave speed, the deviation across the beds of different lengths is equivalent to the seed deviation. The length of the channel does not influence our results any more than the randomness of the packing. Velocity, bed height, and ϕ_0 all influence

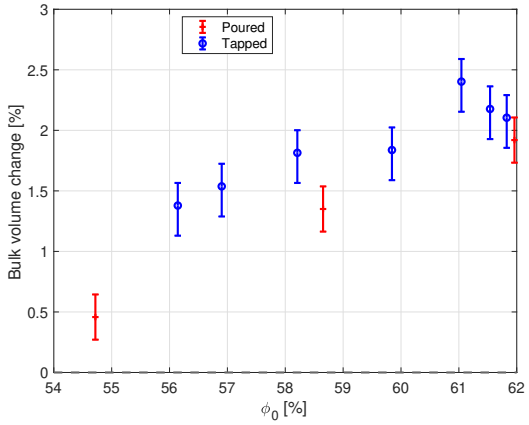


Figure 3.24: **Bulk density change vs ϕ_0.** Percentage change in volume fraction is computed as an average of height changes the measurement region from Figure 3.23 assuming the entire vertical extent of the bed has undergone dilation. Since the dilation band is a fraction of the total bed height, these values are lower bounds. Results are included for both poured and tapped beds.

the magnitude of dilation that occurs. Wave speed is also affected by the piston velocity and packing fraction, but bed height does not impact the initiated c_w more than the random packing (though it does affect c_p, see sec. 3.3.2).

3.3.3 Effect of wave initiation region

We varied the wave initiation region within the 2 m long 20 cm deep compact bed to provide further bounds on when dilation can occur. We modified the P wave initiation process (sec. 4.2.1) in three ways by reducing the region of particles that make up the virtual piston. For the first test (thin strip), the piston still spanned the height of the channel, but only particles within one particle diameter of the origin (x dimension) were given a y velocity. This test evaluates how surface dilation is influenced by greater initial dispersion. For the second and third test, the piston spanned the width of the channel, but we modified the z dimension of particles included. Only particles within 10 cm of the surface are included for the 'top half' test and particles within 10

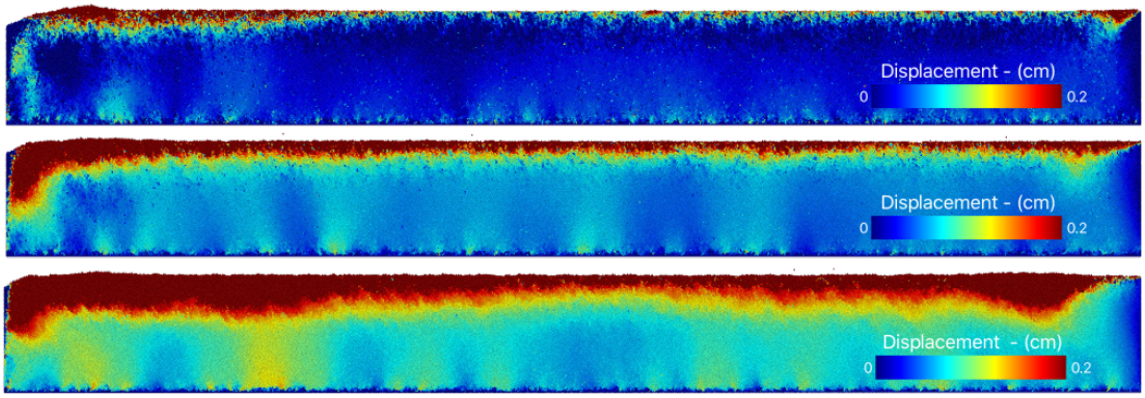


Figure 3.25: **Particle height change.** Each particle is color coded to show it's change in height. We show results for loose (top), medium (middle), and compact (bottom) packing of 2 m beds filled 20 cm deep with particles after a shock was initiated at v_p = 10 m/s. The extent of dilation increases with ϕ_0 and, in the case of the compact bed, a consistent portion of the near surface (to about 5 cm in depth) experienced more than 0.2 cm increase in height.

cm of the floor are included for the 'bottom half' test. This test allows us to evaluate how waves generated at an angle or reflected floor waves might influence surface dilation.

Figure 3.28 shows that for the thin strip case a solitary wave still forms and is able to propagate down the entire channel and affect uniform dilation, albeit at a reduced level. In the top half case there is almost no surface modification, though the bottom half case still produces dilation similar to the full plane piston. Additionally, we found that the results of the 'top half' test were the same as when the full plane piston was used, but no particles were fixed to the floor of the assembly. Therefore, the region of initiation must include a stronger floor for the force in the shock to be radially sustained.

Finally, we generated a shock at each end of a channel to see how the resultant solitary waves interact with each other. Figure 3.29 shows several frames from this interaction performed in the 2 m long channel filled 20 cm deep (ϕ_0 = compact) and a piston velocity $v_p = 10$ m/s. Qualitatively, both the strength and shape of the wave are preserved through the collision, the

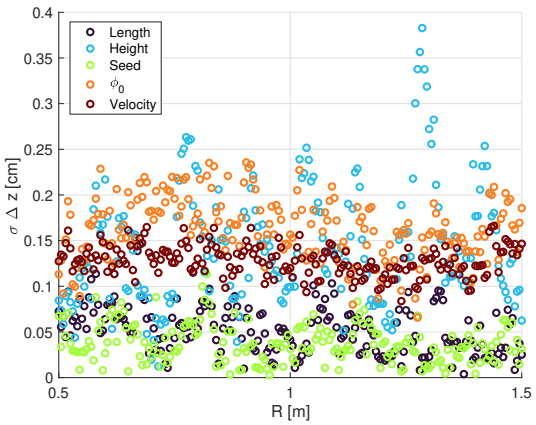


Figure 3.26: $\sigma\Delta z$ **vs radial position.** Deviation is computed for the radial positions in common across the parameters investigated. The legend shows the test from which the deviation is computed.

hallmark of a soliton ([103], [62] - chapter 1.6.4).

3.3.4 Discussion of solitary waves

In our simulations, we have been able to easily create solitary waves as the decay product of an initiated shock. A single, solitary wave front emerges from a lateral impulse in which a constant δ_m compression (Figs. 3.16, 3.19) is maintained. The shape of the wave front and its spatial size (width) are preserved (see the wavefront in Fig. 3.2, top frames from Figs. 3.11 and 3.29, Fig. B.1 frame d, or video OL1). The elastic limit for impact velocities (0.1 m/s) is only appreciably exceeded (less than doubled) by particles in the wave front of the strongest solitary waves (v_m for v_p = 10 m/s in Table 3.8) which supports impulse-induced dilation as a physical result. The spatial size of the wave front is much smaller than the distance it travels and we saw the strongest solitary waves to be sustained over the entire 4 m channel (Fig. 3.19), only terminating upon contact with the end wall. Here we have neither quantified nor predicted the termination distance of the solitary waves we generate, understanding the criteria for lateral solitary wave

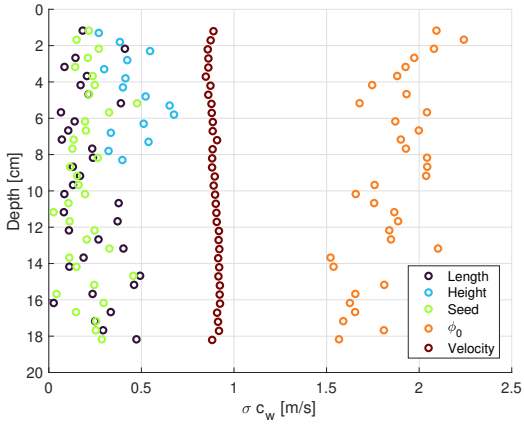


Figure 3.27: **Depth vs σc_w.** Deviation is computed for the depths in common across the parameters investigated. The legend shows the test from which the deviation is computed.

generation and sustainment in a 3D randomly packed granular assembly are important topics for future investigations.

Another subject which deserves further study is the soliton-like behavior of the solitary waves we have generated. In addition to maintaining strength and shape and propagating for much longer distances than the wavefront is wide, our solitary waves also qualitatively preserve shape and strength through a collision (Fig. 3.29). We briefly evaluate our numerically obtained solitary wave speeds against expected soliton speed. Equation 1.43 from [62] (equation 3.9) gives the soliton speed (in a 1D chain) based on particle velocity in the wavefront (v_m, Table 3.8). Equation 3.9 is valid in the sonic vacuum regime which is the case when the granular assembly is weakly compressed. An assembly can be considered weakly compressed when the maximum overlap in the wave front is greater than (not on the same order) as the initial overlap, $\delta_m/\delta_0 \gtrsim 2$ ([62] ch. 1.3).

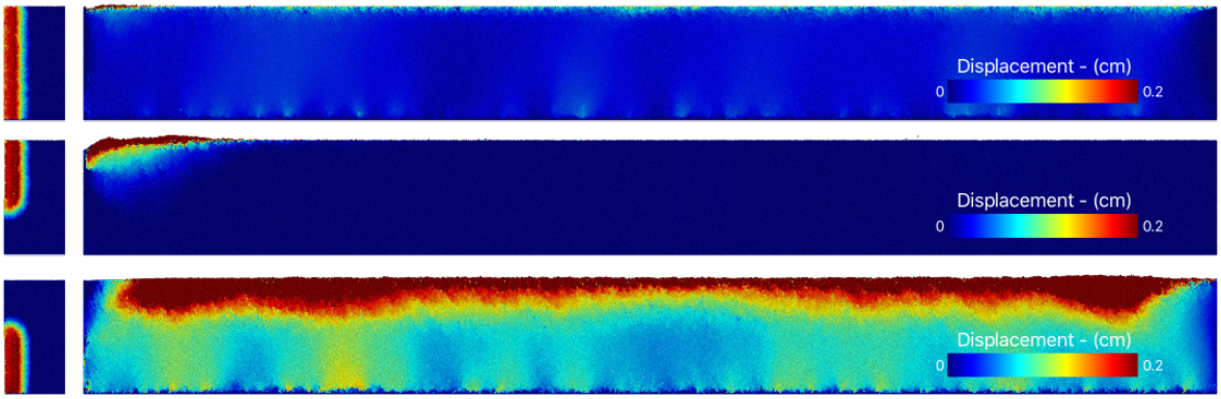


Figure 3.28: **Shock profile and particle height change for various test cases.** Each frame shows the profile of the initiated shock region and the resulting bed height change. The left images show the particle force (same legend as in Fig. 3.2) and the right image colors particles by their z displacement with the embedded color legend in units of m/s. The channels correspond to the thin strip (top), top half (middle), bottom half (bottom) test cases.

$$V_s = \left(\frac{16}{25}\right)^{1/5} \left(\frac{2E}{\pi\rho_p(1-\nu^2)}\right)^{2/5} v_m^{1/5} \tag{3.9}$$

Our strongest solitary waves fall into the weakly compressed regime (Table 3.8), though we include points from any test that had an initial shock decay to a solitary wave in this analysis. We divide equation 3.9 by c_0 of each bed (Table 3.6) to create Figure 3.30 which shows the analytically and numerically calculated Mach number vs v_m. Points are plotted only for waves that were initiated as shocks. All three cases show a similar trend (faster initial increase in Mach at lower v_m), though the loose bed shows reduced Mach number compared to the medium and compact. We believe this is due to some inaccuracies in the wave speed calculation in the loose bed (discussed in sec. 3.3.2). Simulated results from the medium and compact cases agree with the soliton speed at lower velocities, but diverge as v_m increases. While our simulated solitary waves do not follow the trend exactly, they are in the range of what is expected. Note that eq. 3.9

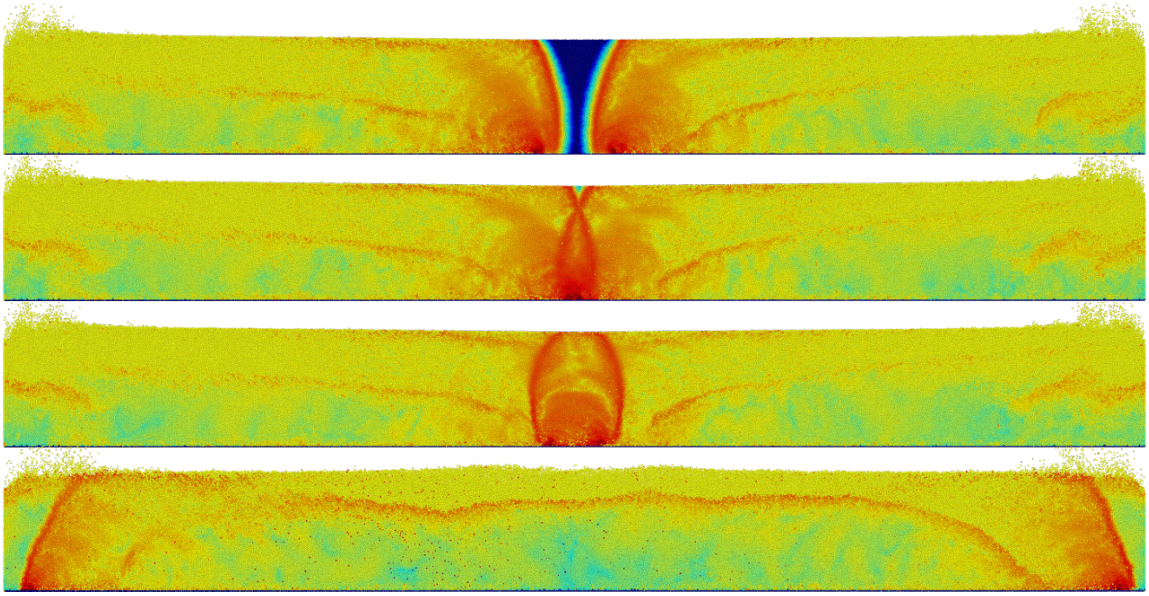


Figure 3.29: **Interacting waves.** Solitary waves with equal strength ($v_p = 10$ m/s) are generated in opposite directions from each end of a 2 m long channel filled 20 cm deep with particles ($\phi_0 =$ compact). From top to bottom the frames correspond to $t = 0.093$, 0.099, 0.104 and 0.195 s. Particles are colored corresponding to the order of magnitude of force experienced (same scale as in Fig. 3.2). The strength of each wave is maintained during and after the collision. The shape of the wavefront is largely maintained, though there is less curvature to the wavefront near the floor of the channel as the waves approach their terminal points (bottom frame).

is derived for 1D particles and does not include any modifications to reflect the material properties implemented in our model (friction, cohesion) nor geometrical effects of the 3D packing. Also recall that our numerical results are averaged over particles within a virtual cell which is 0.5 cm in width which may obscure the trend. We have a grid resolution of about 8 sensors in the wave front ($\sim$15 particles, $\sim$4 cm), but augmenting the results with single designated particle sensors would help to refine the results. Predicting the behavior of laterally propagating solitary waves at the surface of a vacuum interface should be a focus of future work.

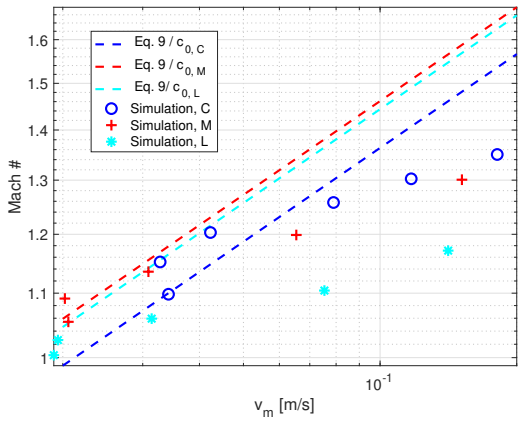


Figure 3.30: **Mach # vs v_m.** Equation 3.9 is divided by c_0 corresponding to the loose (L), medium (M) and compact (C) packed assemblies to produce the predicted soliton speed (dashed lines) for a range of v_m. For the corresponding simulated results (various markers) we find $M = c_p/c_0$ and plot against v_m from table 3.8. Simulated results are only plotted for tests at $v_p \geq 1$.

3.3.5 Dilation and scaling discussion

We've shown that in the absence of atmospheric confinement pressure and under low gravity, a band of grains at the surface of a granular assembly can experience inertial dilation as the result of a laterally propagating solitary wave. First, a granular assembly must be in an initially compact state for a lateral impulse to induce dilation. Surface dilation is then triggered for solitary waves that are barely supersonic ($M > 1.05$, Figure 3.17) and can be sustained over large distances (up to 4 m, so far) as long as the wave is active. The extent of dilation is primarily controlled by c_p since the increases in dilation observed as a result of increasing ϕ_0 or decreasing bed height were fundamentally a result of increased solitary wave speed. This new particle lofting mechanism is capable of affecting surface bulk dilation in our simulations, but how does it scale to other environments?

We do not yet have a method for predicting the final resting height of particles (and thus,

dilation) based on the solitary wave speed, but we can roughly predict the depth to which particles will loft. Our simulations show that a sheet of particles became completely detached following the passage of the solitary wave front. There is an easily discernible cutoff depth for this detached sheet at around 8 cm in depth visible in Figure 3.11 corresponding to the demarcation between particles experiencing large and then zero normal and shear stresses. For the particles to be in a lofted state, they must have acquired some upward velocity, so any particle down to that cutoff depth will have experienced an upward force. The depth dependence on lofting suggests that an imbalance between the forces in the wave front and the overburden is the source of the upward velocity. We define θ as the angle of the wave front which determines the amount of force experienced by a particle and is redirected in the z direction. θ describes the angle between horizontal (y) and the vector normal to the wave front. This vector is normal to the curvature in the force profile of the wave front and the curvature can be seen in Figs. 3.2, top frame of 3.11 and frame d of B.1. Near the surface, the direction normal to the shock front (θ) is greater than 0, while at depth theta is approximately 0 (an x-plane wave). In our simulation, the lofting depth is roughly equivalent to the depth at which the wave front becomes planar so we assume that the cutoff angle for lofting occurs when θ is small (we assume 1°). The wave front shape (and thus θ) can be derived analytically, but we leave that as an exercise for our future work. We then use the constant θ to find the gravitational forces (eq. 3.10) in the vertical direction and balance them with the wavefront forces (eq. 3.11): $F_{grav} = sin(\theta)F_{WF}$.

$$F_{grav} = \left(\phi(\pi R^2)z + \frac{4}{3}\pi R^3\right)\rho_p g \tag{3.10}$$

$$F_{WF} = \mid -k_n(\delta_m - \delta_0)^{3/2} - \gamma_n v_n + k_c A_c \mid \tag{3.11}$$

Solving the balance for depth then gives the loft depth, z_{loft}, in equation 3.12:

$$z_{loft} = \frac{sin(\theta)F_{WF} - \frac{4}{3}\pi R^3 \rho_p g}{\phi \pi \rho_p g R^2} \tag{3.12}$$

Solving for the value of depth that satisfies this equality yields the lofting depth, z_{loft}. The spring force and cohesion depend on the strength of the solitary wave (δ_m) and the damping component depends on impact velocity, which is the maximum velocity of particles in the wave front (v_m). Note that this formulation neglects the effect of friction. We make a few additional simplifying assumptions to use this equation. To solve for the damping force (eq. A.4), we'll use a constant $v_m = 0.1$ m/s (the static limit) which is in the range of what is experienced in our simulations, but really is a function of the wave front strength (δ_m). Also note that this formulation is based on the particle-particle material properties, not bulk properties (particle properties can be orders of magnitude larger than bulk - [157]). We show the procedure to solve for z_{loft} in Figure 3.31, with δ_m/δ_0 = 4 (maximum experienced by our solitary waves). The ratio of the maximum to initial overlap can be though of as describing the strength of the wave, though keep in mind that it is not the same as Mach number.

The depth at which the force balance (x axis) equals unity is the lofting depth, which for the case pictured resulted in z_{loft} ~3 cm for our simulation. While we expect a larger lofting depth, 3 cm is on the order of the 8 cm we observed in Fig. 3.11. Given the numerous assumptions made

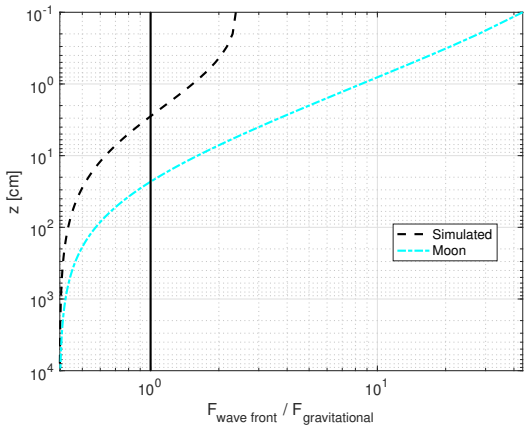


Figure 3.31: z **vs force balance.** The lofting depth z_{loft} occurs when $F_{gravitational}$ and $F_{wavefront}$ are equal (denoted by the solid black line). The simulated and Lunar trends are produced using the material parameters described in the text along with eq. 3.12. When the fraction is greater than 1, wave front forces in the vertical direction exceed gravitational forces and particles will loft above the depth $z_{loft} = z(F_{wf}/F_g = 1)$.

while constructing equation 3.12, it is encouraging that the results are within a factor of three. Using equation 3.12 to consider how the loft depth would change in different conditions also makes intuitive sense. The loft depth will increase for denser particles (increased wave speed) and reduced gravity (decrease of ρ_p and g) and increase for harder particles (increase in E, which is embedded in k_n) while the dependence on particle size (R) is more complicated. Atmospheric pressure would be an additional term on the gravitational side of the equation and would decrease z_{loft}.

3.3.6 Relevance to LCS

As an initial assessment of lateral impulse-induced dilation's candidacy as the LCS formation mechanism, the results we have seen here are encouraging. The solitary waves that induce dilation can be minimally disruptive which is important since the LCS show no visible signs of surface modification. The solitary waves inducing bulk dilation in our simulations occur at low

speeds ($M \gtrsim 1.05$) and have wave fronts in which the maximum compression isn't much more than 1% of the particle radius (1.4% for our strongest solitary wave with δ_m = 16.94 μm, see Table 3.8). The solitary waves inducing the largest dilation response were also able to travel long distances and were only constrained by the size of our channel, although the 4 m propagation distance we observed is much less than is needed for LCS formation ($\sim$100 km). To understand if a laterally propagating solitary wave could be the LCS formation mechanism, more work must be done to predict the strength of the initiated solitary wave and its termination distance. In our simulations, the initiated shock wave needed to be in contact with the hard subsurface floor in order to be maintained and this is likely the case on the Moon as well. Surface regolith undergoes a rapid increase in density in the first 10s of cm of the surface ([15]) and below that there are varying layers of regolith composition that can have abrupt transitions ([175]).

Although the greatest bulk dilation we observed in any of our tests was $\Delta\rho \sim 0.5\%$ which is an order of magnitude less than the expected LCS dilation ($\sim 4\%$)), recall that that our idealized particles (monodisperse) have properties (size, modulus) that differ by orders of magnitude as compared to the Lunar surface regolith grains. We expect an assembly with material properties that more closely resemble the Lunar environment to show greater dilation than seen here. In the Lunar regolith, wave speed (which is dominant in controlling impulse-induced dilation) will increase due to harder particles and dilation will be enhanced by the smaller particles, irregular particle shapes, and polydispersity ([134]). Based on shear band thickness dependence on particle size as a result of planar flow ($\propto D^{-1/3}$, [176]), we expect at least a doubling in the vertical extent of the dilation band as compared to the results presented here.

We use equation 3.12 to evaluate how our simulated results might scale to the Lunar environment. We conduct a sweep over the space $0 < \delta_m/\delta_0 < 5$ as a proxy for solitary wave strength.

We first need to define a few particle properties for an idealized Lunar surface grain. In our simulation, we had a particle elastic modulus of E = 5 MPa which resulted in a bulk modulus around 75 kPa (Table 3.6). If the ratio of bulk-to-particle is the same on the Moon, then this leads to Lunar surface regolith particle with modulus 500 MPa. For the cohesion, we assume a particle-particle value that is also two orders of magnitude greater than the bulk value ([157]), so k_c = 100 kJ/m^3 (scaling from Table 3.2). Using the respective values for our simulated and Lunar particles yields Figure 3.32.

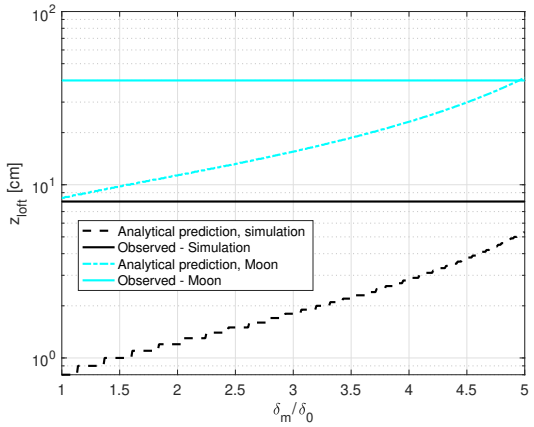


Figure 3.32: z_{loft} **vs shock strength.** We solve equation 3.12 for z_{loft} at varying shock strengths (δ_m/δ_0). The expected lofting depths are approximately achieved for the strongest solitary waves ($\delta_m/\delta_0 = 5$) for both the Moon (cyan) and our simulated (black) conditions. There is a consistent nearly order of magnitude scaling of z_{loft} between our simulated case and the Lunar environment.

In Figure 3.32, the solid lines represent the observed z_{loft} in our simulation (8 cm, black) and hypothesized z_{loft} on the Moon (40 cm [1], cyan). For stronger solitary waves, particles are lofted down to approximately the depths we expect. The loft depth of 40 cm is surpassed for the Lunar grains around δ_m/δ_0 = 5 and approaches our observed 8 cm simulated lofting depth for the same strength. More importantly, there is a roughly constant scaling ratio in z_{loft} of nearly an order of magnitude ($\sim$8.5) for the Lunar surface particles compared to simulated. This is exciting

because, even with our assumptions and the omission of some material parameters (like friction), we approximately capture the scaling between assembles in different environments. Given the scaling of Equation 3.12 discussed in the prior section, the impulse-induced surface dilation seen here may also be active on other airless and low gravity bodies. Developing a complete model (which predicts final bed height change) and understanding the sensitivity of impulse-induced-dilation to various physical and mechanical parameters is the focus of our ongoing research.

3.4 Summary and conclusions

We have constructed and validated an open source tool for investigating inertial dilation and near surface wave propagation in a granular medium exposed to vacuum and microgravity. In our simulations, lateral shock waves were generated via impulsive piston impact and quickly decayed to a solitary wave. We have provided the first characterization and explanation for the particle lofting mechanism that occurs as long as the solitary wave is maintained. The primary results of our work are:

- vertical surface dilation will occur as the result of particle lofting induced by a single laterally propagating granular wave in microgravity and vacuum
- an impulse-induced lateral shock in a randomly packed 3D assembly can decay to a solitary wave which propagates (and affects dilation) over long distances if the shock is generated in contact with a hard subsurface floor
- impulse-induced granular dilation is confined to a narrow region at the grain-vacuum interface and increases with wave speed (which increases with ϕ_0 and height of the assembly's surface above a soft-to-hard particle interface)

- the expression of dilation does not depend on the length of a granular assembly (for the distances inspected in this paper) and would occur in a short channel to the same extent as it would in a longer channel with the same ϕ_0 and depth

We conclude that impulse-induced granular dilation is a plausible LCS formation mechanism and deserves further study. We hypothesize that initial Lunar impact-generated shocks decay to 3D solitary waves which are maintained over large distances, dilating the surface regolith as they travel. Regardless of the outcome, understanding small airless body response to surface waves has applications for understanding the evolutionary history of the solar system as well as future human exploration and construction on the Moon.

Chapter 4: Material parameter influence on the expression of Solitary-Wave-Induced Surface Dilation

This chapter has been written as a stand-alone paper to be submitted shortly after the culmination of this thesis. Please check for the electronic version to find any supplementary videos and updated code.

4.1 Introduction

In this paper we first develop a method to predict the peak force felt by a particle in a randomly packed 3D granular assembly as it experiences a laterally propagating wavefront. Recent simulations by [177] showed that impacts of a lateral piston within a shallow granular channel (exposed to vacuum and microgravity) led to a solitary wave (SW) which propagated over long distances. In this work, we consider briefly the driving mechanism leading to such long range propagation (the SW in [177] was driven through constant impacts with the floor), but our focus is characterizing bulk dilation changes as a result of the SW, not its origin. In the wake of the driven SW wavefront, a region of substantial bulk dilation near the surface is left behind as a result of particle lofting, a phenomenon that we call SW Induced Dilation, or SID. We are particularly interested in characterizing SW wavefront forces in 3D granular channels as our second task in this work is to understand the behavior of SID as a function of particle material proper-

ties. [177] hypothesized that the impulse delivered to particles in the SW wavefront would be enhanced under lunar conditions (i.e. with smaller and harder grains), but this hypothesis relied on several assumptions. One important assumption was that particle velocities within a driven SW wavefront were constant regardless of grain material properties, but this is not the case ([62], eq. 1.41). Additionally, the forces that particles experience will also change as a function of their collisional velocity. Here, we will adapt a method used to calculate SW forces in a 1D granular chain (requiring only a simple rescaling) to predict the peak force experienced by a grain in our randomly packed 3D channels, $F_{m,3D}$. We assess the appropriateness of our 3D SW wavefront force model by comparing predictions to simulated results. We generate driven SW in granular channels filled with particles of varied size, density, and modulus of elasticity under a range of impact velocities using Soft Sphere Discrete Element Method (SSDEM) simulations. Seeing that simulated $F_{m,3D}$ follows the expected power law scaling, we then construct a force balance between these driven SW wavefront forces and gravitational overburden, resulting in an equation that we solve to find the depth to which SID will occur (z_{LD}). We measure the SID response of our channels to the different SWs that we generate by quantifying the height change of the channel (Δz) as well as the bulk volume change as function of depth ($\%\Delta\rho(z)$). Finally, we compare the simulated dilation to the prediction and examine the sensitivity of SID to some important simulation parameters (friction, coefficient of restitution, etc). Our primary motivation is to understand how the magnitude of SID changes as particle hardness increases. A large dilation response for particles with lunar regolith-like properties has implications for SID as the formation mechanism of Lunar Cold Spots (LCS) [1], large distal regions of reduced surface bulk density surrounding craters on the Moon. Before discussing our simulation and results, we review a few important details of granular wave propagation, discuss how such a wave could lead to surface

lofting of particles and consider possible implications for LCS formation.

4.1.1 Granular SWs

Wave propagation in 1D granular chains is an extensively studied topic. In the most idealized case, a wave is initiated in a chain of spheres (particles/grains) by delivering an impulse to the first sphere. [48] first showed that grains at low or no pre-compression develop SW following a strong impact. SW travel in energy packets of roughly 5 particle diameters [62] and when the coefficient of restitution of the particles is unity, no energy is lost while the packet propagates [178]. When the chain has the right amount of pre-compression (not strongly compacted, but also has some finite pre-compression) long lived SW arise ([179], [124]). There are many studies that characterize the properties of SW in both 1D chains and 2D assemblies under varying conditions and there is an overview of the state of the art in [177], section 1.1. In 3D, SW excited via ground impact have even been used as a tool for detecting buried objects ([119], [103], [121], [180]). Here, we are most interested in studies that predict the force on particles within a laterally propagating SW wavefront. [108] gave equations for the force on a grain in a vertically propagating wavefront, but this approach requires knowledge of the maximum displacement in the wavefront (and we are concerned with lateral propagation). Hasan gives equations for the force experienced by a grain in a 1D crystal as it experiences a SW ([181], [182], [183]), but their model requires knowledge of the loading profile. Pal mostly considered elasto-plastic chain propagation ([184]), but they also considered a simple elastic Hertzian model similar to [177]. Their equation for force in the wavefront depends only on the impact velocity and grain material properties (mass, elasticity, and size) [113] and we will use this as the basis for predicting forces felt by a particle

within a 3D driven SW wavefront ($F_{m,3D}$, see sec. 4.2.3), which to the best of our knowledge has not yet been carried out. We propose that $F_{m,3D}$ can be approximated as a simple scaling of the peak forces in SWs propagating in 1D granular chains. We can then consider how changing forces in the wavefront influence the depth range over which surface particles experience lofting via SID and thus bulk density changes.

4.1.2 SW-Induced Surface Dilation

We briefly review the SID mechanism leading to surface bulk dilation as it was initially described before providing some important clarifications on the process. [177] used a lateral piston impact into a 3D granular channel to initiate SW. In those simulations, we described a SW that develops following the brief existence of a planar shock wave. The SW then maintained its strength and shape as it propagated over meter scale distances. As a result of proximity to vacuum, the speed of this wave in the near-surface increases quickly as overburden pressure increases with depth, leading to a curvature in the wavefront as the SW propagates. The SW travels just above the local sound speed, which similarly increases with depth. As particles experience the SW wavefront they undergo a frictional collision with their neighbors and develop an upwards velocity. The curvature of the wavefront ensures this upward motion and the result is an entire sheet of lofted particles on ballistic trajectories. SID also requires a granular assembly to be in a compacted state in order for particle lofting to occur; below a threshold packing fraction, the assembly will compact instead of dilate after experiencing a SW. Particles are only able to loft when the force imparted in the vertical direction by the SW wave exceeds the force particles feel from the overburden and this is wavefront force is where $F_{m,3D}$ will be used. In [177], the

maximum speed of the SW occurred along a rough channel floor and was determined by the piston impact velocity. Since the largest velocity occurs at the floor, the effect of SID is reduced in taller channels (i.e., when surface grains are further from the floor). For the same piston impact speed the wavefront curvature evolves over a greater vertical distance which results in a slower traveling SW at the surface. Collisional velocity is therefore reduced as is the vertical velocity near-surface grains can attain.

We clarify here that the wave generation process used in [177] actually produces two distinct SW, not a shock that decays to a steady SW as initially introduced. The piston impact generates a SW (PSW) which disperses as it propagates while at the same time a second SW (which ultimately overtakes the first) is driven by continual impacts propagating along and within the rough channel floor. The same velocity that acts as an impulse for virtual piston particles is also transmitted through our thin sheet of floor particles and, since the floor is made up of randomly packed particles, the un-fixed grains of the channel in contact with the fixed floor experience oblique impacts. These impacts drive the constant-strength driven SW (DSW) across the channel and the work in [177] (and here) represent an idealized scenario of 'perfect-floor impact' (discussed further in sec. 4.2.1). Without the DSW, the energy of the piston impact would decay through our granular channel over a finite length. In fact, grains are often used as a type of force absorption [122] given their ability to efficiently decimate propagating energy. Any wave traveling over a significant distance through small grains (e.g., 1 mm or less like in [177]) would require an external driver. This work does not seek to explain that external driver and we continue to use the idealized 'perfect-floor impact' to study SW via the DSW. Our focus in this work is to understand how the reaction of near-surface grains to the driven SW changes as the material properties of grains in the channel become regolith-like.

4.1.3 Lunar Cold Spots

LCS are apparent as relatively cold halos surrounding source craters on the Moon. Their low thermal inertia is hypothesized to be the result of bulk density differences down to 40 cm in depth. While the LCS appear around all young craters ([6]) and can extend more than 100 radii from the source, there are no visible signs of surface modification. The LCS halo becomes apparent around 10 crater radii from the source crater, beyond the region where impact ejecta is evident. The interested reader can refer to the LCS literature for further details: [1], [6], [10], [7], [8]. In [177] we hypothesized that SID was a possible LCS formation mechanism given the SW produced bands of near surface dilation that appear to be consistent with expected LCS bulk density changes. However, the material properties of our granular assembly did not represent lunar surface regolith and it is unclear how SID will scale to assemblies with different material properties. Understanding how forces in the SW wavefront ($F_{m,3D}$) scale with material parameters will provide further evidence for SID as the LCS formation mechanism.

In this paper, we will compare bulk density at the surface and at depth to expected density changes for typical LCS. Figure 4.1 shows the hypothesized bulk density profile for background and LCS surface regolith based on Diviner thermal measurements [1]. Density differences are likely constrained to the first 40 cm of surface regolith and are substantial near the surface. Evaluating the percent change between background and LCS regolith, the peak density change of about 10% would occur around 5 cm in depth and the average density change over the entire depth region between LCS and background regolith is about 5%. If SID is involved in LCS creation, we'd expect our simulated SID response to exceed the average expected density change since the channels in our simulations are only a fraction of the total LCS depth (in other words,

our channel is shorter than the lunar 'channel' and a shorter channel leads to greater wave speeds - sec. 4.1.2).

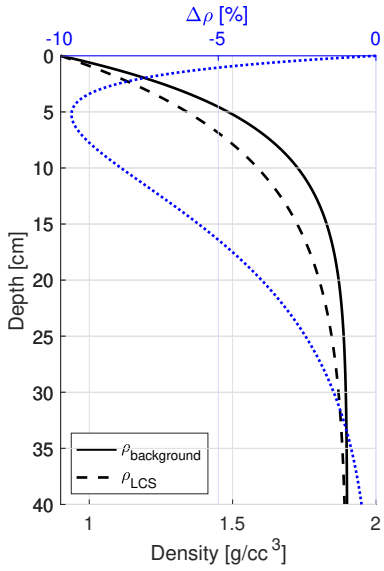


Figure 4.1: **Cold Spot density vs depth.** The lower X axis represents bulk density (black) and the upper X axis represents the percent change in bulk density density (blue), where negative percent change represents dilation. The y axis shows depth in cm and is the shared by both trends. The lunar surface regolith (black solid line) and LCS (black dashed line) are predicted using the method and fit parameters from [1]. Bulk density change (dotted blue line) takes ρ_{LCS} to be a percent difference from $\rho_{background}$. This percent difference can be thought of as 'dilation expected as the result of LCS formation' and we will use it as a reference later when viewing Figs. 4.4 and 4.10.

4.2 Methodology

We discuss our computational model, a method for estimating SW wavefront forces using a 1D chain assumption, and a method for predicting the depth to which particles experience lofting following the passage of a SW. We provide details on our simulation and tests performed, computational resources and data analysis methods.

4.2.1 Simulation setup

Our simulation implementation is largely the same as [177] which used a particle piston to initiate waves within a long, thin granular channel filled with a monodisperse assembly of grains under lunar gravity. The grains are confined by end walls and a rough floor but are subject to periodic boundary conditions in the azimuthal direction which allows our simulated channel to be representative of a volume element within the path of a radially expanding pressure wave. After the channel experiences a lateral impulse delivered by a virtual piston with impact velocity v_0, the PSW decays in strength until the DSW becomes dominant. The maximum v_0 considered corresponds to a fixed portion of c_m (roughly 20% c_m). With the material parameters used in [177] this gives a maximum impact piston velocity v_0 = 10 m/s. We use the same limit here. We select a single channel geometry of 2 meters in length, filled 20 cm deep, and 2 cm wide. For the base case particle size of radius R = 1.25 mm, this fixes the size of our channel (in terms of particle radii) at 1600, 160, and 16 (length, height, width respectively). The decay range and wall effect regions of the channel are usually a function of particle number ($\sim$30 particles in a 1D chain, [62]) so we can therefore keep the same channel geometry while scaling particles size or material parameters and still have a region of the channel which provides an unadulterated view of DSW effects.

We again use *LIGGGHTS* [68], an open source Soft Sphere Discrete Element Method (SSDEM) solver, to perform our simulations. SSDEM is a common methodology used to study low gravity granular dynamics ([140], [67], [141], [77], [142], [143], [55]), but comes with a potentially large computational cost (depending on particle properties) due to integrating the equations of motion at a small time step ($<$1% of Hertz collision time τ_c, eq. 4.6). We can reduce compute

time in many cases by re-using the particle channels that were prepared in [177], but varying particle size (varied R) requires additional channel preparation.

Pre-settled channels

We use (from [177]) 2 meter long channels filled 20 cm deep with a monodisperse particle distribution in three packing configurations (loose[1] ϕ_0 ∼55%, medium[2] ϕ_0 ∼59% and compact[3] ϕ_0 ∼62% channels found at [169]), where $\phi_0 = V_{particles}/V_{channel}$ is the initial packing fraction. The base material parameters of the particles are elastic modulus E = 5 MPa, particle density ρ = 2.5 g/cc (note that any equations involving density should use SI units, kg/m^3) particle radius R = 1.25 mm, cohesion energy density k_c = 1 kPa, Poisson ratio ν = 0.2, sliding friction $\mu = 1$, rolling friction μ_r = 0.8, rolling viscous damping $\gamma_{d,r}$ = 2 and restitution e = 0.5. We will often refer to these material and simulation parameters as the base properties. To investigate how our driven SW propagation is altered by material properties, we take the base case channel, change the parameter of interest, and allow a settling period to reduce background forces before saving the new channel state. The settled channel now has the new material parameters and can be used multiple times (creating multiple SW from different v_0). Given the form of eq. 4.6, altering particle density, size, and modulus all influence the contact time which has implications for our simulation step size. ν also influences τ_c, but the range of ν we investigate is small compared to the order of magnitude sweeps we will conduct in E, ρ and R space. The majority of our simulations have a time step set to $<1\%\tau_c$ which we show in tables 4.1 and 4.2. A few cases (like E = 50 MPa, v_0 = 31.6 m/s) slightly exceed the 1% limit, though we determined that to be

[1] Filename restart2m20cm_loose.static
[2] Filename restart2m20cm_medium.static
[3] Filename restart2m20cm_compact.static

acceptable since results were consistent with simulations with a time step $\ll 1\% \tau_c$. Additionally, the time step is set using the maximum v_0 which occurs at t = 0s when the piston is initiated as well as along the floor as the 'perfect floor impact' velocity travels through particles in the rough base layer. Our time step is smaller than needed in most cases since the surface lofting we are interested in occurs where particle velocities are slower. Tables 4.1 and 4.2 also show the elastic limit, L_e, which is the collision speed above which Hertz theory begins to break down. L_e will be used later (Table 4.6) to discuss the validity of particle collision speeds within the wavefront.

One thing to keep in mind regarding the channel preparation method discussed here is that it is distinctly different from the pouring method used in the next section. Preparation history of the channel does influence channel response and this can be seen later in sec. 4.3.1 when changing ρ using the 'pre-settled' method leads to looser channels (smaller δ_0 in the varied ρ plot of Fig. 4.7) than expected. However, we deem these differences to be negligible given the agreement we will later see with expected behavior (scaling of wavefront forces and surface dilation) across multiple decades of parameter space as well as between channels prepared using both preparation methods (see secs. 4.3.1 and 4.3.3).

New channel filling

The particle sizes used in sec. 4.2.1 are roughly an order of magnitude larger than lunar grains. The large role of cohesion on lunar grain dynamics ([185]) is one example of unique behavior that emerges when particles are relatively small. Since it is not clear how the strength of the SW will change with particle size, we explore both larger and smaller grains than in [177]. When changing particle size it is necessary to re-pour the channels in order to maintain the same

Table 4.1: Channel properties for testing sensitivity to elastic modulus. We give the average initial conditions, velocity limits, and assess the appropriateness of our time step choice in channels of varying E. δ_0 decreases as E increases since the spring repulsion between particles increases and they push apart, resulting in a slightly looser channel (smaller ϕ_0). The largest δ_0 (experienced by the particles with E = 5 MPa) is about 0.3% of R which is sufficiently small. Δt is well below 1% of τ_c for most cases, though this limit is exceeded slightly in few of the cases (up to 1.46% of τ_c). We determined that these tests were still run at a sufficiently small time step given the agreement of the behavior of the SW in theses channels with expectation (sec. 4.3.1). Other particle parameters are constant (R = 1.25 mm, ρ = 2.5 g/cc). We performed two series of tests in these channels, one with v_0 constant at 10 m/s and one where v_0 was a constant portion of c_m (∼20% c_m). A dashed line indicates 'same as above'.

E (MPa)	ϕ_0 (%)	δ_0 (μm)	c_m (m/s)	v_0 (m/s)	τ_c (s)	Δ t (s)	Δ t/τ_c (%)	L_e (mm/s)
5	62.08 ± 0.048	4.23 ± 1.50	47.1	10.0	$2.166x10^{-4}$	10^{-6}	0.46	9.4
20	61.89 ± 0.051	2.18 ± 8.81	94.2	20	$1.733x10^{-4}$	10^{-6}	0.92	18.9
-	-	-	-	10.0	$1.990x10^{-4}$	-	0.81	-
50	61.71 ± 0.055	1.16 ± 0.58	149.1	31.623	$6.848x10^{-4}$	10^{-6}	1.46	29.81
-	-	-	-	10	$8.622x10^{-5}$	-	1.15	-
200	61.63 ± 0.051	0.752 ± 0.512	298.1	63.24	$3.424x10^{-5}$	10^{-7}	0.29	59.63
-	-	-	-	10.0	$4.952x10^{-5}$	-	0.20	-
500	61.55 ± 0.051	0.384 ± 0.312	471.4	100.0	$2.166x10^{-5}$	10^{-7}	0.46	94.28
-	-	-	-	10.0	$3.432x10^{-5}$	-	0.29	-
5,000	61.54 ± 0.049	0.046 ± 0.018	1490.7	316.23	$6.848x10^{-6}$	10^{-7}	1.46	298.14
-	-	-	-	10	$1.366x10^{-5}$	-	0.73	-

ϕ_0. To do this, we scale the filling procedure from [177] by the ratio of the newly investigated particle radius to the base case R = 1.25 mm (ratios shown in Table 4.3). We used a medium filling (sec. 4.2.1) to reduce computation time. To be able to compare SID results across the various particle sizes, we scale the dimensions of our channels by the same factor to maintain a fixed height in length in terms of number of particles (length scales are non dimensionalized by particle radius in this work). We repeat the time step checks for varied R in Table 4.3. All of the channels with varying grain size have a consistent ϕ_0 (just below 59%) except for the 12.5 mm

Table 4.2: Channel properties for testing sensitivity to density. We give the average initial conditions, velocity limits, and assess the appropriateness of our time step choice in channels of varying ρ. The largest δ_0 (experienced by the particles with ρ = 25 g/cc) is about 1% of R which is approximately the limit used in [67]. We judged this large overlap to be acceptable since most cases we evaluated use smaller ρ. δ_0 increases as ρ increases since, as a result of increased mass, the particles have a reduced spring repulsion force. The particles are able to interpenetrate further as ρ increases, leading to more 'compact' (larger ϕ_0) channels. Δt is well below 1% of τ_c for all cases. Other particle parameters and impact velocity are constant (R = 1.25 mm, E = 5 MPa, v_0 = 10 m/s).

ρ_p (g/cm^3)	ϕ_0 (%)	δ_0 (μm)	c_m (m/s)	τ_c (s)	Δ t (s)	Δ t/τ_c (%)	L_e (mm/s)
0.8	61.94 $\pm$ 0.05	2.54 $\pm$ 0.96	83.3	$1.373x10^{-4}$	10^{-6}	0.73	16.7
1.5	62.03 $\pm$ 0.05	3.48 $\pm$ 1.20	60.9	$1.765x10^{-4}$	10^{-6}	0.57	12.2
2.5	62.08 $\pm$ 0.05	4.23 $\pm$ 1.50	47.1	$2.166x10^{-4}$	10^{-6}	0.46	9.4
5.0	62.20 $\pm$ 0.05	5.78 $\pm$ 2.20	33.3	$2.858x10^{-4}$	10^{-6}	0.35	6.7
10.0	62.40 $\pm$ 0.05	8.40 $\pm$ 3.38	23.6	$3.771x10^{-4}$	10^{-6}	0.27	4.7
15.0	62.53 $\pm$ 0.05	10.62 $\pm$ 4.38	19.2	$4.434x10^{-4}$	10^{-6}	0.23	3.8
25.0	62.93 $\pm$ 0.07	14.27 $\pm$ 6.00	14.9	$5.440x10^{-4}$	10^{-6}	0.18	3.0

radius particles which filled slightly looser. This is a result of the scaling procedure, where the particle input velocity is increased 10x over the 1.25 mm radius case but c_m does not change since it is not dependent on R. This means that, for this case only, particles interpentrated more than is physically possible as they impacted the channel during pouring. When the pouring is completed the particles find themselves in a 'too compacted' state and undergo rearrangement to a looser state. Given the consistency in the other particle size channels, we determined that the difference in ϕ_0 (about 2% less) for the 12.5 mm radius is acceptable though it should be considered when analyzing resultant SW forces and the SID response in the channel.

We emphasize here that our 80 particle channel height ($\sim$160R) is only a small fraction of the LCS 40 cm depth. Depending on the size used for lunar surface grains (tens or hundreds of microns), the LCS depth range corresponds to 1,000 to 2,000 particle diameters. Therefore in this paper we are only examining a small segment ($\sim$1%) of the LCS channel. One thing to

keep in mind is that the reduction in height of our channel compared to reality means that, for the same v_0 that we consider in our $160R$ channels, particles near the surface of a taller channel would experience smaller near-surface forces ([177]) and thus see a reduction in the magnitude of SID experienced. Furthermore, the fixed channel height means that smaller particles experience smaller overburden forces than larger particles. If SID is involved in LCS creation, our simulations should over predict dilation compared to the expectation in Fig. 4.1 for the assumed grain properties.

Table 4.3: Channel properties for testing sensitivity to particle size. Particle properties are set with to base case values (E = 5 MPa, ρ = 2.5 g/cm^3, v_0 = 10 m/s). We pour the particles to a medium packing fraction (around 58%) which was chosen as a balance between reducing channel preparation time while achieving a level of ϕ_0 that would still result in SID. We take the elastic limit to be L_e = 9.43 mm/s for all cases since c_m does not depend on R.

R (mm)	ϕ_0 (%)	δ_0 (μm)	τ_c (s)	Δ t (s)	Δ t/τ_c (%)	L (m)	H (cm)	Scale (#)
0.125	58.61 $\pm$ 0.067	0.0996 $\pm$ 0.0359	$2.166x10^{-5}$	10^{-7}	0.46	0.2	2	0.1
0.50	58.87 $\pm$ 0.066	1.027 $\pm$ 0.368	$8.663x10^{-5}$	10^{-7}	1.15	0.8	8	0.4
1.25	58.84 $\pm$ 0.046	4.810 $\pm$ 1.822	$2.166x10^{-4}$	10^{-6}	0.46	2	20	1
5	58.26 $\pm$ 0.083	53.40 $\pm$ 21.57	$8.663x10^{-4}$	10^{-6}	0.12	8	80	4
12.5	56.29 $\pm$ 0.166	208.0 $\pm$ 90.86	$2.17x10^{-3}$	10^{-6}	0.046	20	200	10

We also inspect how polydispersity influences the ability of the SW to dilate surface regolith. Dispersity tends to increase dilation responses ([134]) and so we expect the same to be true for SID. The distributions for the bi- and tri-disperse mixtures we considered are given in Fig. 4.2 and are shown alongside the distribution of lunar surface particles from [14]. Though we used the same filling procedure for these channels as the base case, introducing dispersity decreased ϕ_0 resulting in ϕ_0 = 54.39 $\pm$ 0.03 and 52.46 $\pm$ 0.21 for the bi and tri disperse channels (respectively).

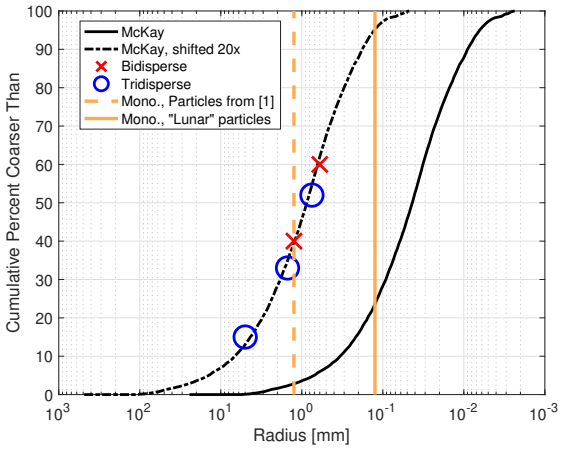


Figure 4.2: **Particle size distributions.** We plot cumulative percent of particles greater than a given size vs particle radius (mm). We use the lunar surface particle distribution from Fig 7.9 of [14] (data harvested with [186]) corresponding to the 63% Agglutinate soils (solid black line). The black dashed line is this same trend from [14], but increased by just over one order of magnitude (20x). The dashed line is the distribution from which we determine our bi-disperse (red Xs) and tri-disperse (blue circles) mixtures. The dashed orange line shows the particle size for the base case monodisperse distribution used in this paper (and in [177]) while the solid orange line shows the size distribution for the monodisperse 'lunar-like' particles used in this paper.

Wave generation

Following either filling procedure, the particle states are saved so that channel preparation is not required for every SW test. After the settled channel state is loaded, we freeze a horizontal sheet of particles to the floor to ensure a rough bottom. We then give particles in a vertical sheet within one particle diameter of the left wall a lateral velocity v_0 and they act as a piston to initiate the PSW. As a result of our rough floor and piston implementation, v_0 is also transmitted through the floor particles. Although floor particles are 'frozen' in the simulation and do not move, their velocity information is updated (the force on the floor particles is set to zero before integrating the equations of motion, but the velocity of the contact is stored separately and is passed to the next particle). When a region of the channel particles in contact with frozen floor particles experiences

this ‘frozen’ velocity, they experience what is essentially an impact. The DSW is driven across the channel by continuous floor impacts. We highlight that the impacts between channel particles and floor particles are oblique; the initial v_0 frozen into the floor propagates laterally. We refer to the length of the channel over which the PSW is active as the blast loading (BL) region. By evaluating the average particle overlap δ, we can characterize dissipation of the PSW (in the BL region) and the strength of the driven DSW.

In the DSW region, the wavefront propagates with constant strength as a result of the sustained floor impacts. Fig. 4.3 shows a comparison between the wavefronts of the initial piston impact and the DSW. The initial wavefront is uniform and flat, but the DSW wavefront is curved as a result of increasing sound speed with depth. The shape of the front is affected by material parameters; harder particles and larger v_0 lead to more curvature near the surface while increasing particle size alone results in a shallower depth range over which curvature exists. For v_0 that are below c_0, the decay of the PSW wavefront can be seen as it traverses the channel since the DSW propagates more slowly in this case. The frozen in v_0 still propagates along the floor of the channel and, instead of generating a DSW, periodically delivers an impulse of sufficient magnitude to perturb particles. When particles are ‘soft’ (lower E), these periodic outbursts do not cause surface dilation, but harder particles ($E > \sim 500$ MPa) experience substantial dilation, at times nearly as much as in the case of a DSW wavefront. We will revisit these lower speed floor impacts in sec. 4.3.5, but here we emphasize that the focus of this work (and therefore $F_{m,3D}$) is to characterize forces in the driven SW wavefront, not the outbursts.

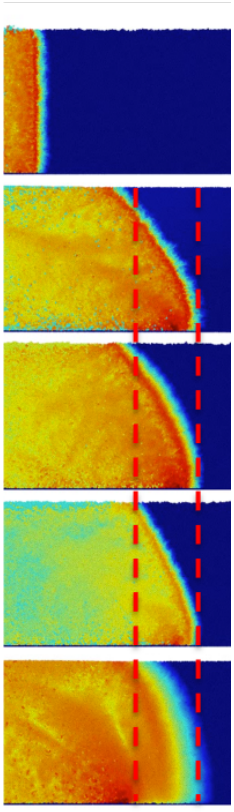


Figure 4.3: **Wavefronts.** We take a cut from various channels to qualitatively demonstrate the piston shock wavefront (top frame) compared to DSW wavefronts with varied curvature as a result of generation in channels of varied material parameters. Particles are colored by the order of magnitude of the force they experience relative to a heuristically chosen reference force (F_{ref}, usually 10^{-6} or 10^{-9} N). The cut for the shock frame (top image) is from the beginning of the channel (adjacent to the left wall), while the SW cuts (all subsequent images) are taken so that we can align their leading edge. In all cases the channel height is $160R$. The particle properties are set to the base parameters and each frame is from a channel with varied parameters. The second and third frames are beds of increased E, but with v_0 a constant portion of c_m (their wavefront shape is roughly the same). The fourth frame is from a channel of reduced particle size ($R = 0.125$ mm) and with $v_0 = 10$ m/s a smaller portion of c_m. There is less curvature to the wavefront. In the fifth frame we show a channel of $R = 12.5$ mm ($v_0 = 10$ m/s) which shows the least curvature out of all the cases. The dashed red lines are guides to compare the wavefronts across the different channels.

4.2.2 Contact model

We use the same approach as [177] to model the grains and collisions within our granular assembly (see the appendix in [177]). We briefly summarize the model here. Our particles

are Hertzian spheres subject to friction (sliding, rolling, twisting) and cohesion. Forces in the normal and tangential (subscripts n and t) direction of the contact frame are given in equation 4.1. The Hertzian spring constant is k $\left((4/3)ER^{1/2}\right)$, particle overlap is δ, v is the relative velocity between two colliding particles, γ is a viscous damping term which depends on material parameters and coefficient of restitution e, k_c is a cohesion energy density, A_c is the contact area, and μ is the friction coefficient. Particles are also subject to a downward uniform gravitational field.

$$\begin{aligned} \mathbf{F}_n &= -k_n\delta_n^{3/2} - \gamma_n v_n + k_c A_c \\ \mathbf{F}_t &= -k_t\delta_t^{3/2} - \gamma_t v_t \\ \mid F_t \mid &\leq \mu_s \mid F_n \mid \end{aligned} \tag{4.1}$$

Using this model we can define several relevant quantities related to wave propagation in the channel. When the channel is in a quasi-static state (pre-impact), a particle at depth will experience a fixed gravitational load based on the weight of particles above it (overburden). Approximating a 3D granular assembly as a 1D stack of particles, we can approximate how δ_0 (initial overlap) changes with depth. We approximate the weight of the overburden as in equation 4.2, where ρ is the particle density. The first term represents the bulk density, the second term is the volume of a column of particles resting on top of a single particle at depth z, and g is gravitational acceleration.

$$F_0 = \rho\phi * z\pi R^2 * g \tag{4.2}$$

Assuming the stack is quasi-static (v is negligibly small), neglecting cohesion, setting the overburden force equal to the normal component of eq. 4.1, and solving for δ_0 leads to the approximate overlap as a function of depth in eq. 4.3. We can evaluate this equation to get an idea of how overlap scales with material properties. Inserting eq. 4.2 into eq. 4.3 shows that δ_0 is proportional to $E^{-2/3}$, $\rho_p^{2/3}$, R, and $z^{2/3}$. Neglecting cohesion is acceptable for the relatively low level of particle-particle cohesion used in most of our simulations and has very little influence on δ_0, though we revisit this assumption later when considering Fig. 4.7.

$$\delta_0 = \frac{2\left(\frac{3(1-\nu^2)}{4E}F_0\right)^{2/3}}{R^{1/3}} \tag{4.3}$$

Knowing the initial overlap, we can also compute the expected sound speed in the assembly. Continuing to use a 1D chain approximation, we give the sound speed c_0 as eq. 4.4 which is eq. 1.7 from [62] modified with a $\sqrt{3}/2$ scaling as was done in [177].

$$c_0 = \frac{\sqrt{3}}{2}\left(\frac{E(2R)^{1/2}}{3(1-\nu^2)m}\delta_0^{1/2}6R^2\right)^{1/2} \tag{4.4}$$

Inserting δ_0 and replacing the particle mass m with ρV ($V = \frac{4}{3}\pi R^3$), sound speed as a function of depth is proportional to $E^{1/3}$ and $\rho^{-1/3}$. Notably, c_0 does not change with particle size when we consider F_0 purely as function of z. However, in this work we will report an average sound speed which is taken as the average of c_0 at each depth within a channel of particles. Since we fix channel height based on number of particle radii ($160R$) we introduce an additional factor of R into eq. 4.2 and we should therefore expect c_0 to scale with $R^{1/6}$ (slight increase with sound speed as particle size increases for our fixed height channels). We also point out that sound speed in a granular assembly (c_0) is much less than the sound of speed within an individual grain which

is given as the material sound speed (c_m) in eq. 4.5 ([151]).

$$c_m = \sqrt{\frac{(1-\nu)E}{(1+\nu)(1-2\nu)\rho}} \tag{4.5}$$

As in [177], we will limit particle impact velocities to less than 20% of c_m. The material sound speed is proportional to $E^{1/2}$ and $\rho^{-1/2}$. Lastly, an important parameter in selecting an appropriate simulation time step is the Hertz contact time, given in equation 4.6.

$$\tau_c = 2.94 \left(\frac{M^2}{\left(\frac{16}{15}\right)^2 E_{eq}^2 R V_{in}} \right)^{1/5} \tag{4.6}$$

4.2.3 SW wavefront particle force

The DSWs investigated in this work propagate laterally within a long granular channel filled randomly with particles. The randomness of the packing leads to highly nonlinear force propagation compared to the linear propagation along a 1D chain. While the increase in dimensionality leads to different dynamical response than in the 1D case, 3D systems do often exhibit the same phenomenon as 1D systems. [130] saw order a two order of magnitude difference in wave speeds between 1D and 3D systems and the power law relationship of shock wave speed to impactor speed is recreated in both geometries ([177], [84], [47], [118]). In this work, we will characterize the behavior of our 3D wavefront by approximating it as a 1D chain. The particles at depth z are thought of as belonging to 1D granular chain which is subject to a finite compression (eq. 4.3) induced by the overburden pressure at that depth. Since we are ultimately interested in understanding how the particle lofting behavior of SID is altered under different conditions, we need a method for predicting the force felt by a particle.

We can use conservation of energy to arrive at an expression for the force experienced by a particle in a SW wavefront. The peak force on the particle in the leading wavefront of a 1D chain can be solved for by equating the energy of a single grain to the kinetic energy of an impactor particle ([111]). Setting the peak force in the chain (F_p) equal to the Hertz spring energy ($\frac{2}{5}k\delta_p^{5/2}$) can be solved to find the peak overlap $\delta_p = (F_p/k)^{2/3}$. Note that for our chosen simulation methodology (sec. 4.2.1) the maximum overlap should not exceed $\sim$1% of the particle radius ([67]). Taking the kinetic energy of an impactor grain to be $\frac{1}{2}mv_0^2$ and isolating F_p, eq. 4.7 appears. [113] found that the coefficient of 0.719 in eq. 4.7 is required to predict the force in the leading SW wavefront of a 1D chain.

$$F_p = 0.719(m^3 E_{eq}^2 R^* v_0^6)^{1/5} \tag{4.7}$$

Arriving at this expression requires several assumptions including that all the energy of the collision goes into the SW and that the energy in the chain is exclusively in the wavefront. Eq. 4.7 also assumes that there is no initial pre-compression on the grains ($\delta_0 = 0$). While that is not the case for the channels we use in this paper (there is some small pre-compression due to gravitational loading), we are going to continue to use δ_0 = 0 in formulating $F_{m,3D}$ assuming that the forces generated by the SW wavefront greatly exceed forces on a particle due to δ_0. Similarly, we neglect the cohesive and damping terms of our model (eq. 4.1) since the spring force should again be much greater than any damping or cohesive force contribution. We are also assuming that the 1D equation which is formulated for linear force transmission can be applied to the case of a 3D SW driven by oblique impacts along the floor. These simplifying assumptions will prove to be justified later in sec. 4.3.3, but should be relaxed in future works. We proceed using the

same form of eq. 4.7, assuming that the forces in the 3D assembly will follow the same power scaling based on material parameters and v_0 as in 1D. We modify eq. 4.7 and write eq. 4.8 for $F_{m,3D}$ and will attempt to determine a numerical leading coefficient C_1 for a grain within the wavefront of a 3D SW. Note that eq. 4.8 reduces to the same form as eq. 4.7 when the definition of k is inserted. In our simulations, we set the particle density as opposed to mass so the expected power law scaling (after inserting m = $\rho\times$Volume) is $F_{m,3D} \sim \rho^{3/5}$, $E^{2/5}$, $v_0^{6/5}$ and R^2.

$$F_{m,3D} = C_1 k \left(\frac{5}{4} m v_0^2 k^{-1}\right)^{3/5} \tag{4.8}$$

In this work we embark on a campaign of numerical simulations using varied material parameters to determine an appropriate value for C_1. We adjust one of the parameters that determine the force (R, E, ρ, v_0) and conduct a series of simulations with the adjusted parameter. Each test results a single average force produced by the SW for that parameter configuration, F_{sim}. Minimizing the objective function $F_{sim} - C_1 F_m$ with respect to C_1 yields the numerical constant of eq. 4.8. Ultimately we want to use $F_{m,3D}$ in a balance with overburden forces to predict the depth at which particles can experience vertical lofting following a laterally propagating SW wavefront (discussed in sec. 4.1.2). As [177] noted, the vertical component of the SW force imparted to particles in the wavefront is likely governed by the curvature of the wavefront in the near surface (see Fig. 4.3). This curvature can be described as the angle between the lateral direction and the wavefront normal direction (θ). Preliminarily we have seen that this wavefront shape can be determined by multiplying the sound speed (eq. 4.4) by a characteristic time scale, which is the number of particles in the wavefront multiplied by the Hertz collision time (eq. 4.6). We did

not implement any methodology for systematically determining the number of particles in the wavefront of our SW and calculating the collision time introduces further complications since we do not yet know of a method for determining the individual particle velocities within the 3D front (done for a 1D chain in [62]) nor how to account for faster particle velocities than expected near the surface (an open topic in the literature [118]). As such, we will continue to assume θ is small ($\sim 1^\circ$) as in [177].

4.2.4 Data analysis

As with sec. 4.2.1, we use largely the same process as detailed in [177] to analyze wave speeds and induced volume change. We briefly review these procedures here. The particle channel is divided into grids and the states of particles falling within a grid bound (force, velocity, stress, ϕ_0) are averaged to produce a 'virtual sensor' state reading at each time step. Taking the average over all the depths at a given radial location in the channel produces the average state at that radial location. We then take the average over a radial measurement range to generate a single average value that can be used to compare results across the parameter space. Error bars that are shown when we report these averages are an indication of the spread of the value (either over the channel length or over the depth we consider) as opposed to a statistical measure. We track the wave by finding the peak lateral force that occurs within each sensor. We determine wave speed by finding the slope of the position vs time data for the peak forces in the BL zone (for the initial wave speed, c_w) and in the middle of the channel (DSW propagating speed, c_p). Force, δ_m, v_m, height change, and depth vs density variation are averaged over a measurement region which is roughly half the channel, with the midpoint located at the center of the channel. We have made

a few modifications within this framework and we detail those here. Along with the *MATLAB* generated plots we show in this paper, numerous videos of our simulations are included as online supplementary material.

Packing fraction

Previously in [177], dilation was measured via channel height change. Here, we also find the packing fraction at depth in order to compare to the expected LCS density change of Fig. 4.1. To do so, we perform a Voronoi tessellation using *Voro++* ([187]) of the channel as was performed in [157]. *Voro++* computes a local packing fraction for each individual grain which becomes another averaged property of the virtual sensors. Tables 4.1, 4.2 and 4.3 include initial packing fraction computed this way for the different channels we consider. Following the passage of the driven SW, we compute the percent change in the channel's bulk volume at each depth as a percent change over ϕ_0 (shown in Figure 4.4). Fig. 4.4 shows that the bulk density change vs depth agrees with the trends identified in [177], that SID increases with increasing ϕ_0 and v_0. The magnitude of SID seen for these particles is smaller than the expected LCS dilation, which is expected since the material properties of the grains in these tests represent much softer particles than lunar regolith grains.

Blast loading identification

The blast loading region (lateral extent of the channel over which the PSW is active) should be a function of particle number [62]. [183] found the length of the decay region in a 1D granular chain to vary slightly with impactor momentum, with a range of 5 to 10 particle diameters for the

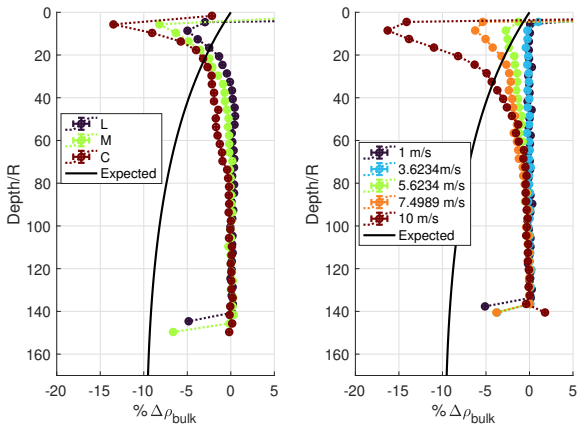


Figure 4.4: **Bulk volume change vs depth.** Percent change in volume ($\%\Delta\rho$) on the x axis vs normalized (by particle radius) depth for varied levels of ϕ_0. **Left)** Channels of 2 meters in length filled 20 cm deep with particles were filled to the loose (L), medium (M), and compact (C) ϕ_0 as described in sec. 4.2.1 were subjected to piston impacts at v_p = 10 m/s. The color scale represents ϕ_0. As ϕ_0 increases, dilation (negative values of $\%\Delta\rho$) increases in both the depth at which it begins (greater than z/R = 100 for ϕ_0 = C) and the peak dilated magnitude (around 14% at $z/R\sim$10) affected. **Right)** The piston impact speed is varied in a single channel of particles (R = 0.5 mm, ϕ_0 = M), with the color legend corresponding to v_p. Dilation increases with increasing v_p. In both plots, the solid line represents the expected LCS percent volume change from Fig. 4.1, normalized by an average lunar surface particle radius of R = 250 μm ([14]).

momentum range considered. In [177] the BL region was approximately 30 cm in length which is approximately 120 particle diameters with their particles (R = 1.25 mm). Since we assume that we can scale the channel length by the same factor that we modify particle size (sec. 4.2.1), we verify that our channels extend a sufficient length beyond the BL region to allow for DSW measurement. For example, the channel in Table 4.3 with micron sized particles results in a 20 cm channel, which is less than the approximate BL region in [177] of about 30 cm. If the BL region is dependent only on particle number, then the shorter channel is acceptable, but if it is not, then channel length should be increased. In this paper we will measure the extent of the BL region by comparing the maximum overlap induced by the SW wavefront (δ_m) to δ_0. When the PSW is active, δ_m/δ_0 should fall rapidly along the length of the channel until reaching a steady

value (when DSW becomes dominant). In this paper, we will define the end of the BL zone as the first post-peak occurrence of δ_m/δ_0 falling within three deviations of the DSW wavefront mean. This process is visualized later in sec. 4.3.4.

4.2.5 Data generation and availability

Following [177], channel preparation occurs on our standalone 44-core workstation and we run piston impact simulations using the University of Maryland High Performance computing cluster, Zaratan. Since we use a fixed channel geometry in this work, the number of particles in each simulation is roughly the same (around 600,000 particles) with some variation for ϕ_0. Output file resolution varies drastically with the selected material parameters and observed phenomenon of interest (PSW vs DSW vs ejected ballistic particles) leading to output files anywhere from 30 to 100+ GB in total size and simulation duration between 45 minutes and three days. Since each parameter sweep involves upwards of 5 tests and we conducted around 30 different sweeps, we do not attempt to publicly host these data. Instead, we provide *LIGGGHTS* input files that can run our simulations ([168]) along with the restart files used to run them at ([169]). Any reader could download these files recreate our results using the latest version of *LIGGGHTS*. While it is not feasible to host all data required to perform the force and overlap tracking of the wavefront, the data required to recreate the results of sec. 4.3.3 is much smaller, requiring only the initial and final output files. The output files from these tests are provided along with the restart files at ([169]).

Readers should be aware that the data used in our analysis is not output at the same rate as the simulation time step rate. In general, we followed the same output guidance as given in

[177] and scaled the output rate using the relevant power law scaling from eq. 4.4 when material parameters are changed. For example, increasing E by 1000 would be a 10x increase in c_0 (since $c_0 \sim E^{1/3}$) requiring a 10x increase in output rate (and corresponding reduction in total simulation time) compared to [177] to capture the SW with sufficient resolution to identify the peak force in each virtual sensor (sec. 5.2.3). However to allow for particles with large ballistic velocities (the hardest particles) to return to the channel surface and also to observer slower phenomenon that we originally expected (sec. 4.3.5), we performed many instances of output adjustment, manually extending the simulation run time to allow more time for particles to reach the channel or increasing the initial high resolution output rate when our peak force detection algorithm required finer resolution. Readers can refer to the input files at ([168]) and review the input file corresponding to the case in question to determine specific details about data output rates, if needed.

4.2.6 Investigated parameters

SID requires a low gravity and vacuum environment. While we simulated SID under these conditions, the material properties of the grains in [177] were not representative of the lunar environment (those particles were an order of magnitude too large and had an elastic modulus closer to rubber than to regolith). We first endeavor to understand how SID will scale by characterizing the forces experienced by particles in our simulated SW wavefronts with respect to order of magnitude changes in density, mass, size, and impact velocity. We then use the results of these simulations to find the coefficient in eqn. 4.8 (discussed in sec. 4.2.3). We show the ranges of E, ρ, v_0, and R we consider in this analysis in Table 4.4.

Table 4.4: Investigated parameters. We give the range of parameter values for the physical quantities evaluated in our SID sensitivity analysis. We give the range of values used as input values in our simulations along with the relevant characteristic condition (with lunar particles referenced for material properties and similar low gravity DEM simulations referenced for simulated parameters). If there is a relevant reference we provide this here as well. Grain properties are given for lunar surface particles (regolith at depths of 0 to 40 cm).

Quantity	Symbol (units)	Range investigated	Characteristic	References
Elastic modulus	E (MPa)	5 - 5000	500	[177], [188]
Particle density	ρ (g/cc)	0.8 - 25	3	[15], [25], [189]
Particle radius	R (mm)	0.125 - 25	0.100	[14]
Piston velocity	v_0 (m/s)	1 - 360	n/a	n/a
Cohesion	k_c (kPa)	0 - 10	0.44 - 1.1	[15], Table 9.12
Friction	μ	0 - 1.8	0.87 - 1.28	[190]
Poison ratio	ν	0.15 - 0.45	0.2 - 0.4	[155], [125], [191]
Gravity	g (m/s^2)	0.1 - 9.8	1.625	
Dispersity	-	Mono-, bi-, tri- disperse	log-normal	[14]
Rolling Friction	μ_r	0 - 1.0	0.8	[77]
Rolling Damping	$\gamma_{d,r}$	0 - 2.5	2	[177], [78]
Restitution	e	0.35 - 0.85	0.5	[156], [157], [158]
Momentum	ρ_i/ρ	0.01 - 10	n/a	n/a

Our particle density range considers the softest and hardest (smallest/largest elastic modulus, respectively) particles found in low gravity settings throughout the solar system. The elastic modulus range encompasses the soft particles of [177] and approaches the hardness of lunar minerals ($E \sim 50$ GPa, for lunar plagioclase [188]). Particle sizes extend two orders of magnitude above the typical lunar particle size discussed in sec. 4.2.1 (R = 125 μm to 12.5 mm). In general we used v_0 between 1 and 10 m/s as in [177], though particles with larger E can undergo collisions at greater speeds since they have a larger c_m. We also conducted a simulation campaign in which both E and v_0 are increased to maintain v_0 at the same portion of c_m (discussed in sec. 4.2.2). We next conducted a sweep in E space using channels of higher and lower density particles (ρ = 5, 1.5 g/cm^3) as well as velocity sweeps in channels filled with particles at the extremes of densities we consider (ρ = 0.8, 25 g/cm^3). The last assembly we prepared was one

filled with lunar-like particles (R = 125 μm, ρ = 3 g/cm^3, E = 500 MPa) which was prepared using the method of sec. 4.2.1. Note that this channel requires a time step of 10^{-8} s which is less than 0.3% of the Hertz collision time. Knowing how the wavefront force changes with these four parameters, we can then evaluate how the force in the SWs compare to the overburden force (described in sec. 4.1.2) in order to understand how the depth of the balance point changes in different environments (e.g., channels with particles of varied material properties or different gravitational loadings, see sec. 4.3.2). We also consider one case of varying impactor momentum in which we vary the mass ratio between the virtual piston and channel grains (designated as ρ_i/ρ, where ρ_i is the density of the piston/impactor particles) analogous to the density ratio of impactor meteor and regolith.

Finally, we compare the predicted behavior of SID to that produced in our simulations (sec. 4.3.3). In addition to the parameters in eq. 4.8, we vary several other important physical parameters which are likely to influence SID (also summarized in Table 4.4). We consider how changes to the Poisson ratio, cohesion, friction, and gravity affect surface bulk dilation. While the lunar regolith size distribution is essentially a continuum, we have so far only considered finite size distributions. We evaluate how SID changes as we move away from a monodisperse assembly with tests conducted in channels filled with bi- and tri-disperse assemblies. Lastly, we also considered DEM simulation parameters (typically used to allow spherical particles to mimic real particle behavior) that are likely to influence simulated SID (rolling friction, rolling viscous damping and coefficient of restitution).

4.3 Results and Discussion

We review the results of our simulations and the outcome of fitting simulated forces to $F_{m,3D}$. We find that wavefront forces in the 3D channel scale the same way as forces in a 1D chain and SID trends are as expected (more SID for harder and smaller particles). We then propose a method for predicting SID based on $F_{m,3D}$ and compare predicted and simulated dilation. Both dilations scale the same way and are within an order of magnitude. Finally, we briefly revisit the outbursts capable of affecting SID after experiencing lower v_0 impacts.

4.3.1 3D SW wavefront forces

First, we assess our hypothesis that the forces in a 3D DSW wavefront follow the same scaling as those experienced by particles experiencing a 1D wavefront. We conducted parameter sweeps for each of the four variables in eq. 4.8 (E, R, ρ and v_0) while holding all other parameters constant. The parameter sweeps over E, ρ and v_0 use pre-filled channels while the particle size sweep (R) required newly filled channels. Once we obtain a single value for the magnitude of the force in the wavefront for each set of parameters within a campaign (as discussed in sec. 5.2.3), we perform a least squares fit to eq. 4.8 (see sec. 4.2.3). The results are presented for each parameter in Fig. 4.5 which shows excellent agreement with expected power law force scaling.

First we consider the upper right plot of Fig. 4.5 which shows F_m vs v_0. The majority of the cases we evaluated in this paper are velocity sweeps in channels with varied material parameters since they were the easiest to setup and quickest to run (see sec. 4.2.1). We first created DSW using varied v_0 in channels filled with particles with base parameters filled to loose, medium, and compact ϕ_0 (sec. 4.2.1). We then repeated this procedure, conducting sweeps through v_0 using

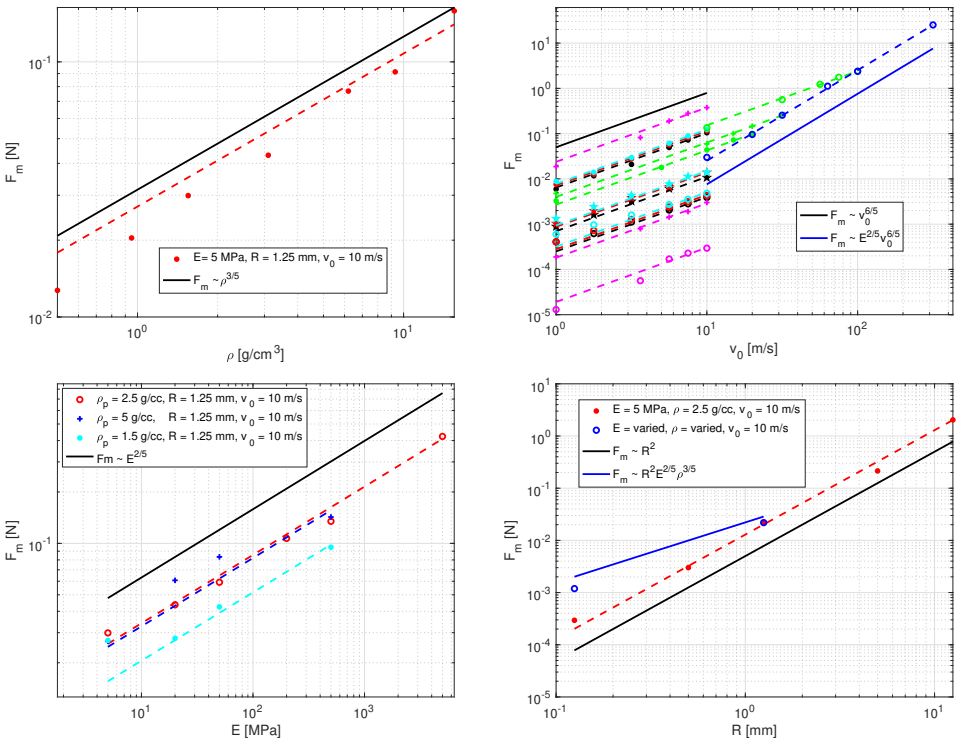


Figure 4.5: F_m **vs** ρ**,** v_0**,** E**, and** R **for varied cases.** Each plot shows average force in our 3D simulated waves vs the parameter of interest (v_0 in the upper right (UR), ρ in the upper left (UL), E in the lower left (LL) and R in the lower right (LR). The average simulated force for the given test is represented by a single data point and dashed lines are the corresponding fit. Solid lines show expected power law trends and are described in the legend of each individual plot. **UR)** Legend entries for the v_0 case are turned off due to over crowding. Star markers represent base case material properties, with cyan, red, and black colors corresponding to compact, medium, and loose ϕ_0, respectively. Solid markers are increased density (ρ = 25 g/cc) and open circles are reduced density (ρ = 0.8 g/cc) which (respectively) increase and decrease the force experienced by particles as a result of the wavefront. The pink trends correspond to varied particle sizes, where the lowest forces are experienced by the smallest particles (R = 125 μm, pink circles) and the highest forces experienced by the largest particles (R = 125 μm, pink plus sign). The green trends represent increasing modulus of elasticity, where E ranges from 5 (green filled circle) to 500 MPa (open green circle). The data and trend in blue represent a campaign of varied v_0 and E, with v_0 scaled to remain a constant portion of c_m. **LL)** We show the base case (with varied R) in red, with blue and cyan corresponding to slightly greater and smaller densities (respectively). **LR)** We included a comparison case of varied E and ρ in addition to R as the blue points which show how the force changes between the base particles and the lunar-like particles (ϕ_0 $\sim$58% and v_0 = 10 m/s. The upper solid blue line shows the expected scaling based on changing E, ρ and R while the lower solid black line shows the expected R^2 scaling. We did not calculate a fit for the comparison case given the paucity of points, but it is clear that the simulated results match the expected scaling.

channels with the largest (ρ = 25 g/cm^3) and smallest (ρ = 0.8 g/cm^3) densities filled to the same three ϕ_0. Increasing packing fraction increases F_m slightly (particles are closer together, have more neighbors, and thus experience greater forces as the wavefront passes by) while the increase or decrease in density leads to order of magnitude shifts in F_m. F_m increases as ρ increases since the impactor particle has more energy which must be absorbed by the spring potential as the DSW wavefront passes. As we continue velocity sweeps, we see that while increasing E the particles are 'harder' and therefore, for the same δ_m, the force imparted to the particles by the wavefront is larger (see eq. 4.1). All the aforementioned parameter sweeps in v_0 agree with expectation based on eq. 4.8, with the force scaling with velocity as $F_m \sim v_0^{6/5}$. Including a second scaling parameter in the form of varied v_0 and E (when the value of impact velocity is scaled to be a constant fraction of c_m, even with increasing E) also agrees with expectation, reproducing nicely the power law $F_m \sim v_0^{6/5} E^{2/5}$ from eq. 4.8. The good agreement with v_0 and $E + v_0$ scaling over varied values of R and ρ justifies our decision to conduct fewer cases when conducting parameter sweeps in ρ, R, and E.

The parameters besides v_0 also show good agreement with expectation and we now walk through the remainder of Fig. 4.5. In addition to the base case parameters where ρ = 2.5 g/cm^3, we performed E sweeps in channels of slightly lower (ρ = 1.5 g/cm^3) and higher (ρ = 5 g/cm^3) density (bottom left plot). In each case the expected $F_m \sim E^{2/5}$ power law is roughly recreated, with F_m increasing with increasing density. The fit is not quite as good in these cases (r^2 of 98.6 and 94.5 for lower and higher ρ, respectively) as in the v_0 parameter sweeps, but this is a result of difficulty in tracking the wavefront location near the surface, and we discuss this in Fig. 4.6. Fig. 4.6 shows the average force vs depth on a particle in the wavefront for particles of varied size. A single data point in any of the plots in Fig. 4.5 corresponds to the average force over all depths

corresponding to a single trend line in Fig. 4.6 (for example, F_m for R = 1.25 mm particles is an average over the green points). In some cases our method of tracking the wavefront by identifying the first peak in force that exceeds a threshold value misidentifies that actual peak for an earlier point, resulting in reduced forces across the sensors of a given depth. This most often happens near the surface (cyan and green) but can sometimes happen at middle depths too (orange). The noise acts to lower the average value of F_m reported and this issue is most evident in the E sweep case with varied ρ. The noise in the results could be resolved by designing a tracking method that applies a filter to the data to help reduce misidentified wavefront location, but we leave that as an item for future work. Despite the noise leading to the outliers in the F_m vs E plot of Fig. 4.5, the fit with eq. 4.8 is still quite good ($r^2 > 0.94$, tab. 4.5) and aligns with the expected power law, $F_m \sim E^{2/5}$.

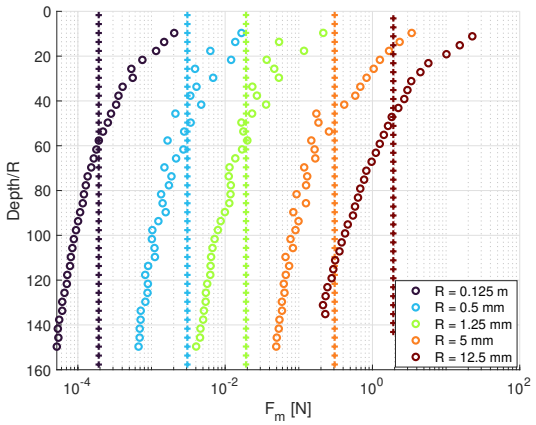


Figure 4.6: **Normalized depth (z/R) vs average F_m.** We show average simulated force at each depth for 3D assemblies of varied size, where the color legend corresponds to particle diameter. Channels are filled to the medium ϕ_0 level of packing and are listed in Table 4.3. Simulated forces are circles and the plus sign markers show the computed force via eq. 4.9 for the given particle radius, base material parameters, and in input velocity of v_0 = 10 m/s.

Assuming that agreement with expectation would extend to the ρ and R sweeps, we performed only a single campaign of tests in each channel. Fig. 4.5 shows that we still follow the

expected scaling: the upper left plot for F_m vs ρ follows $F_m \sim \rho^{3/5}$ and the bottom right plot for F_m vs R follows $F_m \sim R^2$. We included one final case that compares the lunar-like particles to the base particles in the F_m vs R. Though we do not construct a fit, the two points demonstrate that varying E, ρ, and R together still produces the expected scaling. Having confirmed visually that the power law scaling we expected is produced, we assemble all results for the fit to parameter C_1 in eq. 4.8 as well as the goodness of fit (assessed by calculating the r^2 correlation coefficient of the fit) in Table 4.5.

Table 4.5: Goodness of fit. Scaling parameter and r^2 for the cases inspected. Particles are set using the base parameters and then one or more of the components are varied corresponding to the values in fig. 4.5. For the case with varied v_0 and varied E, E values are found in Table 4.1. Packing fraction corresponds to compact (C), medium (M), and loose (L) ϕ_0.

E (MPa)	ρ (g/cc)	R (mm)	v_0 (m/s)	ϕ_0	C_1 x10^3	r^2 (%)
varied	1.5	1.25	10	C	8.1	98.6
varied	2.5	1.25	10	C	9.8	99.2
varied	5	1.25	10	C	6.2	94.5
5	2.5	varied	10	M	7.7	99.7
5	varied	1.25	10	C	17.8	97.6
5	2.5	1.25	varied	L	4.2	99.5
5	2.5	1.25	varied	M	5.3	99.9
5	2.5	1.25	varied	C	5.7	99.4
5	25	1.25	varied	L	9.8	99.8
5	25	1.25	varied	M	10.9	99.9
5	25	1.25	varied	C	11.8	99.9
5	0.8	1.25	varied	L	3.0	99.9
5	0.8	1.25	varied	M	3.3	99.8
5	0.8	1.25	varied	C	3.8	99.9
varied	2.5	1.25	varied	C	9.6	99.9
5	2.5	10	varied	M	9.0	99.1
5	2.5	1	varied	M	1.7	99.3
5	2.5	0.125	varied	M	11.5	97.1
20	2.5	1.25	varied	C	9.3	99.8
50	2.5	1.25	varied	C	9.6	99.9
500	2.5	1.25	varied	C	9.2	99.8

The values found for C_1 are of approximately the same magnitude and fall in the range of 0.002 to 0.012. While the noise in some of the our data likely adds to the variability in C_1, it is also likely that the scaling coefficient itself is dependent on the particle properties of the assembly. This makes sense; adjusting E, ρ, R influences the final geometry of the random packing (as particles become harder and softer they settle into slightly different positions) and it is the specific geometry of a 3D assembly that leads to nonlinear force propagation ([172]). From this work it is not possible to determine the dependence of C_1 on material parameters and impact velocity. However, determining the exact relationship of C_1 to our four parameters of interest is outside the scope of this work - here we seek to determine only if the scaling of F_m in a 3D assembly is similar to that in a 1D assembly. Indeed, we have shown that F_m follows (to a numerical constant) the same scaling as in a 1D chain (eq. 4.7). For the remainder of this paper we will use eq. 4.9 as the forces within a 3D DSW wavefront to assess how SID will scale to granular assemblies with different properties in different environments. We take C_1 to be the mean of the fit values from Table 4.5 with $r^2 > 0.99$ which results in mean and deviation of C_1 of about 7.3x10^{-3} and 3.2x10^{-3}.

$$F_m = C_1 k \left(\frac{5}{4} m v_0^2 k^{-1}\right)^{3/5} \tag{4.9}$$

$$C_1 = (7.3 \pm 3.2) \times 10^{-3}$$

While we do proceed using eq. 4.9, Fig. 4.6 highlights that the result of our efforts in this paper are a prediction of the *average* peak force a particle experiences within the wavefront of a DSW in a 3D randomly packed *shallow* channel. Specifically, in a channel that is approximately

80 particle diameters tall. In Fig. 4.6 we plot the predicted force at each depth using eq. 4.9 alongside the simulated values. The predicted force from eq. 4.9 does not vary with depth while the simulated forces are higher near the surface but decrease towards the floor. Particles experiencing wave propagation near the grain-vacuum interface are known to behave anomalously (mentioned in sec. 4.2.3) and our method of fitting to the averaged force is influenced by the higher than expected magnitudes at the surface. Our fit parameter C_1 therefore will lead eq. 4.9 to underpredict F_m in shorter channels and over predict F_m in taller channels. Nevertheless, the uniformity of the scaling is evident from fig. 4.5 and eq. 4.9 can be used in an initial characterization of the scalability of SID.

Before turning to a scaling analysis, we want emphasize that the overlap experienced by particles in the wavefront (δ_m) is dominant in determining the extent of SID. Figure 4.7 mirrors Fig. 4.5, with each plot showing the initial and maximum overlap experienced in the channel as the result of varying a single parameter (E, R, ρ, and v_0). The maximum force in the channel from Fig. 4.6 echoes δ_m, with larger δ_m in the wavefront near the surface than near the floor. As we will see in the following sections, the cases that exhibit the largest magnitude of SID correspond to those cases in Fig. 4.7 that have the largest difference between δ_0 and δ_m (i.e., large E and v_0, smaller ρ and R), with particle size and elastic modulus having the largest influence. Notably, we show that all cases of varied E with v_0 held to a constant portion of c_m produces the same δ_m. Particles with larger E have smaller δ_0 (they are 'harder') and therefore the largest difference between δ_0 and δ_m and exhibit the largest SID response. Fig. 4.7 also highlights a few instances of the non-physical initial states we mentioned earlier in sec. 4.2.1. The dashed lines in the plots represent the analytical prediction of δ_0 using eq. 4.3 and our simulated channels agree with this prediction nicely for the majority of cases. However, in the particle channels with varied density,

the distributions corresponding to the two largest ρ (orange and dark red) have lower ϕ_0 than would be expected, but this is a result of filling the channel with one set of properties and then adjusting the particle's material properties after a static packing is achieved. It is possible that this kind of discrepancy is responsible for some of the variability in C_1, but we assume in this case that any influence of a 'too loose' or 'too compact' channel is mitigated by our averaging procedure. That assumption can be reevaluated by others; here we will just keep this in mind when considering resultant SID.

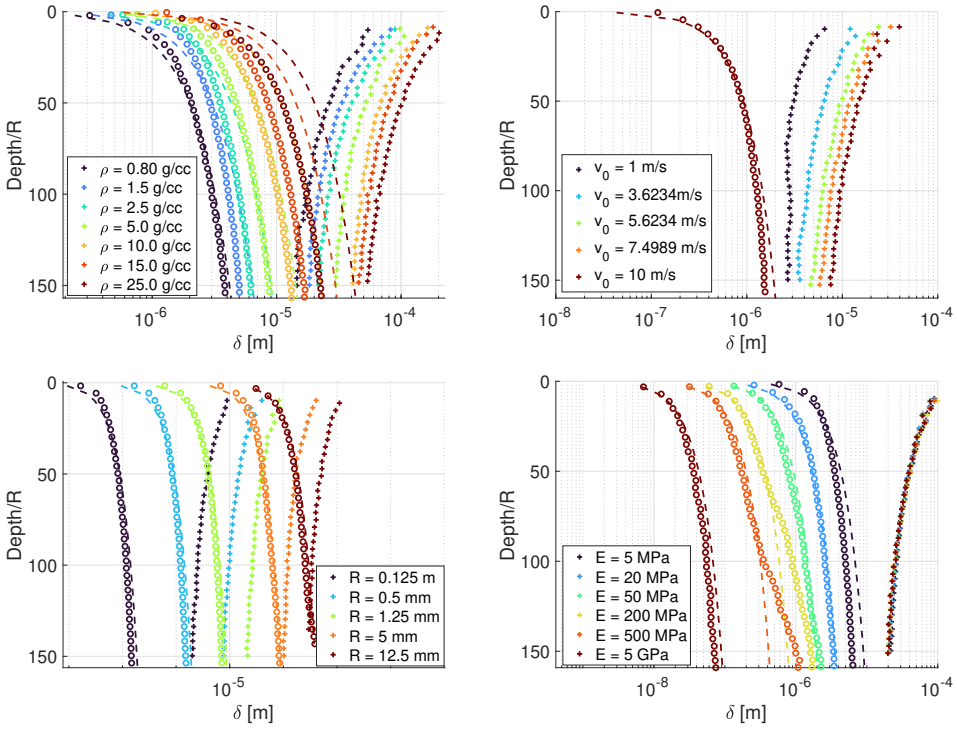


Figure 4.7: **Normalized depth vs δ for varied ρ, v_0, E, and R.** Depth z on the y axis is normalized by particle radius (R) with overlap (δ) on the x axis. We show the trends for varied v_0 in the upper right (UR), ρ in the upper left (UL), E in the lower left (LL) and R in the lower right (LR). Each color legend gives the value to the respective varied parameter with circles, pluses, and dashes corresponding to δ_0, δ_m, and the prediction from eq. 4.2 (respectively). δ_m and δ_0 'pinch' together as depth increases and SID only occurs when there is a substantial difference between the two.

Finally, we briefly confirm the validity of our results by considering produced wave speeds,

maximum impact velocities of particles within a DSW wavefront, and the total overlap experienced by particles during a simulation. We provide the results of this assessment in Table 4.6. The second column grouping compares computed initial PSW and DSW speeds to the calculated wave speed. As we can see, c_0 increases with E and g, slightly increases with R given our fixed channel height (discussed in sec. 4.2.2), but decreases with ρ as expected. The third grouping of columns considers the maximum collision speed of particles in the wavefront compared to L_e, the speed above which the Hertz law can become invalid for describing the contact. In all cases we exceed L_e, but the problem is the worst with low E or large ρ. As we move towards particles that look more like lunar surface grains, v_m is only a few times larger than L_e. The last grouping of columns compares the maximum overlap which should not exceed $1\%R$. Similar to the impact velocity considerations, the cases that are closest to (or exceed) the limit are those with the softest particles. Again, as particles become more lunar-like (larger E), δ_m is a smaller portion of R and the lunar-like particles are less than 0.3% of R. As we saw in Table 4.1, as E increases, ϕ_0 becomes smaller since grains inter-penetrate less (thanks to larger k) which means that, for the same velocity, a channel filled with larger E particles experiences smaller δ_m in the wavefront. We are confident that our simulations model the real effects of impacts propagating along the floor at a fixed speed given the adherence of $F_{m,3D}$ to expected power law trends as well as the validation performed in [177]. That v_m does slightly exceed L_e indicates that particles undergo high stresses which may lead to some fracturing, though we believe this would generate microporosity that is insignificant compared to the reduction in thermal inertia that is achievable through SID. Evaluating grain scale stresses vs fracture limits is an important consideration for future work. Of particular interest is the effect of friction on our results. Sound speed increased with friction as expected, but note that v_m and δ_m are larger for $\mu = 0$ than any of the other friction

cases, while, for cases with $\mu > 0$, these quantities increase with μ as we'd expect.

Table 4.6: Validity details. We assess the physical realness of our results be comparing wave speed, particle speed within the wavefront (v_m) and the maximum overlap particles in the wavefront experience. In all cases the base material parameters are used and the varied parameter of interest is changed to the value given in the table for each test. Impact velocity is set to v_0 = 10 m/s in all cases, except for the velocity sweep which used based material parameters and the velocity listed. ϕ_0 for each of the cases can be found in across Tables 4.1, 4.2 and 4.3, with most being filled to compact fillings except the particle size sweep and lunar-like particles which are filled to a medium ϕ_0. The measured (simulated) values are taken as an average of a given quantity over the entire channel depth - we disregard the deviations in this table and consider the mean values to get a sense of the scaling. For each test we calculate sound speed c_0 (as the average over a depth of $160R$ using eq. 4.4) and compare it to the generated PSW wave speed (c_w) and the DSW speed (c_p) which are found using the same procedure as in [177]. We note that c_w and c_p can fall below the v_0 impact speed since they average over the entire depth of the channel and v_0 is only maintained by impacts along the floor. We do not give a c_p for the E = 5 GPa case as the measurement contained too much noise, caused by outbursts (sec. 4.3.5). We also collect v_m and compare it to the elastic limit (L_e, also found in Tables 4.1, 4.2 and 4.3). Finally, we collect the maximum overlap experienced over the course of each test and compare it to particle radius. The case of E = 50 GPa was included as a reference and was not simulated, hence the 'n/a' for simulated quantities.

Param.	Value (units)	c_0 (m/s)	c_w (m/s)	c_p (m/s)	v_m (mm/s)	L_e (mm/s)	v_m/L_e	δ_m (μm)	$\frac{\delta_m}{R}$ (%)	F_m (mN)
E	5 (MPa)	8.65	14.00	10.84	181.2	9.43	19.2	16.94	1.36	14.00
E	50 (MPa)	18.64	30.42	22.93	213.08	29.81	7.1	6.57	0.53	59.20
E	500 (MPa)	40.17	65.82	55.82	341.49	94.28	3.6	2.55	0.20	134.61
E	5 (GPa)	86.54	136.18	-	501.7	298.14	1.7	0.82	0.07	422.83
E	50 (GPa)	186.44	n/a	n/a	n/a	942.81	n/a	n/a	n/a	n/a
ρ	0.8 (g/cc)	12.65	20.53	15.98	175.7	16.7	10.5	10.19	0.82	12.72
ρ	2.5 (g/cc)	8.65	13.57	10.60	183.5	9.43	19.5	17.17	1.37	29.91
ρ	10 (g/cc)	5.45	8.13	8.30	159.2	4.7	33.9	26.56	2.12	76.82
ρ	25 (g/cc)	4.02	6.19	7.40	85.5	3.0	28.5	28.77	2.30	158.47
R	125 (μm)	5.83	15.40	8.76	154.92	9.43	16.4	1.41	1.13	0.268
R	0.5 (mm)	7.35	15.22	9.04	110.60	9.43	11.7	4.62	0.92	2.73
R	1.25 (mm)	8.65	15.71	9.58	149.14	9.43	15.8	15.65	1.25	27.58
R	5 (mm)	10.78	14.75	9.87	118.05	9.43	12.5	80.20	1.60	375.69
R	12.5 (mm)	12.56	13.79	10.14	52.03	9.43	5.5	225.58	1.80	2,371.3
v_0	1 (m/s)	7.35	9.60	7.06	24.5	9.43	2.6	2.11	0.17	0.18
v_0	3.6 (m/s)	7.35	11.03	7.41	29.15	9.43	3.1	2.04	0.16	0.75
v_0	5.6 (m/s)	7.35	12.06	8.28	60.38	9.43	6.4	3.09	0.25	1.43
v_0	7.5 (m/s)	7.35	12.91	8.64	91.52	9.43	9.7	4.08	0.33	1.89
v_0	10 (m/s)	7.35	13.61	9.23	129.81	9.43	13.8	5.13	0.41	3.00
g	0.1 (m/s^2)	5.44	13.25	9.95	186.0	9.43	19.7	16.64	1.33	23.45
g	1.625 (m/s^2)	8.65	14.00	10.84	181.2	9.43	19.2	16.94	1.36	14.00
g	3.721 (m/s^2)	9.93	14.36	11.45	171.8	9.43	18.2	17.15	1.37	14.02
g	9.8 (m/s^2)	11.68	15.18	12.34	152.3	9.43	16.2	19.08	1.53	14.51
k_c	0 (kPa)	8.65	14.01	10.85	180.72	9.43	19.2	16.85	1.35	14.00
k_c	0.1 (kPa)	8.65	14.00	10.86	180.63	9.43	19.2	16.85	1.35	14.00
k_c	1 (kPa)	8.65	14.00	10.84	181.17	9.43	19.2	16.94	1.36	14.00
k_c	10 (kPa)	8.65	13.84	10.82	183.88	9.43	19.5	17.72	1.42	14.12
μ	0	8.65	10.83	9.13	249.49	9.43	26.46	24.81	1.98	17.66
μ	0.4	8.65	11.57	9.49	159.31	9.43	16.89	15.89	1.27	11.58
μ	1	8.65	14.00	10.84	181.2	9.43	19.22	16.94	1.36	14.00
μ	1.8	8.65	15.03	11.70	211.0	9.43	22.38	18.96	1.52	16.94
E,ρ,R	Lunar-like	25.47	81.10	38.9	380.43	86.07	4.4	0.34	0.27	1.19

4.3.2 Scaling

Now that we have determined an expression for F_m in a 3D DSW wavefront (eq. 4.9), we can compare the force particles experience as a result of the wave to that of the gravitational overburden. SID occurs when particles at depth z experience a vertical force from a SW wavefront that exceeds that overburden force (eq. 4.2) at that same depth (net upward force leads to lofting, with particles setting down to a looser state after a ballistic trajectory [177]). We posit that particles experience this upward force thanks to the near surface curvature of the SW and that this effect remains active until the SW front curvature becomes small (θ = 1°, sec. 4.2.3). We assume that we can take the vertical force felt by particles in our DSW wavefront to be $\mu \times sin(1^\circ)F_{m,3D}$, with the friction coefficient added as though it modifies the vertical force the same way that the μ modifies the normal force to find tangential force in our model (eq. 4.1). It is not entirely clear how to include cohesion in this force balance and, though we've so far assumed that the cohesion in our simulation has a negligible impact on SID, this may not be the case when cohesion is higher than we've considered in this work (a particle-particle cohesive energy density of 1 kPa, which means bulk cohesion would be substantially less than on the Moon). For now we assume there is a differential cohesive force felt in the normal direction which modifies $F_{m,3D}$. The modification is a result of changing cohesive contact area ($A_c = -\frac{\pi}{4}(\delta^2 - 4R\delta)$ for monodisperse particles) with the leading edge of the particle experiencing the initial overlap δ_0 and the trailing edge experiencing the maximum overlap δ_m. We will rearrange the Hertz spring force as we did in sec. 4.2.3 to write $\delta_m = (F_{m,3D}/k)^{2/3}$ and δ_0 is calculated from eqn. 4.2. We designate these contributions as $F_{c,m}$ and $F_{c,0}$ corresponding to the cohesive force as a result of the maximum and initial overlaps. Of course, this is not actually the case since the wavefront

is not a single particle in width, but we use this approximation for this initial characterization. Finally, we can write eq. 4.10, which balances gravitational forces with SW wavefront forces. We can then solve for z_{loft} over a range of varied parameters. We emphasize that this equation only predicts the last depth to which particles of a given size will experience a lifting force as a result of the SW, it cannot be integrated to get a an exact idea of the velocity profile of grains in the subsurface. Forces on grains where there is substantial curvature (i.e, closer to the surface than z_{loft}) are underpredicted by our small angle assumption. This could be resolved in future works by replacing the 1° assumption with an equation that predicts the angle. We also note that, since δ_0 is also a function of depth (and is now included thanks to the cohesion terms), z_{loft} must be solved numerically and we do so using *MATLAB*.

$$\mu \times sin(1^{\circ}) \times (F_{m,3D} - (F_{c,m} - F_{c,0})) = \left(\phi(\pi R^2) z_{loft} + \frac{4}{3}\pi R^3\right) \rho_p g \tag{4.10}$$

Having assembled eq. 4.10, we can now inspect how loft depth changes with varied material parameters or gravitational loading. We solve for z_{loft} for all particles larger than 1 micron (the smallest size particle in the lunar surface regolith profile from Fig. 4.2) for varied E, ρ, k_c, and g using a fixed v_0 = 10 m/s (other parameters are set to the base material parameters, as usual). The solution is illustrated in Fig. 4.8 which shows how the z_{loft} that is a result of SID changes with elastic modulus. While the plot is shown in log-log space to emphasize the order of magnitude increase in z_{loft} for increasing E, note that the trend of z_{loft} with R is actually quite linear. The spring contribution from eq. 4.10 dominates compared to the cohesive contribution.

The x-crossing that is apparent in the plot corresponds to R_c, the critical particle radius above which no particles loft (the solution for z_{loft} becomes negative and cannot be plotted in log-log space). Moving leftward along a given trend line from R_c indicates the depth to which particles of a certain radius (assuming a monodisperse assembly) can acquire vertical velocity. As the trends approach the y-axis (from the right) they are increasing, though slowly compared to the increases that come from varying E. We consider z_{loft} for particles of a given radius to be the loft depth (z_{LD}), that is, the deepest that SID can excavate the particles in each of our channels.

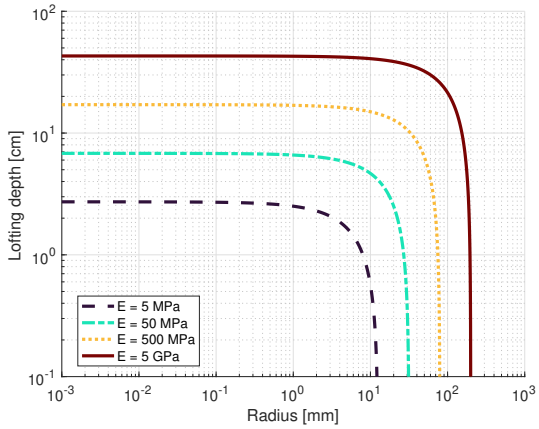


Figure 4.8: **Loft depth vs maximum lofted particle size.** We show the lofting depth on the y axis which is the depth to which particles of a given size (radius, R, on the x axis) can attain an upwards velocity as the result of the SW wavefront.

Since plots for the other parameters are similar (varying a parameter shifts the trends, but the shape is the same) we summarize the results of this same procedure to find R_c and z_{LD} across the parameter space in table 4.7. We see that R_c and z_{LD} move together and increase for harder particles as expected (larger E and μ, smaller R). As the effective weight of the particles is reduced (i.e, decreased ρ or g) the lofting parameters also increase and we should expect to see that gravity is the dominant factor. A one order of magnitude reduction in gravity (from the lunar 1.625 m/s^2 to 0.1 m/s^2) produces the same order of magnitude increase in z_{LD} as a three order

of magnitude increase in E (from 5 MPa to 5 GPa). We expect to see very little effect on SID lofting from cohesion since the spring force is dominant in comparison. There is no change in R_c even for the largest k_c considered, though large k_c does begin to decrease z_{LD} for smaller particles. Cohesion plays a larger role in small particle dynamics ([185]) so it makes sense that smaller particles see a large effect with increasing k_c, albeit still quite small in comparison to contributions from the other parameters. Note that our method of applying friction means that SID cannot occur for frictionless particles. In the next section we compare these predictions to our simulation results.

4.3.3 Dilation

We now evaluate the SID demonstrated in our simulations. We examine the density change at depth for a range of different parameters and also measure the channel height change as a result of the DSW as was done in [177]. As described in sec. 4.2.6, we ran numerous tests while varying material parameters E, R, and ρ as well as several important simulation parameters. To compare results across the parameter space, we evaluate the SID induced using a fixed v_0 of 10 m/s (except for one case, where we increased v_0 to be a constant portion of c_m as E increased). It is easiest to see how SID behaves by examining both the channel height change (Fig. 4.9) affected by the DSW wave as well as how bulk density changes with depth (Fig. 4.10). We consider both plots together as we step through the different parameters evaluated.

First, Fig. 4.9 shows channel height change (Δz), with each subplot showing the percent change in channel height (normalized by R) from an initial $160R$ height vs different material and simulation parameters. The single black line drawn across each subplot indicates the reference

Table 4.7: Loft depth (z_{LD}) and critical radius (R_c) for various material parameters and gravity environments. We solved eq. 4.10 for R in the case where z_{loft} = 0 (the critical radius, R_c, which is the size of the largest particles that could be lofted by SID) and for R = 1.25 mm (the size of the particles we used in our simulations for the cases in the table) to find lofting depth, z_{LD}, the depth to which we expect particles to obtain a vertical velocity (and therefore show bulk density changes). The parameters (besides the listed varied parameter) are set to the base properties, with v_0 = 10 m/s and ϕ_0 = 62%.

Varied Parameter	Value (units)	z_{LD} (cm)	R_c (mm)
E	5 (MPa)	2.42	12.6
E	50 (MPa)	6.53	31.7
E	500 (MPa)	16.83	79.5
E	5 (GPa)	42.69	199.8
E	50 (GPa)	107.64	501.8
ρ	0.8 (g/cc)	3.97	19.9
ρ	3 (g/cc)	2.23	11.7
ρ	10 (g/cc)	1.28	7.2
ρ	25 (g/cc)	0.81	5.0
g	0.1 (m/s^2)	43.74	204.8
g	1.625 (m/s^2)	2.69	12.6
g	3.721 (m/s^2)	1.18	5.5
g	9.8 (m/s^2)	0.45	2.1
k_c	0 (kPa)	2.44	12.6
k_c	0.1 (kPa)	2.44	12.6
k_c	1 (kPa)	2.42	12.6
k_c	10 (kPa)	2.25	12.6
μ	0	n/a	n/a
μ	0.4	0.81	5.0
μ	1	2.42	12.6
μ	1.8	4.58	22.7

value which is the percent height change using the base parameters from [177]. The percent height change axis is scaled similarly for most plots (in the range of -1 to 4 %), but note the larger ranges shown for the first three plots for elastic modulus, particle size, and gravity which have the largest influence on SID (as we predicted in sec. 4.3.2). Second, Fig. 4.10 shows bulk density change ($\%\Delta\rho$) on the x axis for a given depth on the y axis, where the depth is normalized by particle radius. We also include the expected density change from [1] as we initially described

in Fig. 4.1 for reference. There seem to be two categories of SID: 1. a gentle dilation where $\%\Delta\rho$ decreases by 'peeling away' near the surface, and 2. a more energetic rearrangement of particles where the entire channel lifts up and sets back down in a looser state following the DSW. For example, SID in cases where material properties are close to the base material parameters (softer particles, like in Fig. 4.10G) show gentle dilation while the hardest particles in the largest E cases (like those in Fig. 4.10A) demonstrate an energetic rearrangement of the channel, with the grains falling back down to approximately the same (heavily dilated, $\%\Delta\rho \sim -15\%$) post SW packing fraction. Energetic rearrangement occurs when the impulse of a contact with the fixed v_0 traveling through the floor particles (discussed in sec. 4.2.1) delivers sufficient energy to lift entire depth of the channel at the contact point. The DSW wavefront effectively blasts the floor from below across the length of the channel. In the case of energetic rearrangement, we should find that the predicted z_{LD} is larger than the channel height. We again emphasize that the depth range of our channels represents a small portion of the actual LCS depth. On the other hand, when dilation is gentler, forces on the particles give a gradual upward lift that increases density while leaving the initial arrangement of grains mostly intact. Gentle dilation is a result of floor impacts inducing a DSW which sees the force from particle collisions in the wavefront exceeding overburden forces only at some intermediate depth between the surface and the channel floor. For these cases in which our channel height encompasses the predicted z_{LD}, we can collect a simulated lofting depth by evaluating the 'peel away' depth in Fig. 4.10. We will compare and contrast expected and predicted z_{LD} shortly, but first we discuss qualitatively how SID is affected by changes to our investigated parameters.

Considering the elastic modulus, Fig. 4.9A for varied E shows both the case for v_0 held at a constant portion of c_m as E is varied (cyan) and the case where E is increased while v_0 is constant

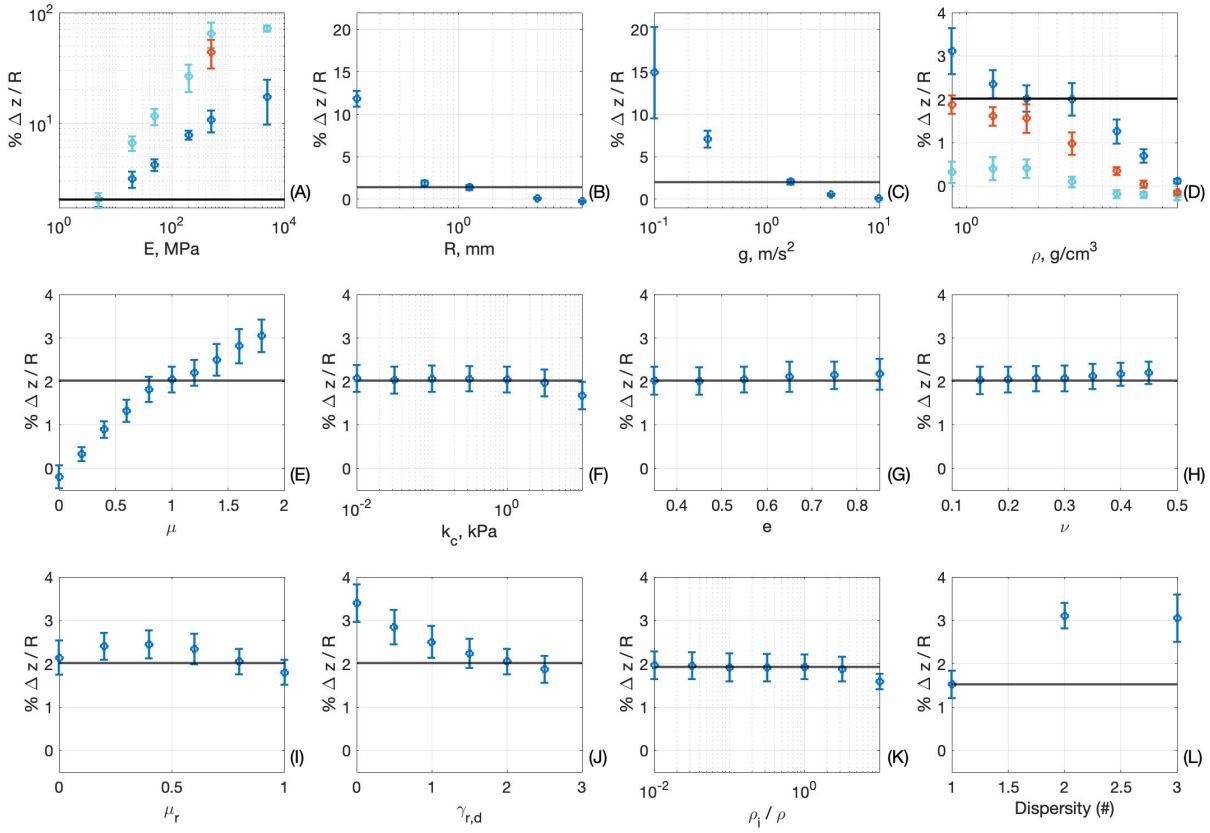


Figure 4.9: **Lofted height vs varied material parameters.** We show normalized percent change in bed height vs a sweep of various material and simulation parameters. The plots correspond to varied **A)** elastic modulus, **B)** radius, **C)** gravity, **D)** density, **E)** sliding friction , **F)** cohesion, **G)** restitution, **H)** Poisson's ratio, **I)** rolling friction **J)** rolling viscous damping **K)** momentum ratio and **L)** dispersity. In each case, the solid black line corresponds to percent bed height change of the reference case (generally a channel filled to 20 cm with particles of R = 1.25 mm, E = 5 MPa, and ρ = 2.5 g/cc. **A)** Shows the case for constant v_0 = 10 m/s in blue and the case where v_0 is a constant portion of c_m in cyan. The single red point corresponds to the lunar-like particles (ρ = 3 g/cc, R = 125 μm) with v_0 = 10 m/s. **D)** Shows bed height change vs particle density for various levels of ϕ_0, with the compact, medium, and loose channels corresponding to blue, red, and cyan markers (respectively). **F)** The data point for $k_c = 0$ was left off given the log nature of the x-axis, but showed the same bed height change as in cases with cohesion ($\Delta z \sim 2\%$).

at 10 m/s (blue). When v_0 is a constant portion of c_m, the two highest E used (500 MPa, 5Gpa) produce approximately the same amount of dilation (nearly 100%). This is a result of energetic rearrangement. Table 4.7 shows that the predicted lofting depth (42 or 107 cm corresponding

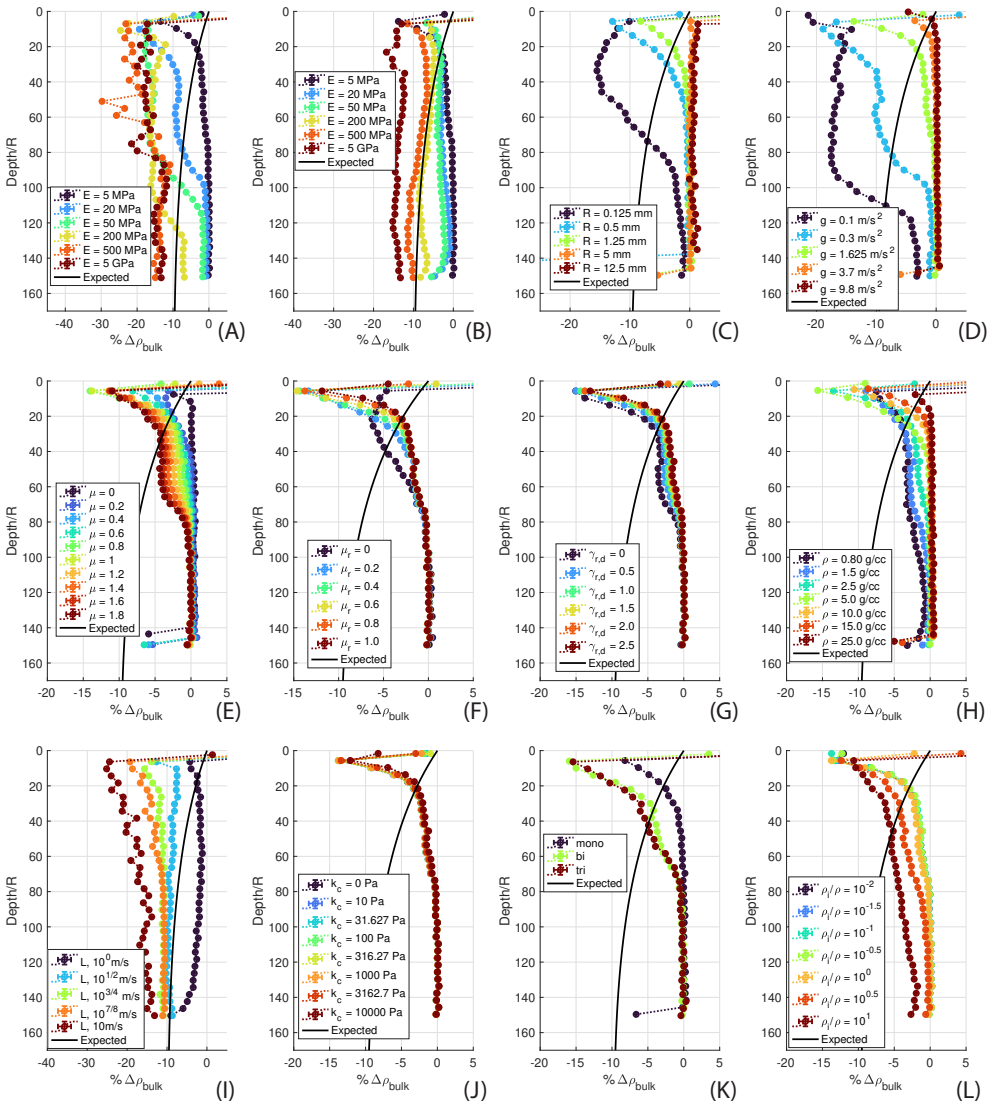


Figure 4.10: **Dilation vs depth.** We show normalized depth (z/R) on the y axis vs percent bulk volume change on the x axis for cases of varying material parameters. Each plot has its own color legend corresponding to the varied parameter of interest. In all but the first case, only a single parameter is varied, with other parameters set to the base case from sec. 4.2.1 and v_0 = 10 m/s. The first plot shows the case of varied E and varied v_0, with v_0 held to the same portion ($\sim$20%) of c_m. The plots correspond to varied **A)** elastic modulus and impact velocity, **B)** elastic modulus, **C)** R, **D)** gravity, **E)** sliding friction, **F)** rolling friction, **G)** rolling viscous damping, **H)** density, **I)** velocity (with lunar-like particles), **J)** cohesion energy density, **K)** dispersity and **L)** impactor momentum ratio. Note that the case for restitution was left off as it is essentially identical to the plot for ν. In all cases the solid black line is the depth-normalized LCS expected bulk dilation from Fig. 4.1.

to the two largest E) exceeds the channel depth we consider (20 cm for this channel). With the lofting depth exceeded, all particles in the channel are lofted as a result of the DSW, and they undergo a similar grain rearrangement, falling to the floor as though they were poured at approximately the same fast rate ('energetic rearrangement'). In other words, there is only so much material in the channel, it is all lofted in any case where z_{loft} exceeds channel height, and the grains are rearranged to a similarly loose state. Smaller E demonstrate the gentler SID response. Fig. 4.10B shows the dilation vs depth for when E is increase but v_0 is held constant. While v_0 = 10 m/s is an impact velocity below c_0 in a channel filled of particles with E = 5 GPa (see Table 4.6), we still see substantial dilation to the same levels induced by v_0 that increase as c_m increases with larger E. This type of dilation (when v_0 driving the DSW through the floor is much less than c_0) causes 'outbursts', where no DSW wavefront is front is formed, but surface dilation still occurs as a result of the impact from below. We will describe outbursts further in sec. 4.3.5. We point to Fig. 4.11 to see how SID increases with increasing E. The image transitions from gentle to energetic SID as E increases (upper three frames) while the last frame shows the result of one of the most 'energetic' cases considered, where increased E coupled with decreased R rearranges the entire channel.

Turning to our other parameters of interest, increases in particle size decrease SID while smaller particles have an easier time lofting as predicted in sec. 4.3.2. In fact, for the largest particles (R = 12.5 mm), SID is nonexistent as can be seen in both Fig. 4.9B and Fig. 4.10C. This agrees with sec. 4.3.2: we predicted a critical radius of R_c = 12.6 mm (see Table 4.7) for particles with E = 5 MPa (as is the case in Fig. 4.9B). We would expect almost no lofting, with any lofting that did occur taking place only at the surface. Note that the channel with R = 12.5 mm particles had a slightly lower ϕ_0 (it originally settled to a looser ϕ_0, see sec. 4.2.1) which

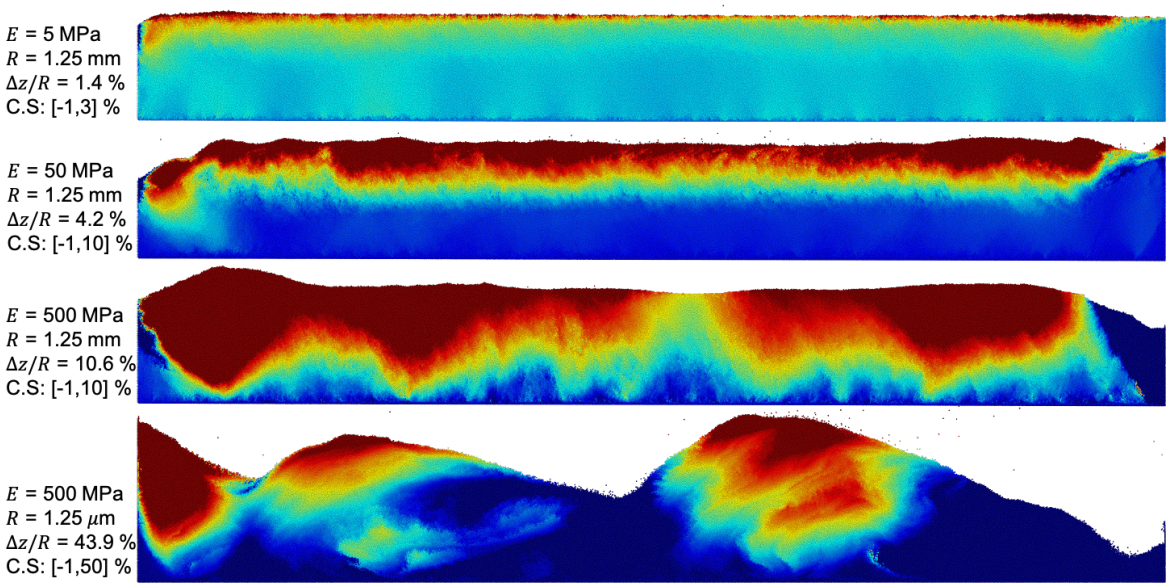


Figure 4.11: **Dilated channels.** Particles are colored by the percent height change with respect to their initial (pre-SW) state. We use *OVITO* to create the image and normalize particle vertical displacement by R, then find the percent difference compared to the initial $160R$ channel height. We show the color scale (C.S) for each frame in a box immediately to the left of the post-SW channel, where darkest blue is represented by the lower value and dark red by the higher value. Each box also includes details on the particle E and R as will as the percent height change corresponding to Fig. 4.9. Frames 1-3 show channels with the base parameters and increasing E while frame 4 shows the case corresponding to the lunar-like particles. All channels experienced a piston impact at v_0 = 10 m/s. Dilation is 'gentler' for the softer particle channels which corresponds to uniform (and smaller in magnitude) dilation that is present in shallow surface depths. As the particles become harder the SID is 'stronger' and most of the particles in the channel are thrown up and set back down in looser heaps.

would reduce SID some (less than 1% change between different ϕ_0 cases at ρ = 2.5 g/cc in Fig. 4.9D). However, particle size is dominant in setting the magnitude of SID (as compared to ϕ_0) as evidenced by the 15% Δz/R for R = 125 μm in Fig. 4.9B.

Our predictions regarding gravity also agree with simulations. We predicted that a single order of magnitude decrease in gravity would show the same magnitude of SID as a three order of magnitude increase in E and this is very nearly the case (compare percent height change in Figs. 4.9C and 4.9A along with frames Figs. 4.10B and 4.10D). We confirm that particle hardness (as

seen by the Hertz spring constant k, which depends on E and R) and gravity are the main factors in determining if and when SID occurs.

Friction, density, and dispersity had a noticeable, though smaller, influence on SID. As predicted in Table 4.7 and confirmed in Figs. 4.9D and 4.10H, there is a small increase in SID with decreasing density and the heaviest particles are unable to loft. This makes sense; F_m depends on R^2 but the mass depends on R^3, so increasing particle size leads to a faster increase in the overburden force than the wavefront force. Increasing friction could lead to a doubling in channel height change in the cases we considered (see Fig. 4.9E and Fig. 4.10E) and can be seen to slightly increase z_{LD}. Notably, the case with $\mu = 0$ showed compaction, not dilation. Even in a channel with a large initial packing fraction ($\phi_0 \sim 62\%$), frictionless spheres cannot exhibit SID. Recall that, when friction is nonzero, the channel can also dilate if the initial packing fraction is low enough ($< 55\%$ for the monodisperse assembly in [177]), though we did not investigate the crossover threshold in this work. Despite the bi- and tri- disperse channels filling to looser packing fractions than the monodisperse case, they saw nearly a doubling in channel height change (Fig. 4.9L) and the dilation vs depth profile for each are quite similar (Fig. 4.10K).

The remainder of the cases investigated either had a small (rolling viscous damping) or negligible affect on the expression of SID. Increased $\gamma_{r,d}$ decreased the channel height change slightly (Fig. 4.9J), but had little affect on the dilation vs depth profile in 4.10G. Rolling friction very slightly increased the extent of SID (see Fig. 4.9I around $\mu_r = 0.4$), but mostly is responsible for giving our simulated bulk volume change vs depth its characteristic shape (Fig. 4.10F). Note how for the case of $\mu_r = 0$ the percent change in bulk density curve is missing the characteristic near surface peak in $\%\Delta\rho$ that 'gentle SID' plots show. The last case we can compare to the sec. 4.3.2 prediction is cohesion, for which we predicted there should be very little influence

on SID. In agreement, Fig. 4.9F shows that there was only a small decrease in the amount of channel height change experienced when particles experienced the largest k_c and the same is seen in Fig. 4.10J. Note that ν and e had essentially no effect on SID (check out either Figs. 4.9G or 4.9H). It makes sense that ν has very little impact on SID since it only enters into eqn. 4.10 by way of the equivalent properties (elastic modulus and radius) and was varied over a small range compared to the other parameters. It is interesting that e has no effect on SID because reducing e generally leads to greater energy dissipation [178]. SID's lack of dependence on e suggests that the magnitude of the impact driven from below is the dominant factor in determining surface lofting compared to the plasticity of the grains within the vacuum-exposed channel.

Increasing impactor momentum by way of increasing the density in the piston particles had very little influence on SID, see Fig. 4.9K. This makes sense; we only altered the mass of piston particles (and thus the PSW), not those in the floor (in the DSW). Note that while the amount of total dilation seen by way of channel height change did not change when impactor momentum was varied in this way, the dilation vs depth in Fig. 4.10L shows a slightly different bulk density change vs depth profile. However, in calculating the total dilation, the increased dilation at deeper levels was canceled out by reduced dilation at the surface. When momentum was increased by increasing v_0 SID increases (Fig. 4.4) since the floor particles sustaining v_0 (and therefore the DSW, and ultimately surface dilation) do experience this increase. We note that increasing impactor velocity slightly increased the length of the PSW (BL) region while increasing momentum has a larger influence (see Figs. 4.12, B and C in sec. 4.3.4). Changing momentum by way of varying mass has a greater effect on the distance over which energy can be transmitted.

Finally, we examined a single case of how SID changed when changing both elastic mod-

ulus and particle size. We show the results of a velocity sweep in a channel filled with lunar-like particles in Fig. 4.10I. Dilation for this channel (particles of E = 500 MPa, which is still one to two orders of magnitude below lunar particles and R = 125 μm, which is on the same order as surface regolith) easily exceeds the level expected, with impacts as low as v_0 $\sim$3 m/s inducing $\%\Delta\rho$ greater than 10% over nearly the entire channel depth. Compared to most of the other cases inspected, the particles in the lunar-like channel (shown in the bottom frame of Fig. 4.11) end up with highly uneven surface. The heaping behavior of this channel demonstrates that smaller particles more easily achieve 'energetic SID'. However, characterizing the dynamics of this behavior requires analysis beyond the single case inspected here. To deal with the uneven surface we restricted the height change measurement shown in Fig. 4.9I to the 'second heap' (average height change between 800R and 1000R in this 1600R channel) which, at around 40% $\Delta z/R$ (0.87 cm height change in a 2 cm channel!), exceeds that of a channel containing particles with the same E but larger R. We point out that the substantial dilation in these cases occurred at low piston speed, when v_0 is less than c_0. As we saw previously for other channels with larger E, the SID induced with the lunar-like particle channel was was the result of outbursts as opposed to a DSW wavefront and will be discussed further in sec. 4.3.5.

Comparison to prediction

We now evaluate how our predictions compare to simulated results for a subset of parameters in Table 4.7. We manually collect the lofting depth from our simulations (z_{SD}, 'simulated depth') for the cases in Fig. 4.10 that show gentle SID and have z_{SD} that is identifiable as the depth which $\%\Delta\rho$ exceeds 1% dilated. These gentle SID cases should correspond to predictions

from Table 4.7 that have z_{LD} less than channel height. We present the results in Table 4.8 and compare z_{SD} to z_{LD} and Δz representative measures of SID.

Table 4.8: Prediction vs comparison table. We find z_{SD} for cases that exhibit gentle SID. We manually identified the depth at which $\%\Delta\rho$ exceeds 1% by examining the different frames of Fig. 4.10, multiplying the depth identified as z_{SD} by the particle R for the corresponding case to recover dimensional units. A value of 0 indicates no dilation or compaction and a value of n/a means that there was no identifiable z_{SD} (e.g., the lofting depth greater than the channel depth). We then compare z_{SD}, z_{LD}, and bed height change.

Varied Param.	Value (units)	v_p (m/s)	Δz (cm)	z_{LD} (cm)	z_{SD} (cm)
E	5 (MPa)	10.0	0.410	2.42	9.1
E, v_0	20 (MPa)	20.0	1.319	10.55	12.8
E, v_0	50 (MPa)	31.623	2.313	26.82	15.3
E	20 (MPa)	10.0	0.624	4.44	n/a
E	50 (MPa)	10.0	0.838	6.53	n/a
E	200 (MPa)	10.0	1.564	11.58	n/a
E	500 (MPa)	10.0	2.128	16.83	n/a
ρ	0.8 (g/cc)	10.0	0.624	3.97	n/a
ρ	2.5 (g/cc)	10.0	0.404	2.42	9.1
ρ	10.0 (g/cc)	10.0	0.252	1.28	5.6
ρ	25 (g/cc)	10.0	0.023	0.81	1.95
g	1.625 (m/s^2)	10.0	0.410	2.69	9.1
g	3.721 (m/s^2)	10.0	0.109	1.18	5.7
g	9.8 (m/s^2)	10.0	0.023	0.45	1.5
k_c	0 (kPa)	10.0	0.411	2.44	9.1
k_c	1 (kPa)	10.0	0.410	2.44	9.1
k_c	10 (kPa)	10.0	0.335	2.25	9.1
μ	0.2	10.0	0.065	0.27	5.7
μ	0.6	10.0	0.264	1.35	8.7
μ	1	10.0	0.410	2.42	9.1
μ	1.4	10.0	0.499	3.50	13.2
μ	1.8	10.0	0.610	4.58	15.7
R	125 (μm)	10.0	0.237	2.66	n/a
R	0.5 (mm)	10.0	0.150	2.58	14.6
R	1.25 (mm)	10.0	0.277	2.42	9.1
R	5 (mm)	10.0	0.057	1.62	0.7
R	12.5 (mm)	10.0	-0.482	0.002	0.0

The expected trends hold true for all three quantities across all parameters; SID increases

with increasing E, increasing v_0, increasing μ, decreasing R, decreasing ρ, and decreasing g. Cohesion has a negligible influence on SID except for all but the largest k_c we considered, which still has only a small influence on SID compared to the other parameters. The total height change of the channel is typically an order of magnitude less than the lofting depth. Comparing z_{LD} to z_{SD}, our predicted lofting depth is, in most cases, several factors smaller (3-4$\times$) than our simulated lofting depth. The discrepancy indicates that our method of solving eqn. 4.10 under-predicts SID, but the closeness of the results and the agreement across multiple orders of magnitude in parameter space given the numerous assumptions we made is a good indicator that we have correctly identified the underlying mechanism. Others investigating SID could improve the accuracy of prediction in the future by relaxing our assumptions.

There are a few outlier cases to discuss. For the cases considering varied E, we would expect the loft depth in channels of increased E and increased v_0 to quickly exceed the depth of the channel, and they do. However, we also see that when v_0 is fixed at 10 m/s and E is increased, the simulated loft depth exceeded the channel height while the predicted loft depth only increased slightly (from 0.4 cm to 2.1 cm). These larger E beds with smaller velocities were dilated by the outbursts we mentioned previously, as opposed to a DSW wavefront. Our prediction of the lofting depth is therefore only valid when it is a sustained uniform wavefront causing dilation. We will briefly discuss the behavior of outbursts in sec. 4.3.5, but future work should consider methods to predict when outbursts occur and to what extent they influence surface dilation. Nonetheless, our results have repeatedly shown that dilation increases as the particles in our channels become more lunar-like which is strong evidence that SID plays a significant role in the formation of LCS. While the method we have developed for predicting SID via loft depth includes numerous assumptions (that a fixed channel height is representative of any channel height, that there is a

single scaling constant C_1 which is not influenced by material parameters itself, that the particles experience $\delta_0 = 0$, that the influence of cohesion is simply the difference between forces generated between contact areas set by δ_m and δ_0) and does not take into account the outbursts that form at large E but low v_0, it can still be used to determine the order of magnitude of the expected SID response, keeping in mind that it is a lower bound.

4.3.4 Blast loading

One thing to be verified is that the blast loading region (region over which the PSW is active) in our simulations behaved as anticipated. We expect the DSW wavefront to overtake the PSW close to the piston initiation site (in terms of lateral distance) to allow for a sufficient length of channel over which to measure the DSW that is unimpeded by the end wall. We found good agreement with expectation and the BL zone varied little with particle properties. Increasing momentum of the impact (larger v_0 or larger ρ_i) had the largest influence on altering BL. Fig. 4.12 visualizes the BL region vs the DSW region by tracking δ_m over the lateral extent of the channels. Channels in which only non-momentum affecting parameters were varied (frames A (ρ), D (g) and E (R)) show little variation in BL. There was a slight increase in BL with increasing density, and decreasing particle size, though mostly the BL region sizes were in the range of 100 to 200 particle diameters. Channels experiencing increased impact momentum (frame B (v_0) and C (ρ_i/ρ)) showed larger changes in BL (as is expected from blast loading tests in a 1D chain [183]), with the increased piston density case having the largest effect. The last image in frame F shows the case of varied E but fixed v_0 = 10 m/s, which demonstrates further evidence of outbursts. Since we track δ_m as the maximum overlap experienced (not just in the wavefront), the

cases with large E are dominated by the δ within the outbursts and no longer resemble the usual PSW decay to driven SW pattern. The BL identified for the two cases of largest E and fixed v_0 are left out of the averaging when computing the mean and deviation BL for each channel (summarized in Table 4.9). In all cases (besides those affected by outbursts), the BL zone is shorter than our $1600R$ channel length, confirming the validity of our channel size scaling choice (see sec. 4.2.1 and 4.2.4).

Table 4.9: Blast loading table. We give the mean ($\overline{BL}$) and deviation (σBL) length of the BL zone for various cases. Each entry represents several tests conducted with the base particle properties and with the indicated test parameter varied over the range from sec. 4.2.6. Units are given in non dimensional channel length (L/R). The velocity sweep case for v_0 comes from a channel with R = 0.5 mm particles. The table is sorted by smallest deviation to largest.

Test Parameter	$\overline{BL}$ (L/R)	σBL (L/R)
e	208.0	0
ν	208.0	0
k_c	208.0	0
E, v_0	197.3	8.3
$\gamma_{r,d}$	200.7	13.0
g	208.8	18.4
μ_r	200.0	19.6
μ	224.0	21.5
E	199.3	63.0
ρ	278.9	68.6
R	300.8	75.2
v_0	232	112.3
ρ_i/ρ	367.0	293.8

4.3.5 Outbursts

We have seen two distinct categories of granular wave behavior that occur when externally driving impacts through a channel using our perfect floor impact method (sec 4.2.1). When v_0 is much larger than the c_0, a single DSW wavefront propagates through the channel, but when v_0

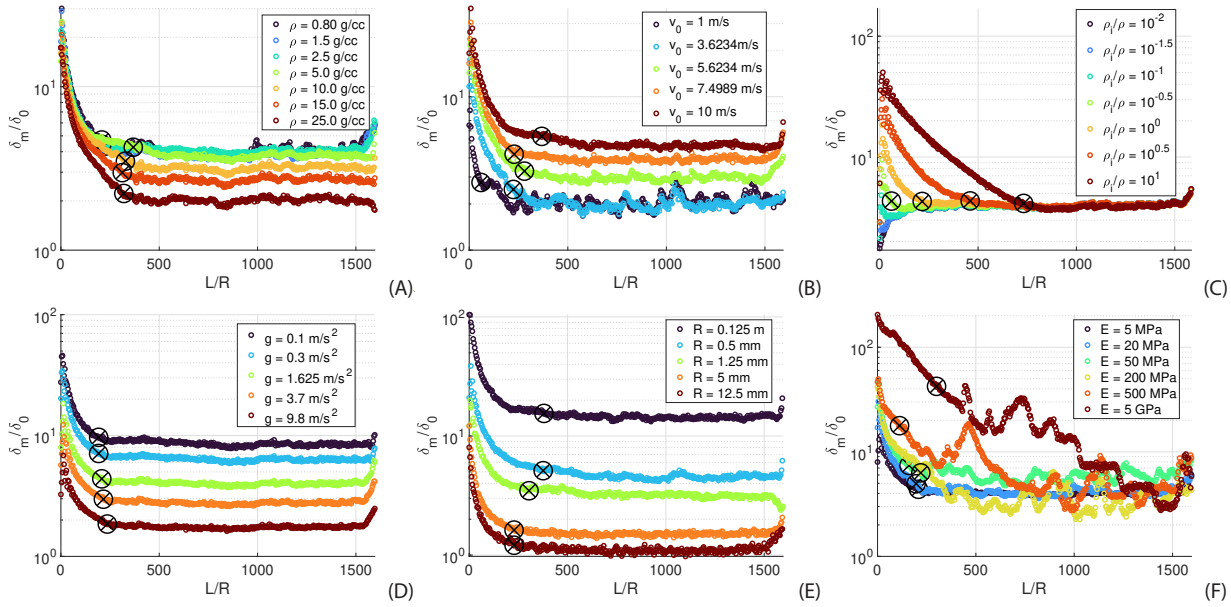


Figure 4.12: **Blast loading via δ_m.** We show the normalized maximum overlap in the SW wavefront (δ_m/δ_0) vs channel length normalized by particle size (L/R) for varied properties. The color legends refer to varied **A)** density, **B)** impact speed, **C)** momentum ratio, **D)** gravity, **E)** radius and **F)** E (for the case with constant v_0 = 10 m/s). When applicable, we indicate the end of the BL zone (end of the PSW, the dissipative region near the left wall) as the black crossed circle. We find the end of the BL zone using the procedure outlined in sec. 4.2.4 (when δ_m/δ_0 becomes close to the average steady value in the DSW). The material parameters have very little effect to the end of the BL zone, which is generally between 200 and 300 R. Changes to momentum have more of an effect on the lateral extent of the BL zone, with increased velocity (frame B) increasing the length of the region somewhat, while changes to momentum by tuning the density of the impactor particles (frame C) could either extend the region quite a bit (out to 800R) or result in no identifiable BL zone for low impactor density. Because we track δ_m as the maximum δ experienced by a particle (as opposed to just the δ experienced by the initial wavefront), plot 6 for varied E is capturing effects from outbursts when E is large.

is near or less than c_0 the result of the driven impacts are periodic outbursts of energy. We show a transition between the two categories in Fig. 4.13, where the bottom images show a clearly driven SW wavefront while the top images show the outbursts as they pulse slowly behind the broken apart wavefront of the PSW. Outbursts are capable of exciting SID on the same order of magnitude as the DSW when particles are harder (through greater E) or smaller (lower R) as we saw in sec. 4.3.3. Understanding differences in the dynamics of the two mechanisms

requires further study since here we have primarily studied the influence of varied v_0 within the driving layer. The properties of the driving layer itself are largely neglected since those particles are 'frozen' in our simulations. Since the floor layer is made up of a sheet of randomly packed particles, we believe the periodic nature of the outbursts to be correlated with the geometry of the packing. We suspect that outbursts occur when the geometry of particles is such that a force chain responsible for propagating the velocity through the floor makes a nearly normal (anti-gravity direction) impact with the channel particles. Then, when E is larger or R is low (or both), the energy delivered through this impulse is sufficiently large to propagate to and dilate grains at the surface. While both the DSW and outbursts induce SID, they rely on an external driver from below. In our simulations this is accomplished with the frozen-in floor velocity, which constantly adds energy through floor impacts to drive the SW (or outbursts). This raises questions about the possible external driver of the surface dilating wave which we leave for the Discussion.

4.3.6 Discussion

There were two main objectives in this paper; 1) develop a method to determine the maximum force $F_{m,3D}$ felt by a particle within a driven 3D SW wavefront and 2) determine how the magnitude of SID changes as that maximum force is scaled to granular mediums with different material properties. Remarkably, the results of our scaling analysis in sec. 4.3.1 and Fig. 4.5 show that $F_{m,3D}$ follows the same power laws that would be experienced by a particle within the SW of a 1D granular chain (eq. 4.7), only at a reduced magnitude. We have seen that there is some variability in the exact value of the scaling parameter C_1 in this work (C_1 = 1-10$\times 10^{-3}$), which may indicate that C_1 itself depends on material properties. Furthermore, $F_{m,3D}$ does not

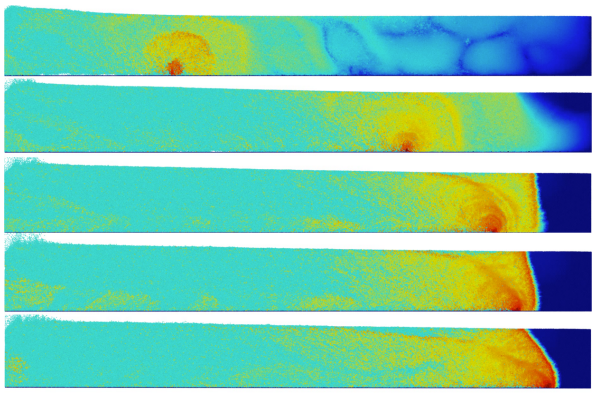


Figure 4.13: **Outburst vs DSW.** Particles are colored by their force magnitude experienced relative to a reference force of 10^{-6} N. The color legend is the same for all frames with the darkest blue at -2 (meaning the force a dark blue particle experiences is 2 orders of magnitude below the reference force) and the darkest red at 7. The images show the same channel (base parameters, but with E set to 500 MPa). From Table 4.6, the sound speed for this channel is c_0 = 40.2 m/s. Each frame represents a different value of the initial piston velocity used, with the frames corresponding to (from top to bottom) a v_0 of **1)** 10 m/s, **2)** 31.6 m/s, **3)** 56.3 m/s, **4)** 74.9 m/s and **5)** 100 m/s (which is approximately 20% of c_m). Frames are taken at different (arbitrary) times and and are selected so that the leading wavefronts (approximate PSW in frames 1 and 2 vs DSW in the others) are aligned. In frames 3-5, the energy delivered through any impact with the driven floor (including glancing oblique impacts) are large enough that a single well defined SW wavefront is created and maintained across the lateral extent of the channel. In frames 1 and 2 the conditions (geometrical arrangement of particles) that provide sufficiently large impact energies lead to occasional outbursts which, while they do not generate a coherent wavefront, are still able to dilate surface particles.

currently capture depth-dependent effects present in the SW wavefront, like the larger than expected forces near the surface (Fig. 4.6). Since our method does not capture these near surface effects, the value of C_1 we determined only applies to granular channels of $160R$ in height and would change for taller (smaller C_1) or shorter (larger C_1) channels. Keeping these limitations in mind, we then proceeded to use $F_{m,3D}$ in a scaling analysis of SID, assuming that the influence of the accuracy of C_1 on our prediction is negligible in comparison to the power law scaling of the material parameters in $F_{m,3D}$.

To address our second goal, we developed a method (equating the wavefront force to the overburden force) that quantifies how SID changes with different material parameters and in

different gravitational environments (eq. 4.10). Solving eq. 4.10 for z_{loft} = 0 gives the R of the largest particles which could be lofted by SID (R_c). Solving eq. 4.10 for z_{loft} given some R gives the depth to which we'd expect those particles to show a dilation response (z_{LD}) as a result of the driven SW wavefront. An increase or decrease in z_{LD} corresponds to increased or decreased SID. Fig. 4.10 shows that $\%\Delta z$ increases as z_{LD} increases, which also results in larger channel height changes ($\%\Delta z$), see Table 4.8. In this work we did not attempt to quantify the velocity profile of grains between the surface and z_{LD} and we are therefore unable to predict how their initial ballistic trajectories result in their rate of return to the surface (which controls $\%\Delta\rho$ and final channel height). Removing the small angle assumption and determining how to calculate the wavefront angle should enable this ability, which would be an interesting topic for future work. While our predicted loft depth was less than the simulated loft depth, they are still on the same order of magnitude and scale similarly in most cases. Our method of predicting SID can serve as a lower bound when predicting the extent of SID on low gravity and airless bodies. As expected, SID increases as particles become smaller and harder and SID decreases with increasing gravity. We are confident in the validity of our results given that particles within our channels that look closest to the lunar regolith undergo impact velocities within the SW that remain close to the elastic limit and do not experience overlaps that exceed 1% of R. There is, however, some disagreement with prediction in a few cases (low v_0 impacts into channels with large E), where the lofting depth increased faster than expected or channels dilated when we did not expect them to. This discrepancy is the result outbursts which roll along the floor slower than a sound wave, but periodically pulse to generate a high force concentration that induces surface dilation.

While we do expect the mechanisms studied here to produce the magnitude of dilation

needed to explain LCS when grains are lunar-like, the long range expression of SID in [177] was artificial. Thanks to the fixed v_0 propagating through the floor in [177] we could maintain DSW or outbursts in our simulation over any distance. The source driving floor impacts in our simulation is not real; it is the result of immovable particles (of the same size as the channel particles) that experience a v_0 which propagates without decay. However, we believe this situation does have a physical analog in the case of two distinct assemblies of grains in contact with one another, where the surface most layer experiences time variant energy injection from a buried layer. We consider an upper assembly (A1) of grains resting on top of and made up of grains that are several orders of magnitude smaller than a lower, buried, assembly of grains (A2). Recall that, in granular systems, energy decay is generally a function of particle number which is why smaller grains are more efficient impact absorbers (smaller grains occupy a smaller lateral extent than the same number of larger grains). Therefore, if our entire combined assembly experiences a uniform lateral impulse, energy would propagate over a much greater physical extent in the buried assembly (A2) made up of larger grains than in A1. If the particles in A2 are large enough compared to the particles in A1, then particles in A2 may experience sufficient velocities in its decaying SW to generate impacts on the A1 layer. Particle velocities in A2 would decrease as its SW decays which suggests that, if this situation were to actually occur, an initially driven SW in A1 (as a result of higher impact velocities) would uniformly dilate the surface over some finite distance until lower particle velocities as a result of decay in A2 lead to outbursts in A1. This hypothetical scenario agrees well with the pattern of the LCS halo, where the surface is strongly and uniformly dilated (possibly due to a driven SW) around the source crater (up to $\sim$100 crater radii), transitioning to a patchy region of intermittent reduced thermal inertia (possibly due to outbursts) that extends beyond the well defined halo ($>$100 crater radii, see images in [1] or [10]).

Moreover, our hypothetical scenario is based on the actual lunar near surface environment. LCS exist in the uniform micron sized grains of the regolith (a ∼10 m thick layer, [7]) which rests atop a layer of (probably) meter sized boulders known as the upper megaregolith ([32], [14], [27]). We encourage readers to consider the previous hypothetical scenario with A1 representing regolith and A2 the upper most portion of large scale ejecta in [9], Fig. 4.22. It is typically assumed that there is an abrupt transition between these two layers, as is the case in [155] when considering sound speed changes between the regolith and megaregolith. The scenario we considered here would support this sudden transition (as opposed to a gradient) between layers. This suggests that LCS are formed as a consequence of energy laterally propagated through a layer of large grains buried underneath a thick sheet of much smaller grains, and are a previously unconsidered process of surface modification as a result of impact induced seismicity on low-gravity airless-bodies.

While there is still more work to be done in understanding the precise impulse-induced lofting mechanism, the extent of dilation we observed in our simulations is strong evidence that such a mechanism is heavily involved in LCS generation. Dilation increases as particles become both smaller (lower R) and as they become harder (higher E). In the case we examined that is closest to lunar particles (E = 500 MPa, R = 125 μm, ρ = 3 g/cc), we see the channel is completely rearranged following the passage of either the SW wavefront or the floor vortex. Our lunar-like channel exhibited a bed height change that is equivalent to ∼44% dilation (Fig. 4.9, frame 1 for the percent height change and Fig 4.10 to see how the lunar-expected dilation is exceeded) with v_0 of only 10 m/s. We expect to see dilation responses in our channels greater than is predicted for LCS since we consider only a fraction of the actual LCS channel height and shorter channels experience faster wave speeds for the same impact speed ([177], [174]). Our channels are $160R$ in depth while an LCS channel exceeds $1000R$ (at least in terms of the depth extent of an LCS over

which dilation is observed, 40 cm). Moreover, the need for an external driver along a subsurface floor suggests that the entire regolith is the LCS channel, a channel height on the order of 10 m. Regardless of the actual lunar channel dimensions, the 2 cm bed height of our lunar-like particles is much less than the 40 cm LCS dilated region and so our results for low speed impacts that show dilation magnitudes exceeding expectation would be reduced as channel height increases. Future work should consider larger assemblies that more closely resemble the LCS scenario, both with taller channels, but also with lower packing fractions. The ϕ_0 we considered in this work (around 58%) are larger than what is found for lunar surface regolith (ϕ_0 of 47 - 54%, [15]). Lower ϕ_0 can be achieved by increasing the dispersity of the particle distribution as we saw in sec. 4.2.1 (the same filling procedure for mono, bi-, and tri-disperse channels produced ϕ_0 of 59, 54 and 52 %, respectively). Although these modifications we describe would reduce the magnitude of dilation as compared to the cases modeled in this work, we believe they provide further support for SID as the LCS formation mechanism. We saw energetic SID in this paper for lunar-like particles, but it is the more gentle SID that would be involved in LCS creation given the dearth of signs of surface modification within the LCS halo.

4.4 Conclusions

In this work we have formulated a method for determining the maximum force a single particle feels as a result of a SW wavefront driven by constant impact with a layer of particles from below. We validated this method by demonstrating that the forces experienced in 3D follow the same scaling laws as in a 1D chain. Using our force prediction, we then constructed a method for analytically characterizing the expression of SID, which showed good agreement with numerical

results (on the same order of magnitude). The primary results of our work are:

- the driven SW wavefront forces follow the same scaling power laws in 1D and 3D granular assemblies with a somewhat constant scaling between 1-10$\times 10^{-3}$ (for channels filled with monodisperse particles to a depth of $160R$)
- SID can be predicted using an equation to balance wavefront forces and gravitational overburden by assuming that the portion of the force from the wavefront felt in the vertical direction is reduced as a component of a small wavefront angle
- SID is primarily affected by the elastic modulus and particle size of grains as well as the gravitational environment:
  - SID increases the most with increasing E, decreasing R and decreasing g
  - SID increases some with decreasing ρ, increasing μ and increasing dispersity
  - SID sees little influence from k_c, e, ν, μ_r and $\gamma_{r,d}$
- Impacts at $v_0 < c_0$ generate periodic outbursts that cause similar magnitudes of surface dilation as those seen from a single, coherent, driven SW wavefront

We expect granular assemblies that have material properties similar to that of lunar surface regolith to produce the same level of bulk dilation as is expected in the production of Lunar Cold Spots. We suspect that, if involved in LCS formation, the driven SW and outbursts we describe here would be maintained in micron scale surface regolith by the decay energy of an impact propagating through an underlying layer of nearly continuous meter scale boulders within the upper megaregolith.

Chapter 5: Runout distance in buried boulder scale granular channels

This chapter has been written as a stand-alone paper to be submitted shortly after the culmination of this thesis. Please check for the electronic version to find any supplementary videos and updated code.

5.1 Introduction

Recent works ([177], ch. 4) have proposed that Lunar Cold Spots (LCS, [1]) form as the result of granular impulse propagation in the surface layer of regolith on the Moon. However, a mechanism that could generate a surface dilating wave remains unknown. Attempting to explain such a driver is the focus of this work. In [177] we saw that laterally propagating granular waves loft particles near a free surface when grains only experience low gravity loading (i.e., they are exposed to vacuum). Chapter 4 showed that the idealized work of [177] would scale appropriately to lunar surface regolith conditions to an extent such that the lofting mechanism (Solitary Wave Induced Dilation, SID) could induce the magnitude of bulk density change thought to occur during the creation of of low thermal inertia surface regolith halo surrounding young impact craters (LCS). However, as ch. 4 pointed out, the far traveling solitary wave (SW) of [177] was artificially driven, resulting in what we called a 'driven SW'. Long distance surface dilation was sustained in our prior works only as the result of continuous impacts that we drove along

the floor of the channel. We believe there to be an intuitive and straightforward solution to sustaining long range SID. We posit that a wave propagating in the regolith and able to affect surface dilation must be driven by impact energy decaying through subsurface topography, i.e. meter scale boulders of the upper megaregolith ([32]). As a result of contact between two distinct granular assemblies (regolith grains with orders of magnitude smaller sizes than the boulders making up a buried layer), the surface layer experiences impact energy decaying through the buried layer as 'impacts-from-below' that generates and maintains a driven SW (and thus induces SID) over long distances. We evaluate this hypothesis by measuring energy decay over a runout distance using Soft Sphere Discrete Element Method (SSDEM) simulations of piston impacts into granular channels. Before describing our simulation methodology, we briefly review LCS and the environment in which they exist, wave mechanics in granular media and elaborate on our hypothesis.

5.1.1 LCS and a possible progenitor

LCS are common features on the Moon, covering approximately 1% of the lunar surface [1]. LCS are apparent as a distal, relatively cold, halo surrounding source craters. The cold signature is a result of reduced thermal inertia regolith (compared to generally compacted regolith, [25]) which is hypothesized to be the result of bulk dilation extending 40 cm in depth over 10-100 crater radii (r_c) in distance (more than 2 km for the smallest LCS in [1]). The cold halo exists beyond the region of proximal visible ejecta and there is no sign of surface modification. Many LCS halos[1] show a uniform pattern of reduced thermal inertia surrounding a young crater, while

[1]As viewed at `https://quickmap.lroc.asu.edu/`. Turn on the filter under LRO Diviner > Nighttime Soil Temperature and zoom in.

others can experience segments that see an abrupt termination of the halo near the source (like on the right hand side of the LCS in [1], Fig. 4). LCS halos exhibit segments of arc where distinct rays extend much further than the average halo radius. In fact, even the more average segments of the halo see patchy regions of reduced thermal inertia beyond the edge of the coherent halo. As such, we emphasize that the radial extent of LCS halos (around 10-100r_c) reported in [1] and [6] are averages.

In [177] we proposed that a laterally propagating near-surface wave generated by the hemispherical release of impactor energy into the bulk ([9]) might induce dilation while active. We were able to observe this mechanism (SID) though our SSDEM simulations of lateral piston impact into a granular channel. We hypothesized SID to be at least involved in LCS formation and in ch. 4 confirmed the scaling behavior of induced dilation to support LCS levels of bulk volume change when the vacuum-exposed channel is made up of particles with material properties like lunar regolith [14]. However, ch. 4 also pointed out that the long range propagation observed in [177] was the result of artificially driven SW; SW that were sustained by impacts maintained through particles making up the bumpy floor of our channels. A surface layer made up of micron scale grains would require some external input energy to maintain a wavefront over LCS scale distances. However, as briefly introduced in ch. 4, we believe there is a simple natural mechanism that can act as near-surface SW driver. That mechanism is enabled by an abrupt transition between the uniform micron sized grains of surface regolith and the meter scale boulders of the megaregolith.

5.1.2 Surface regolith vs megaregolith

Lunar regolith is the layer of 100 μm sized grains [14] exposed to vacuum on the surface of the Moon. The regolith is fine-grained and highly uniform thanks to eons of impact gardening ([9], [12]) and is sometimes referred to as 'rock-free regolith', [1]. In the lunar highlands the regolith layer is around 15 m thick while in the mare, 5 m [7]. The layer below the surficial regolith is known as the megaregolith, a term that has been used to describe the upper lunar crust ranging in depths from 2 to 20 km (see [27] for a good overview of the near-surface structure). Here we are most interested in what [27] calls the 'upper megaregolith', the region just below the surficial regolith and extending to approximately 2 km in depth. The largest LCS crater diameters in [1] and [6] are less than 2 km; all current LCS surround simple craters (craters less than 15-20 km in size [9]). Since the maximum transient depth extent experienced during crater production is a fraction of the ultimate crater diameter ([192]), the energy released during LCS production must be entrained within the upper megaregolith. The floor of the surficial regolith (or the ceiling/beginnings of the upper megaregolith) is thought to be composed of meter scale boulders ([32], [14], [33], [26], [193]). [26] used data from the ground penetrating radar on the Yutu-2 rover to reveal stratification within a layer (12 to 24 m depth) of the upper megaregolith. This near-regolith layer contains an upper segment made of evenly distributed 0.2 to 1 m sized boulders, while the lower region is more heterogeneous, containing clumps of boulders up to 3 m in size interspersed with 1 m boulders and (what is probably) fine grained material. Regardless of the exact size of boulder, a sharp transition between the regolith and the underlying megaregolith is supported by both seismic analysis of the Moon ([155], [29], [31], [9]) and radar images from [26]. We suspect that, in the context of SID (sec. 5.1.1), the boulders of the upper megaregolith

are able supply the external driver along the floor of the regolith needed to support a long range surface dilating SW. Given the behavior of energy propagating in granular chains, we suspect that impactor energy decaying through a chain of boulder scale grains could both persist over LCS halo scale distances and also sustain particle-particle impact velocities large enough to drive surface dilating waves through the regolith.

5.1.3 Energy decay in granular chains

Typically, granular assemblies are not known for supporting long distance impulse propagation. Collisions between grains act to dissipate energy ([48], [178], [113]) and so, quite the opposite, granular assemblies are often employed to efficiently dissipate energy ([194], [115], [122], [181]). In those works the energy of the initial impulse typically decays over a length scale of less than 30 grains, but can be attenuated even more rapidly depending on the exact geometry of an assembly (1D or 2D, varied size and mass ratios). Additionally, depending on the amount of order (anti-randomness) in the assembly, wave decay can exhibit either exponential or power law decay in space and time ([195]). Works like [196] and [197] studied power law decay, while [198] characterized exponential decay. [198] used an assembly 1000 grains in length and saw an initial, fast period of energy decay follow by a slow regime of decay, where the amount of randomness in their system determined the transition point. With high randomness [198] saw their decay wave transition from the fast to the slow decay regime around 100 particle diameters, reaching a level less than 1% of the initial input energy around 700 grains. The channels we used in [177] are this same size (1600 particle radii, or 800 particles in length) and so they should be more the sufficient length to observe the energy decay in a 3D randomly packed granular channel,

at least for the fast decay region where particle velocities are higher. Ultimately we are concerned with the distance over which particle velocities within the decaying wave front are large enough to induce a driven surface wave (sec. 5.1.1). We suspect that, given the efficient energy dissipation of grains, particle velocities needed to sustain SID exist only for a relatively short portion (in time and non dimensional particle number space) of the total propagated distance.

Despite their efficient decimation of energy, grains are still, we feel, the likely driver of surface SID. The reason for our optimism lies in the nature of granular assemblies to exhibit behaviors that depend on a fixed number of grains rather than any material property or external disturbance. For example, the wavelength of a SW wavefront packet is typically 5 grains ([62], [181]), as is the width of a wall sheath region that exists when grains flow down a planar wall ([152]). Supposing that, in the megaregolith, energy were decaying in boulders of 1 m diameter, any impulse would decay around 30 m from the initiation site (much shorter than the average LCS halo size). However, this prediction assumes that the roughly 30 grain decay length mentioned in the prior paragraph is the same in a 1D chain as it is in a higher dimensional assembly. Sometimes the fixed grain number assumption holds true for all geometries ([199] - plane wave in 2D and 3D traveling at approximately the same speed as in a 1D chain), but other times it does not. For example, [150] saw in their 2D assembly that wave fronts extended to widths of 10 or even 50 particles (an order of magnitude larger than in 1D chain). There is no prior work we have found that has characterized granular wave decay distances and particle velocities in long, 3D randomly packed channels to the extent needed to assess our hypothesis.

5.1.4 Formation hypothesis

We hypothesize the Lunar Cold Spots are the result of impactor energy decaying in the upper megaregolith. Upon direct contact of an impactor with the upper megaregolith layer, a solitary wave is initiated in the meter scale boulders there and decays over a fixed number of grains. We suspect the energy of the impact to be dissipated within roughly the same order of magnitude grain number in the megaregolith as for the 100 micron sized regolith. In the upper megaregolith boulders, decay distance likely approaches length scales on the order of 2 km (the lower bound for the LCS halo radial extent). As a consequence of the abrupt transition between granular assemblies, grains making up the floor of the regolith layer experience the decay energy of the upper megaregolith SW as constant oblique impacts from below. These 'floor impacts' drive a SW in the surface regolith over long distances, affecting SID in its wake and generating the reduced bulk density of the LCS halo. Initially, while the energy in the decaying upper megaregolith SW is substantial, surface regolith is fluffed uniformly (leading to the coherent near crater halo, $<$100 radii distant). As energy decays and the randomness of the assemblies lead to impacts that less frequently trigger surface dilation (the 'outbursts' of ch. 4), leading to the patchy reduced low thermal inertia surfaces that exist beyond the average halo extent. We show a diagram of this scenario in Fig. 5.1. Given the large scales involved, microgravity, and vacuum needed to emulate the lunar surface, we employ a modeling approach to assess our hypothesis.

5.2 Methodology

We briefly review our chosen contact model, simulation method, and wave generation procedure. We also describe our method of applying overburden pressure to the channel and review

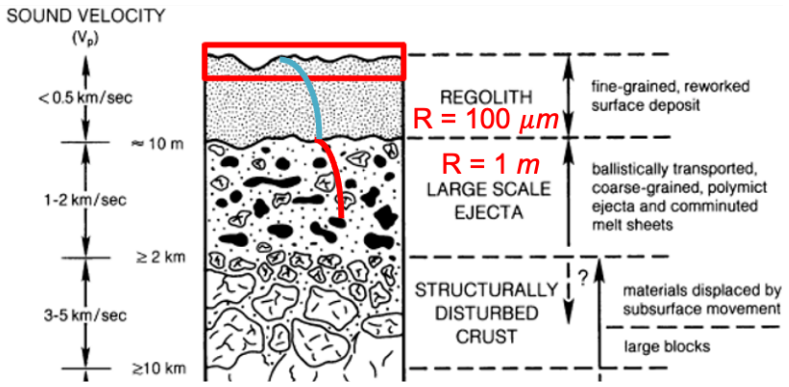


Figure 5.1: **Hypothesis diagram.** Diagram of our hypothesis laid over the near surface structure figure from [9]. Boxed in red is the approximate cold spot region. The megaregolith wave (red) propagating to the right (impact occurred off the page to the left) drives the surface dilating wave (blue).

our procedure for quantifying distance traveled by the SW before it terminates (runout distance). Lastly, we discuss the different parameters considered when evaluating runout.

5.2.1 Simulation overview

We generate a single SW within long, thin, granular channels following the method of [177] and ch. 4. The channel exists under a uniform downward gravitational field (g = 1.625 m/s^2). In addition to our previously considered vacuum-exposed case, the channels in this work can be pressurized using a large weighted plate (sec. 5.2.2). We model piston impacts into these channels using Soft Sphere Discrete Element Method (SSDEM) solver, *LIGGGHTS* [68]. Grains within the channels are modeled as Hertzian spheres subject to sliding friction, rolling friction and cohesion. We point the reader to the appendix of [177] for the full details of the implementation. The dominant force in our contact model is the spring force which is proportional to the Hertzian spring constant, $k = \frac{4}{3}E\sqrt{R}$, which depends on particle radius R and elastic modulus E. The contact force generated between particle-particle collisions follows a power law relationship with

the particle overlap, δ ($F = \frac{4}{3}k\delta^{3/2}$). δ is a key parameter in SSDEM simulations and should not exceed 1% of R. In this paper we are focused on understanding grain-size effects on granular wave decay. We scale the geometry of an initial 'base case' assembly (with R = 1.25 mm) corresponding to the size ratio of grains inspected (e.g., larger grains at R = 12.5 mm would see their channel dimensions scaled up 10x) which fixes the height and length of our channels in terms of particle radii ($160R$ vs $1600R$, respectively). We provide channel geometries for the range of R we consider in Table 5.1.

Table 5.1: Channel geometries. We show channel length (L) and height (H) for varied particle size (sorted by increasing radius, R). The scale number compares the chosen particle to the base case (R = 1.25 mm) from [177]. Channels contain around 560,000 particles depending on the exact packing fraction achieved.

R (mm)	L (m)	H (m)	Scale (#)
0.125	0.2	0.02	0.1
0.50	0.8	0.08	0.4
1.25	2	0.2	1
5	8	0.8	4
12.5	20	2	10
125	200	20	100
1,250	2000	200	1000

We consider two classes of particles in this work. First we consider soft particles (E = 5 MPa and ρ = 2.5 g/cc) which are the same as used in [177] and ch. 4. For the soft particle cases we can bypass channel preparation and re use the restart files prepared in ch. 4. Our focus will be mostly on the second class (hard particles with E = 50 GPa and ρ = 3 g/cc) which require new channels to be prepared. We used the density of surface grains and an elastic modulus that has been used for lunar plagioclase ([188]) as these particles are intended to be analogous to regolith. Hard particle channels are prepared using the same pouring approach as ch. 4, applying the scaling factor from Table 5.1 to the base case filling procedure. The only difference

in this work is that we fix the inserted particle velocity to 2 m/s instead of scaling the insertion velocity as in [177]. The fixed insertion velocity is a necessity of considering larger particles, as boulders (R = 1.25 m) traveling at 2 m/s and accelerating over the height of the channel (200 m) to the floor experienced too large impact velocities. Removing insertion velocity scaling leads to channels of a larger range of initial packing fraction ϕ_0, but we can constrain the effect on runout by characterizing decay in the variable ϕ_0 channels prepared in [177]. Note that we do not consider soft particles for the largest sizes ($R > 12.5$ mm) nor hard particles for the smallest sizes ($R < 1.25$ mm). Large particles with an elastic modulus on the order of MPa result in non physical overlap for particles at the bottom of the channel ($\delta_0 \sim R$) and small particles with GPa elastic modulus result in very small time step (time steps evaluated as 1% of the Hertz collision time, τ_c [177]). Table 5.2 summarizes the initial conditions and required time step (Δt) for our two classes of particles. Other required material and simulation parameters are set to the 'base' values of ch. 4, of which the most important to keep in mind are friction μ = 1.0, cohesion k_c = 1 kPa, restitution e = 0.55 and Poisson ratio ν = 0.2. After obtaining a 'settled channel' (forces from preparation are low enough, [177]), we initiate a wave and measure its decay. In some cases we inspect the influence of layer thickness by varying channel height (h_c) which uses the same settling procedure after deleting particles above some desired layer thickness. For the cases where we consider the sensitivity of decay to a certain material parameter (ρ, e, ν, μ), we adjust the parameter and allow for additional settling time (ch. 4) before initiating the wave.

We generate our SW using a virtual piston. Particles within a vertical sheet residing against one wall of the channel are given an initial velocity and act as a lateral impulse, generating a SW wavefront. We can easily scale the mass of particles within the piston by altering their density to some ratio of the channel particles (ρ_p/ρ) to consider effects on runout, analogous to an impactor

Table 5.2: Initial conditions and timestep considerations. We provide the achieved packing fraction and corresponding δ_0 for channels filled with the various particle sizes we consider when particles (ρ = 3 g/cm^3) are soft (E = 5 MPa) vs hard (E = 50 GPa). We also show the corresponding material sound speed c_m which informs the maximum v_0 that can be used following the approximate $0.2c_m$ limit used in [177] and ch. 4. We then use the maximum v_0 considered here (10 m/s for E = 5 MPa, 1 km/s for E = 50 GPA) to find the smallest collision time (τ_c, see [177]) our particles will undergo. Here we confirm that our SSDEM time step (Δt) is appropriate (it is less than 1% of collision time, [67]).

	E = 5 MPa, ρ = 2.5 g/cc, c_m = 43.03 m/s				E = 50 GPa, ρ = 3 g/cc, c_m = 4.30 km/s			
R (mm)	ϕ_0 (%)	δ_0 (μm)	Δt (s)	Δ t/τ_c (%)	ϕ_0 (%)	δ_0 (μm)	Δt (s)	Δt/τ_c (%)
0.125	58.61 ± 0.07	0.10	10^{-7}	0.43	-	-	-	-
0.50	58.87 ± 0.07	1.03	10^{-7}	1.07	-	-	-	-
1.25	58.84 ± 0.05	4.81	10^{-6}	0.43	56.50 ± 0.07	0.011	10^{-8}	0.43
5	58.26 ± 0.08	53.40	10^{-6}	1.07	$\pm$	-	-	-
12.5	56.29 ± 0.17	208.0	10^{-5}	0.43	53.44 ± 0.10	0.518	10^{-7}	0.43
125	-	-	-	-	56.76 ± 0.07	24.74	10^{-6}	0.43
1,250	-	-	-	-	58.73 ± 0.07	1069.2	10^{-5}	0.43

that is more or less dense than the impacted megaregolith layer. While we do implement the same rough floor as in [177] and ch. 4, there is no velocity driven through the rough floor and thus no driven SW (as discussed in ch. 4). Therefore, only the piston-generated SW emerges and it dissipates as it propagates. We are primarily interested in measuring the distance energy can propagate and the peak velocity (v_m) that particles within the decaying wave attain. We again limit piston velocities to 20% of the material sound speed (ch. 4). Simulations are run for 500,000 time steps, with output generated every 250 steps for the first 12,000 steps and every 2,000 steps thereafter.

5.2.2 Overburden pressure

In the cases where we inspect changes to behavior as a result of pressurization, we use a massive 'overburden plate' to simulate varying amounts of regolith resting atop our channels.

The overburden plate (inserted into *LIGGGHTS* as an STL object) is rectangular, with the same width and length of the channel, but half the height (h_{op} = 10 cm or 100 m in the R = 1.25 mm or 1.25 m cases, respectively). We place the plate into our simulated domain just above the surface of channel grains (which is mostly flat due to the filling procedure), with the bottom of the plate aligned with the maximum particle height (plus one particle radius). We then let the plate fall and compress the assembly under gravity. Once forces from the compression reach a steady level, we generate a SW as previously described. The plate can be scaled the same way that channel geometry is in Table 5.1. With a fixed size, we have the density of the plate ρ_{op} available as a tuning parameter in setting the plate mass (m_{op}) to a corresponding mass of regolith (m_r). Keeping in mind our channel geometry (fixed length and width) and equating the mass of regolith in a sheet of thickness h_r (with particles of ρ and assuming a compacted lunar packing fraction of ϕ_L = 0.54, see [15], Table 9.5) to the mass of the overburden plate we find ρ_{op}. We then use eqn. 5.1 (ρ_{op}) to populate Table 5.3 which shows the range of overburden pressures consider in this work. These pressures correspond to the thickness of lunar surface regolith covering the upper-megaregolith (around 5 m in the mare, 15 m in the highlands, [7]). Note that all pressurized cases achieved the same initial state, a consequence of allowing the massive plate to drop onto the particles. We'd expect a gradual compression to increase ϕ_0 and δ_0.

$$
\begin{aligned}
m_{op} &= \rho_{op}(wLh_{op}) \\
m_r &= \phi_L\rho(wLh_r) \\
\rho_{op} &= \phi_L\rho\frac{h_r}{h_{op}}
\end{aligned}
\tag{5.1}
$$

Table 5.3: Overburden pressure. We examine pressurization effects using the hard boulders from Table 5.2 (E = 50 GPa, R = 1.25 m). For these sized particles, h_{op} = 100 m. Note that maximum overburden pressure is just more than half of Earth sea level atmospheric pressure.

h_r (m)	ρ_{op} (kg/m^3)	P_{op} (kPa)	ϕ_0 (%)	δ_0 (mm)
0	-	0	58.7 ± 0.07	1.07 ± 0.4
1	16.2	2.63	59.0 ± 0.06	3.77 ± 1.3
5	81	13.16	59.0 ± 0.06	3.77 ± 1.3
10	162	26.33	59.0 ± 0.06	3.77 ± 1.3
20	324	52.65	59.0 ± 0.06	3.77 ± 1.3

We approximate the pressure felt by a single particle at the overburden-grain interface (P_{op}) in eq. 5.2 as the weight of the overburden column (using lunar gravity, g_L) divided by the surface area of a particle in the buried channel (the particle surface area cancels out since we are considering a column of regolith with the same radius as the underlying particles):

$$P_{op} = h_{op}\rho_{op}g_L \tag{5.2}$$

5.2.3 Data analysis

We employ same process as detailed in [177] and ch. 4 to analyze the decaying SW we generate. Along with the the input scripts provided at our public repository, the procedure outlined here and in our prior works enables any interested reader to recreate our results. Following each simulation run, we post process-output using *MATLAB*. The channel is divided into a 2D grid (channel is segmented in the lateral and depth directions) and each grid element ('virtual sensor') tracks average particle properties over time. Finding the maximum overlap (δ_m) or particle velocity (v_m) and their corresponding time allows us to build a strength history of the SW as

it propagates along the channel. Note that there can be significant noise in our results, especially when the strength of the wave is low compared to background forces, a consequence of our 2D grid and averaging procedure. To report a single value for δ_m/δ_0 or v_m at any given lateral position, we perform a further averaging over the sensors at each depth (around 40). Since a primary interest of this work involves understanding the general scaling of runout distance in channels filled with particles of sizes ranging from micron to boulder-scale, we deem the consequences of the averaging acceptable (mostly, noise in δ when near δ_0) as it will be neglibile compared to the orders of magnitude scaling we investiagate. We now describe the different runout distances that will make up our measurements. We are mostly interested the distance over which dilation would be expected to occur (D_D), but we will also consider the absolute distance traveled (distance before the wave fully terminates, D_A) and a transition distance (distance traveled before the wave transitions between decay regimes, D_T).

Runout distances

The absolute runout distance traveled by the wave, D_A, gives a sense for the total lateral distance that energy propagates within the granular channel as the result of a piston impact. Ideally, we'd assess this as the point at which the overlap experienced by particles within the propagating wavefront return to their initial state $\delta_m/\delta_0 = 1$. However, selecting the point at which this crossing is achieved proved to be difficult as we show in Fig. 5.2 (the zoomed in box). As a result of our averaging procedure and low strength of the wave near the far end of the channel, the normalized overlap becomes noisy (an effect exacerbated at looser ϕ_0) far from the initiation site. We therefore classify D_A as the distance traveled by the SW before $\delta_m/\delta_0 = 1.05$,

which we manually identify using plots like the one in Fig. 5.2 (we repeated this process for all cases in Fig 5.3). The transition runout distance D_T is also measured manually as the point of the bend in each curve.

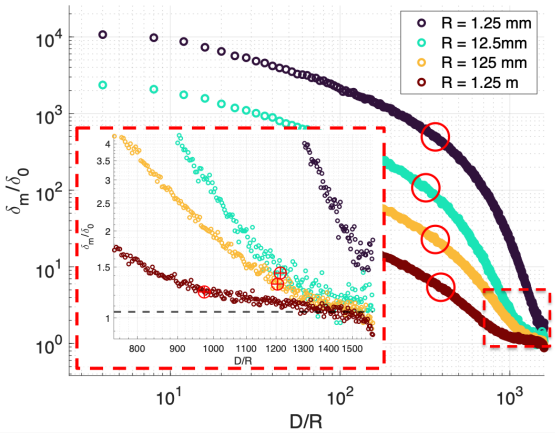


Figure 5.2: **Determining $D_{A,T}$.** Normalized particle overlap vs normalized distance (D/R) for varied particle sizes. The dashed box zooms in on where D_A and D_T are measured, we manually select the 1.05 crossing (the dashed black line in the zoomed portion). Note that we can observe the absolute runout when we define it as we have (δ_m/δ_0 = 1.05), but the actual absolute runout (δ_m/δ_0 = 1) extends beyond the bounds of our $1600R$ channels. The transition region between two regimes of power law decay is also manually selected as the bend in each of the curves (D_T, corresponding to the red plused-circle points). While the actual trends are a bit obscured, they can be better viewed in Fig. 5.3,D. Open red circles represent the maximum overlap at D_D and we identify their channel location using Fig. 5.5.

We are primarily interested in understanding the distance over which the decaying energy might be able to induce surface dilation, D_D. We find the lateral distance traveled before the particle velocity in the wavefront, v_m, falls below the velocity required for dilation, v_D. We find v_D using equation 4.10 from ch. 4, which we first used to find the depth to which near surface particles would be expected to loft (thus, the depth of dilation) as a result of collisional velocity at the floor of the channel. Solving eqn. 4.10 for velocity given the expected 40 cm LCS depth predicted by [1] results in a needed v_D = 4 m/s collisional velocity between particles in a sub layer with the particles of the regolith. According to our hypothesis (sec. 5.1.4), particles in the

sub layer (meter scale boulders of the upper megaregolith) would be providing this impact, so this test is mostly relevant to our boulder-filled channels. Similar to D_A we classify D_D manually, though this process is more straightforward (we just find the v_D crossing in v_m plot, Fig. 5.5) as seen in Fig. 5.2. Note that our assumed constant value for v_D corresponds to average LCS modification depth. Since the amount of thermal inertia reduction decreases with radial distance from the impact site (the distal temperature differences between background and cold spot are smaller), the depth of modification would necessarily be reduced as well. This assumption would lead to underestimates of D_D.

5.2.4 Investigated parameters

We explore a range of parameters and their influence on wave runout in our granular channels. The selection of these parameters is driven by considerations the material properties of regolith grains and megaregolith boulders, the geometry of a hypothesized sub layer, and details of the impact. We consider:

- a range of sizes from small grains just larger than lunar regolith scale particles ($R < 100$ μm, [14]) to the meter scale boulders in the megaregolith (sec. 5.2.1), with the boulders being our primary focus
- soft (E = 5 MPa, [177]) and hard particles (E = 50 GPa, comparable to lunar plagioclase [25])
- ϕ_0 from 55% - 62% from [177]
- piston velocity v_p up to $\sim$20% of c_m (10 m/s for E = 5 MPa, 1 km/s for E = 50 GPa)

- e from 0.1 to 0.8 (the range exhibit by rock-rock impacts in [200], extended to include the results from impacts between meter scale granite spheres in [201])
- P_{op} corresponding to values from unloaded vacuum to 20 m regolith cover (sec. 5.2.2)
- μ from 0.2 (nearly frictionless spheres) to 1.8 (gravel, [190])
- ρ centered on that of lunar grains (2.5 to 3.5 g/cc, ρ_L = 3 g/cc [25])
- ν ranging from 0.2 to 0.4 ([155], [125], [191])
- Impactor density ratios within 25% of the background ($0.75 \leq \rho_p/\rho \leq 1.25$)
- Layer thickness from the $160R$ channels from [177] to the $10R$ layer of boulders buried blow the regolith seen with ground penetrating radar in [26]

Those tests listed after item three (ϕ_0) all occur in channels filled with boulders: R = 1.25 m, E = 50 GPa, ρ = 3 g/cc. The remainder of the paper presents and discusses the results of our findings regarding runout.

5.3 Results and Discussion

We visualize and tabulate the numerical results of our simulations before discussing the influence of the parameters varied on runout distances.

5.3.1 Runout results

Table 5.4 summarizes our numerical results and Figures 5.3, 5.4, and 5.5 show (for the most noteworthy cases) δ_m/δ_0 vs radial distance, δ_m/δ_0 vs time and v_m vs time (respectively).

We'll often refer to these three plots as the 'combined trend plots' going forward. Note that the varied parameter of interest is in the same location in each of the plots (for example, frame G corresponds to varied v_p in the boulder scale particles across each of the three plots) and that the plots are organized (generally) from left to right by greatest influence on D_D. Since pressurization had a negligible effect on D_D (Fig. 5.5C), we chose to run all other cases in the non pressurized state to reduce computation time. Pressurization does, however, reduce the total overlap earlier in the channel (Fig. 5.4C) and increases particle velocities later in the channel (Fig. 5.5C). Before we discuss length scales, we highlight the broad agreement over all the tests with respect to decay rates.

The decaying SW in our channel capture the entirety of the fast decay regime, though only a small portion of the slow decay (this is acceptable since we are more concerned with D_D, which occurs within the fast decay regime), which can be seen in both Figs. 5.3 and 5.4. Here we highlight the time decay which agrees with granular wave decay in 1D chains. In all cases the fast decay regime briefly attains the universal power law for decay as described in [196] and [197], where energy decays in time depending on a power law around -0.71 (added as a trend line to plots in Fig. 5.4,D). Changes in particle size and h_c show the most pronounced effect on the time it takes to reach D_T, while μ and ϕ_0 have a small influence (all other test have little to no effect). The wave speed has a weak dependence on R as a result of our fixed $160R$ channel heights (ch. 4), and so therefore as particle size increases the same speed wave must travel over a greater physical extent (though approximately same number of particles, see, for example, Fig. 5.4,D), increasing the time to reach any of the decay distances. Similarly, reducing channel height increases average wave speed (ch. 4), shifting the transition points earlier in time (Fig. 5.4,B). Also note that the effect of any level of pressurization Fig. 5.4,C was to transition between decay

Table 5.4: Runout results. We show the runout distances from our simulations for absolute, transition, and dilation runout for the various parameters we considered. The parenthetical term following each parameter indicates material properties where S and H denote soft and hard particles, respectively, and B represents boulders (particles with material properties R = 1.25 m, E = 50 GPa and ρ = 3 g/cc). For all three cases we collect runout distance (D_A, D_T, D_D) in terms of number of particle radii traveled along the channel before the respective criteria is met (sec. 5.2.3). For transition and dilation runout we also log the time (t_{D_T}, t_{D_D}) and non-dimensional overlap (δ_{D_T}, δ_{D_D}) at the respective runout distance. Note that ρ, ν and e are omitted from the table as they had virtually no influence on runout. The table is broken into sections with the top, middle, and bottom corresponding to material property, impactor momentum and packing effects, respectively. v_p is fixed at 20% of c_m except in the varied velocity tests and all channels are of height $160R$, except for the h_c cases.

Param.	Value (units)	D_A (#R)	D_T (#R)	t_{D_T} (ms)	δ_{D_T} (ND)	D_D (#R)	t_{D_D} (ms)	δ_{D_D} (ND)
$R\,(E_s)$	.125 (mm)	656	300	22.92	1.17	-	-	-
$R\,(E_s)$	0.5 (mm)	712	380	56.19	1.22	-	-	-
$R\,(E_s)$	1.25 (mm)	1,132	652	92.76	1.26	-	-	-
$R\,(E_s)$	5 (mm)	1,211	824	186.9	1.19	-	-	-
$R\,(E_s)$	12.5 (mm)	1,360	1,100	1,258	1.18	-	-	-
$R\,(E_h)$	1.25 (mm)	-	-	-	-	364	0.71	496.0
$R\,(E_h)$	5 (mm)							
$R\,(E_h)$	12.5 (mm)	1422	960	80	1.20	320	6.75	107.6
$R\,(E_h)$	125 (mm)	1450	1,304	433	1.13	364	66.2	22.8
$R\,(E_h)$	1,250 (mm)	1400	1,356	2,041	1.24	392	626	5.5
$\mu\,(B)$	0.2	796	652	1,447	1.14	246	538.9	5.2
$\mu\,(B)$	0.6	1,120	844	1,639	1.29	328	571.9	5.4
$\mu\,(B)$	1.0	1,400	960	2,041	1.25	392	626	5.5
$\mu\,(B)$	1.4	1,440	1,100	2,105	1.38	442	703.2	5.4
$\mu\,(B)$	1.8	1,501	1,169	2,150	1.40	478	739.5	5.5
$v_p\,(B)$	100 m/s	896	508	1,210	1.31	69	129	5.5
$v_p\,(B)$	177.8 m/s	1,106	625	1,460	1.29	126	218	5.3
$v_p\,(B)$	316.2 m/s	1,246	712	1,695	1.27	196	314	5.6
$v_p\,(B)$	562.3 m/s	1,320	856	1,923	1.25	285	480	5.5
$v_p\,(B)$	1 km/s	1,400	960	2,041	1.25	391	626	5.5
$\rho_p/\rho\,(B)$	0.5	1,400	899	1,774	1.28	267	430	5.5
$\rho_p/\rho\,(B)$	0.75	1,400	912	1,916	1.27	337	546	5.5
$\rho_p/\rho\,(B)$	1.0	1,400	960	2,041	1.25	391	626	5.5
$\rho_p/\rho\,(B)$	1.25	1,400	1,048	2,152	1.28	433	713	5.5
$\rho_p/\rho\,(B)$	2.5	1,400	1,268	2,480	1.25	582	907	5.5
$\rho_p/\rho\,(B)$	5.0	1,400	1,369	2,720	1.26	738	1,050	5.5
$\phi_0\,(E_s)$	55 (%)	799	515	90	1.27	-	-	-
$\phi_0\,(E_s)$	59 (%)	1,132	652	93	1.26	-	-	-
$\phi_0\,(E_s)$	62 (%)	1,360	683	84	1.29	-	-	-
$h_c\,(B)$	10 (#R)	135	111	230	1.16	49	60	39.7
$h_c\,(B)$	20 (#R)	312	238	690	1.21	90	110	29.5
$h_c\,(B)$	40 (#R)	550	450	976	1.12	160	238	12.0
$h_c\,(B)$	80 (#R)	952	600	1,209	1.24	261	410	6.6
$h_c\,(B)$	120 (#R)	1,150	760	1,619	1.24	330	513	5.7
$h_c\,(B)$	160 (#R)	1,400	960	2,002	1.25	392	649	5.5
$P_{op}\,(B)$	0.0 (kPa)	1,400	960	2,041	1.25	392	626	5.5
$P_{op}\,(B)$	2.63 (kPa)	1,400	601	1,041	1.46	395	626	1.88
$P_{op}\,(B)$	13.16 (kPa)	1,400	601	1,041	1.46	395	626	1.88
$P_{op}\,(B)$	26.33 (kPa)	1,400	601	1,041	1.46	395	626	1.88
$P_{op}\,(B)$	52.65 (kPa)	1,400	601	1,041	1.46	395	626	1.88

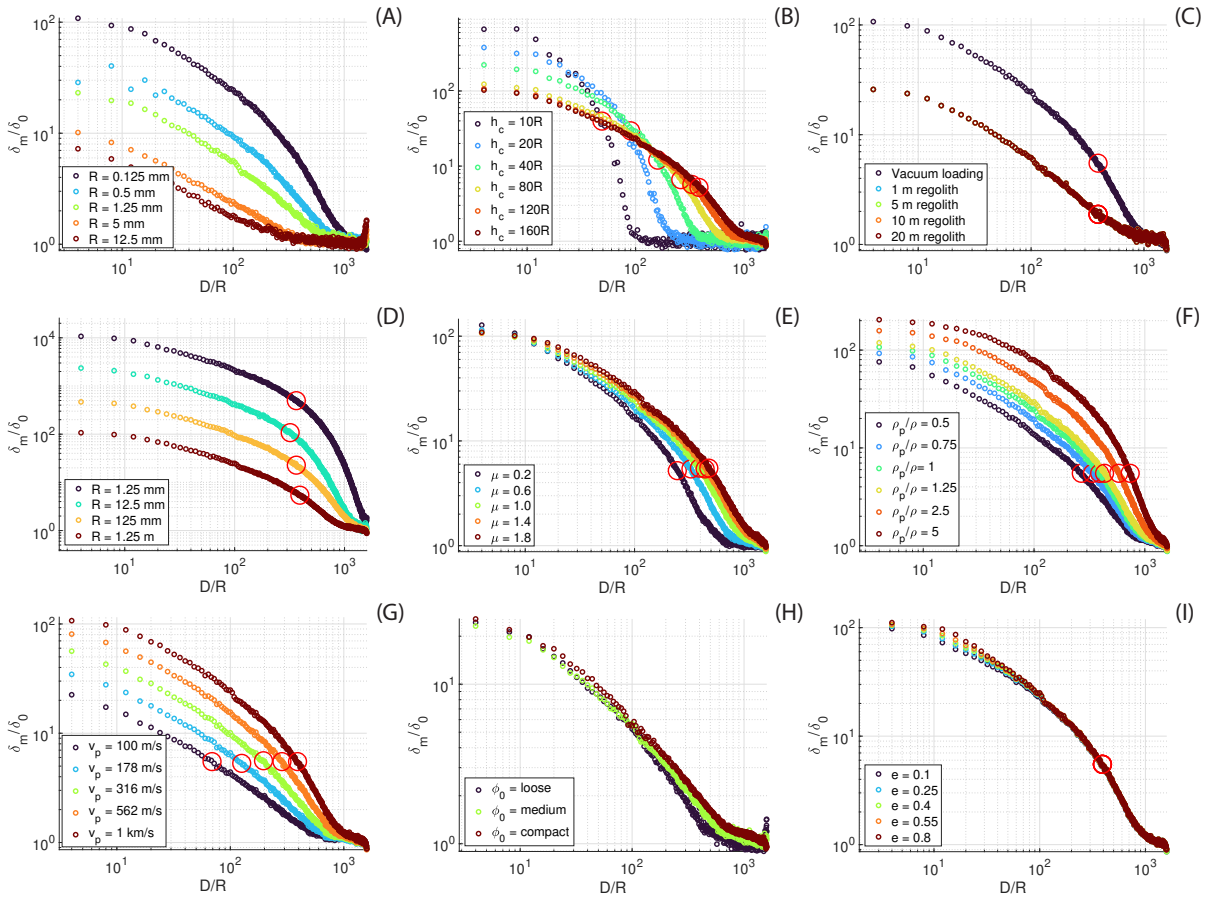


Figure 5.3: **Normalized overlap vs normalized lateral distance.** We plot the maximum overlap normalized by the initial overlap at each radial position along the channel after a wave has been initiated and until it has reached the end of the channel, with channel position normalized by particle radius. Red circles indicate D_D as in Fig. 5.2. The color legends in the different plots correspond to varied **A)** size (soft), **B)** channel height, **C)** overburden pressure, **D)**, size (hard), **E)** friction, **F)** piston density ratio, **G)** piston velocity, **H)** packing fraction, **I)** coefficient of restitution. Note that D_D is not marked in cases A and H since soft particles cannot support v_m that exceed v_D (see Fig. 5.5).

regimes sooner in time (by the same amount).

We have not quantified the power law in the slow regime since we are primarily interested with the dilation threshold and not the transition time, but all cases appear to qualitatively approach the same slower decay rate. We point out that the two largest particle sizes inspected with soft particles (R = 5 mm and 12.5 mm, Fig. 5.4,A) appear not to approach the universal power

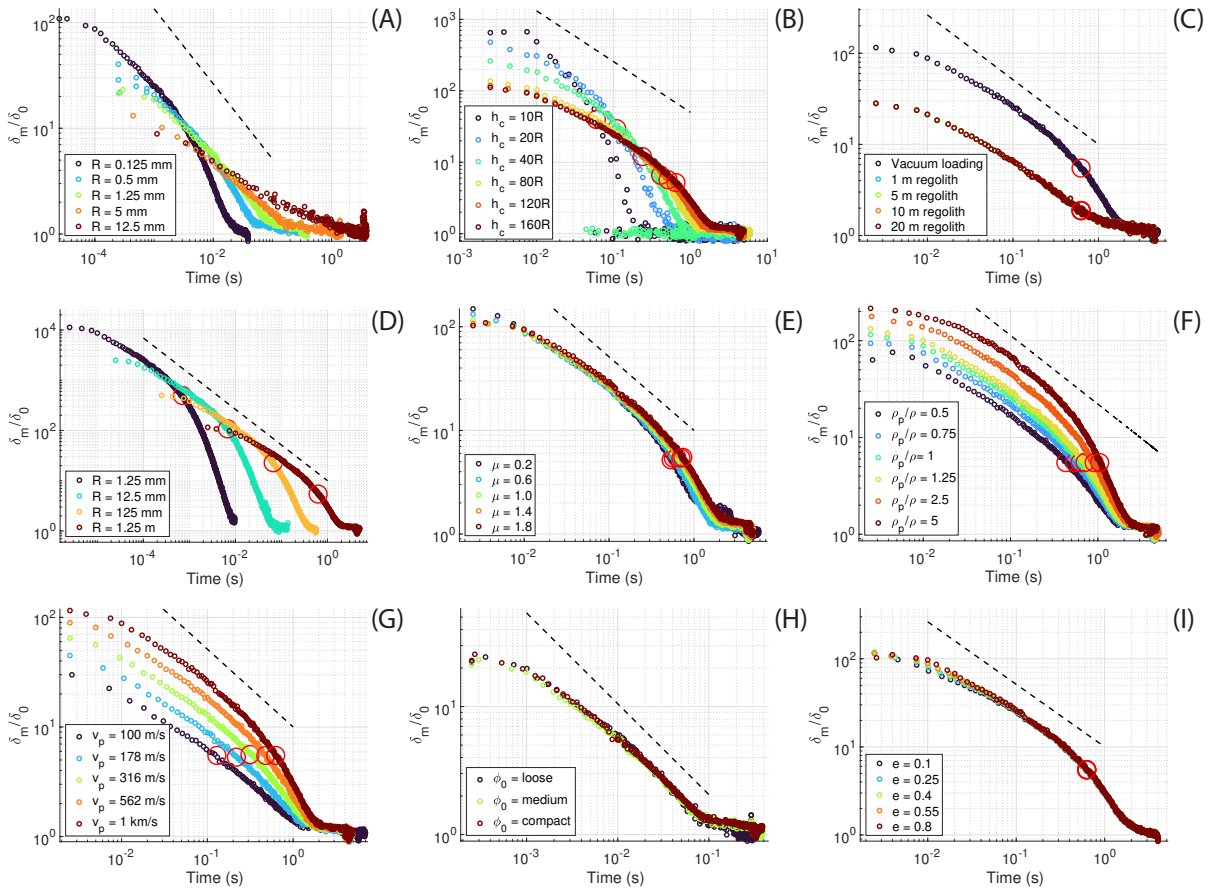


Figure 5.4: **Normalized overlap vs time.** We plot the maximum overlap normalized by the initial overlap at each radial position along the channel, with channel position normalized by particle radius. Red circles indicate D_D. The black dashed line is the same in all the plots, showing the universal power law decay with time seen in 1D granular chains. The color legends in the different plots correspond to varied **A)** R (soft), **B)** h_c, **C)** P_{op} **D)**, R (hard), **E)** μ, **F)** ρ_p/ρ, **G)** v_p, **H)** ρ, **I)** e. Note that D_D is not marked in cases A and H since soft particles cannot support v_m that exceed v_D (see Fig. 5.5).

law. Zooming in very closely, however, suggests that they achieve the decay rate, only very briefly (on the scale of single digit number of particles). Examining this discrepancy is, again, outside the scope of this work, especially since the soft particles are more like rubber ($E \sim$3 MPa rather than 10s of GPa scale regolith). One last point regarding the decay rate is that it is not clear if there are only two decay regimes linked by a single transition region or if there is actually a third decay regime and two different transition points. This detail is most obvious in Fig. 5.4,D

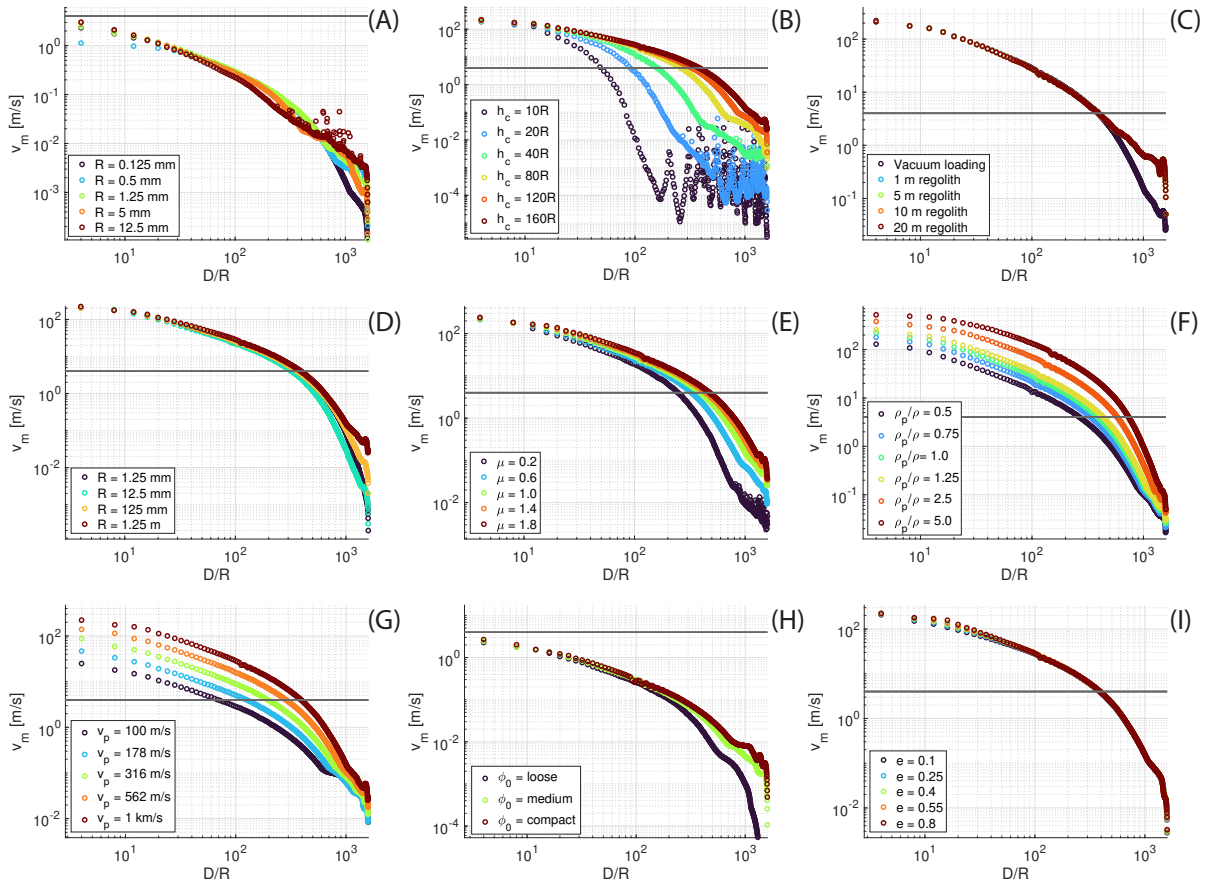


Figure 5.5: **Maximum particle velocity vs time.** We plot the maximum particle velocity experienced in the decaying wavefront at each radial position along the channel, with channel position normalized by particle radius. The solid black lines represents the v_D velocity threshold, below which we do not anticipate a surface dilating wave to be supported. The color legends in the different plots correspond to varied **A)** R (soft), **B)** h_c, **C)** P_{op} **D)**, R (hard), **E)** μ, **F)** ρ_p/ρ, **G)** v_p, **H)** ρ, **I)** e.

for the smallest particles where the particles follow an intermediate decay rate between fast and slow (the slow regime only being briefly achieved as a result of our channel length) for a greater duration (compared to most other cases).

Dilated runout

We find that D_D is primarily affected by momentum and packing effects, though friction (a proxy for the roughness of our particles) does also have some effect. The influence of these parameters on D_D can be seen in Fig. 5.5 by observing the number of particle radii elapsed before v_m in the decaying wave drops below v_D. The packing of the bed changes as more particles are squeezed into the same volume (greater ϕ_0 increases the number of contact points per particle) or as the thickness of the bed changes (average wave speed wave increases as channel height decreases, [174], [177]). Although we examined ϕ_0 (Fig. 5.5,H) using the soft particles (which do not produce $v_m > v_D$ except for the first particle or two), drawing a line through the point two orders of magnitude below the initial velocity (an approximation based on the other trends) suggests there is a slightly larger increase in D_D with ϕ_0 than earlier in the channel (you'll likely have to zoom in to see the differences at channel positions < 100 particle radii). Decreasing the layers had the greatest effect on D_D (Fig. 5.5,B) thanks to the reduced wave speeds previously mentioned. This is somewhat of a pressure effect as well, since when the channel is taller, grains near the floor experience greater overburden pressure, meaning they should sustain larger v_m (as we see in (Fig. 5.5,C)).

The effects of momentum changes on D_D are evident in Fig. 5.5,G (velocity) and 5.5,F (impactor density compared to background). These tests insert more energy into the channel with greater speeds or greater density to piston particles. For the same assembly conditions (same potential energy), increasing impactor momentum provides a greater energy differential to the grains and thus greater v_m. Velocity and impactor density effects appear to be comparable. Concerning material parameters, increasing μ (Fig. 5.5,E) increased D_D: rougher particles allow

for greater decay distances (elevated forces from the friction contribution at each compact point). We cannot quantify the trend in E since we only ran the two cases of soft and hard particles, but clearly increasing E increases D_D given that the soft case does not exceed the v_D threshold (Fig. 5.5,A) while the hard case (Fig. 5.5,D). We can also see that increasing particle radius R has no effect on v_m. We did not include ρ (increased D_D by $2R$ from ρ = 2.5 to 3.5 g/cc), e (increased D_D by $6R$ from $e = 0.1$ to 0.8), or ν in Table 5.4 because their effects were very small or negligible. The plots for ν and ρ are similarly omitted since they are practically identical to e, shown in the I frames across the combined trend plots.

For those tests that have noticeable effects on dilated runout, we fit the data in Table 5.4 to get an idea of how D_D scales with each parameter. We made Table 5.5 which summarizes our curve fitting, for which we found a generalized power law to give the best fits ($r^2 > 99.9\%$). While we do report the initial goodness of fit here, more measurements could be obtained in a future work to ensure statistical significance. The trends are plotted in Fig 5.7 which shows the appropriateness of the fits as well as the relative increase compared to the other parameters (since the y-axis is the same for each plot). We then use these trends to find a scaling multiplier in order to consider how our tests might scale to the actual conditions of impact. First recall that the v_p we consider here are still at least an order of magnitude smaller than actual lunar hypervelocity impact (25-30 km/s, [9]). Second, while [177] and ch. 4 used a base friction parameter μ = 1 which is in the range of lunar values ([15], [190]), μ = 1.8 is likely a better choice for regolith ([190] found 1.8 to be a good choice when approximating gravel runout using SSDEM). Finally, the width of the buried boulder region in [26] was around 12 m, which is closely aligned with our h_c = 10 case. We use these estimated multiplicative scaling factors in sec. 5.3.1 to estimate how the results in this work might scale to the lunar environment. We caution readers when using

these trends over large ranges of parameter space as the generalized power law fit cannot capture the entire range. We say this because some of the fits in Table 5.5 produce non physical results when evaluated at their extremes. Velocity and channel height have negative y-intercepts which is troublesome since this implies that a 0 velocity impact or that a channel height of 1 (i.e., a 1D chain) would produce a negative D_D. However, v_p = 0 should correspond to D_D = 0 (no impact) and h_c = 1 would likely correspond to a value of D_D around 10, certainly not a negative number. Some piecewise model is likely needed to fully describe each trend.

Table 5.5: Dilated runout fit coefficients and multiplier estimation. We first list the coefficients that result from fitting the various parameters that influence D_D to a generalized power law of the form $D_D = Cx^{p_1} + p_2$, where x should be replaced by the parameter of interest. The right half of the table estimates the amount by which to scale D_D (D_D multiplier) when the designated parameter changes from the base to the target value (with units defined where necessary). We find the multiplier by plugging the fit parameters on the left hand side of the table into the generalized power law, assessing D_D for the base and target quantities, then taking the ratio of the target to the base value. As an example, if the velocity of impact into our channel increased from 1 km/s to 25 km/s, we'd expect D_D (which is $391R$ in the boulder case from Table 5.4) to increase to 1,877R.

Param.	C	p_1	p_2	r^2 (%)	Base (units)	Target (units)	D_D mult.
v_p	46.43	0.363	-178.2	1.00	1×10^3 m/s	25×10^3 m/s	4.23
h_c	35.15	0.506	-66.46	99.96	$160R$	$10R$	0.12
μ	262.40	0.363	128.10	99.91	1.0	1.8	1.16
ρ_p/ρ	1278. 7	0.1494	-887.22	99.99	1.0	2.0	1.36

Absolute and transition runout

First, recall that D_A as we've defined it in this work does not represent the actual absolute decay (δ_m/δ_0 = 1), but an adjusted threshold (δ_m/δ_0 = 1.05) that we've chosen to make identifying D_A more tractable (the signal becomes noisier as the energy remaining in the wave approaches the same level as the background). It also turned out that our channels are too short to capture

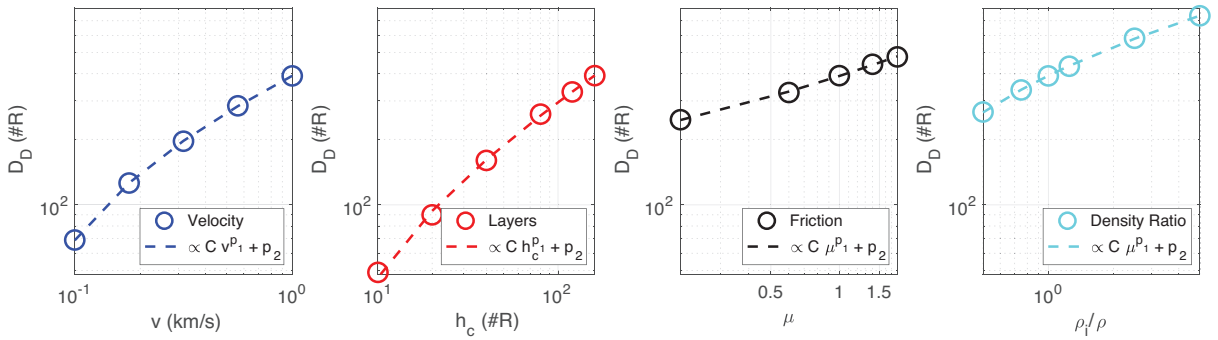


Figure 5.6: **Dilated runout trends.** We plot dilated runout vs varied parameter for the values from Table 5.4 and the fits from Table 5.5. The plots form left to right show D_D vs velocity, channel height, friction parameter and piston vs background particle density ratio (respectively). The power law fit (dashed line) coefficients correspond to those in Table 5.5.

the actual D_A. These details can be seen across all the plots in Figs. 5.3, 5.4 and 5.5, although they are most apparent in the earlier zoomed in box of Fig. 5.2. For this case (hard particles of varied size, corresponding to frame D in the combined trend plots) the zoomed image shows that our adjusted threshold occurs very near the end of our $1600R$ channels, and in the case of the smallest particles actually exceeds the channel length. The differences in D_A are likely attributable to the different packing fractions of these beds, see Table 5.2. Using the combined trend plots to populate Table 5.4, we see that D_A increases with particle size when particles are soft (Figs. 5.3,A), but seems weekly dependent on particle size when particles are hard (Figs. 5.3,D). We will reconcile this discrepancy later in sec. 5.3.1. Friction (Figs. 5.3,E), velocity (Figs. 5.3,G), channel height h_c (frames B), and ϕ_0 (Figs. 5.3,H). Impactor density ratio (Figs. 5.3,F), and the level of pressurization (Figs. 5.3,C) did not change D_A.

Transition runout D_T is also most easily seen in the zoomed in Fig. 5.2 where the transition has been manually identified and labeled as the point where the curve bends, switching from a fast to slow power law decay (see the prior section). We collected the transition points and they

are also given in Table 5.4. Every parameter investigated appears to influence D_T. Increasing packing fraction (Figs. 5.3,H), friction (Figs. 5.3,E), velocity (Figs. 5.3,G), impactor density ratio (Figs. 5.3,F), channel height (Figs. 5.3,B) and particle size (Figs. 5.3, A and D) increased transition runout in both time and space. Further analysis of D_A and D_T would be interesting avenues for future works to explore (and those works would want to use a longer channel), but since we are primarily concerned with D_D we leave our analysis of absolute and transition runout here.

Decay distances

Ultimately we need to compare the physical extent (not particle number) of runout to that of the LCS halo in order to assess our hypothesis. We use the smallest average LCS halo extent of 2 km [1] as our reference. Multiplying the particle radius by the runout values in Table 5.4, we create Fig. 5.7. In this plot we consider how runout distance changes with particle size. We plot D_A for both hard and soft particles of varied size (on the left) as well as D_D for the hard particles in various cases (on the right). Contrary to the apparent size dependence of the runout distances in Table 5.4, we found the best fit to the data be to a power law dependence on particle radius R, $D_{D,A,T} = C \times R^1$, where C is a constant. This is in agreement with our initial suspicion (sec. 5.1.3) that decay distances would be a function of particle number alone. For D_A we fit the soft and hard particles as one set which also support this linear trend ($C_A \approx$ 1,500, $r^2 = 99.99\%$), suggesting that the soft particle measurements at $R = 5$ mm and 12.5 mm are anomalous (supported also by the agreement between the soft and hard particle cases at $R = 1.25$ mm). The fit to D_D was similarly good ($C_D \approx 320$, $r^2 = 99.97\%$). Note that we did not plot D_T

since we only have three data points which is not quite sufficient for a fit (at least 4 is better to to rule out any curvature). However, D_T looks to follow the same power law with R ($C_T \approx$ 1,355, r^2 = 100%). The fits imply that dilation, transition and absolute runout distances are universal constants (for a given impact velocity, channel geometry, and particle roughness) corresponding to 160, 678, and 750 particles before the decay threshold is met. Finally, we plot one point that is most comparable lunar conditions. For the majority of this work we considered assemblies of 160 particle radii in height, meaning our boulder scale channel is 200 m tall, much larger than region of boulders seen between 12 and 24 m depth using the ground penetrating radar in [26]. If the SW is entrained in this 12 m layer then our h_c = 10R (D_D = 49R) channel is about the same thickness. Using the multipliers in Table 5.5 for velocity, density ratio and friction (and assuming we can take their product), this gives a scaled up $D_D(h_c = 10)$ = 410 m. This is about an order of magnitude less than the threshold we set, but we have not done any analysis to compare the energy of our impacts to the energy involved in generating a comparably sized crater. Following the 10-100 crater radii average extent from [1] we estimate the minimum (corresponding to our 21 m predicted minimum, an over estimate, with 10r_c halo extent) and maximum (corresponding to a 2 km diameter crater with 100r_c halo extent) cold spot extent to range from 115 m to 100 km. This range (visualized in the right image of Fig. 5.7) easily includes the scaled up 10R channel D_D ($\sim$410 m), and the minimum is only twice the distance of the unscaled case (61 m).

5.3.2 Discussion

There are two primary findings of this work specific to granular dynamics phenomenon. First, we find randomly packed 3D granular assemblies to exhibit the same power law decay as

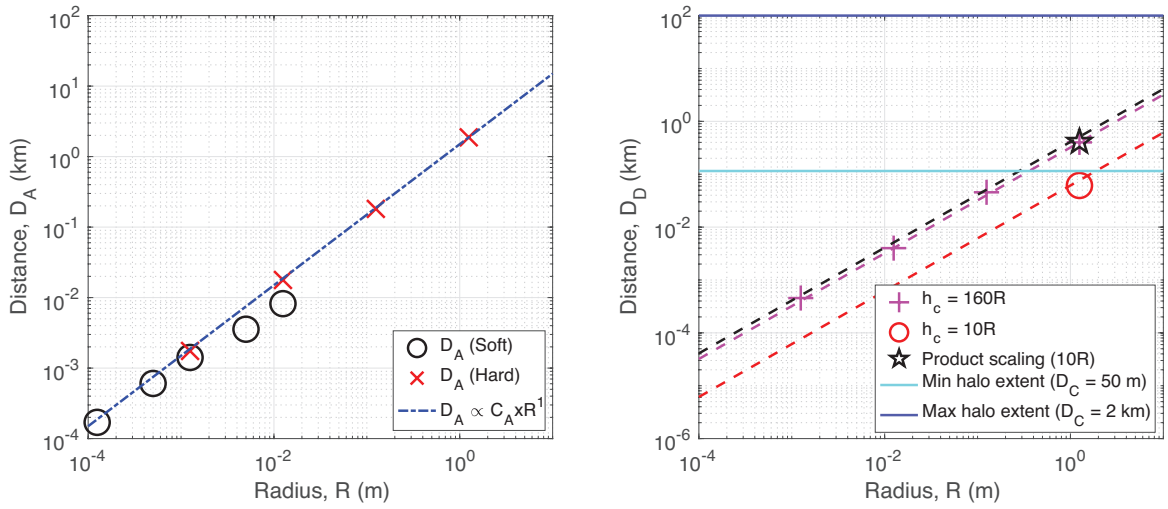


Figure 5.7: **Decay fits. Left)** Absolute runout distance vs particle radius for varied tests using the 160R tall channel and v_p = 0.2c_m. We consider D_A for hard particles (E = 50 GPa, red x) and soft particles (E = 5 MPa, black circle). The blue dashed line is a single combined fit to the measurements of soft and hard particles following a power law of R. **Right)** Dilation runout distance vs particle radius. Here we only consider the hard particles and show D_D for those cases conducted in the h_c = 160R (pink plus) and h_c = 10R (red circle) cases. The single black star represents D_D from the 10R channel, scaled up with velocity, friction, and density ratio, as described in the text. The dashed lines are a power law fit with R for the h_c = 160R case and an assumed power law trend for the other two cases.

in 1D granular chains. The second is that runout distance is universal for 3D randomly packed granular assemblies of the same geometry, particles of the same friction parameter and for the same impact momentum. This holds true for all three categories of runout we defined. Note that this particle number distance until decay increases with momentum and channel height and the scaling analysis in Table 5.5 should be taken as an initial characterization to be refined.

Our results have several implications for LCS formation. First, we have shown that although the initial impulse decays as it propagates, v_m exceeding v_D can be maintained over large distances, suggesting the presence of a driven solitary wave in the surface layer over the same extent. The channels we inspected (160R in height) saw v_m above the threshold to be maintained on hundred meter scale distances, while the shorter channel at 10R (which is more similar

in thickness to the layer of boulders suspected to lie just below the regolith) only showed 10s of meters of distance where a surface wave could be maintained. However, our scaling analysis suggests that with greater impact velocities and more physically real particles (rougher or aspherical particles), decay distances approach LCS halo scale extents (>400 m). Greater impact velocities would translate to larger overlaps experienced by particles in the wavefront and the higher stresses associated with these large overlap collisions might lead to fracturing and breaking earlier in the channel (closer to the crater), perhaps even explosively. Future work could investigate the possibility that the initially higher energy source decaying along the regolith-megaregolith interface may vaporize existing volatiles (if present at that layer) and allow them to escape to the surface.

Another implication of these modeling results is related to the structure of the layer of boulders in the upper megaregolith and how that relates to the surface expression of the cold spot halo. The layer of boulders seen by the ground penetrating radar in [26] suggested the layer was filled with 1 m and 3 m sized boulders. Supposing that the average boulder size is 1 m but pockets of 3 m boulders are randomly interspersed, the R^1 scaling on decay distance would lead to a tripling in the dilation distance between the two sizes. The LCS rays might therefore be indicative of a force chain comprised of particularly large boulders. Furthermore, radial angles of low thermal inertia material in the LCS halo that end abruptly may be indicative of buried features (crack or void) where the distribution of boulders underneath the regolith is not uniform enough to transmit the decaying wave (the force chain is broken). A radial angle of low thermal inertia being reestablished at some later point after an earlier than anticipated termination implies that the decaying energy in the buried layer continued to propagate while the surface dilating wave was temporarily suppressed in the regolith, indicative of a large boulder or some material

with larger than typical amounts of cohesion.

Given that this work supports our hypothesis by way of showing long range impulse propagation, we can try to constrain the minimum sized LCS-hosting craters by considering that the impactor must strike the buried layer of boulders in order to initiate the decaying SW. We suspect the minimum apparent crater diameter (D_c) to correspond with the maximum transient crater depth (d_t) which we find by rearranging the equation from [202], $D_c = (d_t/0.29)^{1/0.93}$. For a cold spot to form in our hypothesis, the impactor must strike the boulders of the megaregolith (the transient crater depth must be coincident with the boulders of the megaregolith). Assuming that d_t just barely contacts these boulders yields D_c to be around 21 m in the mare (about 5 m of regolith cover) and about 71 to 90 m in the highlands (15 to 20 m of regolith cover, see sec. 5.1.2). These D_c correspond to minimum LCS halo extents (using the 10 crater radii lower bound) of 115 m and 355 m to 450 m (respectively). The approximated mare D_C of 21 m is plausible, but the highlands minimum D_c (71 to 90 m) are larger than the smallest LCS halos found in [6] (D_C = 43 m). Our approach is therefore an over estimate, and more careful consideration of the process of initially generating the buried-boulder decaying wave is required. Finally we point out that since this method of formation is a consequence of granular dynamics (two disparately sized assemblies in contact) in low gravity and low pressure (vacuum), any solar system body that hosts these conditions and possess a regolith layer covering a buried layer of larger particles is likely to form low thermal inertia halos around fresh impact craters.

There are several limitations to be kept in mind regarding this work. First is that this is a modeling effort built up through many approximations that could yet prove to be incorrect. The assumptions in the loft depth equation from ch. 4 should be relaxed (primarily, to account for depth influence on wavefront forces), which may alter the threshold velocity we used here. In-

creasing or decreasing this threshold would decrease or increase dilated runout distances, respectively. While we used a proxy to emulate particles of increasing roughness (altering the friction parameter), our particles are still monodisperse. However, there is a high degree of dispersity to the size distribution of the regolith and (presumably) the megaregolith. Future works should consider the effect of both aspherical particles as well as dispersity. Likely, dispersity will reduce runout distances as the number of particle contacts increase, but presently it is unclear what form this dispersity takes (i.e, the extent and quality of regolith filling the spaces between the boulders of the upper megaregolith is unknown). However, directly simulating the regolith-megaregolith transition is presently intractable. The four order of magnitude difference between the average particle size in the layers coupled with the R^3 dependence on volume means that there would be 1×10^{12} more small particles that would fill the same volume as compared to the large particles. The surface layer does not necessarily need to be the same height as the base layer, but even a surface layer that is a fraction of a percent of the thickness of a base layer (made of a sheet of particles one large particle radius thick) would still contain hundreds of millions of particles. We know of no current particle-particle code that can simulate a scenario involving such a quantity of particles. Therefore, this concept requires experimental validation. The minimum requirements for such an experiment are low gravity (probably in the form of a drop tower) and vacuum. However, the test would need to be performed in a sizable channel, although the necessary length is not yet clear. We do not yet know the minimum size ratio required for the surface SW to be generated. The only place we know this phenomenon to exist (regolith-megaregolith boundary) has a four order magnitude difference in particle size between the disparate assemblies. A surface layer of micron sized particles would then require buried layer to contain 10 mm sized particles. A one meter channel could therefore capture decay in a sub layer that covered a lateral distance of

100 particles. This seems sufficient based on the current work and the specifics of the assembly and geometry (material properties, thickness of the sub layer) could be used to tune the decay distance so that all three regions of decay are observable (with shorter channels and lower speed impacts).

5.4 Conclusions

In this work we conducted a set of simulations using SSDEM to study the behavior of granular wave decay in long, 3D granular channels that are randomly packed with spherical, monodisperse particles. We characterized wave decay via δ_m and v_m experienced by particles within the decay wavefront in space and time in order to classify three classes of runout distance. We measured absolute runout (overlap in the wavefront returns to initial conditions), the transition runout (time, overlap, and lateral position at the time of transition between fast and slow decay regimes) and dilation runout (time, overlap, and lateral position before v_m fell below the requisite velocity needed to loft particles in lunar condition, calculated to be approximately 4 m/s) which all scale with particle radius as R^1. Our goal was to evaluate a part of our hypothesis: that Lunar Cold Spots form when a surface dilating wave is generated in the regolith by impulse energy from the initial impact as it decays through meter scale boulders of the upper megaregolith. The main findings of this work are:

- Runout distances depend only on particle number for assemblies of the same geometry (same packing, same height channel)
- 3D granular wave decay follows the same universal power law decay as seen in 1D chains and similarly switches between this fast decay and a later, slower decay regime

- Provided initial estimates of scaling effects for parameters that affect dilation distance: momentum (v, ρ_p/ρ), μ, ϕ_0

- The requisite particle-particle velocity threshold (needed for a surface dilating wave to form) can be maintained to near LCS scale distances (hundreds of meters)

To give an answer to the question posed in [3] ("By what process does the regolith become fluffier?"), we suggest that cold spot regolith is fluffed up by a surface solitary wave driven from below by the decay of impact energy through boulders at the regolith-megaregolith boundary. This implies that impacts on any low-gravity, low-pressure planetary surface covered with regolith and possessing an underlying layer of larger boulders would see low thermal inertia halos surrounding fresh craters.

Chapter 6: Conclusion and Future Work

In this work work we investigated a possible formation mechanism for Lunar Cold Spots, large distal regions of reduced thermal inertia surrounding young impact craters on the Moon. We used Soft Sphere Discrete Element Modeling to study two main concepts. First, we investigated the behavior of grains in a laterally propagating wavefront close to the vacuum exposed surface in a low-gravity environment. Second, we characterized the extent over which an impulse initiated by the impact could propagate. Through this work, we determined a formation mechanism that plausibly explains both the magnitude of surface dilation and a method for that propagation to be sustained over 100+ m distances. We cannot conclude that our proposed fluffing mechanism (surface dilating solitary wave driven from impact energy decaying in buried boulders) is *the* formation mechanism, but the results of the investigation we've undertaken here do provide strong evidence supporting our hypothesis. We review the evidence, summarizing below the previously uncharacterized behaviors of granular systems we have studied.

First, we showed that grains near the surface loft as the result of experiencing a supersonic laterally propagating solitary wavefront (SW). Particles in the wavefront undergo collisions with their neighbors and are vertically redirected, achieving a ballistic trajectory before setting back down to a looser state. The directionality of the collision is enforced by the curvature in the wavefront near the surface which is a consequence of quickly increasing wave speeds along with

increasing overburden pressure at depth. An entire sheet of particles is lofted in the wake of the wavefront, with the thickness of this lofted sheet increasing as a granular assembly is in an increasingly compacted initial state. While we suspected that the sheet of dilated bulk density was analogous to the estimated 40 cm thick sheet of dilated material that makes up the LCS low thermal inertia halo, the particles considered in our initial work were not representative of lunar regolith.

Next, we showed that this lofting behavior would scale from our initial idealized case to lunar conditions. We showed that forces in the laterally propagating wavefront scale the same way as 1D chains do, though the 3D force is a fraction of the 1D chain force (two to three orders of magnitude less). While in a 1D chain the force in the wavefront is a result of a normal impact into the chain at some velocity, the method of wavefront force prediction we produced relied on a velocity being transmitted though the rough floor of our channel. Using the SW force prediction we determined, we balanced the forces in the wavefront with forces in the solitary wave to find our lofting depth equation which predicts the depth to which particles can be perturbed as the result of the passing wavefront. This equation has good agreement with our simulated results and predicts a loft depth similar to that expected on the Moon (40 cm). The SW we studied here and initially were able to propagate long distances because they were driven through the channel, and therefore represented an idealized scenario where a surface wave is maintained by constant input energy from below. Understanding that the surface wave required some method exogenous to the regolith to be maintained in the regolith led us to consider how energy of the impact would propagate through deeper layers.

Lastly, we studied the behavior of wave decay in meter scale boulders analogous to those that have been seen to underly the regolith layer with ground penetrating radar. Largely we found

that the behavior of granular wave decay in a 3D randomly packed channel matched the behavior of a 1D chain: decay length scales are a function of particle number, the decay rate matched the expected universal power law in the fast decay regime and transitioned to a slow decay regime. Determining that decay distance scaled with particle radius elucidated that the initial impulse energy could indeed be propagated near LCS halo extent length scales when decaying through meter sized boulders. Using our previously derived lofting depth equation, we then estimated that the particle velocity in the decaying wavefront of a buried layer (needed to explain the hypothesized 40 cm worth of dilated surface regolith) to be around 4 m/s. A scaling analysis based on sensitivity of dilation runout distance to the different parameters we evaluated (mainly, larger impactor velocities than we can consider with our model) supports the ability of the decaying subsurface wave to maintain a surface dilating wave over hundreds of meters, within one order of magnitude of the average extent expected for the LCS halo.

There are of course limitations to the current work, leading to many avenues of consideration for future studies. Though we use a few flavors of friction and cohesion to make our particles more real, they are still a collection of spheres. Even more so, monodisperse spheres. Future works must consider the influence of dispersity and aspherical particles on the surface dilating wave as well as the decaying buried wave. Our equation for lofting depth used a single scaling parameter even though we found some variability to the value of this parameter with the material parameters of the particles in an assembly. Likely this scaling factor also has some relationship to material parameters or the geometry of the packing itself and so this should be considered. Furthermore, we used a small angle assumption to approximate the vertical force transmitted to particles experiencing the surface dilating wave (allowing them to loft and achieve a looser state), but we believe this angle can be calculated. Finally, if our modeling efforts are

truly producing a previously unknown physical result, the minimum size ratio that is needed between the surface and the buried particles in order to observe the effect (buried decaying wave generating a surface wave) is not known. Simulating two such disparate size distributions in contact with one another is at least computationally challenging if not intractable at present so it may be necessary to conduct an experiment in a low-gravity and vacuum. It would perhaps be a good idea to relax some of our modeling assumptions or see independent verification of our proposed fluffing mechanism before setting up such an experiment.

Understanding the cold spot formation mechanism has important implications for the Moon. Both the thickness of the cold spot low thermal inertia surface material and the radial extent of the halo (and rays) reveal details about the impactor (velocity, density compared to the background material), the subsurface topography (i.e., the size distribution of boulders) and perhaps even the location of boulders or other anomalous features (and possibly interesting for resource utilization) near the surface but obscured by regolith. On the other hand, our formation mechanism might also lead to the release of volatiles, leaving the halo around fresh craters depleted as compared to the background. Importantly, this fluffing mechanism would not be unique to the Moon, but we would expect it to occur on any low gravity, low pressure planetary body that has surface regolith covering a layer of larger, buried particles. We agree with Bandfield et al. that LCS would be present on Mercury or Vesta and we also suspect that atmospheric pressure on Mars might be low enough that this same mechanism leads to the low thermal inertia halos seen there. If rubble pile asteroids have a regolith layer covering an underlying layer of larger boulders, perhaps the mechanism we've described here played a role in the suspected reshaping of Didymos following the Double Asteroid Redirect Test (DART) impact. Ultimately, even if we have pointed toward the actual fluffing mechanism, many questions remain. In addition to those

topics already identified as future work, understanding the erasure of the cold spot halo would be another ripe area of research.

Appendix A: Contact model

Here we describe the details of our selected contact model. Our granular assembly is a collection of spheres subject to Hertz contact law ([148]) which accurately captures wave propagation in granular media ([61]). We also include static and rolling friction ([74]) and cohesion ([149]) in our force model. Here we provide an overview of our model considering two monodisperse particles in contact. When two particles of radius R come into contact they begin to experience a nonlinear restorative elastic force proportional to the amount of overlap (δ), $F \propto \delta^{3/2}$. Normal and tangential directions are with respect to the particle contact. When the overlap is purely normal (δ_n) the restorative elastic force ($F_{n,e}$, eq. A.1) comes from the sphere's stiffness, k_n.

$$\begin{aligned} F_{n,e} &= -k_n \delta_n^{3/2} \\ k_n &= \frac{4}{3} E_{eq} \sqrt{R_{eq}} \end{aligned} \tag{A.1}$$

Equivalent radius (R_{eq}) and mass (m_{eq}) are given in eq. A.2. Equivalent compressive (E_{eq}) and shear (G_{eq}) strengths are provided in eq. A.3.

$$R_{eq} = \frac{R_1 R_2}{R_1 + R_2}$$
$$m_{eq} = \left[\frac{1}{m_1} + \frac{1}{m_2}\right]^{-1} \tag{A.2}$$

$$E_{eq} = \left[\frac{1-\nu_1^2}{E_1} + \frac{1-\nu_2^2}{E_2}\right]^{-1}$$
$$G_{eq} = \cdots$$
$$\left[\frac{2(2+\nu_1)(1-\nu_1)}{E_1} + \frac{2(2+\nu_2)(1-\nu_2)}{E_2}\right]^{-1} \tag{A.3}$$

There is also a normal damping force ($F_{n,d}$, eq. A.4) which depends on particle normal velocity (v_n) and the normal damping coefficient (γ_n) which depends coefficient of restitution (e), in addition to material properties already defined. Intermediate quantities in eq. A.4 are defined in eq. A.5.

$$F_{n,d} = -\gamma_n v_n$$
$$\gamma_n = -2\sqrt{\frac{5}{6}}\beta\sqrt{S_n m_{eq}} \tag{A.4}$$

$$\beta = \frac{ln(e)}{\sqrt{ln(e)^2 + \pi^2}}$$

$$S_n = 2E_{eq}\sqrt{R_{eq}\delta_n} \tag{A.5}$$

Finally, the normal force also captures the [149] cohesive force (F_c, eq. A.6). This depends on the particle's cohesion energy density, k_c, and particle contact area, A_c ([68]), shown here in eq. A.7).

$$\mathbf{F}_c = k_c A_c \tag{A.6}$$

$$A_c = -\frac{\pi}{4}\frac{1}{c_{12}^2}(c_{12} - R_1 - R_2)(c_{12} + R_1 - R_2)\cdots$$

$$(c_{12} - R1 + R_2)(c_{12} + R_1 + R_2)$$

$$c_{12} = \delta_n - R_1 - R_2 \tag{A.7}$$

The total normal contact force (eq. A.8) is then $F_n = F_{n,e} + F_{n,d} + F_c$.

$$\mathbf{F}_n = -k_n\delta_n^{3/2} - \gamma_n v_n + k_c A_c \tag{A.8}$$

The tangential contact forces are similar to the normal forces, but with a constraint to appropriately capture Coulomb sliding friction. The tangential elastic force ($F_{t,e}$, eq. A.9) depends on the particle's tangential stiffness, k_t, which depends on the tangential overlap, δ_t.

$$F_{t,e} = -k_t \delta_t$$

$$k_t = 8G_{eq}\sqrt{R_{eq}\delta_n} \tag{A.9}$$

As before, there is a tangential damping force ($F_{t,d}$ eq. A.10) which depends on particle tangential velocity (v_t) and the tangential damping coefficient (γ_t). Intermediate quantities in eq. A.10 are defined in eq. A.11.

$$F_{t,d} = -\gamma_t v_t$$

$$\gamma_t = -2\sqrt{\frac{5}{6}}\beta\sqrt{S_t m_{eq}} \tag{A.10}$$

$$\beta = \frac{ln(e)}{\sqrt{ln(e)^2 + \pi^2}}$$

$$S_t = 8G_{eq}\sqrt{R_{eq}\delta_n} \tag{A.11}$$

The total tangential contact force (eq. A.12) is then $F_t = F_{t_e} + F_{t,d}$. However, F_t is re-scaled and δ_t becomes 'historical' when the contact is in the Coulomb sliding regime (μ_s - sliding friction coefficient). Including contact history is important for capturing shear behavior of an assembly ([203]).

$$\mathbf{F}_t = -k_t \delta_t^{3/2} - \gamma_t v_t$$

$$\mid F_t \mid \leq \mu_s \mid F_n \mid \tag{A.12}$$

Rolling friction is included to provide packing support and mimic aspherical particles. Rolling ([204], [205]) and twisting ([205]) friction are needed to accurately capture shear response. See [74] for a comprehensive overview of the model and a helpful diagram (their Figure 3). We provide a brief overview here. We model rolling friction (eq. A.13) as an elastic-plastic-spring-dashpot (EPSD) which includes a spring torque ($M_{r,k}$) and a viscous damping torque ($M_{r,d}$).

$$\mathbf{M}_r = \mathbf{M}_{r,k} + \mathbf{M}_{r,d} \tag{A.13}$$

The spring torque is computed incrementally (eq. A.14) using the relative rotation between the particles ($\Delta\boldsymbol{\theta}$) and the rolling spring stiffness, k_r. The spring torque depends on the rolling friction parameter (μ_r) and is limited to the torque achieved at full mobilization ($M_{r,k}^m = \mu_r R_{eq} F_n$) which allows for cyclic rolling. The relative rotation implementation of rolling friction also captures twisting (torsional) friction ([77]).

$$\mathbf{M}_{r,k}^{t+\Delta t} = \mathbf{M}_{r,k}^{t} + \Delta\mathbf{M}_{r,k}$$

$$\Delta\mathbf{M}_{r,k} = -k_r \Delta\boldsymbol{\theta}$$

$$\mid M_{r,t+\Delta t}^{k} \mid \leq M_{r,k}^{m}$$

$$k_r = 2.55 k_n \mu_r^2 R_{eq}^2 \tag{A.14}$$

The damping torque (eq. A.15) depends on the relative rolling angular velocity ($\dot{\boldsymbol{\theta}}$) and is dependent on the rolling damping parameter, γ_r. The full model from [74] allows for different damping regimes but our implementation considers the case where viscous damping torque is active only before the particle has become fully mobilized as was done in [77].

$$\mathbf{M}_{r,d}^{t+\Delta t} = -\gamma_r \dot{\boldsymbol{\theta}} \text{ while } \mid M_{r,t+\Delta t}^{k} \mid \leq M_{r,k}^{m}$$

$$\text{else } = 0 \tag{A.15}$$

In equation A.16 we give the governing equations which are integrated at each step. Torque, normal and tangential contact forces, and gravity are included. Gravitational force is $F_g = m\boldsymbol{g}$, with g the gravitational acceleration vector. $\mathbf{x}_i$ is the particle state, $\mathbf{r}_{c,i}$ the vector connecting the centers of the colliding particles, I_i the equivalent moment of inertia of the contact, and $\boldsymbol{\omega}_i$ the angular velocity:

$$m_i \ddot{\mathbf{x}}_i = \mathbf{F}_{n,i} + \mathbf{F}_{t,i} + \mathbf{F}_{g,i}$$
$$I_i \frac{d\boldsymbol{\omega}_i}{dt} = \mathbf{r}_{c,i} \times \mathbf{F}_{t,i} + \mathbf{M}_{r,i} \tag{A.16}$$

We use $\Delta t < 0.01\tau_c$ (eq. A.17, [79]), with V_{in} the incident particle velocity and M and R the mass and radius of the incident particle.

$$\tau_c = 2.94 \left(\frac{m_{eq}^2}{\left(\frac{16}{15}\right)^2 E_{eq}^2 R V_{in}} \right)^{1/5} \tag{A.17}$$

Appendix B: Wave Visualization

We provide a visualization of the laterally propagating wave as it decays from the initially induced shock and propagates through our granular assembly as a solitary wave. Figure B.1 shows the force evolution of particles in the bed over time.

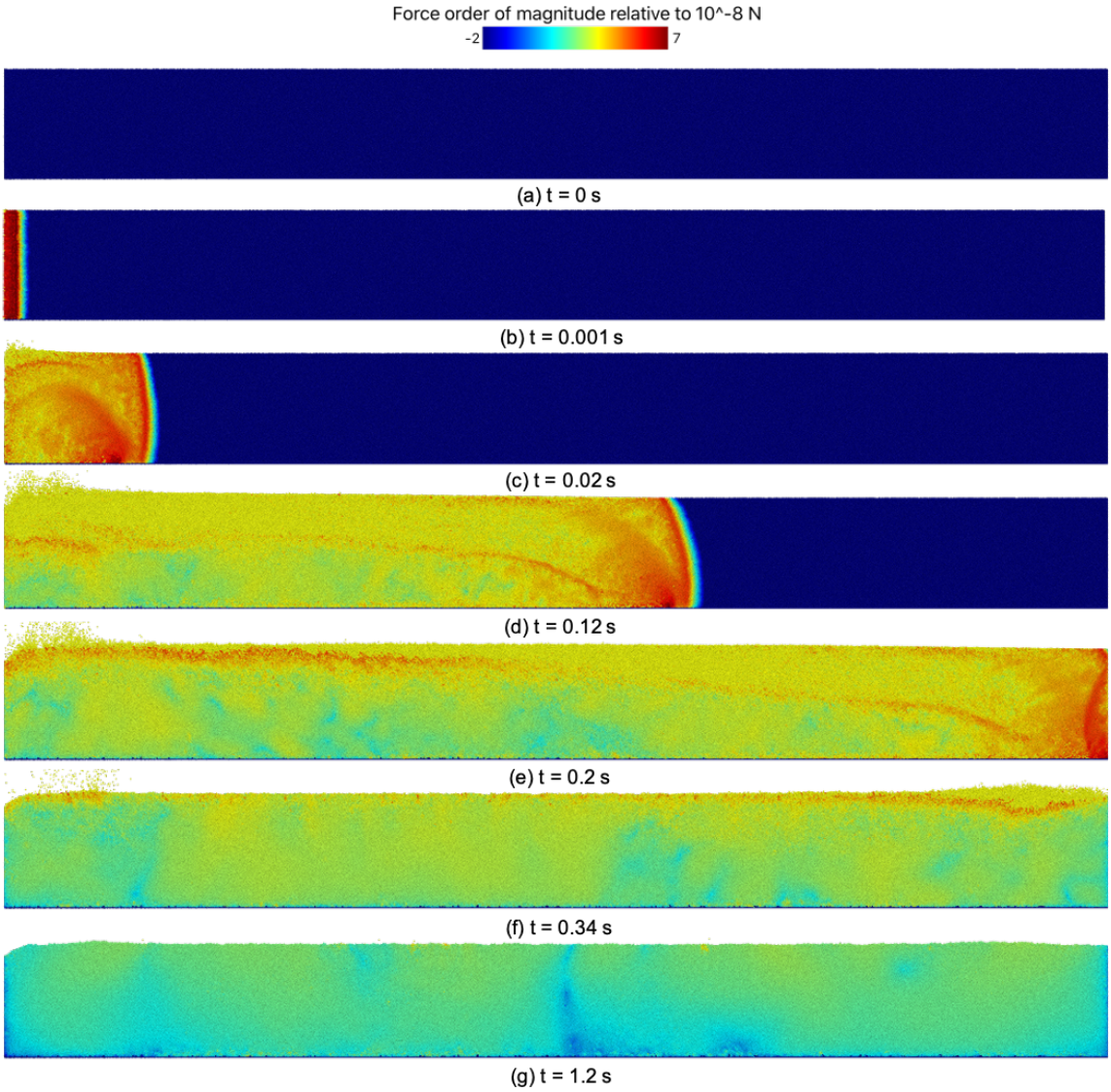


Figure B.1: **Wave Visualization.** Wave propagation seen through force visualization. We performed the shocking procedure on a 2 m channel filled 20 cm deep with grains (compact packing). Each particle is colored based on a scale that represents the order of magnitude force experienced, relative to 10^{-8} N. Frame (a) is the settled particle bed. In Frame (b), the shock has been initiated and the wavefront is uniform. In Frame (c) the wave is propagating as a solitary wave and the front has acquired curvature due to slower surface speeds than those at depth. Frame (d) shows the beginning of the reflected floor wave and mobilization of surface particles in the first 1m of the channel is already evident. In Frame (e) the shock has just reached the end wall and Frame (f) shows that the reflected wave terminates before it can travel back down the channel. The reflected floor wave reaches the surface grains, though note the thin strip of particles that do not experience a force from this reflection. These are the fully detached particles. Frame (g) show that the surface modification remains while the bed begins to settle. The small high force region at the surface in the middle of the channel is the result of an ejected particle returning to the surface, which does not further modify bed height.

Bibliography

[1] J.L. Bandfield, E. Song, P.O. Hayne, B.D. Brand, R.R. Ghent, A.R. Vasavada, and D.A. Paige. Lunar cold spots: Granular flow features and extensive insulating materials surrounding young craters. *Icarus*, 231:221–231, 2014. https://doi.org/10.1016/j.icarus.2013.12.017.

[2] W.W. Mendell and F.J. Low. Preliminary results of the Apollo 17 infrared scanning radiometer. *The Moon*, 9(1-2):97–103, 1974. https://doi.org/10.1007/BF00565396.

[3] P.O. Hayne, J.L. Bandfield, M.A. Siegler, A.R. Vasavada, R.R. Ghent, J.-P. Williams, B.T. Greenhagen, O. Aharonson, C.M. Elder, P.G. Lucey, et al. Global regolith thermophysical properties of the Moon from the Diviner Lunar Radiometer Experiment. *J. of Geophys. Res.: Planets*, 122(12):2371–2400, 2017. https://doi.org/10.1002/2017JE005387.

[4] J.L. Bandfield, R.R. Ghent, A.R. Vasavada, D.A. Paige, S.J. Lawrence, and M.S. Robinson. Lunar surface rock abundance and regolith fines temperatures derived from LRO Diviner Radiometer data. *J. of Geophys. Res.: Planets*, 116(E12), 2011. https://doi.org/10.1029/2011JE003866.

[5] D.A. Paige, M.C. Foote, B.T. Greenhagen, J.T. Schofield, S. Calcutt, A.R. Vasavada, D.J. Preston, F.W. Taylor, C.C. Allen, K.J. Snook, et al. The Lunar Reconnaissance Orbiter Diviner Lunar Radiometer Experiment. *Space Sci. Rev.*, 150(1-4):125–160, 2010. https://doi.org/10.1007/s11214-009-9529-2.

[6] J.-P. Williams, J.L. Bandfield, D.A. Paige, T.M. Powell, B.T. Greenhagen, S. Taylor, P.O. Hayne, E.J. Speyerer, R.R. Ghent, and E.S. Costello. Lunar Cold Spots and Crater Production on the Moon. *J. of Geophys. Res.: Planets*, 123(9):2380–2392, 2018. https://doi.org/10.1029/2018JE005652.

[7] J. Venkatraman, T. Horvath, T.M. Powell, and D.A. Paige. Statistical estimates of rock-free lunar regolith thickness from Diviner. *Planetary and Space Science*, 229:105662, 2023. https://doi.org/10.1016/j.pss.2023.105662.

[8] T.M. Powell, T. Horvath, V.L. Robles, J.-P. Williams, P.O. Hayne, C.L. Gallinger, B.T. Greenhagen, D.S. McDougall, and D.A. Paige. High-resolution nighttime temperature and rock abundance mapping of the Moon using the Diviner Lunar Radiometer Experiment with a model for topographic removal. *J. of Geophys. Res.: Planets*, 128(2):e2022JE007532, 2023. https://doi.org/10.1029/2022JE007532.

[9] F. Hörz, R. Grieve, G. Heiken, P. Spudis, and A. Binder. Lunar surface processes. In A user's guide to the Moon Lunar sourcebook, editor, *Heiken, Grant H. and Vaniman, David T. and Bevan, M. F.*, volume 7, pages 61–120. Press Syndicate of the University of Cambridge, New York, 1991.

[10] J.R. Hill and P.R. Christensen. Well-preserved low thermal inertia ejecta deposits surrounding young secondary impact craters on Mars. *J. of Geophys. Res.: Planets*, 122(6):1276–1299, 2017. https://doi.org/10.1002/2016JE005210.

[11] T.M. Powell, J.-P. Williams, B.T. Greenhagen, P.O. Hayne, and D.A. Paige. Discovery of a Lunar Cold Spot at the Apollo 16 South Ray Crater. *LPI Contributions*, 2806:2780, 2023. https://ui.adsabs.harvard.edu/abs/2023LPICo2806.2780P/abstract.

[12] E.S. Costello, R.R. Ghent, M. Hirabayashi, and P.G. Lucey. Impact gardening as a constraint on the age, source, and evolution of ice on Mercury and the Moon. *J. of Geophys. Res.: Planets*, 125(3):e2019JE006172, 2020. https://doi.org/10.1029/2019JE006172.

[13] S. Creech, J. Guidi, and D. Elburn. Artemis: an overview of NASA's activities to return humans to the Moon. In *2022 IEEE Aerospace Conference*, pages 1–7. IEEE, 2022. https://doi.org/10.1109/AERO53065.2022.9843277.

[14] D.S. McKay, G. Heiken, A. Basu, G. Blanford, S. Simon, R. Reedy, M.F. Bevan, and J. Papike. The lunar regolith. In Lunar Sourcebook: a user's guide to the Moon, editor, *Heiken, Grant H. and Vaniman, David T. and Bevan, M. F.*, volume 7, pages 285–356. Press Syndicate of the University of Cambridge, New York, 1991.

[15] W.D. Carrier III, G.R. Olhoeft, and W. Mendell. Physical properties of the lunar surface. In Lunar Sourcebook: A user's guide to the Moon, editor, *Heiken, G.H. and Vaniman, D.T. and Bevan, M.F.*, pages 475–594. Press Syndicate of the University of Cambridge, New York, 1991.

[16] C. Li, J. Liu, X. Ren, W. Zuo, X. Tan, W. Wen, H. Li, L. Mu, Y. Su, H. Zhang, et al. The Chang'e 3 mission overview. *Space Sci. Rev.*, 190:85–101, 2015. https://doi.org/10.1007/s11214-014-0134-7.

[17] T.N. Gowd and F. Rummel. Effect of confining pressure on the fracture behaviour of a porous rock. In *Int. J. of Rock Mech. and Mining Sci. & Geomech. Abstracts*, volume 17, pages 225–229. Elsevier, 1980. https://doi.org/10.1016/0148-9062(80)91089-X.

[18] S.E. Wiggins, B.C. Johnson, T.J. Bowling, H.J. Melosh, and E.A. Silber. Impact fragmentation and the development of the deep lunar megaregolith. *J. of Geophys. Res.: Planets*, 124(4):941–957, 2019. https://doi.org/10.1029/2018JE005757.

[19] K. Sadigh, C.-Y. Chang, J.A. Egan, F. Makdisi, and R.R. Youngs. Attenuation relationships for shallow crustal earthquakes based on California strong motion data. *Seismological Res. Lett.*, 68(1):180–189, 1997. http://dx.doi.org/10.1785/gssrl.68.1.180.

[20] K.E. Daniels. Rubble-pile near Earth objects: Insights from granular physics. *Asteroids: Prospective Energy and Mat. Resour.*, pages 271–286, 2013. https://doi.org/10.1007/978-3-642-39244-3_11.

[21] S.R. Taylor. Lunar science: an overview. *J. of Earth Sys. Sci.*, 114:587–591, 2005. https://doi.org/10.1007/BF02715941.

[22] R.W. Carlson. Analysis of lunar samples: Implications for planet formation and evolution. *Science*, 365(6450):240–243, 2019. https://doi.org/10.1126/science.aaw7580.

[23] P. Brown, R.E. Spalding, D.O. ReVelle, E. Tagliaferri, and S.P. Worden. The flux of small near-Earth objects colliding with the Earth. *Nature*, 420(6913):294–296, 2002. https://doi.org/10.1038/nature01238.

[24] H.A Perko, J.D. Nelson, and W.Z. Sadeh. Surface cleanliness effect on lunar soil shear strength. *J. of Geotech. and Geoenv. Eng.*, 127(4):371–383, 2001. https://doi.org/10.1061/(ASCE)1090-0241(2001)127:4(371).

[25] JE Colwell, SR Robertson, M Horányi, X Wang, A Poppe, and P Wheeler. Lunar dust levitation. *J. of Aero. Eng.*, 22(1):2–9, 2009. https://doi.org/10.1061/(ASCE)0893-1321(2009)22:1(2).

[26] C. Li, Y. Su, E. Pettinelli, S. Xing, C. Ding, J. Liu, X. Ren, S.E. Lauro, F. Soldovieri, X. Zeng, et al. The Moon's farside shallow subsurface structure unveiled by Chang'E-4 Lunar Penetrating Radar. *Sci. Adv.*, 6(9):eaay6898, 2020. https://doi.org/10.1126/sciadv.aay6898.

[27] James E Richardson and Oleg Abramov. Modeling the formation of the lunar upper megaregolith layer. *The Planetary Science Journal*, 1(1):2, 2020. https://doi.org/10.3847/PSJ/ab7235.

[28] G. Latham, M. Ewing, J. Dorman, F. Press, N Toksoz., G Sutton., R. Meissner, F. Duennebier, Y. Nakamura, R. Kovach, et al. Seismic data from man-made impacts on the Moon. *Science*, 170(3958):620–626, 1970. https://doi.org/10.1126/science.170.3958.620.

[29] A.M. Dainty, M.N. Toksöz, K.R. Anderson, P.J. Pines, Y. Nakamura, and G. Latham. Seismic scattering and shallow structure of the Moon in Oceanus Procellarum. *The Moon*, 9:11–29, 1974. https://doi.org/10.1007/BF00565388.

[30] M. N. Toksöz, A.M Dainty, S.C. Solomon, and K.R. Anderson. Structure of the Moon. *Reviews of Geophysics*, 12(4):539–567, 1974. https://doi.org/10.1029/RG012i004p00539.

[31] M.R. Cooper, R.L. Kovach, and J.S. Watkins. Lunar near-surface structure. *Rev. of Geophys.*, 12(3):291–308, 1974. https://doi.org/10.1029/RG012i003p00291.

[32] T.W. Thompson, W.J. Roberts, W.K. Hartmann, R.W. Shorthill, and S.H. Zisk. Blocky craters: Implications about the lunar megaregolith. *The moon and the planets*, 21:319–342, 1979. https://doi.org/10.1007/BF00897360.

[33] M.A. Ivanov, A.T. Basilevsky, A.M. Abdrakhimov, I.P. Karachevtseva, A.A. Kokhanov, and J.W. Head. Crater Boguslawsky on the Moon: Geological structure and an estimate of the degree of rockiness of the floor. *Solar Sys. Res.*, 49:367–382, 2015. https://doi.org/10.1134/S0038094615060039.

[34] H.M. Jaeger, S.R. Nagel, and R.P. Behringer. The physics of granular materials. *Rev. of Mod. Phys.*, 49(4):32–38, 1996. https://doi.org/10.1103/RevModPhys.68.1259.

[35] S. Matsumura, D.C. Richardson, P. Michel, S.R. Schwartz, and R.-L. Ballouz. The Brazil nut effect and its application to asteroids. *Month. Not. of the R. Astro. Soc.*, 443(4):3368–3380, 2014. https://doi.org/10.1093/mnras/stu1388.

[36] O. Reynolds. LVII. On the dilatancy of media composed of rigid particles in contact. With experimental illustrations. *The Lond., Edinb., and Dublin Philosoph. Mag. and J. of Sci.*, 20(127):469–481, 1885. https://doi.org/10.1080/14786448508627791.

[37] J. Duran. *Sands, powders, and grains: an introduction to the physics of granular materials*. Springer Science & Business Media, 2012. https://doi.org/10.1007/978-1-4612-0499-2.

[38] E.R. Nowak, J.B. Knight, E. Ben-Naim, H.M. Jaeger, and S.R. Nagel. Density fluctuations in vibrated granular materials. *Phys. Rev. E*, 57(2):1971, 1998. https://doi.org/10.1103/PhysRevE.57.1971.

[39] J.B. Knight, C.G. Fandrich, C.N. Lau, H.M. Jaeger, and S.R. Nagel. Density relaxation in a vibrated granular material. *Phys. Rev. E*, 51(5):3957, 1995. https://doi.org/10.1103/PhysRevE.51.3957.

[40] P. Philippe and D. Bideau. Compaction dynamics of a granular medium under vertical tapping. *Europhys. Lett.*, 60(5):677, 2002. https://doi.org/10.1209/epl/i2002-00362-7.

[41] N.J. Van der Elst, E.E. Brodsky, P.-Y. Le Bas, and P.A. Johnson. Auto-acoustic compaction in steady shear flows: Experimental evidence for suppression of shear dilatancy by internal acoustic vibration. *J. of Geophys. Res.: Solid Earth*, 117(B9), 2012. https://doi.org/10.1029/2011JB008897.

[42] C. Wensrich. Dissipation, dispersion, and shocks in granular media. *Powder Tech.*, 126(1):1–12, 2002. https://doi.org/10.1016/S0032-5910(02)00003-7.

[43] C. Wensrich. Numerical modeling of quaking in tall silos. *Int. J. of Mech. Sci.*, 45(3):541–551, 2003. https://doi.org/10.1016/S0020-7403(03)00057-2.

[44] Y. Wang, C.M. Wensrich, and J.Y. Ooi. Rarefaction wave propagation in tapered granular columns. *Chem. Eng. Sci.*, 71:32–38, 2012. https://doi.org/10.1016/j.ces.2011.12.023.

[45] R. Kobyłka, J. Horabik, and M. Molenda. Development of a rarefaction wave at discharge initiation in a storage silo—DEM simulations. *Particuology*, 36:37–49, 2018. https://doi.org/10.1016/j.partic.2017.03.006.

[46] A. Leonard, C. Daraio, A.P. Awasthi, and P. Geubelle. Effects of weak disorder on stress-wave anisotropy in centered square nonlinear granular crystals. *Phys. Rev. E*, 86(3):031305, 2012. https://doi.org/10.1103/PhysRevE.86.031305.

[47] S. van den Wildenberg, R. van Loo, and M. van Hecke. Shock waves in weakly compressed granular media. *Phys. Rev. Letters*, 111(21):218003, 2013. https://doi.org/10.1103/PhysRevLett.111.218003.

[48] V.F. Nesterenko. Propagation of nonlinear compression pulses in granular media. *J. Appl. Mech. Tech. Phys.(Engl. Transl.);(United States)*, 24(5), 1984. https://doi.org/10.1007/BF00905892.

[49] R.-L. Ballouz, K.J. Walsh, P. Sanchez, K.A. Holsapple, P. Michel, D.J. Scheeres, Y. Zhang, D.C. Richardson, O.S. Barnouin, M.C. Nolan, et al. Modified granular impact force laws for the OSIRIS-REx touchdown on the surface of asteroid (101955) Bennu. *Mon. Not. of the R. Astro. Soc.*, 507(4):5087–5105, 2021. https://doi.org/10.1093/mnras/stab2365.

[50] H. Miyamoto, H. Yano, D.J. Scheeres, S. Abe, O. Barnouin-Jha, A.F. Cheng, H. Demura, R.W. Gaskell, N. Hirata, M. Ishiguro, et al. Regolith migration and sorting on asteroid Itokawa. *Science*, 316(5827):1011–1014, 2007. https://doi.org/10.1126/science.1134390.

[51] T. Shinbrot, T. Sabuwala, T. Siu, M.V. Lazo, and P. Chakraborty. Size sorting on the rubble-pile asteroid Itokawa. *Phys. Rev. Lett.*, 118(11):111101, 2017. https://doi.org/10.1103/PhysRevLett.118.111101.

[52] E. Wright, A.C. Quillen, J. South, R.C. Nelson, P. Sanchez, L. Martini, S.R. Schwartz, M. Nakajima, and E. Asphaug. Boulder stranding in ejecta launched by an impact generated seismic pulse. *Icarus*, 337:113424, 2020. https://doi.org/10.1016/j.icarus.2019.113424.

[53] S.D. Raducan, M. Jutzi, A.F. Cheng, Y. Zhang, O. Barnouin, G.S. Collins, R.T. Daly, T.M. Davison, C.M. Ernst, T.L. Farnham, et al. Physical properties of asteroid Dimorphos as derived from the DART impact. *Nat. Astro.*, pages 1–11, 2024.

[54] G. Tancredi, P-Y Liu, A. Campo-Bagatin, F. Moreno, and B Dominguez. Lofting of low speed ejecta produced in the DART experiment and production of a dust cloud. *Mon. Not. of the R. Astro. Soc.*, 2022. https://doi.org/10.1093/mnras/stac3258.

[55] P. Sánchez, D.J. Scheeres, and A.C. Quillen. Transmission of a seismic wave generated by impacts on granular asteroids. *The Planet. Sci. J.*, 3(10):245, 2022. https://doi.org/10.3847/PSJ/ac960c.

[56] A.C. Quillen, Y. Zhao, Y. Chen, P. Sánchez, R.C. Nelson, and S.R. Schwartz. Impact excitation of a seismic pulse and vibrational normal modes on asteroid Bennu and associated slumping of regolith. *Icarus*, 319:312–333, 2019. https://doi.org/10.1016/j.icarus.2018.09.032.

[57] A.C. Quillen, M. Neiderbach, B. Suo, J. South, E. Wright, N. Skerrett, P. Sánchez, F.D. Cúñez, P. Miklavcic, and H. Askari. Propagation and attenuation of pulses driven by low velocity normal impacts in granular media. *Icarus*, 386:115139, 2022. https://doi.org/10.1016/j.icarus.2022.115139.

[58] Y. Nakamura, G.V. Latham, and H.J. Dorman. Apollo lunar seismic experiment—Final summary. *J. of Geophys. Res.: Solid Earth*, 87(S01):A117–A123, 1982. https://doi.org/10.1029/JB087iS01p0A117.

[59] A. Di Renzo and F.P. Di Maio. Comparison of contact-force models for the simulation of collisions in DEM-based granular flow codes. *Chemical engineering science*, 59(3):525–541, 2004. https://doi.org/10.1016/j.ces.2003.09.037.

[60] M. Paulick, M. Morgeneyer, and A. Kwade. Review on the influence of elastic particle properties on DEM simulation results. *Powder Tech.*, 283:66–76, 2015. https://doi.org/10.1016/j.powtec.2015.03.040.

[61] C. Coste and B. Gilles. On the validity of Hertz contact law for granular material acoustics. *The Euro. Phys. J. B-Condens. Matter and Complex Sys.*, 7(1):155–168, 1999. https://doi.org/10.1007/s100510050598.

[62] V.F. Nesterenko. *Dynamics of heterogeneous materials*. Springer Science & Business Media, 2013. https://doi.org/10.1007/978-1-4757-3524-6.

[63] G.S. Collins. Numerical simulations of impact crater formation with dilatancy. *J. of Geophys. Res.: Planets*, 119(12):2600–2619, 2014. https://doi.org/10.1002/2014JE004708.

[64] H.A. Makse, N. Gland, D.L. Johnson, and L.M. Schwartz. Why effective medium theory fails in granular materials. *Phys. Rev. Lett.*, 83(24):5070, 1999. https://doi.org/10.1103/PhysRevLett.83.5070.

[65] P.A. Cundall and O.DL. Strack. A discrete numerical model for granular assemblies. *Géotechnique*, 29(1):47–65, 1979. https://doi.org/10.1680/geot.1979.29.1.47.

[66] D.C. Richardson, K.J. Walsh, N. Murdoch, and P. Michel. Numerical simulations of granular dynamics: I. Hard-sphere discrete element method and tests. *Icarus*, 212(1):427–437, 2011. https://doi.org/10.1016/j.icarus.2010.11.030.

[67] S.R. Schwartz, D.C. Richardson, and P. Michel. An implementation of the Soft-Sphere Discrete Element Method in a high-performance parallel gravity tree-code. *Granular Matter*, 14(3):363–380, 2012. https://doi.org/10.1007/s10035-012-0346-z.

[68] C. Kloss, C. Goniva, A. Hager, S. Amberger, and S. Pirker. Models, algorithms and validation for opensource DEM and CFD–DEM. *Prog. in Comp. Fluid Dyn., an Int. J.*, 12(2-3):140–152, 2012. https://doi.org/10.1504/PCFD.2012.047457.

[69] T. Leps, P.E. Glick, D. Ruffatto III, A. Parness, M.T. Tolley, and C. Hartzell. A low-power, jamming, magnetorheological valve using electropermanent magnets suitable for distributed control in soft robots. *Smart Mat. and Struct.*, 29(10):105025, 2020. https://doi.org/10.1088/1361-665X/abadd4.

[70] T. Leps and C. Hartzell. High fidelity, Discrete Element Method simulation of magnetorheological fluids using accurate particle size distributions in LIGGGHTS extended with mutual dipole method. *Mat. Res. Express*, 8(8):085701, 2021. https://doi.org/10.1088/2053-1591/ac113c.

[71] C. Sunday, N. Murdoch, S. Tardivel, S.R. Schwartz, and P. Michel. Validating N-body code CHRONO for granular DEM simulations in reduced-gravity environments. *Mon. Notices of the Roy. Astronom. Soc.*, 498(1):1062–1079, 2020. https://doi.org/10.1093/mnras/staa2454.

[72] K. Yu, H.A. Elghannay, and D. Tafti. An impulse based model for spherical particle collisions with sliding and rolling. *Powder Tech.*, 319:102–116, 2017. https://doi.org/10.1016/j.powtec.2017.06.049.

[73] C.-Y. Wu, C. Thornton, and L.-Y. Li. Coefficients of restitution for elastoplastic oblique impacts. *Adv. Powder Tech.*, 14(4):435–448, 2003. https://doi.org/10.1163/156855203769710663.

[74] J. Ai, J.-F. Chen, J.M. Rotter, and J.Y. Ooi. Assessment of rolling resistance models in discrete element simulations. *Powder Technol.*, 206(3):269–282, 2011. https://doi.org/10.1016/j.powtec.2010.09.030.

[75] Ying Yan and Shunying Ji. Discrete Element Modeling of direct shear tests for a granular material. *Int. J. for Num. and Anal. Meth. in Geomech.*, 34(9):978–990, 2010. https://doi.org/10.1002/nag.848.

[76] R. Ramírez, T. Pöschel, N.V. Brilliantov, and T. Schwager. Coefficient of restitution of colliding viscoelastic spheres. *Phys. Rev. E*, 60(4):4465, 1999. https://doi.org/10.1103/PhysRevE.60.4465.

[77] P. Sánchez and D.J. Scheeres. Disruption patterns of rotating self-gravitating aggregates: A survey on angle of friction and tensile strength. *Icarus*, 271:453–471, 2016. https://doi.org/10.1016/j.icarus.2016.01.016.

[78] M.A.J. Holmes, R. Brown, P.A.L. Wauters, N.P. Lavery, and S.G.R. Brown. Bending and twisting friction models in soft-sphere discrete element simulations for static and dynamic problems. *Appl. Math. Modelling*, 40(5-6):3655–3670, 2016. https://doi.org/10.1016/j.apm.2015.10.026.

[79] M.S. Abd-Elhady, S. Abd-Elhady, C.C.M. Rindt, and A.A. Van Steenhoven. Force propagation speed in a bed of particles due to an incident particle impact. *Adv. Powder Tech.*, 21(2):150–164, 2010. https://doi.org/10.1016/j.apt.2009.11.009.

[80] M.S. Abd-Elhady, C.C.M. Rindt, and A.A. van Steenhoven. Contact time of an incident particle hitting a 2D bed of particles. *Powder Technol.*, 191(3):315–326, 2009. https://doi.org/10.1016/j.powtec.2008.10.024.

[81] M.S. Abd-Elhady, C.C.M. Rindt, J.G. Wijers, and A.A. Van Steenhoven. Modelling the impaction of a micron particle with a powdery layer. *Powder Tech.*, 168(3):111–124, 2006. https://doi.org/10.1016/j.powtec.2006.06.013.

[82] R. Berger, C. Kloss, A. Kohlmeyer, and S. Pirker. Hybrid parallelization of the LIGGGHTS open-source DEM code. *Powder Tech.y*, 278:234–247, 2015. https://doi.org/10.1016/j.powtec.2015.03.019.

[83] C. Thornton and Z. Ning. A theoretical model for the stick/bounce behaviour of adhesive, elastic-plastic spheres. *Powder Tech.*, 99(2):154–162, 1998. https://doi.org/10.1016/S0032-5910(98)00099-0.

[84] L.R. Gómez, A.M. Turner, M. van Hecke, and V. Vitelli. Shocks near jamming. *Phys. Rev. Letters*, 108(5):058001, 2012. https://doi.org/10.1103/PhysRevLett.108.058001.

[85] J.R. Royer, B. Conyers, E.I. Corwin, P.J. Eng, and H.M. Jaeger. The role of interstitial gas in determining the impact response of granular beds. *Europhys. Lett.*, 93(2):28008, 2011. https://doi.org/10.1209/0295-5075/93/28008.

[86] H.-J. Tillemans and H.J. Herrmann. Simulating deformations of granular solids under shear. *Physica A: Stat. Mech. and its Appl.*, 217(3-4):261–288, 1995. https://doi.org/10.1016/0378-4371(95)00111-J.

[87] C. Wensrich. Experimental behaviour of quaking in tall silos. *Powder Technol.*, 127(1):87–94, 2002. https://doi.org/10.1016/S0032-5910(02)00105-5.

[88] S. Sture, N.C. Costes, S.N. Batiste, M.R. Lankton, K.A. AlShibli, B. Jeremic, R.A. Swanson, and M. Frank. Mechanics of granular materials at low effective stresses. *J. of Aero. Eng.*, 11(3):67–72, 1998. https://doi.org/10.1061/(ASCE)0893-1321(1998)11:3(67).

[89] V. Tournat, V.Y. Zaitsev, V.E. Nazarov, V.E. Gusev, and B. Castagnède. Experimental study of nonlinear acoustic effects in a granular medium. *Acoustical Phys.*, 51(5):543–553, 2005. https://doi.org/10.1134/1.2042573.

[90] C.S. Campbell. Stress-controlled elastic granular shear flows. *J. of Fluid Mech.*, 539:273–297, 2005. https://doi.org/10.1017/S0022112005005616.

[91] K.J. Walsh, R.-L. Ballouz, E.R. Jawin, C. Avdellidou, O.S. Barnouin, C.A. Bennett, E.B. Bierhaus, B.J. Bos, S. Cambioni, H.C. Connolly Jr, et al. Near-zero cohesion and loose packing of Bennu's near subsurface revealed by spacecraft contact. *Sci. Adv.*, 8(27):eabm6629, 2022. https://doi.org/10.1126/sciadv.abm6229.

[92] N. Murdoch, B. Rozitis, K. Nordstrom, S.F. Green, P. Michel, T.-L. de Lophem, and W. Losert. Granular convection in microgravity. *Phys. Rev. Lett.*, 110:018307, Jan 2013. https://link.aps.org/doi/10.1103/PhysRevLett.110.018307.

[93] J.V. Farr. *Loading rate effects on the one-dimensional compressibility of four partially saturated soils*. University of Michigan, 1986.

[94] K.A. Holsapple. The scaling of impact processes in planetary sciences. *Ann. Rev. of Earth and Planet. Sci.*, 21(1):333–373, 1993. https://doi.org/10.1146/annurev.ea.21.050193.002001.

[95] K.M. Aoki and T. Akiyama. Simulation studies of pressure and density wave propagations in vertically vibrated beds of granules. *Phys. Rev. E*, 52(3):3288, 1995. https://doi.org/10.1103/PhysRevE.52.3288.

[96] V. Gusev, V. Aleshin, and V. Tournat. Reflection of nonlinear acoustic waves from the mechanically free surface of an unconsolidated granular medium. *Acta Acustica United w. Acustica*, 94(2):215–228, 2008. https://doi.org/10.3813/AAA.918025.

[97] A. Goldshtein, M. Shapiro, and C. Gutfinger. Mechanics of collisional motion of granular materials. Part 4. Expansion wave. *J. of Fluid Mech.*, 327:117–138, 1996. https://doi.org/10.1017/S0022112096008488.

[98] M. Omidvar, M. Iskander, and S. Bless. Stress-strain behavior of sand at high strain rates. *Int. J. of Impact Eng.*, 49:192–213, 2012. https://doi.org/10.1016/j.ijimpeng.2012.03.004.

[99] G. Lu and M. Fall. State-of-the-art modelling of soil behaviour under blast loading. *Geotech. and Geolog. Eng.*, 36:3331–3355, 2018. https://doi.org/10.1007/s10706-018-0560-5.

[100] E. Brown and H.M. Jaeger. The role of dilation and confining stresses in shear thickening of dense suspensions. *J. of Rheology*, 56(4):875–923, 2012. https://doi.org/10.1122/1.4709423.

[101] J. Duffy and R.D. Mindlin. Stress-strain relations and vibrations of a granular medium. *J. of Appl. Mech.*, 24(4):585–593, 1957. https://doi.org/10.1115/1.4011605.

[102] C. Coste, E. Falcon, and S. Fauve. Solitary waves in a chain of beads under Hertz contact. *Phys. Rev. E*, 56(5):6104, 1997. https://doi.org/10.1103/PhysRevE.56.6104.

[103] S. Sen, M. Manciu, and J.D. Wright. Solitonlike pulses in perturbed and driven Hertzian chains and their possible applications in detecting buried impurities. *Phys. Rev. E*, 57(2):2386, 1998. https://doi.org/10.1103/PhysRevE.57.2386.

[104] J. Hong, H. Kim, and J.-P. Hwang. Characterization of soliton damping in the granular chain under gravity. *Phys. Rev. E*, 61(1):964, 2000. https://doi.org/10.1103/PhysRevE.61.964.

[105] M. Shoaib and L. Kari. Discrete element simulation of elastoplastic shock wave propagation in spherical particles. *Adv. in Acoust. and Vib.*, 2011, 2011. https://doi.org/10.1155/2011/123695.

[106] S. Chakravarty and S. Sen. Possibility of useful mechanical energy from noise: the solitary wave train problem in the granular chain revisited. *Granular Matter*, 20(3):1–10, 2018. https://doi.org/10.1007/s10035-018-0811-4.

[107] A. Shukla and C. Damania. Experimental investigation of wave velocity and dynamic contact stresses in an assembly of disks. *Exp. Mech.*, 27(3):268–281, 1987. https://doi.org/10.1007/BF02318093.

[108] S. Sen and R.S. Sinkovits. Sound propagation in impure granular columns. *Phys. Rev. E*, 54(6):6857, 1996. https://doi.org/10.1103/PhysRevE.54.6857.

[109] E.T. Owens and K.E. Daniels. Sound propagation and force chains in granular materials. *Europhys. Lett.*, 94(5):54005, 2011. https://doi.org/10.1209/0295-5075/94/54005.

[110] M. Nishida, K. Tanaka, and T. Ishida. DEM simulation of wave propagation in two-dimensional ordered array of particles. In *Shock Waves*, pages 815–820. Springer, 2009. https://doi.org/10.1007/978-3-540-85181-3_3.

[111] A.P. Awasthi, K.J. Smith, P.H. Geubelle, and J. Lambros. Propagation of solitary waves in 2D granular media: A numerical study. *Mech. of Materials*, 54:100–112, 2012. https://doi.org/10.1016/j.mechmat.2012.07.005.

[112] A. Leonard, F. Fraternali, and C. Daraio. Directional wave propagation in a highly nonlinear square packing of spheres. *Exp. Mech.*, 53(3):327–337, 2013. https://doi.org/10.1007/s11340-011-9544-6.

[113] R.K. Pal, A.P. Awasthi, and P.H. Geubelle. Characterization of wave propagation in elastic and elastoplastic granular chains. *Phys. Rev. E*, 89(1):012204, 2014. https://doi.org/10.1103/PhysRevE.89.012204.

[114] R.F. Waymel, E. Wang, A.P. Awasthi, P.H. Geubelle, and J. Lambros. Propagation and dissipation of elasto-plastic stress waves in two dimensional ordered granular media. *J. of the Mech. and Phys. of Solids*, 120:117–131, 2018. https://doi.org/10.1016/j.jmps.2017.11.007.

[115] A. Leonard, C. Chong, P.G. Kevrekidis, and C. Daraio. Traveling waves in 2D hexagonal granular crystal lattices. *Granular Matter*, 16(4):531–542, 2014. https://doi.org/10.1007/s10035-014-0487-3.

[116] Q. Zhang, W. Li, J. Lambros, L.A. Bergman, and A.F. Vakakis. Pulse transmission and acoustic non-reciprocity in a granular channel with symmetry-breaking clearances. *Granular Matter*, 22(1):1–16, 2020. https://doi.org/10.1007/s10035-019-0982-7.

[117] V. Tournat and V.E. Gusev. Acoustics of unconsolidated "model" granular media: An overview of recent results and several open problems. *Acta Acustica united w. Acustica*, 96(2):208–224, 2010. https://doi.org/10.3813/AAA.918271.

[118] K. Tell, C. Dreißigacker, A.C. Tchapnda, P. Yu, and M. Sperl. Acoustic waves in granular packings at low confinement pressure. *Rev. of Sci. Instr.*, 91(3):033906, 2020. https://doi.org/10.1063/1.5122848.

[119] A.J. Rogers and C.G. Don. Location of buried objects by an acoustic impulse technique. *Acoustics Australia*, 22:5–5, 1994.

[120] S. Sen and M. Manciu. Solitary wave dynamics in generalized Hertz chains: An improved solution of the equation of motion. *Phys. Rev. E*, 64(5):056605, 2001. https://doi.org/10.1103/PhysRevE.64.056605.

[121] S. Sen, T.R. Krishna Mohan, D.P. Visco Jr, S. Swaminathan, A. Sokolow, E. Avalos, and M. Nakagawa. Using mechanical energy as a probe for the detection and imaging of shallow buried inclusions in dry granular beds. *Int. J. of Mod. Phys. B*, 19(18):2951–2973, 2005. "https://doi.org/10.1142/S0217979205031997".

[122] S. Sen, T.R. Krishna Mohan, and M. Tiwari. Impact dispersion using 2D and 3D composite granular packing. *KONA Powder and Particle J.*, page 2017014, 2017. https://doi.org/10.14356/kona.2017014.

[123] S.R. Hostler and C.E. Brennen. Pressure wave propagation in a granular bed. *Phys. Rev. E*, 72(3):031303, 2005. https://doi.org/10.1103/PhysRevE.72.031303.

[124] T. Jiao, W. Chen, Y. Takato, S. Sen, and D. Huang. Revisiting nesterenko's solitary wave in the precompressed granular alignment held between fixed ends. *Granular Matter*, 25(2):17, 2023.

[125] G.H. Sutton and F.K. Duennebier. Elastic properties of the lunar surface from Surveyor spacecraft data. *J. of Geophys. Res.*, 75(35):7439–7444, 1970. https://doi.org/10.1029/JB075i035p07439.

[126] O. Mouraille, O. Herbst, and S. Luding. Sound propagation in isotropically and uni-axially compressed cohesive, frictional granular solids. *Eng. Fracture Mech.*, 76(6):781–792, 2009. https://doi.org/10.1016/j.engfracmech.2008.09.001.

[127] F.R. Botello, A. Castellanos, and V. Tournat. Ultrasonic probing of cohesive granular media at very low consolidation. *Ultrasonics*, 69:193–200, 2016. https://doi.org/10.1016/j.ultras.2015.11.011.

[128] J.H. Agui and C.M. Creager. High impact wave propagation studies in lunar granular systems. In *Earth and Space 2018: Eng. for Extreme Environ.*, pages 99–108. American Society of Civil Engineers Reston, VA, 2018. https://doi.org/10.1061/9780784481899.011.

[129] X. Zeng, J.H. Agui, and M. Nakagawa. Wave velocities in granular materials under microgravity. *J. of Aero. Eng.*, 20(2):116–123, 2007. https://doi.org/10.1061/(ASCE)0893-1321(2007)20:2(116).

[130] S.AM. El Shourbagy, S. Okeda, and H.-G. Matuttis. Acoustic of sound propagation in granular materials in one, two, and three dimensions. *J. of the Phys. Soc. of Japan*, 77(3):034606–034606, 2008. https://doi.org/10.1143/jpsj.77.034606.

[131] H.A. Burgoyne, J.A. Newman, W.C. Jackson, and C. Daraio. Guided impact mitigation in 2D and 3D granular crystals. *Procedia Eng.*, 103:52–59, 2015.

[132] R.D.JI. Fonseka, A.P. Awasthi, J. Lambros, and P.H. Geubelle. Shockwaves in jammed ductile granular media. *J. of Appl. Mech.*, 89(5):051003, 2022. https://doi.org/10.1115/1.4053622.

[133] R.D.JI. Fonseka, P.H. Geubelle, and J. Lambros. Effect of confinement on the impact response of a granular array. *Exp. Mech.*, 62(5):849–862, 2022. https://doi.org/10.1007/s11340-022-00819-9.

[134] X. Jia, C. Caroli, and B. Velicky. Ultrasound propagation in externally stressed granular media. *Phys. Rev. Lett*, 82(9):1863, 1999. https://doi.org/10.1103/PhysRevLett.82.1863.

[135] J.D. Goddard and A.K. Didwania. Computations of dilatancy and yield surfaces for assemblies of rigid frictional spheres. *The Quart. J. of Mech. and Appl. Math.*, 51(1):15–44, 1998. https://doi.org/10.1093/qjmam/51.1.15.

[136] H.A. Makse, N. Gland, D.L. Johnson, and L. Schwartz. Granular packings: Nonlinear elasticity, sound propagation, and collective relaxation dynamics. *Phys. Rev. E*, 70(6):061302, 2004. https://doi.org/10.1103/PhysRevE.70.061302.

[137] C. Thornton. Numerical simulations of deviatoric shear deformation of granular media. *Géotechnique*, 50(1):43–53, 2000. https://doi.org/10.1680/geot.2000.50.1.43.

[138] K. Tanaka, M. Nishida, T. Kunimochi, and T. Takagi. Discrete Element Simulation and experiment for dynamic response of two-dimensional granular matter to the impact of a spherical projectile. *Powder Tech.*, 124(1-2):160–173, 2002. https://doi.org/10.1016/S0032-5910(01)00489-2.

[139] Z. Ning, A. Khoubani, and T.M. Evans. Shear wave propagation in granular assemblies. *Comput. and Geotechnics*, 69:615–626, 2015. https://doi.org/10.1016/j.compgeo.2015.07.004.

[140] P. Sánchez and D.J. Scheeres. Simulating asteroid rubble piles with a self-gravitating soft-sphere distinct element method model. *The Astrophys. J.*, 727(2):120, 2011. https://doi.org/10.1088/0004-637X/727/2/120.

[141] G. Tancredi, A. Maciel, L. Heredia, P. Richeri, and S. Nesmachnow. Granular physics in low-gravity environments using discrete element method. *Mon. Notices of the Roy. Astronom. Soc.*, 420(4):3368–3380, 2012. https://doi.org/10.1111/j.1365-2966.2011.20259.x.

[142] J.V. DeMartini, D.C. Richardson, O.S. Barnouin, N.C. Schmerr, J.B. Plescia, P. Scheirich, and P. Pravec. Using a discrete element method to investigate seismic response and spin change of 99942 Apophis during its 2029 tidal encounter with Earth. *Icarus*, 328:93–103, 2019. https://doi.org/10.1016/j.icarus.2019.03.015.

[143] Y. Zhang, P. Michel, D.C. Richardson, O.S. Barnouin, H.F. Agrusa, K. Tsiganis, C. Manzoni, and B.H. May. Creep stability of the DART/Hera mission target 65803 Didymos II. the role of cohesion. *Icarus*, 362:114433, 2021. https://doi.org/10.1016/j.icarus.2021.114433.

[144] J. O'Donovan, E. Ibraim, C. O'sullivan, S. Hamlin, D. Muir Wood, and G. Marketos. Micromechanics of seismic wave propagation in granular materials. *Granular Matter*, 18(3):1–18, 2016. https://doi.org/10.1007/s10035-015-0599-4.

[145] K.J. Berger and C.M. Hrenya. Predicting regolith erosion during a lunar landing: Role of continuous size distribution. *J. of Aero. Eng.*, 30(5):04017027, 2017. https://doi.org/10.1061/(ASCE)AS.1943-5525.0000735.

[146] H. Otto, K. Kerst, C. Roloff, G. Janiga, and A. Katterfeld. CFD–DEM simulation and experimental investigation of the flow behavior of lunar regolith JSC-1A. *Particuology*, 40:34–43, 2018. https://doi.org/10.1016/j.partic.2017.12.003.

[147] R.C. Hurley and J.E. Andrade. Friction in inertial granular flows: competition between dilation and grain-scale dissipation rates. *Granular Matter*, 17(3):287–295, 2015. https://doi.org/10.1007/s10035-015-0564-2.

[148] R.D. Mindlin and H. Deresiewicz. Elastic spheres in contact under varying oblique forces. *J. of Appl. Mech.*, 20(3):327–344, 1953. https://doi.org/10.1115/1.4010702.

[149] K.L. Johnson, K. Kendall, and A.D. Roberts. Surface energy and the contact of elastic solids. *Proc. of the R. Soc. of Lond. A. Math. and Phys. Sci.*, 324(1558):301–313, 1971. https://doi.org/10.1098/rspa.1971.0141.

[150] L.R. Gómez, A.M. Turner, and V. Vitelli. Uniform shock waves in disordered granular matter. *Phys. Rev. E*, 86(4):041302, 2012. https://doi.org/10.1126/sciadv.aay6898.

[151] G.T. Mase, R.E. Smelser, and G.E. Mase. *Continuum Mechanics for Engineers*. CRC press, 2009. https://doi.org/10.1201/9780429174391.

[152] P. Gupta, J. Sun, and J.Y. Ooi. DEM-CFD simulation of a dense fluidized bed: Wall boundary and particle size effects. *Powder Tech.*., 293:37–47, 2016. https://doi.org/10.1016/j.powtec.2015.11.050.

[153] A.V. Potapov and C.S. Campbell. Propagation of elastic waves in deep vertically shaken particle beds. *Phys. Rev. Lett.*, 77(23):4760, 1996. https://doi.org/10.1103/PhysRevLett.77.4760.

[154] A. Stukowski. Visualization and analysis of atomistic simulation data with OVITO–the Open Visualization Tool. *Modelling and Sim. in Mat. Sci. and Eng.*, 18(1):015012, 2009. https://doi.org/10.1088/0965-0393/18/1/015012.

[155] R.L. Kovach and J.S. Watkins. The velocity structure of the lunar crust. *The Moon*, 7(1):63–75, 1973. https://doi.org/10.1007/BF00578808.

[156] K.T. Chau, R.H.C. Wong, and J.J. Wu. Coefficient of restitution and rotational motions of rockfall impacts. *Int. J. of Rock Mech. and Mining Sci.*, 39(1):69–77, 2002. https://doi.org/10.1016/S1365-1609(02)00016-3.

[157] Y. Zhang, D.C. Richardson, O.S. Barnouin, P. Michel, S.R. Schwartz, and R.-L. Ballouz. Rotational failure of rubble-pile bodies: Influences of shear and cohesive strengths. *The Astrophys. J.*, 857(1):15, 2018. https://doi.org/10.3847/1538-4357/aab5b2.

[158] J. Wang, M. Zhang, L. Feng, H. Yang, Y. Wu, and G. Yue. The behaviors of particle-wall collision for non-spherical particles: Experimental investigation. *Powder Tech.*, 363:187–194, 2020. https://doi.org/10.1016/j.powtec.2019.12.041.

[159] T.P. Gouache, C. Brunskill, G.P. Scott, Y. Gao, P. Coste, and Y. Gourinat. Regolith simulant preparation methods for hardware testing. *Planet. and Space Sci.*, 58(14-15):1977–1984, 2010. https://doi.org/10.1016/j.pss.2010.09.021.

[160] H.P. Zhang and H.A. Makse. Jamming transition in emulsions and granular materials. *Phys. Rev. E*, 72(1):011301, 2005. https://doi.org/10.1103/PhysRevE.72.011301.

[161] J. Wang, M. Lei, H. Yang, K. Xu, S. Xu, P. Zhao, and Y. Song. Effects of coefficient of friction and coefficient of restitution on static packing characteristics of polydisperse spherical pebble bed. *Particuology*, 57:1–9, 2021. https://doi.org/10.1016/j.partic.2020.12.013.

[162] S.V. Mykulyak. Features of nonlinear wave propagation in a layer of a granular medium. *Phys. Mesomech.*, 17(2):157–162, 2014. https://doi.org/10.1134/S1029959914020088.

[163] J.-S. Lee and J. C. Santamarina. Bender elements: Performance and signal interpretation. *J. of Geotech. and Geoenviron. Eng.*, 131(9):1063–1070, 2005. https://doi.org/10.1061/(ASCE)1090-0241(2005)131:9(1063).

[164] O. Mouraille, W.A. Mulder, and S. Luding. Sound wave acceleration in granular materials. *J. of Stat. Mech.: Theory and Exp.*, 2006(07):P07023, 2006. https://doi.org/10.1088/1742-5468/2006/07/P07023.

[165] W. Li, E.N. Hahn, X. Yao, T.C. Germann, B. Feng, and X. Zhang. On the grain size dependence of shock responses in nanocrystalline sic ceramics at high strain rates. *Acta Materialia*, 200:632–651, 2020. https://doi.org/10.1016/j.actamat.2020.09.044.

[166] Z. Ning and T.M. Evans. Discrete element method study of shear wave propagation in granular soil. In *Proceedings of the 18th International Conference on Soil Mechanics and Geotechnical Engineering, France, Paris*, pages 1031–1034, 2013.

[167] Z. Shojaaee, J.-N. Roux, F. Chevoir, and D.E. Wolf. Shear flow of dense granular materials near smooth walls. I. Shear localization and constitutive laws in the boundary region. *Phys. Rev. E*, 86(1):011301, 2012. https://doi.org/10.1103/PhysRevE.86.011301.

[168] E.S. Frizzell. Shock induced dilation, validation code, 2023. https://doi.org/10.5281/zenodo.7608511.

[169] E.S. Frizzell. Shock induced dilation, restart files and single run output code, 2023. https://doi.org/10.5281/zenodo.7608668.

[170] Y. Zhang, D.C. Richardson, O.S. Barnouin, C. Maurel, P. Michel, S.R. Schwartz, R.-L. Ballouz, L.AM. Benner, S.P. Naidu, and J. Li. Creep stability of the proposed AIDA mission target 65803 Didymos: I. Discrete cohesionless granular physics model. *Icarus*, 294:98–123, 2017. https://doi.org/10.1016/j.icarus.2017.04.027.

[171] A.K. Subramaniyan and C.T. Sun. Continuum interpretation of virial stress in molecular simulations. *Int. J. of Solids and Struct.*, 45(14-15):4340–4346, 2008. https://doi.org/10.1016/j.ijsolstr.2008.03.016.

[172] J.D. Goddard. Nonlinear elasticity and pressure-dependent wave speeds in granular media. *Proc. of the R. Soc. of Lond. S. A: Math. and Phys. Sci.*, 430(1878):105–131, 1990. https://doi.org/10.1098/rspa.1990.0083.

[173] L. Li and R.M. Holt. Particle scale reservoir mechanics. *Oil & Gas Sci. and Tech.*, 57(5):525–538, 2002. https://doi.org/10.2516/ogst:2002035.

[174] E. Somfai, J.-N. Roux, J.H. Snoeijer, M. Van Hecke, and W. Van Saarloos. Elastic wave propagation in confined granular systems. *Phys. Rev. E*, 72(2):021301, 2005. https://doi.org/10.1103/PhysRevE.72.021301.

[175] W.Z. Fa, M.-H. Zhu, T.T. Liu, and J.B. Plescia. Regolith stratigraphy at the chang'E-3 landing site as seen by lunar penetrating radar. *Geophys. Res. Lett.*, 42(23):10–179, 2015.

[176] L.S. Mohan, K.K. Rao, and P.R. Nott. A frictional Cosserat model for the slow shearing of granular materials. *J. of Fluid Mechanics*, 457:377–409, 2002. https://doi.org/10.1017/S0022112002007796.

[177] E.S Frizzell and C.M. Hartzell. Simulation of lateral impulse induced inertial dilation at the surface of a vacuum-exposed granular assembly. *Gran. Matt.*, 25(4):75, 2023. https://doi.org/10.1007/s10035-023-01363-6.

[178] Marian Manciu, Surajit Sen, and Alan J Hurd. Impulse propagation in dissipative and disordered chains with power-law repulsive potentials. *Physica D: Nonlinear Phenomena*, 157(3):226–240, 2001. url=https://doi.org/10.1016/S0167-2789(01)00302-5.

[179] Y. Takato and S. Sen. Long-lived solitary wave in a precompressed granular chain. *Europhysics Letters*, 100(2):24003, 2012. https://doi.org/10.1209/0295-5075/100/24003.

[180] D.P Visco Jr, S. Swaminathan, TR-K. Mohan, A. Sokolow, and S. Sen. Impulse penetration into idealized granular beds: behavior of cumulative surface kinetic energy. *Phys. Rev. E*, 70(5):051306, 2004. https://doi.org/10.1103/PhysRevE.70.051306.

[181] M. Arif Hasan and Sia Nemat-Nasser. Universal relations for solitary waves in granular crystals under shocks with finite rise and decay times. *Phys. Rev. E*, 93:042905, Apr 2016.

[182] M Arif Hasan and Sia Nemat-Nasser. Basic properties of solitary waves in granular crystals. *Journal of the Mechanics and Physics of Solids*, 101:1–9, 2017.

[183] M. Arif Hasan and Sia Nemat-Nasser. Shock-induced solitary waves in granular crystals. *Phys. Rev. E*, 97:022205, Feb 2018.

[184] R.K. Pal, A.P. Awasthi, and P.H. Geubelle. Wave propagation in elasto-plastic granular systems. *Granular Matter*, 15(6):747–758, 2013. https://doi.org/10.1007/s10035-013-0449-1.

[185] Christine M Hartzell and Daniel J Scheeres. The role of cohesive forces in particle launching on the moon and asteroids. *Planetary and Space Science*, 59(14):1758–1768, 2011.

[186] Ankit Rohatgi. Webplotdigitizer: Version 4.6, 2022. https://automeris.io/WebPlotDigitizer.

[187] C Rycroft. Voro++: a three-dimensional voronoi cell library in c++. 1 2009. https://doi.org/10.2172/946741.

[188] D.M Cole, M.A Hopkins, and L Taylor. Particle descriptions and grain contact laws for Lunar materials: Their implementation in a discrete element model. In *Earth and Space 2012: Engineering, Science, Construction, and Operations in Challenging Environments*, pages 208–217. 2012. https://doi.org/10.1061/9780784412190.024.

[189] J Hanus, M Viikinkoski, F Marchis, J Durech, M Kaasalainen, M Delbo, D Herald, E Frappa, T Hayamizu, S Kerr, et al. Volumes and bulk densities of forty asteroids from ADAM shape modeling. *A&A*, 2017. https://doi.org/10.1051/0004-6361/201629956.

[190] Y. Yu, D.C. Richardson, P. Michel, S.R. Schwartz, and R.-L. Ballouz. Numerical predictions of surface effects during the 2029 close approach of asteroid 99942 Apophis. *Icarus*, 242:82–96, 2014. https://doi.org/10.1016/j.icarus.2014.07.027.

[191] P Morgan, M Grott, B Knapmeyer-Endrun, M Golombek, P Delage, P Lognonné, S Piqueux, I Daubar, N Murdoch, C Charalambous, et al. A pre-landing assessment of regolith properties at the InSight landing site. *Space Science Rev.*, 214:1–47, 2018. https://doi.org/10.1007/s11214-018-0537-y.

[192] H.J. Melosh. *Planetary Surface Processes*. Cambridge Planetary Science. Cambridge University Press, 2011. https://doi.org/10.1017/CBO9780511977848.

[193] Tiantian Liu, Kai Wünnemann, and Greg Michael. 3d-simulation of lunar megaregolith evolution: Quantitative constraints on spatial variation and size of fragment. *Earth and Planetary Science Letters*, 597:117817, 2022. https://doi.org/10.1016/j.epsl.2022.117817.

[194] Surajit Sen, Marian Manciu, Robert S Sinkovits, and Alan J Hurd. Nonlinear acoustics in granular assemblies. *Granular Matter*, 3(1-2):33–39, 2001.

[195] L. Ponson, N. Boechler, Y.M. Lai, M.A. Porter, P.G. Kevrekidis, and C. Daraio. Nonlinear waves in disordered diatomic granular chains. *Phys. Rev. E*, 82(2):021301, 2010.

[196] J. Hong. Universal power-law decay of the impulse energy in granular protectors. *Phys. Rev. Lett.*, 94(10):108001, 2005. https://doi.org/10.1103/PhysRevLett.94.108001.

[197] S. Sen, J. Hong, J. Bang, E. Avalos, and R. Doney. Solitary waves in the granular chain. *Phys. Reports*, 462(2):21–66, 2008. https://doi.org/10.1016/j.physrep.2007.10.007.

[198] M. Manjunath, A.P. Awasthi, and P.H. Geubelle. Wave propagation in random granular chains. *Phys. Rev. E*, 85(3):031308, 2012. https://doi.org/10.1103/PhysRevE.85.031308.

[199] M. Manjunath, A.P. Awasthi, and P.H. Geubelle. Plane wave propagation in 2D and 3D monodisperse periodic granular media. *Gran. Matt.*, 16:141–150, 2014. https://doi.org/10.1007/s10035-013-0475-z.

[200] S.-S. Wu. *Rockfall evaluation by computer simulation*, volume 1031. Transp. Res. Rec, 1984.

[201] D.D Durda, N. Movshovitz, D.C. Richardson, E. Asphaug, A. Morgan, A.R. Rawlings, and C. Vest. Experimental determination of the coefficient of restitution for meter-scale granite spheres. *Icarus*, 211(1):849–855, 2011. https://doi.org/10.1016/j.icarus.2010.09.003.

[202] R.A.F. Grieve. Terrestrial impact structures. *Ann. Rev. Earth and Planet. Sci.*, 15(1):245–270, 1987.

[203] J. Fleischmann, R. Serban, D. Negrut, and P. Jayakumar. On the importance of displacement history in soft-body contact models. *J. of Comput. and Nonlin. Dyn.*, 11(4), 2016. https://doi.org/10.1115/1.4031197.

[204] A. Mohamed and M. Gutierrez. Comprehensive study of the effects of rolling resistance on the stress–strain and strain localization behavior of granular materials. *Gran. Matt.*, 12(5):527–541, 2010. https://doi.org/10.1007/s10035-010-0211-x.

[205] M. Jiang, Z. Shen, and J. Wang. A novel three-dimensional contact model for granulates incorporating rolling and twisting resistances. *Comput. and Geotechnics*, 65:147–163, 2015. https://doi.org/10.1016/j.compgeo.2014.12.011.